Fundamental physics with black holes and scalar fields

Jamie Bamber

Supervisors: Prof Pedro G. Ferreira and Dr Katy Clough

University College

University of Oxford

A thesis submitted for the degree of

Doctor of Philosophy in Astrophysics

Trinity 2023

I dedicate this thesis to my parents, for your constant love and support.

Statement of Originality

I hereby declare that no part of this thesis has been submitted in support of another degree, diploma, or other qualification at the University of Oxford or other higher learning institute. The research work in part II of this thesis is based on the following publications, completed during my studies in Oxford:

1. Jamie Bamber, Katy Clough, Pedro G. Ferreira, Lam Hui, and Macarena Lagos, *Phys. Rev. D* **103**, 044059 (2021) [1]

2. Jamie Bamber, Oliver J. Tattersall, Katy Clough, and Pedro G. Ferreira, *Phys. Rev. D* **103**, 124013 (2021) [2]

3. Jamie Bamber, Josu C. Aurrekoetxea, Katy Clough, and Pedro G. Ferreira, *Phys. Rev. D* **107**, 024035 (2023) [3]

4. Jamie Bamber, *Phys. Rev. D* **107**, 024013 (2023) [4]

I hereby declare that the research presented is original and entirely my own, with the following exceptions and clarifications:

Chapter 3 is based on Paper 1. I conducted all the numerical simulations, analytic calculations and research, with KC and PGF helping with editing and structure and writing the conclusion and abstract, and LH and ML helping with editing and advice.

Chapter 4 is based on Paper 2. The idea for a perturbative method to compute QNM for static metric perturbations comes from OJT, who also conducted the validation studies for static exponential and power-law potentials shown in appendix C.3. I extended this idea to time-varying spacetimes and growing black holes, deriving the results presented in the main text, and prepared the original draft, with subsequent editing by PGF and KC.

Chapter 5 is based on Paper 3. I conducted all of the simulations and calculations, and wrote the original draft. JCA helped with improving the presentation of the figures, and editing the text, along with PGF and KC.

Chapter 6 is based on Paper 4, which is entirely my own work.

Acknowledgements

I am extremely grateful to my supervisors Pedro G. Ferreira and Katy Clough for their tremendous support and inspiration throughout my DPhil studies, and for training me in the tools of gravitational physics and Numerical Relativity. Their steadfast patience, advice and willingness to share their vast expertise and experience has been invaluable to all the work in this thesis.

In addition to my supervisors I am also deeply indebted to my research collaborators: Lam Hui and Macarena Lagos for their advice and guidance for the work presented in chapter 3, and Oliver Tattersall for the original inspiration for the perturbative quasi normal mode approach presented in chapter 4 and the validation studies for static potentials shown in appendix C.3. I would particularly like to acknowledge Josu C. Aurrekoetxea for his contribution to the work presented in chapter 5, his enthusiastic support over the last couple of years in Oxford, and for showing me how to make plots beautiful.

The wider GRChombo collaboration has provided one of the most helpful and friendly research communities one could ask for, with Dina Traykova, Miren Radia, Robin Croft and Thomas Helfer deserving special acknowledgment. I would also like to thank Ulrich Sperhake and Sebastian Kahn for sharing their black hole binary initial data parameters with us, and to Helvi Witek and Taishi Ikeda for helpful conversations.

Thank you to Pedro Cunha and Paolo Pani for inviting me to talk about my work, and to Tim Dietrich for inviting me to visit his group in Potsdam (even though the COVID pandemic scuppered those plans).

I would also like to acknowledge everyone in the Oxford Astrophysics subdepartment who has supported me during my DPhil, including Ashling Gordon for patiently solving every administrative issue, and to all my fellow DPhil students for their camaraderie and for making this a fantastic journey.

The work presented in this thesis was conducted using the following computational resources: the Glamdring cluster, Astrophysics, Oxford; the Leibnitz Supercomputing Centre SuperMUC-NG under PRACE grant Tier-0 Proposal 2018194669; the Jülich Supercomputing Center JUWELS HPC under PRACE grant Tier-0 Proposal 2020225359; and the STFC DiRAC (Distributed Research

utilising Advanced Computing) resources of COSMA7 in Durham, DiAL3 at Leicester, and the Cambridge Service for Data Driven Discovery (CSD3), part of which is operated by the University of Cambridge Research Computing on behalf of the STFC DiRAC HPC Facility, under the project ACSP218. The DiRAC component of CSD3 was funded by BEIS capital funding via STFC capital grants ST/P002307/1 and ST/R002452/1 and STFC operations grant ST/R00689X/1, while the equipment for DiAL at Leicester was funded by BEIS capital funding via STFC capital grants ST/K000373/1 and ST/R002363/1 and STFC DiRAC Operations Grant ST/R001014/1. Special thanks goes to Thomas Helfer for allowing me to use part of his allocation on Frontera [5], the NSF funded supercomputer at the Texas Advanced Computing Center (TACC) at The University of Texas at Austin.

Abstract

One well-motivated proposal to address the limitations of the Standard Model and General Relativity (GR) is the addition of one or more novel *scalar fields*. In this thesis we will study the interaction of scalar field dark matter (DM) with black holes (BHs), and scalar fields in theories of modified gravity.

The Nobel-Prize-winning detection of gravitational waves (GWs) has opened up a new area of astrophysics. Scalar fields can form dense clouds around BHs, so as most GWs are produced from BH binary mergers, one might be able to detect scalar DM with GW astronomy. We will start by exploring the formation of such clouds, conducting novel simulations of scalar DM accretion onto a spinning Kerr BH, characterising the growth, and estimating the potential for GW signals.

A binary BH merger can be divided into the early inspiral, the highly relativistic merger, and the post-merger "ringdown". First we will examine the ringdown, deriving a novel analytic perturbative formula to estimate the shift in the GW quasi-normal mode frequencies due to an accreting cloud. We will show that the contribution from the accretion rate, previously neglected, can dominate the shift.

For the early inspiral we will simulate the accretion of scalar DM around BHs on fixed orbits, finding that there is a preferred, quasi-stationary scalar field profile. For the highly relativistic regime we use full Numerical Relativity. We will examine the impact of different initial scalar distributions, showing that the quasi-stationary profile is an attractor solution, and that naively superimposing matter onto a quasi-circular binary can produce unphysical eccentricity.

Lastly, we will explore scalar fields beyond GR. Scalar-tensor theories are a popular modified-gravity model, yet they often predict "fifth forces" which are tightly constrained. It has been shown that for scale-invariant gravity the fifth force is highly suppressed. However, this result was obtained in a particular *frame*, and quantum effects make the choice of frame highly non-trivial. We will discuss how one can apply a covariant formalism to extend the result to *all* frames, and show that the usual dichotomy of "Jordan" versus "Einstein" frame can be better understood as a geometric continuum.

Table of contents

List of figures **iv**

I Background Material 1

1 Introduction **2**

1.1 Fundamental physics today 3
1.2 General Relativity 4
1.3 Scalar fields and strong gravity 18

2 Numerical Relativity **26**

2.1 The 3+1 decomposition 27
2.2 Einstein's equations in 3+1 29
2.3 Numerical stability and well-posedness 31
2.4 Improved formulations and conformal transformations 32
2.5 Gauge choice 34
2.6 Matter evolution 35
2.7 Initial data 35
2.8 Fixed background 38
2.9 GRChombo 38

II Research 40

3 The growth of accretion driven scalar field clouds around Kerr black holes **41**

3.1 Framework and numerical setup 45
3.2 Analytic framework 49
3.3 Numerical results 61

3.4 Gravitational waves . . . 74
3.5 Summary and discussion . . . 79

4 The QNM of growing dirty black holes 81
4.1 The perturbed metric of accreting dark matter . . . 83
4.2 Quasi-normal mode equations on the perturbed background . . . 87
4.3 Perturbative method for computing the quasi-normal modes . . . 90
4.4 Complex massive scalar field accretion . . . 95
4.5 Summary and discussion . . . 98

5 Black hole merger simulations in wave DM environments 100
5.1 Modelling wave DM around black holes . . . 104
5.2 Fixed orbit simulations . . . 106
5.3 GR evolution with G=0 . . . 109
5.4 GR evolution with G=1 . . . 113
5.5 Summary and discussion . . . 116

6 Fifth forces and frame invariance 118
6.1 Background . . . 121
6.2 Selecting a frame: a geometric approach . . . 125
6.3 Computing fifth forces with the geometric approach . . . 127
6.4 Scale-invariant theory . . . 132
6.5 The field space metric and higher-order corrections . . . 133
6.6 Summary and discussion . . . 136

7 Conclusions 138
7.1 Black holes and scalar clouds: accretion . . . 138
7.2 Black holes and scalar clouds: quasi-normal modes . . . 139
7.3 Black holes and scalar clouds: binary mergers . . . 140
7.4 Beyond GR: fifth forces and frame invariance . . . 141

III Extra Material 143

A Numerical Relativity 144
A.1 The Lie derivative . . . 144
A.2 The CCZ4 evolution equations . . . 145

B The growth of accretion driven scalar hair around Kerr black holes 147
B.1 Code validation and coordinate choice 147
B.2 Conserved fluxes 149
B.3 Convergence tests 150

C The QNM of growing dirty black holes 153
C.1 Perturbation theory 153
C.2 Method in Schwarzschild coordinates 155
C.3 Testing the method 158

D Black hole merger simulations in wave DM environments 163
D.1 Numerical implementation and convergence tests 163

E Fifth force constraints 166

Bibliography 167

List of figures

1.1 Finkelstein diagram 9
1.2 Stages of a black hole binary merger. 14
1.3 LIGO/Virgo/KAGRA black holes and neutron stars. 15
1.4 Dark matter candidates 23
1.5 Cosmological simulations of structure formation with "fuzzy" light scalar dark matter and particle cold dark matter. 23

2.1 Foliation of spacetime 28
2.2 Black hole binary with AMR in GRChombo 39

3.1 Visualisation of the 2D scalar field profile around a spinning black hole 42
3.2 The energy density and angular momentum density of a scalar field cloud around a spinning black hole 44
3.3 Schwarzschild effective potential 53
3.4 Kerr quasi-effective potential 55
3.5 Angular momentum per unit mass for a scalar field and an orbiting massive particle around a Kerr black hole 57
3.6 Scalar field radial profile vs spin: $l = m = 0$ 62
3.7 Scalar field radial profile: evolution over time 62
3.8 Scalar field profile compared to stationary and perturbative solutions 63
3.9 Scalar field radial profile vs black hole spin: $l = m = 1$ 64
3.10 Radial energy density profile vs black hole spin 65
3.11 Mass flux into the scalar field vs l, m 66
3.12 Radial energy density profile vs scalar field initial l, m 67
3.13 Mass flux into the scalar field cloud vs μ 67
3.14 Radial energy density profile vs μ 68
3.15 Mass flux into the scalar field cloud vs alignment angle α 69

3.16 Mass flux into the scalar field cloud vs α: smaller radius 69
3.17 Radial energy density profile vs alignment angle α 70
3.18 Visualisation of the scalar field energy density for different α 71
3.19 Angular momentum flux into the scalar cloud vs scalar field initial l, m 73
3.20 Ratio of ρ_J/ρ_E to m/μ 73
3.21 Real scalar field cloud emitting radiation 75

5.1 Evolution of the scalar field and energy density on a fixed orbit black hole binary background 106
5.2 Normalised density and scalar field profiles along half of the fixed orbit binary axis 108
5.3 Comparison of the initial scalar field data profiles 110
5.4 Evolution of the scalar field $|\varphi|$ profile for different initial data . . . 112
5.5 Black hole orbital trajectories 115

6.1 t-channel tree diagram for fermion-fermion scattering. 130

7.1 Scalar dark matter cloud around a black hole binary 141

B.1 Code check: mass flux conservation 150
B.2 Convergence test: mass flux conservation 151
B.3 Convergence test: relative error in mass flux 152
B.4 Mass flux: improvement with increasing resolution 152

C.1 Power law potential quasi-normal modes: analytic vs numeric . . . 160

D.1 Convergence test: constraint satisfying initial data 164
D.2 Convergence test: black hole puncture trajectory 165

E.1 Fifth force constraints 166

Part I

Background Material

Chapter 1

Introduction

This thesis is divided into three parts: background material, research and extra material.

The first part consists of two chapters: chapter 1 describes the general theoretical background and some of the broad unsolved questions which motivate this area of research, while chapter 2 gives an overview of Numerical Relativity (NR), the method of simulating General Relativity on a computer, and a key tool in strong gravity research and for the work presented in part II of the thesis. Readers familiar with the field may wish to skip over one or both of these chapters, however they are intended to provide broader context and define concepts we shall use later.

The second part contains the core of the thesis, describing original research work and results concerning scalar fields and strong gravity across four key areas. First in chapter 3 we will study the the accretion of scalar field dark matter (DM) clouds around Kerr black holes using novel numerical simulations, exploring how the growth depends on the parameters of the system, and relating the results to analytic perturbative models of the growth process. We will also estimate the monochromatic gravitational wave (GW) signal from such accreting scalar clouds, and discuss whether they could be detected by current and future GW detectors. In chapter 4 we will explore how such an accreting cloud of matter could affect the quasi-normal mode frequencies of the final "ringdown" portion of a binary black hole (BH) merger, and derive a novel perturbative analytic formula for the time-dependent frequency shifts. We find that the contribution from accretion, previously neglected, can in fact dominate over the non-accretion contribution. In chapter 5 we will first examine scalar field accretion around a black hole binary in the early inspiral regime of a BH binary merger. We find that the field quickly

settles into a persistent quasi-stationary spiral profile which grows over time. We then conduct simulations of the highly relativistic regime using full NR, exploring the impact of different initial data including both the quasi-stationary scalar profile and alternative choices. In chapter 6 we will consider scalar fields in scalar-tensor theories of modified gravity. We will show how one can resolve the ambiguity between quantum scalar-tensor theories in different frames using a novel geometric approach, and how this can be applied to the calculation of fifth forces to arbitrary perturbative order. In particular, we will use this to show that scale-invariant scalar-tensor theories can evade fifth force constraints in all frames.

Finally, the last part of the thesis contains more detailed derivations omitted in the main text, and additional material for each of the chapters described in part II including convergence tests and validation studies.

Throughout we will use Einstein summation convention and the mostly plus metric signature $(-,+,+,+)$. In this part, and in part II chapter 6, will use Planck units $\hbar = G = c = 1$. In chapters 3,4 and 5 we will use geometric units $G = c = 1$, as will be made clear.

1.1 Fundamental physics today

Modern fundamental physics can be said to a large extent rely on two extremely successful theories: the Standard Model of particle physics, which describes the interactions of elementary particles on small scales, and Einstein's General Theory of Relativity, which describes gravity and gravitational dynamics on large scales, including the evolution of the universe as a whole.

Both theories (as of the time of writing) have passed all experimental tests with flying colours, including both detailed studies of high energy proton collisions at the Large Hadron Collider (LHC) [6, 7], and novel astrophysical observations such as the radio imaging of the shadows of the supermassive black holes M87* and Saggitarius A* by the Event Horizon Telescope (EHT) [8, 9].

However, there are good reasons to think that these theories cannot be the complete picture of fundamental physics. In this thesis we will describe how we can use black holes and gravitational waves to explore theories of new scalar fields, which might provide solutions to some of the big unsolved problems in physics today.

1.2 General Relativity

1.2.1 Fundamentals

Einstein's theory of special relativity, first published in 1905 [10], was based on the two fundamental postulates: that the laws of physics appear identical in all inertial frames of reference (frames of reference with no acceleration), and that the speed of light is constant for all observers (in order to ensure Maxwell's equations remain invariant). General Relativity goes further with two additional postulates:

- **Principle of general covariance:** the laws of physics appear the same to *all observers*.
- **The equivalence principle:** all particles in free fall in the same gravitational field experience the same acceleration, regardless of their mass (i.e. inertial mass equals gravitational mass).

From these simple ideas an entirely new understanding of space, time and the universe was derived.

A fundamental idea is that gravity is described using geometry, as the curvature of spacetime. Spacetime itself is as a manifold, specifically a four dimensional, smooth, connected, Lorentzian manifold. A manifold is a space that can be one-to-one mapped to $\mathbb{R}^N$, where N is the dimension of the space, using coordinates x^μ. A vector $v^\mu(x)$ at a point x is an element of the local tangent space $\mathcal{T}_x$ at that point. The local geometry of the spacetime is determined by a metric $g_{\mu\nu}(x)$ which defines an inner product between vectors, where the inner product of two vectors v^μ, u^μ is $g_{\mu\nu}v^\mu u^\mu$.

The inner product also allows us to also define covectors $v_\mu = g_{\mu\nu}v^\nu$ which are elements of the dual "cotangent" space $\mathcal{T}_x^*$ [11, 12]. The inner product of two infinitesimal displacement vectors dx^μ at a point specifies a coordinate invariant "interval" or "line element",

$$ds^2 = g_{\mu\nu}(x)dx^\mu dx^\nu. \tag{1.1}$$

The inverse metric $g^{\mu\nu}$ is defined such that $g^{\mu\nu}g_{\nu\lambda} = \delta^\mu_\lambda$, the Kronecker delta. Hence indices can be raised by contracting with $g^{\mu\nu}$ and lowered by contracting with $g_{\mu\nu}$, where *contracting* refers to the sum over one upstairs and one downstairs index. In flat space we recover special relativity and the Minkowski metric $g_{\mu\nu} = \eta_{\mu\nu} := \text{diag}(-1, 1, 1, 1)$ in Cartesian coordinates. At any point in the manifold

we can define a set of local inertial coordinates such that the spacetime appears locally flat and the metric appears locally Minkowski in the infinitesimal region of that point. Vectors can be classified according to their inner product with themselves: if $g_{\mu\nu}v^\mu v^\nu > 0$ the vector v^μ is *spacelike*, if $g_{\mu\nu}v^\mu v^\nu < 0$ the vector is *timelike* and if $g_{\mu\nu}v^\mu v^\nu = 0$ the vector is *null*. In Minkowski spacetime a vector in the time direction $t^\mu = \delta^\mu_0 = (1,0,0,0)$ is timelike and a vector in a spatial direction is spacelike.

In order to satisfy the principle of general covariance, we want our physical laws to be invariant under a (passive) change of coordinates $x^\mu \to x'^\mu$. This means it is useful to work with objects called "tensors", which transform under a coordinate change as

$$T'^{a_1 a_2 \ldots a_n}_{b_1 b_2 \ldots b_m} = \frac{\partial x'^{a_1}}{\partial x^{c_1}} \frac{\partial x'^{a_2}}{\partial x^{c_2}} \cdots \frac{\partial x'^{a_n}}{\partial x^{c_n}} \frac{\partial x^{d_1}}{\partial x'^{b_1}} \frac{\partial x^{d_2}}{\partial x'^{b_2}} \cdots \frac{\partial x^{d_m}}{\partial x'^{b_m}} T^{c_1 c_2 \ldots c_n}_{d_1 d_2 \ldots d_m}. \tag{1.2}$$

A tensor with n upstairs indices and m downstairs indices is called a type (n,m) tensor. The metric $g_{\mu\nu}$ is a type $(0,2)$ tensor, vectors and covectors are type $(1,0)$ and $(0,1)$ respectively, and scalars with no indices are type $(0,0)$. The contraction of a vector and a covector $u_\mu v^\mu$ or the inner product two vectors and the metric $g_{\mu\nu}v^\mu u^\mu$ gives a scalar, and in general contracting two tensors together gives another tensor.

The spacetime partial derivative ∂_μ of a tensor is not necessarily a tensor. Instead we define a *covariant* derivative denoted ∇_μ such that the covariant derivative of a type (n,m) tensor is always a type $(n,m+1)$ tensor. For a vector it is

$$\nabla_\mu V^\nu = \partial_\mu + \Gamma^\mu_{\nu\lambda} V^\lambda, \tag{1.3}$$

where $\Gamma^\mu_{\nu\lambda}$ is called the connection, usually chosen to be the Levi-Civita connection which is given in index form by the Christoffel symbols

$$\Gamma^\mu_{\nu\lambda} = \frac{1}{2} g^{\mu\alpha} \left(\partial_\nu g_{\alpha\lambda} + \partial_\lambda g_{\nu\alpha} - \partial_\alpha g_{\nu\lambda} \right). \tag{1.4}$$

Note that the connection coefficients are symmetric in the lower two indices $\Gamma^\mu_{\nu\lambda} = \Gamma^\mu_{\lambda\nu}$. For a scalar φ we have simply $\nabla_\mu \varphi = \partial_\mu \varphi$. One can also show that

$$\nabla_\lambda g_{\mu\nu} = 0. \tag{1.5}$$

Unlike partial derivatives in flat space, covariant derivatives do not always commute, with $[\nabla_\mu, \nabla_\nu] V^\alpha := R^\alpha_{\beta\mu\nu} V^\beta$. The $R^\alpha_{\beta\mu\nu}$ is called the Riemann curvature tensor. Written in lowered form it is antisymmetric in two pairs of indices

$R_{\alpha\beta\mu\nu} = -R_{\beta\alpha\mu\nu} = R_{\beta\alpha\nu\mu}$ and symmetric such that $R_{\alpha\beta\mu\nu} = R_{\mu\nu\alpha\beta}$. It can be written in terms of the connection and its derivatives, and as its name suggests contains information about the curvature of the spacetime. We can use it to define the Ricci tensor $R_{\mu\nu} := R^{\alpha}_{\alpha\mu\nu}$ and the Ricci scalar $R := R^{\alpha}_{\alpha}$. Einstein's field equations (1.6) describe how the curvature of spacetime, encoded via the Einstein tensor $G_{\mu\nu}$ which is a function of $g_{\mu\nu}$ and its derivatives, relates to matter, encoded via the (symmetric) energy-momentum tensor $T_{\mu\nu}$,

$$G_{\mu\nu} = 8\pi T_{\mu\nu}, \tag{1.6}$$

where the (symmetric) Einstein tensor $G_{\mu\nu} := R_{\mu\nu} - \frac{1}{2}g_{\mu\nu}R$. The Einstein equations can also be written in trace reversed form as

$$R_{\mu\nu} = 8\pi \left(T_{\mu\nu} - \tfrac{1}{2}g_{\mu\nu}T\right), \tag{1.7}$$

where $T = g^{\mu\nu}T_{\mu\nu}$. Conservation of energy and momentum is expressed via the conservation of the energy-momentum tensor, $\nabla_{\mu}T^{\mu\nu} = 0$.

In local inertial coordinates we recover special relativity, and in special relativity the 4-momentum of a particle in an inertial frame is $p^{\mu} = (E, \boldsymbol{p})$ where E is the energy and $\boldsymbol{p}$ the relativistic 3-momentum. The inner product of p^{μ} with itself using the Minkowski metric is

$$g_{\mu\nu}p^{\mu}p^{\nu} = p^{\mu}p_{\mu} = -E^2 + |\boldsymbol{p}|^2 = -m_0^2, \tag{1.8}$$

where m_0 is the particle rest mass, so for massive particles with $m_0 > 0$ the 4-momentum is a timelike vector. The 4-momentum is related to the 4-velocity $u^{\mu} = \mathrm{d}x^{\mu}/\mathrm{d}\tau$, where τ is the proper time, by $p^{\mu} = m_0 u^{\mu}$, so $u^{\mu}u_{\mu} = -1$ and u^{μ} is also timelike. For massless particles like photons $p^{\mu}p_{\mu} = 0$ so p^{μ} is a null vector. The photons trajectory is parallel to p^{μ}, so we can define $p^{\mu} = \mathrm{d}x^{\mu}/\mathrm{d}\lambda$ where λ is an affine parameter which parameterises the photon's trajectory curve. As scalars are coordinate invariant, these relations $u^{\mu}u_{\mu} = -1$ for massive particles and $p^{\mu}p_{\mu} = 0$ for photons must hold generally, which means that particles travel along *geodesics*, which are trajectories that extremise the path length between two points, $\int \mathrm{d}s = \int \sqrt{g_{\mu\nu}\mathrm{d}x^{\mu}\mathrm{d}x^{\nu}}$, integrated along the trajectory. Curvature in the metric therefore affects particle motion, producing what we measure as gravitational force. As John Wheeler summarised [13]:

"Matter tells space how to curve, space tells matter how to move."

In other words, matter moves along geodesic paths determined by the spacetime curvature, which in turn is sourced by the matter energy-momentum. We can also derive the Einstein field equations by applying the principle of least action to the Einstein-Hilbert action

$$S = \frac{1}{16\pi}\int \mathrm{d}^4x\sqrt{-g}R + S_M, \tag{1.9}$$

where S_M includes all the matter terms with

$$T_{\mu\nu} = -\frac{2}{\sqrt{-g}}\frac{\delta S_M}{\delta g^{\mu\nu}}. \tag{1.10}$$

Although the Einstein field equations look simple, they are really a system of 10 non-linear, second-order, coupled partial differential equations (PDEs), and it is very challenging to find explicit analytic solutions, except in some simple cases with lots of symmetry or very weak fields. A useful concept is that of a *Killing vector field* or "Killing vector", a vector X^μ which satisfies the Killing equation

$$\nabla_\mu X_\nu + \nabla_\nu X_\mu = 0, \tag{1.11}$$

or equivalently $\mathcal{L}_{\vec{X}} g_{\mu\nu} = 0$ (see appendix A.1). If the metric is independent of a coordinate σ then δ^μ_σ is a Killing vector [14].

Due to general covariance we are free to choose different coordinates to work in. This freedom can also be described as *gauge* freedom, and instead of specifying coordinates explicitly we may instead want to choose coordinates implicitly by imposing conditions on our tensor fields, a procedure termed *gauge fixing*.

1.2.2 Black holes

In the same year that Albert Einstein published his theory of General Relativity Karl Schwarzschild – while serving in the German army during WW1 – derived the first exact non-trivial solution of the Einstein equations [15]. The Schwarzschild metric describes the spacetime outside a static spherically symmetric mass, and is given by

$$\mathrm{d}s^2 = -\left(1-\frac{2M}{r}\right)\mathrm{d}t^2 + \left(1-\frac{2M}{r}\right)^{-1}\mathrm{d}r^2 + r^2\left(\mathrm{d}\theta^2 + \sin^2\theta\mathrm{d}\phi^2\right), \tag{1.12}$$

where r, θ, ϕ are spherical polar coordinates and M is the mass. It was soon noted that this solution has a peculiar behaviour: if the radius of the object is less than the Schwarzschild radius, $R_s = 2M = 2GM/c^2$ then the metric appears to diverge

giving an apparent singularity. The Schwarzschild radius is $R_s = 2.95(M/M_\odot)$km for an object mass M, where $M_\odot$ denotes the mass of the Sun.[1] Eventually it was realised that this corresponds to an "event horizon", a surface inside of which nothing, not even light, could escape, and that the collapse of massive stars could form such objects dubbed "black holes". To see this we can construct new coordinates which vary smoothly across $r = R_s$. For a photon on a radial null geodesic $\mathrm{d}s^2 = g_{tt}\mathrm{d}t^2 + g_{rr}\mathrm{d}r^2 = 0$ so

$$\frac{\mathrm{d}t}{\mathrm{d}r} = \pm\sqrt{-\frac{g_{rr}}{g_{tt}}} = \pm\left(1 - \frac{2M}{r}\right)^{-1}, \tag{1.13}$$

$$t = \pm\, r_* + const., \tag{1.14}$$

where $r_* := r + 2M\ln\left|\frac{r}{2M} - 1\right|$ is the so-called "tortoise" coordinate (named after Zeno's paradox of Achilles and a tortoise) and the $\pm$ is for outgoing and ingoing photons respectively. This motivates a new time coordinate $t' = t + 2M\ln\left|\frac{r}{2M} - 1\right|$ so that $t' = -r$ for ingoing photons and $t' = r + 4M\ln\left|\frac{r}{2M} - 1\right|$ for outgoing photons. The line element in these "ingoing" coordiantes is

$$\mathrm{d}s^2 = -\left(1 - \frac{2M}{r}\right)\mathrm{d}t'^2 + \frac{4M}{r}\mathrm{d}t'\mathrm{d}r + \left(1 + \frac{2M}{r}\right)\mathrm{d}r^2 + r^2\left(\mathrm{d}\theta^2 + \sin^2\theta\mathrm{d}\phi^2\right). \tag{1.15}$$

The metric components no longer diverge at $r = R_s = 2M$, as it is merely a coordinate singularity, while the divergence at $r = 0$ persists. Plotting the paths of the two families of geodesics in t', r coordinates gives a so-called ingoing Finkelstein diagram (Fig. 1.1). We see that for $r < R_s$ all null geodesics go towards $r = 0$, so no photon trajectory can escape to infinity. Timelike geodesics from a point must lie within the *light cone* bounded by the forward-pointing null geodesics from that point, so massive particles also cannot escape once they cross $r = R_s$. We may note that the limiting condition occurs when the outgoing null geodesics u^μ are tangent to the surface $r = const.$. In general a hypersurface $f(x) = const.$ has normal covector $n_\mu = \nabla_\mu f(x)$ which is perpendicular to its tangent vectors. Therefore the normal covector for this hypersurface satisfies $n_\mu u^\mu = 0$, but as $u^\mu u_\mu = 0$ one can show that u^μ is both tangent *and* normal to the hypersurface, that $n_\mu \propto u_\mu$, and that therefore $n^\mu n_\mu = 0$. This means n^μ is a null vector and the hypersurface is a *null hypersurface*. In general all event horizons are null hypersurfaces [14].

[1] For comparison the radius of the Sun is $\sim 6.96 \times 10^5$km.

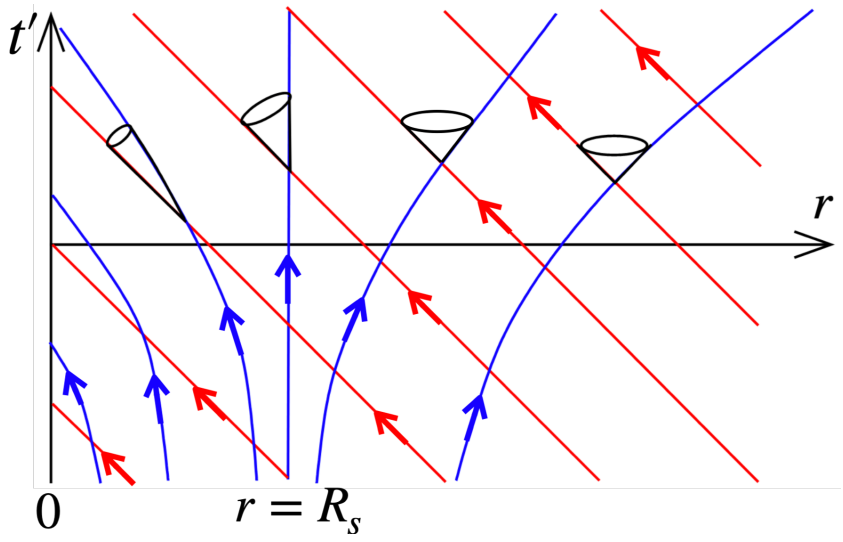

Figure 1.1: **Finkelstein diagram**. Ingoing null geodesics are shown in red and outgoing in blue, with light cones shown in black. We see that for $r < R_s$ both ingoing and "outgoing" geodesics only go inwards as the light cones tip over (figure adapted from [16]).

In 1963 Roy Kerr discovered the exact solution for a rotating black hole, the Kerr metric [17], given in Boyer Lindquist (BL) coordinates $\{t,\, r,\, \theta,\, \phi\}$ by [18]:

$$ds^2 = -\left(1 - \frac{2Mr}{\Sigma}\right) \mathrm{d}t^2 - \frac{4aMr\sin^2\theta}{\Sigma}\mathrm{d}t\mathrm{d}\phi + \frac{\Sigma}{\Delta}\mathrm{d}r^2 + \Sigma \mathrm{d}\theta^2 + \frac{\mathcal{A}}{\Sigma}\sin^2\theta \mathrm{d}\phi^2, \quad (1.16)$$

or equivalently

$$ds^2 = -\frac{\Sigma\Delta}{\mathcal{A}}\mathrm{d}t^2 + \frac{\Sigma}{\Delta}\mathrm{d}r^2 + \Sigma\mathrm{d}\theta^2 + \frac{\mathcal{A}}{\Sigma}\sin^2\theta\left(\mathrm{d}\phi - \Omega \mathrm{d}t\right)^2, \quad (1.17)$$

where

$$\mathcal{A} = (r^2 + a^2)^2 - \Delta a^2 \sin^2\theta\ , \quad (1.18)$$

$$\Delta = r^2 - 2Mr + a^2, \quad (1.19)$$

$$\Sigma = r^2 + a^2\cos^2\theta, \quad (1.20)$$

$$\Omega = \frac{2aMr}{\mathcal{A}}, \quad (1.21)$$

and $a = J/M$ is the Kerr spin parameter, with J being the angular momentum and M the mass of the black hole. We can also define the dimensionless spin parameter $\chi = a/M$ which takes a value between 0 (Schwarzschild) and 1 (extremal spinning). As the metric is independent of coordinates t, ϕ there are two Killing vectors, δ^μ_t and δ^μ_ϕ, associated with the conservation of energy and angular momentum

respectively. To find the event horizons we can look for null hypersurfaces of constant r, with

$$g^{\mu\nu}n_\mu n_\nu = g^{\mu\nu}\delta^r_\mu\delta^r_\nu = g^{rr} = 1/g_{rr} = \frac{\Delta}{\Sigma} = 0. \tag{1.22}$$

Solving $\Delta = 0$ gives two solutions $r = r_\pm \equiv M \pm \sqrt{M^2 - a^2}$ denoted the outer and inner horizon respectively. For $a \to 0$ these reduce to the Schwarzschild horizon $r = 2M$, and one can prove that in BL coordinates $r = r_\pm$ are indeed event horizons. The region between the outer horizon and the surface $g_{tt} = 0$ is called the *ergosphere*. This has several peculiar properties. In the local inertial coordinates of an observer with 4-velocity u^μ a particle has 4-momentum $p^\mu = (E, \boldsymbol{p})$ and $u^\mu = (1, 0, 0, 0)$, so the energy measured by the observer is $E = -u^\mu p_\mu$ in all coordinates as E is scalar. For stationary observers $u^\mu \propto \delta^\mu_t$ this energy is conserved as δ^μ_t is a Killing vector. Far from the black hole u^μ and p^μ are always timelike or null, meaning $E \geq 0$ as we might expect. However, within the ergosphere $g_{tt} > 0$ so the 4-velocity of stationary observers becomes spacelike, and $E = -g_{tt}u^t p^t$ can be negative: particles can have *negative energy*![2] In addition, consider a photon emitted in the ϕ direction. Initially it has $\mathrm{d}r = \mathrm{d}\theta = 0$, so

$$\mathrm{d}s^2 = g_{tt}\mathrm{d}t^2 + 2g_{t\phi}\mathrm{d}t\mathrm{d}\phi + g_{\phi\phi}\mathrm{d}\phi^2 = 0, \tag{1.23}$$

$$\frac{\mathrm{d}\phi}{\mathrm{d}t} = \frac{-g_{t\phi}}{g_{\phi\phi}} \pm \sqrt{\left(\frac{g_{t\phi}}{g_{\phi\phi}}\right)^2 - \frac{g_{tt}}{g_{\phi\phi}}}. \tag{1.24}$$

Within the ergosphere $g_{\phi\phi} > 0, g_{tt} > 0$ and $g_{t\phi} < 0$ for $a > 0$ so the only solutions have $\frac{\mathrm{d}\phi}{\mathrm{d}t} > 0$. In other words, no matter what the photon is dragged along in the same direction as the rotation of the black hole, a phenomenon known as *frame dragging*. The minimum angular velocity of a particle on the outer event horizon itself is $\Omega_H = \Omega(r = r_+) = \chi/(2r_+)$ [14].

Despite their exotic nature, a set of uniqueness theorems – dubbed "no-hair" theorems – state that the properties of black holes can be fully determined by a small number of parameters: their mass M, angular momentum J, and electric charge Q, and cannot support non-trivial profiles of other fields [22–25] dubbed "hair". The electric charge Q is usually assumed to be negligible for astrophysical black holes, as any initial charge is rapidly neutralised by the ionized host environment [26, 27].

[2] Although these negative energy particles cannot escape to infinity, this phenomenon underpins the Penrose process and superradiance [19–21].

These theorems apply under both General Relativity and a broad class of extensions which are of cosmological interest [28–30]. However, they depend on a number of restrictive assumptions, and violating one or more of these may allow black holes to acquire "hair" [25, 29, 31], motivating a great deal of research.

Black holes formed from the collapse of massive stars are typically thought to range in mass from $\sim 3M_\odot$ to order $10^2 M_\odot$ with an empty "mass-gap" between $\sim 50 - 130M_\odot$ due to the pair instability[3] [32, 33]. Supermassive black holes found at the centres of galaxies and dwarf galaxies are thought to range from $10^5 - 10^{10} M_\odot$ [34]. There are currently few observational constraints on so-called Intermediate-Mass Black Holes with masses $10^2 - 10^4 M_\odot$, however they could potentially be formed though mergers of stellar origin black holes in globular clusters, among other mechanisms [35]. Finally some people have proposed that black holes of much smaller masses, so called "primordial black holes" [36, 37], could have been formed in the early universe.

If the collapsed core of a massive star has mass between $1.4M_\odot$ to $\sim 2M_\odot$, the nuclear forces and neutron degeneracy pressure are sufficient to halt gravitational collapse and instead of a black hole a neutron star is formed [38, 39]. These can be thought of as similar to a giant atomic nucleus, with an outer layer of closely packed atomic nuclei, and inner layers of more neutron-rich nuclear material and potentially an inner core of ultra-dense quark-gluon plasma. The precise equation of state, and hence the radius, of neutron stars is uncertain, however the radius of a typical neutron star has been estimated as $\sim$ 10–12km [38, 40, 41]. Highly magnetised rotating neutron stars can emit strong beams of electromagnetic radiation from their poles. If these sweep the Earth as the star rotates they appear as highly regular repeating pulsed radio sources called "pulsars" [38, 42].

1.2.3 Gravitational waves

Unlike in Newtonian gravity, where changes in the gravitational field are assumed to propagate instantly, in General Relativity oscillations in the spacetime metric propagate at the speed of light as gravitational waves. The idea of gravitational waves had been suggested prior to 1915, based on the analogy between gravity and electromagnetism, however Einstein was able to (eventually) derive a gravitational wave equation directly from the weak field limit of the Einstein equations [43]. If

[3] An instability associated with the production of electron-positron pairs which causes stars to explode completely in supernovae without forming a black hole remnant.

$g_{\mu\nu} = \eta_{\mu\nu} + h_{\mu\nu}$, where $h_{\mu\nu}$ is a small perturbation about flat Minkowski space, we can expand the Einstein field equations to first order in $h_{\mu\nu}$ and obtain the sourced wave equation

$$-2G_{\mu\nu} \approx \Box \bar{h}_{\mu\nu} = -16\pi T_{\mu\nu}, \tag{1.25}$$

where $\Box = \nabla_\alpha \nabla^\alpha = \partial_\alpha \partial^\alpha = -\partial_t^2 + \nabla^2$ is the flat space d'Alembertian, we assume $T_{\mu\nu}$ is order $h_{\mu\nu}$, $\bar{h}_{\mu\nu} := h_{\mu\nu} - \frac{1}{2}\eta_{\mu\nu}h$ is the trace reversed perturbation with trace $h = \eta_{\mu\nu}h^{\mu\nu}$, and we use the *De Donder* or *Lorenz* gauge with $\partial_\mu \bar{h}^{\mu\nu} = 0$.

In vacuum, with $T_{\mu\nu} = 0$, we can make an additional gauge choice to set $h_{\mu 0} = h = \partial_i h^{ij} = 0$, defining the *transverse-traceless gauge*. We hence reduce the original ten degrees of freedom of the symmetric $h_{\mu\nu}$ to two remaining physical degrees of freedom, corresponding to two polarisations of gravitational waves. We can describe this as

$$h_{ij}^{TT} = \begin{bmatrix} h_+ & h_\times & 0 \\ h_\times & -h_+ & 0 \\ 0 & 0 & 0 \end{bmatrix}_{ij} \cos(\omega(t-z)), \tag{1.26}$$

for a gravitational wave travelling in the z direction, where $h_+, h_\times$ are the amplitudes of the "plus" and "cross" polarisations respectively. The amplitude of a gravitational wave from an oscillating source can be approximately given by the lowest order quadrupole radiation which is

$$\left[h_{ij}^{TT}\right]_{\text{quad}} = \frac{1}{r}\frac{2G}{c^4}\ddot{Q}_{ij}(t - r/c), \tag{1.27}$$

where r is the distance to the source, an overdot denotes a time derivative, and the quadrupole is

$$Q^{ij} := \int \mathrm{d}x^3 \rho \left(x^i x^j - \tfrac{1}{3}|\boldsymbol{x}|^2 \delta^{ij}\right), \tag{1.28}$$

where ρ is the mass density. For a source made up of two orbiting bodies of total mass M and velocity v this gives

$$h_{ij}^{TT} \sim \frac{1}{r}\frac{2GM}{c^2}\left(\frac{v}{c}\right)^2, \tag{1.29}$$

so the strongest signals will come from sources of large mass, nearby, moving at relativistic speeds. This includes some of the most cataclysmic events in the universe, such as core-collapse supernovae and in particular binary black hole and neutron star mergers.

As a gravitational wave passes through space it distorts the distance between free falling bodies, and we can use this effect to detect the signal. The laser interferometers of LIGO [44] (the Laser Interferometer Gravitational-Wave Observatory in the USA) and Virgo [45] (in Italy) made the first direct detection of gravitational waves from a binary black hole merger in 2015 [46], and subsequent sensitivity upgrades have allowed for the detection of 90 individual gravitational wave events as of early 2023 [47] (see Fig. 1.3). Another detector, KAGRA [48], came online in 2020 and more are planned, including the space based LISA [49] and future third generation detectors such as the Einstein Telescope [50] and Cosmic Explorer [51].

1.2.4 Black hole binary mergers

All the gravitational wave signals detected to date have been from the mergers of compact binaries: binary systems of two black holes, two neutron stars or one of each. As they orbit they progressively lose energy due to the emission of gravitational waves, causing the orbital separation to decrease and the frequency to increase, until they eventually merge [52]. The simplest case is for two black holes with spins aligned along the axis of the orbital angular momentum of the binary, in which case the orbital motion is confined to a two dimensional plane. The binary merger and corresponding gravitational wave signal can be divided into three regimes:

1. **The early inspiral**. This is the regime where the compact objects are widely separated and slowly moving with $v/c \ll 1$ where v is the velocity. As the strength of the gravitational wave signal depends on $(v/c)^2$ the amplitude and energy of the gravitational waves emitted is very small, and the binary separation and frequency change only very slowly. As a consequence this is the regime where the binary spends most of its lifespan. This regime can be well described using post-Newtonian (PN) theory (see [53] for a review) where corrections to the Newtonian gravity solution are systematically added order-by-order in small parameter $\epsilon = (v/c)^2$.

2. **The highly relativistic merger**. This regime includes the last few orbits before merger and the actual merger itself, where the compact objects are moving at relativistic speeds, are very close together, and the gravity is very

strong. For comparable mass binaries this regime can only be well modelled using Numerical Relativity.

3. **The ringdown**. The final stage of most compact object mergers is the formation of a daughter black hole.[4] The black hole is formed in an excited state and "rings" like a bell, radiating energy in the form of gravitational waves until it settles down into a stable configuration. These decaying oscillations can be well described using black hole perturbation theory.

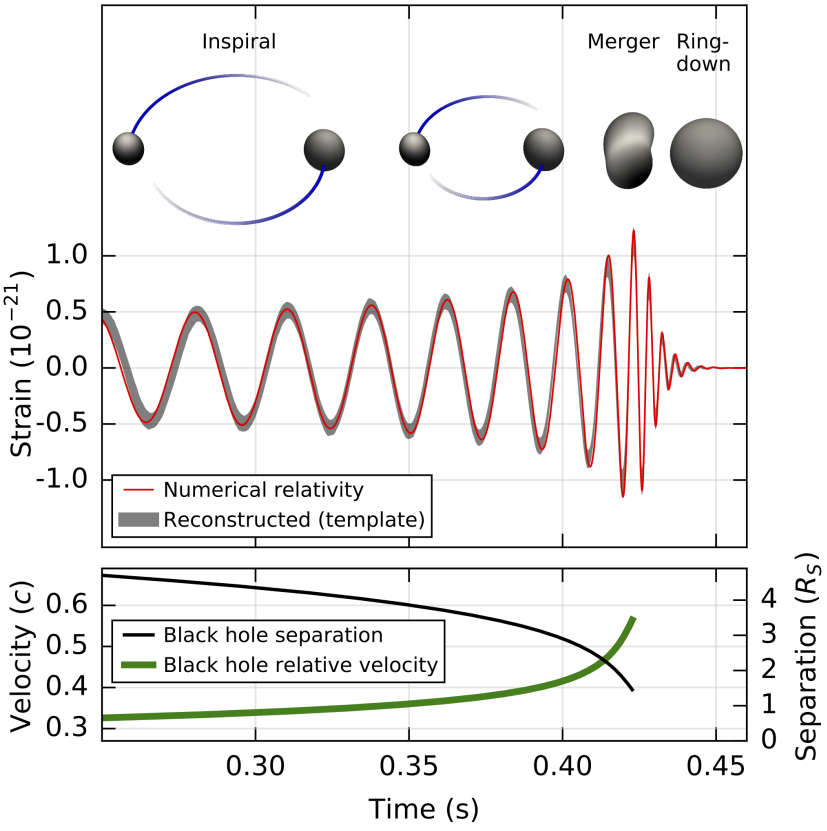

Figure 1.2: **Stages of a black hole binary merger.** The reconstructed best-fit gravitational wave strain of the first event detected by LIGO, GW150914, together with a Numerical Relativity model. Also shown are the separation and velocity of the black holes (figure from [46]).

The parameters describing a black hole binary merger include the total mass $M_1 + M_2$ of the two objects, the mass ratio $q = M_1/M_2$, the (dimensionless) spins

[4] Low mass neutron star mergers can instead form a bigger neutron star [54].

of the two objects $\vec{\chi}_1$ and $\vec{\chi}_2$, the distance to the detector, the position on the sky, and the inclination of the binary relative to the detector frame.

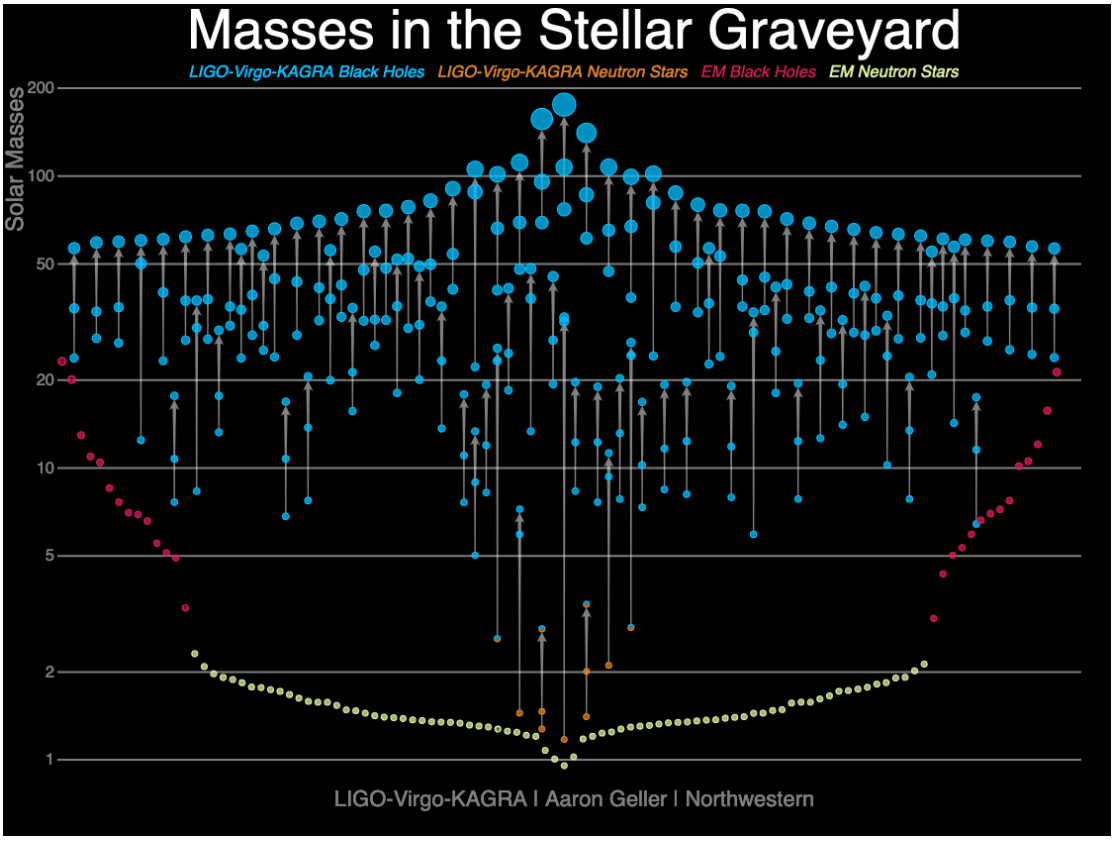

Figure 1.3: **LIGO/Virgo/KAGRA black holes and neutron stars.** This diagram shows all the compact objects inferred from gravitational wave signals at LIGO-Virgo-KAGRA along with those constrained by electromagnetic oberva-tions, arranged by mass. Figure by Aaron Geller, Northwestern University, and LIGO-Virgo.

1.2.5 Quasi-normal modes

The gravitational waves produced in the final "ringdown" regime are dominated by a discrete set of damped oscillatory modes dubbed *quasi-normal modes* (QNM), whose frequencies are strictly determined by the underlying spacetime, and in the case of standard General Relativity and an isolated Kerr black hole are uniquely determined by the black hole mass and spin. As such measuring these frequencies provides, in principle, an excellent test of the nature of gravity and the structure

of the spacetime. For detailed reviews of QNM theory see [55–58], however we will briefly summarise the basics here.

Consider small perturbations around a Schwarzshild black hole $g_{\mu\nu} = g^{(0)}_{\mu\nu} + h_{\mu\nu}$ where $g^{(0)}_{\mu\nu}$ is the Schwarzschild metric and $h_{\mu\nu}$ the perturbation. In spherical coordinates (t, r, θ, ϕ) we look for oscillating solutions $h_{\mu\nu} = H_{\mu\nu}(r, \theta, \phi)e^{-\mathrm{i}\omega t}$. Because of the spherical symmetry we can decompose the perturbations into two sets of tensor spherical harmonics referred to as *odd* (or *axial*) and *even* (or *polar*) according to their transformation under parity. Odd modes with angular numbers l, m transform as $(-1)^{l+1}$ under parity transformation $(\theta, \phi) \to (\pi - \theta, \pi + \phi)$ while even modes transform as $(-1)^l$. The odd and even modes are [56, 59–61]:

$$h^{(o)}_{\mu\nu,lm} = \begin{bmatrix} 0 & 0 & h_0(r)B^{lm}_\theta & h_0(r)B^{lm}_\phi \\ 0 & 0 & h_1(r)B^{lm}_\theta & h_1(r)B^{lm}_\phi \\ \mathrm{sym} & \mathrm{sym} & 0 & 0 \\ \mathrm{sym} & \mathrm{sym} & 0 & 0 \end{bmatrix} e^{-\mathrm{i}\omega_{lm}t}, \tag{1.30}$$

$$h^{(e)}_{\mu\nu,lm} = \begin{bmatrix} H_0(r)f & H_1(r) & 0 & 0 \\ \mathrm{sym} & H_2(r)/f & 0 & 0 \\ 0 & 0 & K(r)r^2 & 0 \\ 0 & 0 & 0 & K(r)r^2\sin\theta \end{bmatrix} Y^{lm}e^{-\mathrm{i}\omega_{lm}t}, \tag{1.31}$$

where "sym" indicates a symmetric entry, B^{lm}_μ are the odd parity vector spherical harmonics, $f = (1 - 2M/r)$, the Y^{lm} denote spherical harmonics and (o/e) odd/even modes. Only the $l \geq 2$ modes can radiate as gravitational waves. Expanding the Einstein field equations in terms of these perturbations one can show that the two sets of functions $h_0(r), h_1(r)$ and $H_0(r), H_1(r), K(r)$ for each l, m can be described in terms of master variables $\Psi^{(o/e)}_{lm}(r)$ which obey Schrödinger-like master equations

$$\left[\partial^2_{r_*} + \omega^2_{lm} - V^{(o/e)}_l\right]\Psi^{(o/e)}_{lm} = 0, \tag{1.32}$$

where r_* is again the tortoise coordinate and

$$V^{(o)}_l := \left(1 - \frac{2M}{r}\right)\left(\frac{l(l+1)}{r^2} - \frac{6M}{r^3}\right), \tag{1.33}$$

$$V^{(e)}_l := 2\left(1 - \frac{2M}{r}\right)\frac{\lambda^2 r^2[(\lambda+1)r + 2M] + 9M^2(\lambda r + M)}{r^3(\lambda r + 3M)^2}, \tag{1.34}$$

$$\lambda := \tfrac{1}{2}(l+2)(l-1). \tag{1.35}$$

The potentials $V^{(o/e)}_l$ are called the Regge-Wheeler and Zerilli potentials respectively. For an isolated black hole in an asymptotically flat spacetime physical solutions cannot have gravitational waves entering from $r = \infty$ or leaving the black

hole horizon. So we impose boundary conditions that the perturbation must be ingoing at the horizon and outgoing at $r = \infty$:

$$\Psi e^{-\mathrm{i}\omega t} \to \propto \begin{cases} e^{-\mathrm{i}\omega(t+r)} & r \to 2M, \\ e^{-\mathrm{i}\omega(t-r)} & r \to \infty. \end{cases} \tag{1.36}$$

This produces an eigenvalue problem for ω_{lm} with a set of discreet complex solutions $\omega_{nlm} = \omega^R_{nlm} + \mathrm{i}\omega^I_{nlm}$ where n is the overtone number $n = 0, 1, 2, \ldots$. The real part ω^R_{nlm} sets the oscillation frequency and is order $\sim 1/M$, while the imaginary part determines the decay timescale. The initial phase and amplitude of each QNM in the ringdown signal cannot be determined from perturbation theory alone and requires comparison to Numerical Relativity simulations or observations, however in general we expect the $n = 0,\ l = m = 2$ mode to dominate.

For a Schwarzschild black hole the frequencies only depend on n and l, and are identical for even and odd modes (the potentials are said to be *isospectral*). Perturbation theory can also be applied to the spinning Kerr black hole, although the lack of spherical symmetry makes the problem harder. Teukolsky [62] showed that a similar decomposition can be found for perturbations in Kerr using the Newman-Penrose formalism [63] resulting in another Schrödinger-like equation which can be used to obtain QNMs, however the frequencies then have a non-trivial dependence on the azimuthal number m and black hole spin χ, and the even and odd modes are no longer isospectral.

1.2.6 Unresolved questions

Despite the tremendous success of both the Standard Model of particle physics and General Relativity, there remain significant unresolved problems that suggest these theories do not present a complete picture of fundamental physics. These include:

- **Quantum gravity**. General Relativity is a classical theory, but ideally we would like a quantum version where we can unify gravity with the other fundamental forces. However, when described as a quantum field theory General Relativity is *nonrenormalizable*, and as such cannot be extended to arbitrarily high energies without an infinite number of parameters [64, 65]. There is also the question of why gravity appears much weaker than the other fundamental forces (10^{24} times weaker than the weak nuclear force) [66].

- **Dark energy**. Observations of type Ia supernovae suggest the universe is undergoing a period of accelerated expansion. Combined with measurements of the cosmic microwave background, this suggests that about 68% [67] of the energy budget of the observable universe is made up of a very homogeneous vacuum-energy-like component with negative pressure, termed "dark energy" [68, 69]. The current ΛCDM standard model of cosmology [70] includes a small but non-zero cosmological constant term accounting for this dark energy, and quantum field theory does predict such a vacuum energy, but with scales some 60 orders of magnitude too large without exceptional fine tuning [71, 72].

- **Dark matter**. Observations of the rotation curves of galaxies, gravitational lensing, and studies of large scale structure among other measurements suggest that 80% of the matter (and 27% of the total energy budget) in the universe is made up of a non-radiating component, dubbed "dark matter", which cannot be fully accounted for by Standard Model particles [73].

- **Inflation**. In order to explain the observed flatness and homogeneity of the universe many physicists today support the idea of *inflation* [74], whereby the universe underwent a period of rapid accelerated growth at very early times. However, the inflation model requires one or more new "inflaton" fields, or some other new physics mechanism, to produce the expansion (see [75] for a review of different inflation models).

1.3 Scalar fields and strong gravity

One popular proposal to address one of more of these questions is the addition of one or more new fundamental scalar fields. A scalar field is a field which can be described by a single number at every point in spacetime, and where the corresponding particles are spin-zero bosons. A simple action for General Relativity with a scalar field φ can be given by

$$S = \int \mathrm{d}^4x\sqrt{-g}\left[\frac{1}{16\pi}R - \tfrac{1}{2}\nabla_\mu\varphi^*\nabla^\mu\varphi - V(\varphi) + \dots\right], \tag{1.37}$$

where "φ^*" denotes the complex conjugate of φ and the "…" indicate possible higher-order interactions. The potential $V(\varphi)$ for a scalar field of mass m_s and no

additional self interactions is

$$V(\varphi) = \tfrac{1}{2} m_s^2 \varphi^* \varphi, \tag{1.38}$$

which you could also consider as a Taylor expansion around the minimum of a more general potential. Equation (1.37) is for a complex scalar field, but one can obtain the equivalent for a real scalar field by simply neglecting the imaginary part of φ. The mass m_s can be thought of either in terms its corresponding rest mass energy $E_s = m_s c^2$, usually expressed in electron-Volts (eV), or in terms of its reduced Compton wavelength

$$\lambda\!\!\!^{-} = \frac{\hbar}{m_s c}, \tag{1.39}$$

with $\lambda\!\!\!^{-} = 1/m_s$ in Planck units. The discovery of the Higgs boson [76, 77] demonstrates that fundamental scalar fields exist in nature, and there are several reasons to consider the possibility of new as-yet undiscovered examples. The QCD axion is a scalar field which has been proposed as a possible solution to the strong CP problem in particle physics [78–80]. It has a non-minimal[5] coupling to Standard Model particles[6], and for the original axion model its mass is bounded by astrophysics and cosmology to around 10^{-5}–10^{-3}eV [81] although different models have been proposed which evade these constraints [78, 82]. String theory predicts multiple novel scalar fields with a wide range of possible masses [83–85].

1.3.1 Scalar fields from modified gravity

Another motivation for considering scalar fields is the study of modified gravity. Despite the great successes of General Relativity much effort has gone into developing alternatives, motivated by the unresolved questions listed in section 1.2.6. Many modified gravity theories can be classed as "scalar-tensor" theories [86, 87], whereby General Relativity is extended with the addition of an additional degree of freedom in the form of a scalar field, coupled to gravity in a non-trivial way. Such scalar fields could be fundamental, or they can arise in effective field theories as the low energy or dimensionally reduced limit of more fundamental fields.

Scalar-tensor theories have been proposed as models for dark energy [88] and inflation (in which case the scalar field is called the "inflaton") [89], and in the low

[5] "Non-minimal" meaning more than the basic gravitational coupling.

[6] Note that even scalar fields without non-minimal couplings to the Standard Model, which thus do not solve the strong CP problem, are often termed "axion-like particles" or just "axions" in the literature.

coupling limit resemble a theory with a minimally coupled scalar field of some mass m_s as in (1.37). For a scalar field to be a candidate for dark energy the mass needs to be very small, $10^{-32}\text{eV} \lesssim m_s \lesssim 10^{-18}\text{eV}$ [85], where 10^{-32}eV corresponds to the Hubble scale $m_s \sim H_0$ where H_0 is the Hubble constant, the present expansion rate of the universe.

The most general scalar-tensor theory with a single real scalar field and second-order equations of motion can be given by the Horndeski action [90]

$$S = \int \mathrm{d}^4x\sqrt{-g}\sum_{n=2}^{5} L_n + S_\mathrm{m}, \tag{1.40}$$

where S_m is again the standard matter action, with

$$L_2 = G_2(\varphi, X), \tag{1.41}$$

$$L_3 = -\,G_3(\varphi, X)\Box\varphi, \tag{1.42}$$

$$L_4 = G_4(\varphi, X)R + G_{4,X}(\varphi, X)\left((\Box\varphi)^2 - \varphi_{;\alpha;\beta}\varphi^{;\alpha;\beta}\right), \tag{1.43}$$

$$L_5 = G_5(\varphi, X)G_{\alpha\beta}\varphi^{;\alpha;\beta} - \frac{1}{6}G_{5,X}(\varphi, X)\left[(\Box\varphi)^3 - 3\varphi^{;\alpha;\beta}\varphi_{;\alpha;\beta}\Box\varphi + 2\varphi_{;\alpha;\beta}\varphi^{;\alpha;\mu}\varphi^{;\beta}_{;\mu}\right], \tag{1.44}$$

where $X := -\frac{1}{2}\nabla_\mu\varphi\nabla^\mu\varphi$ and $\varphi_{;\alpha;\beta} := \nabla_\alpha\nabla_\beta\varphi$ [91, 92]. We recover General Relativity and the Einstein-Hilbert action (1.9) with $G_4 = \frac{1}{16\pi}$, $G_5 = 0$, and the minimally coupled scalar field action (1.37) with $G_2 = X - V(\varphi)$, $G_3 = 0$. Many modified gravity theories of cosmological and theoretical interest including $f(R)$ gravity, K-essence, Quintessence, Galileons, Brans–Dicke and Einstein–scalar–Gauss-Bonnet gravity (EsGB) can be shown to be special cases of the Horndeski theory [93, 94]. It is also possible to generalise Horndeski and go beyond second-order equations of motion, while still maintaining only a single scalar degree of freedom and avoiding unwanted instabilities, with the so-called beyond-Horndeski or GLPV theories [95–97]. These can then be further extended to the class of Degenerate Higher-Order Scalar-Tensor (DHOST) theories [97]. Expanding the Horndeski action to second order in derivatives we can recover a generalised Brans-Dicke theory of the form

$$S = \int \mathrm{d}^4x\sqrt{-g}\left[F(\varphi)R - \tfrac{1}{2}\nabla_\mu\varphi\nabla^\mu\varphi - V(\varphi) + L_\mathrm{m}(g_{\mu\nu}, \text{matter})\right], \tag{1.45}$$

where it is made explicit that the matter part of the Lagrangian depends on both the metric and the matter fields. One feature of scalar-tensor theories is that they can be expressed in different guises or "frames" via field redefinitions. Equation

(1.45) describes a "Jordan" frame if $F(\varphi)$ depends on φ. If we perform a *Weyl transformation*, a local rescaling of the metric tensor, $g_{\mu\nu} \to \Omega^2(\varphi)\tilde{g}_{\mu\nu}$ we can obtain a new action

$$S = \int \mathrm{d}^4x\sqrt{-\tilde{g}}\left[\frac{1}{16\pi}\tilde{R} + \cdots + \tilde{L}_{\mathrm{m}}(\Omega(\varphi)^2\tilde{g}_{\mu\nu}, \mathrm{matter})\right], \tag{1.46}$$

in rescaled quantities where the gravity sector is now as in GR, but the matter sector picks up additional couplings to φ. This is termed the "Einstein frame". The extent to which the two frames are really physically equivalent, especially in the quantum theory, has been a matter of much debate and will be discussed in chapter 6. We will also go beyond scalar-tensor theories with a single additional degree of freedom, and instead consider an arbitrary number of fields which can lead to interesting dynamics.

1.3.1.1 Fifth forces

Modified gravity theories are tightly constrained by laboratory experiments, measurements of the motions of satellites and planets in the solar system, measurements of distant pulsars, and cosmological observations, all of which are currently consistent with General Relativity. The gravitational wave signal from the merger of two neutron stars in 2017 [98], and a corresponding observation of an optical counterpart [99], showed that gravitational waves travel at the speed of light to within one part in 10^{15}, further ruling out a whole array of theories [93, 100, 101]. For scalar-tensor theories, a generic result is that the exchange of the scalar particle with a non-minimal coupling gives rise to an additional long-range "fifth force"[7] [102–104]. The exchange of a new particle of mass m_s coupling to matter gives a Yukawa [105] potential of the form

$$V_{\mathrm{fifth}}(r) = -\alpha\frac{GM_1M_2}{r}e^{-m_sr}. \tag{1.47}$$

The magnitude of α has been constrained by observations and experiment across a range of length-scales (see Fig. E.1). However, one can construct scalar-tensor theories which evade these constraints. These include screening mechanisms such as Chameleon [106, 107], symmetron [107–110], environment-dependent-dilaton and Damour-Polyakov screening [111, 112] and the Vainshtein mechanism [113, 114], along with scale-invariant theories which we shall discuss further in chapter 6.

[7] So-called because they act in addition to the standard four fundamental forces of nature.

1.3.2 Scalar fields as dark matter

One or more novel scalar fields with non-zero mass are a popular candidate for dark matter. The average galactic dark matter densities as measured from observations of galactic rotation curves are at best of the order of $M_\odot/\mathrm{pc}^3$ or $\mathrm{GeV}/\mathrm{cm}^3$, with the local density in the Solar neighbourhood of the order $\sim 0.01 M_\odot/\mathrm{pc}^3$ or $\sim 0.1\mathrm{GeV}/\mathrm{cm}^3$ [115–119]. If the mass of the scalar field is $m_s \ll 30\mathrm{eV}$, then the typical spacing between the bosonic particles is much smaller than the de Broglie wavelength, such that the collection of dark matter particles is best described as a *classical* scalar field (see [82, 120–124] for reviews). In the spectrum of different dark matter candidates (Fig. 1.4) such light scalar fields are included under "ultra-light" dark matter also termed "wave-like" dark matter as it shows wave-like properties. In contrast the conventional cold dark matter (CDM) used in the standard model of cosmology typically assumes a particle-like nature with $m_s \gtrsim 30\mathrm{eV}$. Very light scalar fields, with $m_s \sim 10^{-20} - 10^{-22}\mathrm{eV}$, termed "fuzzy dark matter" [124, 125], have been proposed as a possible solution to the "core-cusp" problem of structure formation [126], as they smooth out structure formation on small cosmological scales [123, 125, 127–129]. However, other more recent results suggest that the cores produced by fuzzy dark matter may not fit observations, and that the core-cusp problem may instead be resolved by the inclusion of baryonic effects [130–132]. While it has been argued that these observations[8] exclude ultra-light DM across almost the entire mass range [133–136], uncertainties in the astrophysical modelling and data interpretation may call these bounds into question [121, 137]. Moreover, they do not exclude models with multiple scalar fields or multiple dark matter components. As a result, scalar-field DM remains a key candidate of interest.

1.3.3 Scalar fields and black holes

As we expect that the primary interaction of scalar field dark matter will be via gravity, the ultra-strong gravity regimes around black holes provide an excellent scope for testing these models [138]. A minimally coupled massive scalar field has a Klein-Gordon equation of motion

$$\left[\Box - m_s^2\right] \varphi = 0, \tag{1.48}$$

[8] Of dwarf spheroidal galaxies, the Lyman-α forest and the subhalo mass function, among others.

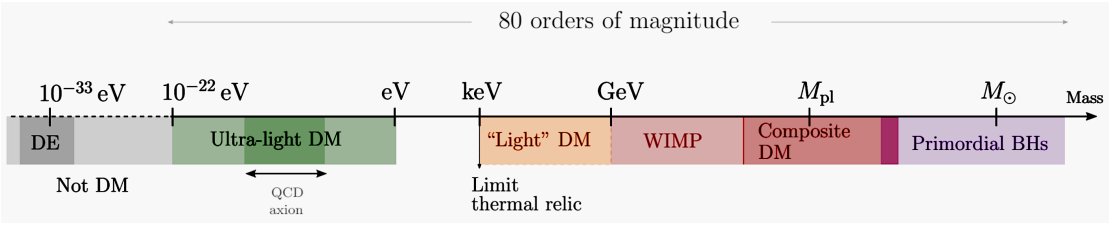

Figure 1.4: **Dark matter candidates**: sketch of different candidates over a wide range of mass scales (figure from [121]). Light scalar field dark matter falls in the "ultra-light DM" range.

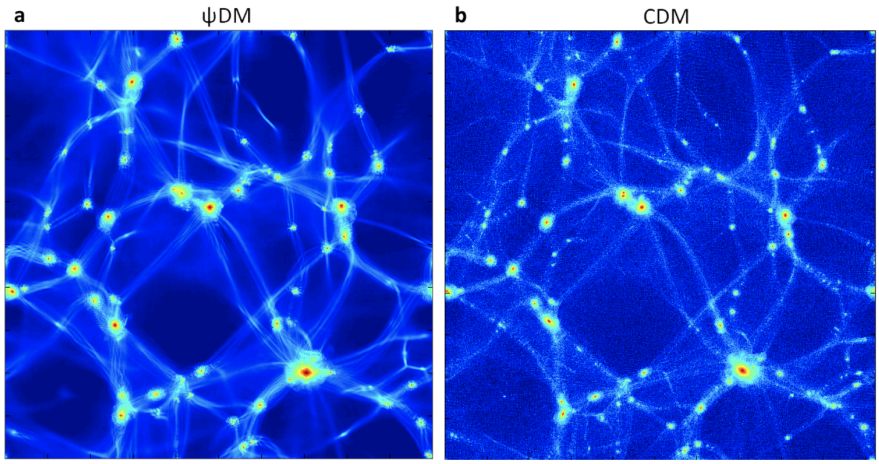

Figure 1.5: **Cosmological simulations of structure formation with light scalar dark matter and particle cold dark matter**. Figure taken from Schive et al. (2014) [128]. The scalar field dark matter (left) reproduces the same cosmic structure on large scales, while smoothing out structures on smaller scales.

where $\Box = \nabla_\mu \nabla^\mu$. If we try and solve this equation in a Kerr black hole spacetime, and look for an oscillating solution $\varphi \propto e^{-i\omega t}$, we obtain an equation of the form [18, 139]

$$\left[\partial^2_{r_*} + \omega^2_{lm} - V_{l,m}(r;\omega,\chi)\right](r\varphi_{lm}) = 0, \tag{1.49}$$

which is the spin-zero radial Teukolsky equation, and where φ has been decomposed into angular modes $\varphi = \sum_{lm} \varphi_{lm}(r) e^{im\phi} S_{lm}(\theta)$ where $e^{im\phi}S_{lm}(\theta)$ are oblate spheroidal harmonics[9]. Here $\frac{dr_*}{dr} = r^2/\Delta$ where Δ is as in (1.19). For $r \gg M$ we can approximate this as

$$\left[\partial^2_r + \omega^2_{lm} - m^2_s + \frac{2m_s M}{r} - \frac{l(l+1)}{r^2}\right](r\varphi_{lm}) = 0, \tag{1.50}$$

[9]These are the equivalent of spherical harmonics for oblate spheroidal coordinates, for more details see [140].

We can recognise this as almost identical to the Schrödinger equation of an electron in a hydrogen atom, dominated by a $1/r$ potential, and with a "gravitational fine structure constant" of $\alpha_g := m_s M$. This approximation is termed the "gravitational atom" [139, 141–143]. Solutions with $\omega < m_s$ represent bound states, $\omega = m_s$ marginally bound and $\omega > m_s$ unbound. For $\alpha_g \ll 1$ it can be shown that the discrete set of bound states have frequencies (and therefore energies) that can be approximated as

$$\omega_{nlm} \approx m_s \left[1 - \left(\frac{\alpha_g}{l+n+1}\right)^2\right]^{1/2} + \mathrm{i} m_s \gamma_l r_+ \left(m\Omega_H - m_s\right) \alpha_g^{4l+5}, \tag{1.51}$$

where $n = 0, 1, 2, 3 \ldots$, γ_l is a constant that depends on l [10], $r_+ = M(1+\sqrt{1-\chi^2})$ is the radius of the outer horizon and $\Omega_H = \chi/(2r_+)$ is the horizon angular velocity. If the complex part of the frequency is negative the mode decays with time, as scalar dark matter disperses to infinity and falls into the black hole, with a decay timescale $1/\mathrm{Im}\{\omega\}$. However, if an instability condition is satisfied

$$m_s < m\Omega_H, \tag{1.52}$$

then the imaginary component becomes positive and the mode can grow exponentially with time. Including the backreaction in full GR the spin and mass of the black hole correspondingly decreases. This is the phenomenon of *superradiance* whereby a bosonic field can extract energy and angular momentum from a highly spinning black hole via repeated scattering in the ergosphere (see [21] for a detailed review). The cloud keeps growing until the angular momentum of the black hole decreases to the point where the inequality is saturated. Superradiance has been widely studied as one mechanism to generate scalar dark matter clouds around spinning back holes from small initial fluctuations. Another, simpler, formation mechanism is gravitational accretion from a diffuse scalar field dark matter environment, which we will explore in chapter 3. Scalar field profiles that decay with time, such as the "gravitational atom" bound states, are typically not considered "black hole hair", as that label is reserved for truly stationary or static solutions. Nonetheless, these states can be extremely long lived, surviving for cosmological times, and as such have been dubbed "black hole wigs" [144–147].

[10] From Detweiler (1980) [139]: $\gamma_l \approx \frac{2^{4l+2}(2l+1+n)!}{(l+1+n)^{2l+4}n!}\left[\frac{l!}{(2l)!(2l+1)!}\right]^2 \prod_{j=1}^{l}\left[j^2(1-\chi^2)+m_s r_+(m\Omega_H - m_s)^2\right]$.

1.3.4 Scalar fields and black hole binaries.

Although scalar field clouds around isolated black holes could potentially emit gravitational waves on their own (as discussed in 3.4 and [138]), the observations of GW signals from binary black hole mergers motivates the possibility of using these to detect fundamental scalar fields. In principle any matter environment that contributes to the energy momentum tensor will in turn modify the metric, resulting in changes to all three regimes of the gravitational wave signal. These changes could result from any kind of matter, from standard baryonic matter like plasma-filled accretion disks to dark matter clouds, with the spatial distribution and physical nature of the matter giving rise to distinctive signatures at each stage [148–150, 150–163]. Therefore, even a minimally coupled scalar field dark matter environment could produce a signal. The wave-like nature of light scalar field dark matter means it behaves very differently from particle-like dark matter around merging binaries, however accurately modelling the dynamics and gravitational wave signal from such scalar field binaries has many challenges as we will explore in chapter 5. The potential impact of a scalar dark matter cloud on the final ringdown regime is explored in chapter 4.

Chapter 2

Numerical Relativity

This chapter presents an overview of the key ideas in Numerical Relativity, largely based on the popular reference works of Alcubierre (2008) [12] and Baumgarte and Shapiro (2010) [164].

As advertised in section 1.2.1 although the Einstein field equations look simple, they are really a system of 10 non-linear, second-order, coupled PDEs, and it is very challenging to find explicit analytic solutions, except for a few very simple cases with high degrees of symmetry or weak fields. This motivates the idea of solving the equations *numerically* on a computer, a discipline termed "Numerical Relativity" (NR). Numerical methods have been used to solve the Einstein equations for a long time, however key theoretical developments and the increasing power of supercomputing facilities has led to significant advances in the last couple of decades.

The essential idea is to write the Einstein equations as a initial value, or Cauchy, problem.[1] We need some evolution equations

$$\partial_t \boldsymbol{u} = \boldsymbol{F}(\boldsymbol{u}, \partial_i \boldsymbol{u}, \partial_i \partial_j \boldsymbol{u}), \tag{2.1}$$

where $\boldsymbol{u}(t, x^i)$ is a set of dynamic evolution variables, i, j denote spatial indices, and the functions $\boldsymbol{F}$ only depend on at most second-order spatial derivatives due to the second-order nature of the Einstein equations. Equations without time derivatives $\boldsymbol{G}(\boldsymbol{u}, \partial_i \boldsymbol{u}, \partial_i \partial_j \boldsymbol{u}) = 0$ are *constraints* that must be satisfied at all times. We also need some initial data for $t = 0$, i.e. $\boldsymbol{u}(0, x^i)$, which satisfies the constraints, and some suitable boundary conditions at the spatial boundary of the domain

[1] A slightly different approach using characteristic hypersurfaces is reviewed by Winicour [165]

(because with a finite computer we need to work with a finite computational domain). Given those ingredients we can in principle numerically integrate (2.1) to obtain the solution at $t > 0$.

However, there are several important challenges to overcome. The first is that in General Relativity, due to the coordinate freedom, there is no universal notion of "time": different observers in different reference frames will have different perspectives on what constitutes "time" and "space". Hence we first need to choose how we split our 4 dimensional spacetime into a $3+1$ dimensional decomposition of 3 dimensions of space and 1 of time.

2.1 The 3+1 decomposition

To perform this decomposition we *foliate* the spacetime into a set of 3-dimensional spatial hypersurfaces Σ indexed by parameter t which is interpreted as time. The normal vector to the hypersurfaces is n^μ, and the spatial coordinates x^i for $i = 1, 2, 3$ are the coordinates within the hypersurface perpendicular to n^μ (see Fig. 2.1). We decompose the metric as

$$\mathrm{d}s^2 = g_{\mu\nu}\mathrm{d}x^\mu \mathrm{d}x^\nu = -\alpha^2 \mathrm{d}t^2 + \gamma_{ij}(\mathrm{d}x^i + \beta^i \mathrm{d}t)(\mathrm{d}x^j + \beta^j \mathrm{d}t). \tag{2.2}$$

The *lapse* function α determines the proper time interval $\mathrm{d}\tau = \alpha \mathrm{d}t$ between hypersurfaces separated by time $\mathrm{d}t$, moving along a normal vector. The *shift vector* β^i determines how much the spatial coordinates shift between successive hypersurfaces, relative to the normal vector. Due to coordinate freedom we can choose different α and β^i, and this determines the foliation of the spacetime. We also have a spatial metric γ_{ij} which defines a spatial line element $\mathrm{d}\sigma^2 = \gamma_{ij}\mathrm{d}x^i \mathrm{d}x^j$ within a hypersurface. The coordinates $x^\mu = (t, x^i)$ are called the *adaptive basis*. The 4-dimensional metric and its inverse can be expressed in terms of these quantities

$$g_{\mu\nu} = \begin{pmatrix} -\alpha^2 + \beta_k\beta^k & \beta_i \\ \beta_j & \gamma_{ij} \end{pmatrix}, \qquad g^{\mu\nu} = \begin{pmatrix} -1/\alpha^2 & \beta^i/\alpha^2 \\ \beta^j/\alpha^2 & \gamma^{ij} - \beta^i\beta^j/\alpha^2 \end{pmatrix}, \tag{2.3}$$

where $\beta_i = \gamma_{ij}\beta^j$, γ^{ij} is the inverse of γ_{ij}, and in general we assume from now on that indices of spatial tensors are raised and lowered with γ_{ij}. One can also show that the four dimensional volume element $\sqrt{-g} = \alpha\sqrt{\gamma}$ where $\gamma = \det(\gamma_{ij})$. The normal vector written in the adaptive basis is

$$n^\mu = -\alpha \nabla^\mu t = (1/\alpha, -\beta^i/\alpha), \qquad n_\mu = (-\alpha, 0, 0, 0), \tag{2.4}$$

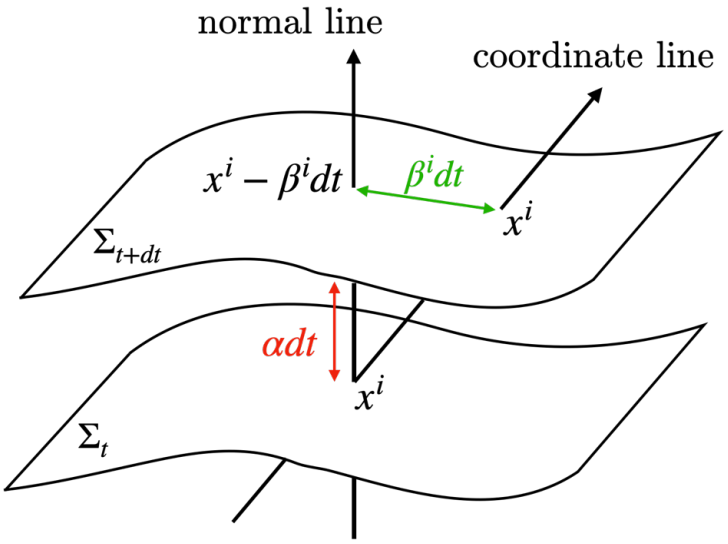

Figure 2.1: **Foliation of spacetime** by 3-dimensional spacelike hypersurfaces Σ.

and one can see it is normalised and timelike such that $n^\mu n_\mu = -1$. *Eulerian* observers are those moving with velocity n^μ, so those moving normal to the hypersurfaces. The spatial metric γ_{ij} can also be thought of as the spatial components of the 4D metric induced on the hypersurfaces

$$\gamma_{\mu\nu} = g_{\mu\nu} + n_\mu n_\nu. \tag{2.5}$$

The projection operator onto a spatial hypersurface is

$$P^\mu_\nu = \delta^\mu_\nu + n^\mu n_\nu = \gamma^\mu_\nu, \tag{2.6}$$

and the time vector parallel to lines connecting points of the same spatial coordinates x^i on different hypersurfaces is

$$t^\mu = \alpha n^\mu + \beta^\mu, \tag{2.7}$$

where the 4-dimensional shift is defined as $\beta^\mu = (0, \beta^i)$. As GR is a theory about spacetime curvature, we also need to define curvature in the $3+1$ decomposition. There are two types:

- **Intrinsic curvature**. This is the curvature of the spatial hypersurfaces. It is given by the three dimensional Riemann tensor ${}^{(3)}R^i_{jkl}$ defined as usual but with the 3D spatial metric γ_{ij} instead of the 4D $g_{\mu\nu}$ metric.

- **Extrinsic curvature**. This is related to how the 3D hypersurfaces are embedded in the 4D spacetime, and how the hypersurface deforms as you move along a normal. It is defined terms of how much the normal vector changes as we move along the spatial hypersurface, given by the projection of the gradient

$$K_{\mu\nu} = -P^{\alpha}_{\mu}\nabla_{\alpha}n_{\mu}. \tag{2.8}$$

  One can show it is symmetric, the time components of $K^{\mu\nu}$ are zero, and although the time components of $K_{\mu\nu}$ are non-zero all the information is effectively contained in the spatial part K_{ij}.

One can also relate the extrinsic curvature to the *Lie derivative* (see appendix A.1 for more detail) of the spatial metric along the normal direction

$$K_{\mu\nu} = -\frac{1}{2}\mathcal{L}_{\vec{n}}\gamma_{\mu\nu}. \tag{2.9}$$

The trace of the extrinsic curvature, often called the *mean curvature* or *expansion*, is

$$K = g^{\mu\nu}K_{\mu\nu} = \gamma^{ij}K_{ij} = -\mathcal{L}_{\vec{n}}\sqrt{\gamma} = -\nabla_{\mu}n^{\mu}, \tag{2.10}$$

and it corresponds to the fractional change in the 3D volume element of the Eulerian observers as they move along the normal lines. Negative K corresponds to expanding space and positive K to collapsing one. We can use the definition of the time vector t^{μ} and properties of the Lie derivative to obtain

$$K_{ij} = -\frac{1}{2}\mathcal{L}_{\vec{n}}\gamma_{\mu\nu} = -\frac{1}{2\alpha}\left(\mathcal{L}_{\vec{t}} - \mathcal{L}_{\vec{\beta}}\right)\gamma_{ij} = -\frac{1}{2\alpha}\left(\partial_t\gamma_{ij} - D_i\beta_j - D_j\beta_i\right), \tag{2.11}$$

where D_{μ} is the covariant derivative on the hypersurface given by $D_{\mu} = P^{\nu}_{\mu}\nabla_{\nu}$.

2.2 Einstein's equations in 3+1

We now need to write the Einstein equations in the 3+1 language. The general idea is to contract different terms with n^{μ} and P^{μ}_{ν} to separate out the spatial and time-related parts.

To begin we project the 4D Riemann tensor $R_{\mu\nu\lambda\sigma}$ (with the first index lowered with $g_{\mu\nu}$) onto the spatial hypersurface

$$P^{\mu}_{\alpha}P^{\nu}_{\beta}P^{\lambda}_{\gamma}P^{\sigma}_{\delta}R_{\mu\nu\lambda\sigma} = {}^{(3)}R_{\alpha\beta\gamma\delta} + K_{\alpha\gamma}K_{\beta\sigma} - K_{\alpha\delta}K_{\beta\gamma}, \tag{2.12}$$

what are termed the *Gauss-Codazzi* equations. If we swap one of the projection matrices with a normal vector we get

$$P^{\mu}_{\alpha}P^{\nu}_{\beta}P^{\lambda}_{\gamma}n^{\sigma}R_{\mu\nu\lambda\sigma} = D_{\beta}K_{\alpha\gamma} - D_{\alpha}K_{\beta\gamma}, \tag{2.13}$$

the *Codazzi-Mainardi* equations. If we contract the Riemann tensor with two projection operators using alternate indices we find

$$\begin{aligned} P^{\mu\lambda}P^{\nu\sigma}R_{\mu\nu\lambda\sigma} =& (g^{\mu\lambda} + n^{\mu}n^{\lambda})(g^{\nu\sigma} + n^{\nu}n^{\sigma})R_{\mu\nu\lambda\sigma}, \\ =& R + 2n^{\mu}n^{\nu}R_{\mu\nu} = 2n^{\mu}n^{\nu}G_{\mu\nu}. \end{aligned} \tag{2.14}$$

where the $n^{\mu}n^{\nu}n^{\lambda}n^{\sigma}R_{\mu\nu\lambda\sigma}$ term vanishes due to symmetry properties of the Riemann tensor. From contracting the Gauss-Codazzi equations (2.12) we get

$$P^{\mu\lambda}P^{\nu\sigma}R_{\mu\nu\lambda\sigma} = {}^{(3)}R + K^2 - K_{\mu\nu}K^{\mu\nu}, \tag{2.15}$$

Then putting these together and using $G_{\mu\nu} = 8\pi T_{\mu\nu}$ we get

$$\boxed{\mathcal{H} = {}^{(3)}R + K^2 - K_{ij}K^{ij} - 16\pi\rho = 0,} \tag{2.16}$$

where $\rho = n^{\mu}n^{\nu}T_{\mu\nu}$ is the energy density measured by the Eulereian observers. Provided we use suitable variables this equation does not involve any time derivatives. Hence it is not related to the evolution, but instead an elliptic equation that must be satisfied on each spatial hypersurface termed the *Hamiltonian constraint*. If we also contract the Codazzi-Mainardi equations (2.13) we obtain

$$g^{\alpha\gamma}P^{\mu}_{\alpha}P^{\nu}_{\beta}P^{\lambda}_{\gamma}n^{\sigma}R_{\mu\nu\lambda\sigma} = P^{\nu}_{\beta}n^{\sigma}R_{\nu\sigma} = P^{\nu}_{\beta}n^{\sigma}G_{\nu\sigma} = g^{\alpha\gamma}\left(D_{\beta}K_{\alpha\gamma} - D_{\alpha}K_{\beta\gamma}\right). \tag{2.17}$$

Defining the momentum density measured by Eulerian observers as $S^{\mu} := -P^{\mu\nu}n^{\sigma}T_{\nu\sigma}$, and again using the Einstein field equations to eliminate $G_{\mu\nu}$, we find the second important result

$$\boxed{\mathcal{M}^{i} = D_{j}\left(\gamma^{ij}K - K^{ij}\right) - 8\pi S^{i} = 0.} \tag{2.18}$$

Again, provided we choose the right variables this equation also is free of time derivatives, giving a second set of elliptic equations termed the *momentum constraints*. We are not free to simply choose any spatial metric γ_{ij} and $\partial_t\gamma_{ij}$ (via K_{ij}) as initial data. In order to satisfy the Einstein equations we have to satisfy these constraints.

We have so far used the $n^{\mu}n^{\nu}G_{\mu\nu}$ and $P^{\mu\alpha}n^{\nu}G_{\mu\nu}$ projections of the Einstein equations to get the Hamiltonian and momentum constraints respectively. We already have a suitable first order evolution equation for γ_{ij} from (2.11)

$$\boxed{\partial_t\gamma_{ij} = -2\alpha K_{ij} + D_i\beta_j + D_j\beta_i.} \tag{2.19}$$

To get the evolution equation for $K_{\mu\nu}$ we can use the remaining $P^{\mu\alpha}P^{\nu\beta}G_{\mu\nu}$ projections to obtain

$$\boxed{\begin{aligned}\partial_t K_{ij} =&\beta^k\partial_k K_{ij} + K_{ki}\partial_j\beta^k + K_{kj}\partial_i\beta^k - D_iD_j\alpha \\ &+ \alpha\left({}^{(3)}R_{ij} + KK_{ij} - 2K_{ik}K^k_j\right) + 4\pi\alpha(\gamma_{ij}(S-\rho) - 2S_{ij}),\end{aligned}} \tag{2.20}$$

where $S_{\mu\nu} := P^\alpha_\mu P^\beta_\nu T_{\alpha\beta}$ is the spatial stress tensor measured by the Eulerian observers and $S = g^{\mu\nu}S_{\mu\nu}$ is its trace. We also need suitable evolution equations for the matter, and we need to determine α and β^i, however due to gauge freedom we can choose these gauge functions to be whatever is most convenient.

This 3+1 decomposition was first formulated by Arnowitt, Deser and Misner in 1962 [166] for use in quantum gravity, and thus is termed the *ADM formulation* or *ADM decomposition*. The standard version presented here is not quite the same as that in the original 1962 paper, instead it corresponds to a reformulation by York (1979) [167] where (2.20) has an added multiple of the Hamiltonian constraint $\mathcal{H}$ compared to the version in [166]. As $\mathcal{H} = 0$ for physical spacetime this doesn't change the physics, but does change the mathematical properties of the equations.

2.3 Numerical stability and well-posedness

One can obtain many different physically equivalent formulations of the evolution equations described above by redefining variables and by adding or subtracting multiples of the constraints $\mathcal{H}$ and $\mathcal{M}^i$.

The second big challenge in NR is finding a formulation such that the problem is *well-posed*. For a problem involving a system of PDEs to be well-posed it must have a unique solution for any set of valid initial data, and the solution must depend continuously on the initial data. In other words, a small change in the initial data should not give an arbitrarily large change in the solution.

This is a necessary condition for numerical stability, as otherwise tiny numerical errors in the initial data could give arbitrarily large errors in the result. It is not a *sufficient* condition for good numerical behaviour, as even a well-posed problem can give large errors, but at least they won't be *arbitrarily* large. Formally, continuous dependence[2] on the initial data means there exist constants K, α such that for any two sets of valid initial data $\boldsymbol{u}_1(0, x^i), \boldsymbol{u}_2(0, x^i)$ with unique solutions

[2] In the sense of Lipschitz continuity [168].

$\boldsymbol{u}_1(t, x^i), \boldsymbol{u}_2(t, x^i)$

$$\|\boldsymbol{u}_1(t, x^i) - \boldsymbol{u}_2(t, x^i)\| \leq Ke^{\alpha t}\|\boldsymbol{u}_1(0, x^i) - \boldsymbol{u}(0, x^i)\|, \tag{2.21}$$

at all times $t \geq 0$[3], where $\|\cdot\|$ denotes a suitable norm, such as the L_2 norm $\|\boldsymbol{v}\|^2_{L_2} := \int_{\mathbb{R}^3} \boldsymbol{v}^\dagger \boldsymbol{v}\, \mathrm{d}x\mathrm{d}y\mathrm{d}z$ where "$\dagger$" denotes the conjugate transpose. If the system of PDEs is linear the condition reduces to

$$\|\boldsymbol{u}(t, x^i)\| \leq Ke^{\alpha t}\|\boldsymbol{u}(0, x^i)\|, \tag{2.22}$$

for any valid initial data $\boldsymbol{u}(0, x^i)$ and unique solution $\boldsymbol{u}(t, x^i)$. For the initial data to be "valid" it must both satisfy the equations and its norm must be bounded [164, 169, 170][4].

A system of PDEs can be shown to have a well-posed initial value problem if it is *strongly hyperbolic*. Suppose we can write our evolution equations as

$$\partial_t \boldsymbol{u} + \boldsymbol{M}^i \partial_i \boldsymbol{u} = \boldsymbol{S}(\boldsymbol{u}), \tag{2.23}$$

where the i index spans the spatial dimensions, $\boldsymbol{S}(\boldsymbol{u})$ is a source term and the $\boldsymbol{M}^i$ are called *characteristic matrices*. For an arbitrary unit vector $s_i = (s_1, s_2, s_3)$ we define the *principle symbol* matrix $\boldsymbol{P}(\vec{s}) := \boldsymbol{M}^i s_i$. If this has real eigenvalues and a complete set of eigenvectors for any s_i the system is *strongly hyperbolic*[5], if it has real eigenvalues but not a complete set of eigenvectors the problem is *weakly hyperbolic*. Unfortunately, the ADM formulation can be shown to be strongly hyperbolic only if the momentum constraint is satisfied at all times, which due to numerical errors is not generally true, which means that the ADM initial value problem is typically only weakly hyperbolic and not well-posed.

2.4 Improved formulations and conformal transformations

A major step forward in NR was the development of a strongly hyperbolic formulation of the evolution equations by Baumgarte, Shapiro, Shibata and Nakamura, termed the "BSSN" formulism [172–174].[6]

[3] If this condition holds only up to some finite time T the problem is *locally* well-posed. If it is true for all time the problem is *globally* well-posed.

[4] Note that well-posedness does not necessarily require that the initial data is smooth and continuous [164, 171].

[5] If all the eigenvalues are also all distinct the system is *strictly hyperbolic*.

[6] Sometimes also termed "BSSNOK" to acknowledge the contributions of Oohara and Kojima to the original paper by Nakamura.

One key idea is to use a conformal transformation. We define the conformal factor $\chi = \gamma^{-1/3}$ (not to be confused with the dimensionless black hole spin) such that the conformally rescaled spatial metric $\tilde{\gamma}_{ij} := \gamma_{ij}\chi$ has a unit determinant. This definition ensures that χ goes to zero at a black hole singularity instead of blowing up as $1/r$, and that $\tilde{\gamma}_{ij}$ stays order 1. As $r \to \infty$ the conformal factor tends to 1. The extrinsic curvature is decomposed into its trace K and a conformally rescaled traceless part $\tilde{A}_{ij}$ as

$$K_{ij} = \frac{1}{\chi}\left(\tilde{A}_{ij} + \tfrac{1}{3}K\tilde{\gamma}_{ij}\right). \tag{2.24}$$

Finally we define the conformal connection functions

$$\tilde{\Gamma}^i := \tilde{\gamma}^{jk}\tilde{\Gamma}^i_{jk} = -\partial_j\tilde{\gamma}^{ij}, \tag{2.25}$$

and promote them to evolution variables, where $\tilde{\Gamma}^i_{jk}$ are the connection coefficients for the conformal spatial metric. Multiples of the constraints are added to the evolution equations to achieve strong hyperbolicity and hence stable numerical evolution. The evolution variables are then $\{\chi, K, \tilde{A}_{ij}, \tilde{\gamma}_{ij}, \tilde{\Gamma}^i\}$.

Other well-posed formulations have also been derived. Franz Pretorius (2004) developed a decomposition of the Einstein equations into generalised harmonic coordinates (GHC) [175], which allowed him to perform the very first NR simulation of a black whole binary through the final orbit, merger, and ringdown in 2005 [176, 177].

However, the formulation used in the work presented in this thesis is the CCZ4 formulation by Alic et al. (2012) [178] based on the Z4 system [179–181]. The key idea is to introduce a new 4-vector Z^μ such that

$$R_{\mu\nu} + \nabla_{(\mu}Z_{\nu)} = 8\pi\left(T_{\mu\nu} - \tfrac{1}{2}g_{\mu\nu}T\right). \tag{2.26}$$

Comparing (2.26) with (1.7) we see that if $Z_\mu(t, x^i) = 0$ for all t, x^i we recover the Einstein field equations. Therefore instead of imposing the Hamiltonian and momentum constraints directly it is sufficient to maintain $Z_\mu = 0$, and choose initial data that satisfies $Z_\mu(0, x^i) = 0$, $\partial_t Z_\mu(0, x^i) = 0$. Taking the divergence of (2.26) we obtain a wave equation

$$\Box Z_\mu + R_{\mu\nu}Z_\nu = 0, \tag{2.27}$$

so that any deviation from $Z_\mu = 0$ propagates at a finite speed, and we add damping terms

$$R_{\mu\nu} + \nabla_{(\mu}Z_{\nu)} + \frac{\kappa_1}{\alpha}\left[n_\mu Z_\nu + n_\nu Z_\mu - (1+\kappa_2)g_{\mu\nu}n_\sigma Z^\sigma\right] = 8\pi\left(T_{\mu\nu} - \tfrac{1}{2}g_{\mu\nu}T\right), \tag{2.28}$$

so that for $\kappa_1 > 0, \kappa_2 > -1$ any non-zero Z_μ, and thus any constraint violations, are exponentially damped to zero, unlike in the case of BSSN. We use the default GRChombo choices of $\kappa_1 = 0.1$ and $\kappa_2 = 0$.

The same conformal transformation is used as in BSSN, except two new evolution variables are defined, $\Theta := n^\mu Z_\mu$ and $\hat{\Gamma}^i$ where

$$\hat{\Gamma}^i = \tilde{\Gamma}^i + 2\tilde{\gamma}^{i\mu} Z_\mu, \tag{2.29}$$

is used as an evolution variable in place of $\tilde{\Gamma}^i$, with an additional damping parameter κ_3.[7] The evolution variables are then $\{\chi, K, \tilde{A}_{ij}, \tilde{\gamma}_{ij}, \hat{\Gamma}^i, \Theta\}$. The full evolution equations are not particularly enlightening and can be found in [178] and [183], however they are included in appendix A.2 for completeness.

2.5 Gauge choice

As discussed above we also need to choose a gauge via the gauge functions α, β^i. Although in principle any gauge should give physically equivalent results, in practice the gauge choice is very important to achieve stable numerical evolution over long times, and the best choice may depend on the physical system you want to simulate.

The choice of lapse α is termed "choosing the slicing", as it determines how the spacetime is "sliced" into hypersurfaces. One of the most popular choices is the *alpha-driver* or *Bona-Masso*-type slicing

$$\partial_t \alpha = -\mu_1 \alpha^{\mu_2} (K - 2\Theta) + \mu_3 \beta^i \partial_i \alpha. \tag{2.30}$$

For $\mu_1 = 2, \mu_2 = \mu_3 = 1$ this reduces to what is called "1+log" slicing

$$\boxed{\partial_t \alpha = -2\alpha(K - 2\Theta) + \beta^i \partial_i \alpha.} \tag{2.31}$$

This has a key advantage for dealing with black holes in that for $\beta^i = 0$ the lapse decreases exponentially to zero for regions of collapsing spacetime with $K > 0$. This means the evolution will "freeze" near collapsing matter, avoiding any singularities. The downside is that normal observers are pulled towards, and eventually

[7] Note that we use a rescaled $\kappa_1 \to \kappa_1/\alpha$ compared to the original formulation [178] to avoid instabilities of black hole spacetimes with $\kappa_3 = 1$, a suggestion proposed in [182] and discussed in [183].

fall into, the black hole. To fix this we use the so-called *gamma-driver* shift condition

$$\boxed{\begin{aligned}\partial_t \beta^i &= \tfrac{3}{4} B^i, \qquad (2.32)\\ \partial_t B^i &= \tfrac{3}{4}\alpha \partial_t \tilde{\Gamma}^i - B^i. \qquad (2.33)\end{aligned}}$$

The so-called *moving punctures method* [184, 185] is the combination of the 1+log α slicing and the gamma-driver shift condition. It was a key step to achieving practical simulations of black hole binary mergers, and is now the standard choice for spacetimes with black holes. Near the centre of the black hole the hypersurface in this gauge condition asymptotes to a finite distance from the singularity, forming a characteristic "trumpet" shape [186] when pictured in four dimensions.

2.6 Matter evolution

In chapters 3 and 5 the matter we consider is a minimally coupled massive scalar field obeying the Klein-Gordon equation of motion (1.48), which we consider as scalar field dark matter.

To get suitable evolution equations we decompose the second-order Klein-Gordon equation to two first-order evolution equations

$$\boxed{\begin{aligned}\partial_t \varphi &= \alpha \Pi + \beta^i \partial_i \varphi, \qquad (2.34)\\ \partial_t \Pi &= \alpha \gamma^{ij} \partial_i \partial_j \varphi + \alpha \left(K\Pi - \Gamma^k \partial_k \varphi - m_s^2 \varphi \right)\\ &\quad + \partial_i \varphi \partial^i \alpha + \beta^i \partial_i \Pi, \qquad (2.35)\end{aligned}}$$

where Π is the conjugate momentum of φ defined via (2.34). For a complex scalar field we can define it in terms of two real scalar fields $\varphi = \varphi_{\mathrm{Re}} + \mathrm{i}\varphi_{\mathrm{Im}}$ and their conjugate momenta $\Pi = \Pi_{\mathrm{Re}} + \mathrm{i}\Pi_{\mathrm{Im}}$ and evolve the real and imaginary parts separately according to (2.34)(2.35).

2.7 Initial data

The final big challenge for Numerical Relativity simulations is obtaining constraint satisfying initial data. As we have seen, the γ_{ij} and K_{ij} we specify on the initial hypersurface need to satisfy the Hamiltonian (2.16) and momentum (2.18) constraints. If we have matter in our simulation this is a highly non-trivial problem.

There are several different approaches to solving these elliptic equations to obtain constraint satisfying data (see [187] and references therein). In chapter

5 we use the novel *Conformal-Transverse-Traceless-K* (CTTK) method. The full details of the method can be found in Aurrekoetxea, Clough and Lim (2022) [188], however we will summarise the key points here. The CTTK method is based on the CTT (Conformal-Transverse-Traceless) method. We use a redefined conformal factor

$$\psi := \chi^{-1/4}, \tag{2.36}$$

such that

$$\gamma_{ij} = \psi^4 \tilde{\gamma}_{ij}. \tag{2.37}$$

We also define a new conformally rescaled traceless extrinsic curvature

$$\bar{A}_{ij} := \psi^2 A_{ij} = \psi^6 \tilde{A}_{ij}, \tag{2.38}$$

and we decompose this into a transverse-traceless part $\bar{A}^{TT}_{ij}$ and a longitudinal vector W^i,

$$\bar{A}_{ij} = \bar{A}^{TT}_{ij} + \tilde{D}_i W_j + \tilde{D}_j W_i - \tfrac{2}{3}\tilde{\gamma}_{ij}\tilde{D}_k W^k, \tag{2.39}$$

where $\tilde{D}_i$ denotes the covariant derivative with respect to the conformal spatial metric. The Hamiltonian (2.16) and momentum (2.18) constraints become

$$\tilde{D}^2\psi = \tfrac{1}{8}{}^{(3)}\tilde{R}\psi - \psi^{-7}\bar{A}_{ij}\bar{A}^{ij} + \psi^5\left(\tfrac{1}{12}K^2 - 2\pi\rho\right), \tag{2.40}$$

$$(\tilde{\Delta}_L W)^i = \tfrac{2}{3}\psi^6\tilde{\gamma}^{ij}\tilde{D}_j K + 8\pi\psi^{10}S^i, \tag{2.41}$$

$$\tilde{D}_j\bar{A}^{ij}_{TT} = 0. \tag{2.42}$$

where $\tilde{\Delta}_L$ is the vector Laplacian and ${}^{(3)}\tilde{R}$ the Ricci scalar of the conformal spatial metric. To simplify the equations we assume $\tilde{\gamma}_{ij} = \delta_{ij}$ (i.e. assume a conformally flat space), and $\bar{A}^{ij}_{TT} = 0$ (no initial transverse-traceless modes). This means ${}^{(3)}\tilde{R} = 0$. We can make a further simplification by requiring $W_i = V_i + \partial_i U$, and $\nabla^2 U = -\frac{1}{4}\partial_j V^j$ for some scalar function U. The equations then reduce to

$$\nabla^2 U = -\tfrac{1}{4}\partial_j V^j, \tag{2.43}$$

$$\nabla^2\psi = -\tfrac{1}{8}\bar{A}_{ij}\bar{A}^{ij}\psi^{-7} + \left(\tfrac{1}{12}K^2 - 2\pi\rho\right)\psi^5, \tag{2.44}$$

$$\nabla^2 V_j = \psi^{10} 8\pi S_j + \psi^6 \tfrac{2}{3}\partial_j K. \tag{2.45}$$

We can then try to solve these Poisson equations for ψ and V_i and use those to recover $\tilde{\gamma}_{ij}$, $\bar{A}_{ij}$ and therefore $\tilde{A}_{ij}$. Our approach is to linearise around some initial guess ψ_0, V^i_0 with $\psi = \psi_0 + \delta\psi$, $V^i = V^i_0 + \delta V^i$, then numerically solve for the corrections $\delta\psi, \delta V^i$ using a non-linear Poisson solver. We then update the guesses

and iterate until the results converge. In the CTT method a common approach to uncouple the Hamiltonian equation (2.44) and momentum equation (2.45) is to set $K = const.$. However, there is a problem with this approach: if the sign of the coefficient in the right hand side of the (2.44) equation does not match the sign of the power of ψ, we are not guaranteed unique solutions. Hence this becomes a problem for $2\pi\rho > \frac{1}{12}K^2$.

One way around this is to instead work with a rescaled density, $\tilde{\rho} = \psi^5\rho$. Unfortunately this means we lose control over the matter distribution as we can only set $\tilde{\rho}$ as our input not ρ, and in the case of a scalar field we cannot then reconstruct φ and Π. Even if you avoid this latter problem by using a rescaled φ and Π as inputs, you are still faced with a loss of control over the initial matter conditions. Therefore, the CTTK method uses an alternative, perhaps more natural, approach, which is to set

$$K^2 = 24\pi\rho, \tag{2.46}$$

and solve for K algebraically. This does mean that we need to solve (2.43), (2.44) and (2.45) as a fully coupled set of equations, however this can be done successfully (the precise technical details can be found in [188]). The reason this approach can be thought of as "more natural" is that naively you would expect matter density to locally curve spacetime and thus influence the extrinsic curvature K. So allowing K to change with ρ is a more natural choice than fixing $K = const.$. If we want to obtain initial data for both scalar fields and black holes, as in chapter 5, then we can further decompose $\psi, \bar{A}_{ij}$ as

$$\psi = \psi_{\rm BH} + \psi_*, \tag{2.47}$$

$$\bar{A}^{ij} = \bar{A}^{ij}_{\rm BH} + \bar{A}^{ij}_*. \tag{2.48}$$

The black hole terms $\psi_{\rm BH}, \bar{A}^{ij}_{\rm BH}$ can be obtained from Bowen-York analytic solutions for initial data for boosted black holes [189–191], and the $\psi_*, \bar{A}^{ij}_*$ can then be solved as small corrections using the method outlined above.

We also need to specify an initial lapse and shift. We choose the popular "pre-collapsed" lapse [170]

$$\alpha = \psi^{-2} = \chi^{1/2}, \tag{2.49}$$

and vanishing shift $\beta^i = B^i = 0$.

2.8 Fixed background

In NR simulations we typically work in units of order the Schwarzschild radius R_s which scales with the black hole's mass M. Average galactic dark matter densities are of the order $\rho_{\rm DM} \sim 0.01 M_\odot {\rm pc}^{-3}$ [116, 127]. Expressed in simulation units this is

$$\rho_{\rm DM} R_s^2 \sim 10^{-30} \left(\frac{\rho_{\rm DM}}{M_\odot {\rm pc}^{-3}} \right) \left(\frac{M}{10^6 M_\odot} \right)^2 , \tag{2.50}$$

which is far below even the level of numerical noise in our simulation. The Einstein equations (1.6) show that the effect of the matter on the spacetime metric, the "backreaction", is of order $T_{\mu\nu}$ so of order the density. Hence for simulations examining accretion from a diffuse galactic dark matter background we are justified in neglecting the backreaction, and evolving the spacetime as if it were in vacuum. We term this the "fixed background" approach. In chapter 3 we don't evolve the metric with Numerical Relativity at all and just keep it as a Kerr black hole, and only evolve the matter according to (2.34) and (2.35). In the model of the early inspiral regime in chapter 5 section 5.2 we instead evolve the metric according to an analytic solution for two isotropic black holes in fixed circular Keplerian orbits. The main advantage of the fixed background approach is that it is computationally much cheaper than the full Numerical Relativity evolution. As the Klein-Gordon equation is linear we can rescale the scalar field so it is order ~ 1, while keeping the physical density the same. This allows us to model these low-density regimes numerically without having to deal with inconveniently small numbers.

In regions where the scalar dark matter density is significantly enhanced (for instance a cloud formed after long period of accretion and pile up, or a superradiant cloud) the backreaction may become significant, as we explore in chapter 4 and chapter 5 section 5.4.

2.9 GRChombo

There are many different Numerical Relativity codes out there, all with different capabilities and their own advantages and disadvantages (for a summary see [192]). The code used for the work in this thesis is GRChombo [193, 194], an open source `C++` code based on Chombo [195], a general solver for partial differential equations using finite difference and finite volume methods and adaptive mesh refinement (AMR) [196].

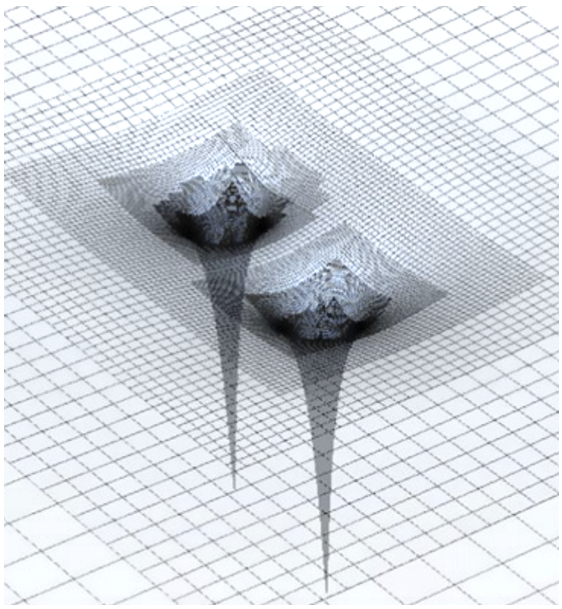

Figure 2.2: **Black hole binary with AMR in GRChombo**. This 3D plot shows the conformal factor χ on the z axis, and the grid structure on the x, y plane, for a GRChombo simulation of a black hole binary merger. Note how the conformal factor decreases from 1 far from the black holes to 0 at the black hole centres, and regions of higher resolution are concentrated around the two black holes (figure adapted from Fig. 7 in [194]).

The technical details of how it works can be found in [193], [194] and [183]. However, the key idea is that the evolution variables are defined on a series of nested grids. The grid spacing decreases by 2 as you go from an outer grid to an inner grid, and the integration time step dt also decreases by 2. This increase in resolution allows you to use high resolution in regions where it is important, such as near the black hole horizon or regions of high density (see Fig. 2.2), and low resolution elsewhere, such as regions of low density far from the black hole. The code can dynamically alter the layout of the grids to adjust the resolution as needed, and this is what makes it "adaptive mesh refinement", and particularly suited to problems with matter or fundamental fields. In the work presented here we used 4th-order Runge-Kutta integration, however higher-order methods can also be used.

The code is typically run in parallel on thousands of CPUs, where different processors are assigned different sections of the grid to evolve, and communicate via the Message Passing Interface (MPI).

Part II

Research

Chapter 3

The growth of accretion driven scalar field clouds around Kerr black holes

As described in section 1.3.2 a low mass "axion-like" scalar field is a well motivated candidate for dark matter. It could have non-trivial self interactions or non-minimal couplings, however the simplest case is a real scalar field φ with mass μ (see note on units) and a potential $V(\varphi) \approx \frac{1}{2}\mu^2\varphi^2$, minimally coupled to Einstein gravity.

Note on units

In this chapter and the subsequent two chapters we shall typically work not in terms of m_s, the physical scalar field mass, but in terms of $\mu = m_s c/\hbar = \lambda\!\!\!^{-1}$, the inverse reduced Compton wavelength, or the dimensionless quantity $\alpha_g = r_g\mu$, $r_g = GM/c^2$ being the gravitational radius of the black hole. In Planck units $\mu = m_s$, however when dealing with black holes it is more convenient to use geometric units $G = c = 1$ with $M \sim 1$, in which case $\hbar \neq 1$, $\mu = m_s/\hbar \neq m_s$ and $\alpha_g = M\mu$. The factors of $\hbar$ only become important when we express the scalar mass numerically in terms of eV, hence we shall simply refer to μ as "the scalar mass", even though it is really an inverse length scale.

Analytic solutions for the stationary profile of scalar clouds have been obtained for a massive scalar field obeying the Klein-Gordon equation on fixed black hole background metric [18, 197, 198] (where the backreaction of the scalar field on the metric is neglected) based on the confluent Heun function [199]. For $r \gg M$ the scalar field obeys an equation which approximates the Schrödinger equation governing the electron in a hydrogen atom, as discussed in section 1.3.3. Hence

in this non-relativistic limit the field profiles become energy levels analogous to those of hydrogen.

A key question is how these clouds could form dynamically. The mechanism of superradiance (see section 1.3.3) has received much attention, however as discussed the bosonic mass and the black hole mass and spin must satisfy an instability condition which may not be realised in nature.

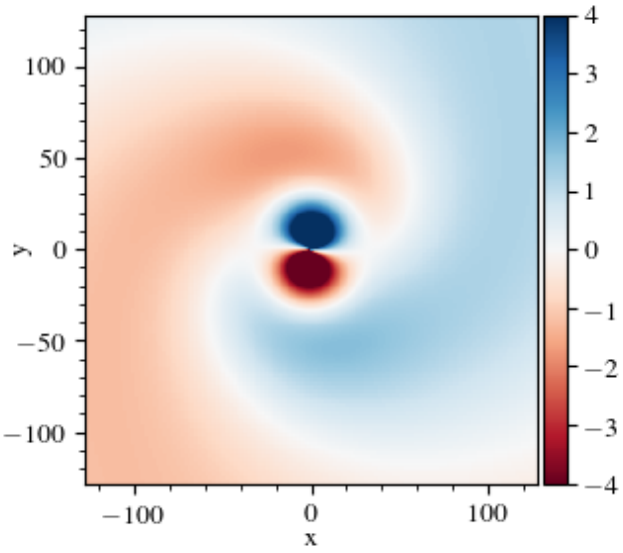

Figure 3.1: **Visualisation of the 2D scalar field profile φ/Φ_0 around a spinning BH**, after a time $t = 800M$. The initial scalar profile at $t = 0$ is set as a $l = m = 1$ spherical harmonic. The scalar and BH masses are given by $\mu = 0.4$ and $M = 1$ respectively, and the dimensionless BH spin is set to $\chi = 0.7$ (aligned with the scalar spin axis). At this point the maximum amplification of the scalar field is of order $|\varphi/\Phi_0| \sim 10$, where Φ_0 is the initial amplitude, but this will continue to grow over time.

By moving beyond the superradiant mechanism and its requirements we can consider how scalar hair could form under a broader class of conditions. As shown by Jacobson [31], giving the field a non-trivial time dependence far from the black hole is one way of violating the assumptions of the no-hair theorems and gives rise to the growth of a non-trivial profile. In [198, 200] the Jacobson effect was explored as an alternative, simpler mechanism for growing scalar hair. In flat space the scalar field can have a global non-trivial time dependence of the form $e^{-i\mu t}$ [198]. We can therefore impose this as the asymptotic condition for the field, rather than requiring it to decay to zero as in superradiant bound states. The physical

interpretation of this condition is that we have a non-zero asymptotic density – that is, the clouds arise from simple gravitational accretion from a cosmological background. Unlike superradiance, it does not rely on a particular value of $M\mu$, but wave-like effects will be most pronounced in the regime $M\mu \lesssim 1$, which is particularly relevant to the case of light bosonic dark matter.[1]

The numerical simulations in [200] demonstrated the growth of a non-trivial profile with and without backreaction on the metric, assuming a spherically symmetric Schwarzschild BH and DM environment. In this work we go further and consider the impact of angular momentum on the accretion of the scalar field, including the interplay of both non-zero asymptotic angular momentum in the scalar field and a spinning Kerr black hole. We study a range of scalar masses, characterising deviations from uniform spherically symmetric accretion, and their impact on the cloud growth. Fig. 3.1 and Fig. 3.2 illustrate one example of the resulting clouds. Astrophysically, the non-zero asymptotic angular momentum may arise from rotating galactic DM halos or from the merger of a compact object binary where each object has its own scalar cloud.

The formalism and setup for our numerical work is described in Sec. 3.1, with further detail in appendix B. In Sec. 3.2 we develop a perturbative analytic framework to describe the accretion onto the BH as a function of the various parameters. We then confirm these predictions and compare them to the full non linear evolution by performing simulations as described Sec. 3.3. In Sec. 3.4 we highlight the potential for our scalar clouds with angular momentum to generate continuous monochromatic gravitational wave signals, and quantify their amplitude. In Sec. 3.5 we summarise our findings and propose directions for future work.

[1] The corresponding bosonic mass scales are $\sim 10^{-11}$eV for a typical astrophysical BH mass $10M_\odot$, and $\sim 10^{-19}$eV for a supermassive BH of mass $10^9 M_\odot$ [198].

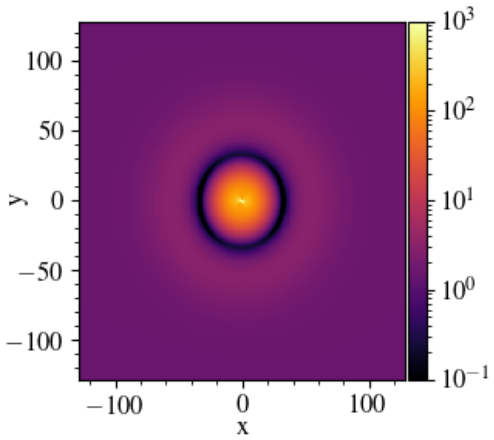

(a) Scalar field energy density ρ_E/ρ_0

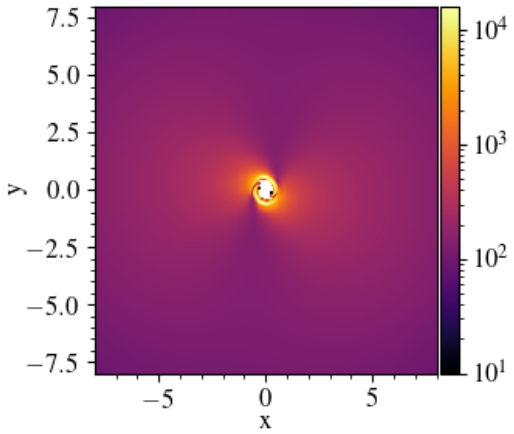

(b) Scalar field energy density ρ_E/ρ_0 (zoomed in)

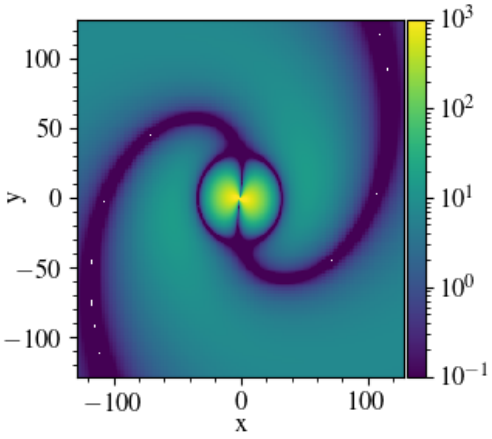

(c) Scalar field angular momentum density magnitude $|\rho_J|/\rho_0$

Figure 3.2: **Visualisation of the energy density ρ_E/ρ_0 and angular momentum density ρ_J/ρ_0 profiles** for the same parameters and at the same time as in Fig. 3.1 with $l = m = 1, \mu = 0.4, M = 1, \chi = 0.7, t = 800$, on a logarithmic scale. The initial density $\rho_0 = \frac{1}{2}\Phi_0^2\mu^2$ where Φ_0 is the initial amplitude of the field. Note that for a real scalar field with non-zero angular momentum there is a non axisymmetric, rotating component to both energy and angular momentum densities.

3.1 Framework and numerical setup

In this section we lay out the formalism and methods we will use to study the cloud growth. For this work we describe the Kerr black hole not in Boyer-Lindquist coordinates, as in (1.16), but in "Quasi-Isotropic Kerr" (QIK) coordinates of [201–204]. These are obtained by introducing the quasi-isotropic radial coordinate R, related to the BL radius r via

$$r = R\left(1 + \frac{r_+}{4R}\right)^2 . \tag{3.1}$$

(Note that we use a Cartesian realisation of these coordinates where $R^2 = x^2 + y^2 + z^2$ and $\{x, y, z\}$ are related to $\{R, \theta, \phi\}$ in the usual Cartesian manner).

In QIK coordinates $\{t, R, \theta, \phi\}$, the line element is

$$\mathrm{d}s^2 = -\alpha^2\,\mathrm{d}t^2 + \gamma_{ij}(\mathrm{d}x^i + \beta^i\,\mathrm{d}t)(\mathrm{d}x^j + \beta^j\,\mathrm{d}t), \tag{3.2}$$

where

$$\begin{aligned} \alpha &= \sqrt{\frac{\Delta\Sigma}{\mathcal{A}}}, \quad \beta^\phi = -\frac{2aMr}{\mathcal{A}}, \\ \gamma_{ij}\mathrm{d}x^i\mathrm{d}x^j &= \frac{\Sigma r}{R^2(r - r_-)}\mathrm{d}R^2 + \Sigma\mathrm{d}\theta^2 + \frac{\mathcal{A}}{\Sigma}\sin^2\theta\mathrm{d}\phi^2, \end{aligned} \tag{3.3}$$

and the other β^i components vanish. The advantage of this is that the coordinate location of the outer horizon is fixed at $R = R_+ = r_+/4$, which maintains a finite value $M/4$ in the extremal spin limit. One difficulty is that the lapse α goes to zero at the horizon, so they are not horizon penetrating. We use an analytic continuation such that inside the horizon the lapse becomes

$$\alpha = -\sqrt{\left|\frac{\Delta\Sigma}{\mathcal{A}}\right|}. \tag{3.4}$$

Further details regarding this choice and a comparison to horizon penetrating Kerr-Schild coordinates are provided in appendix B.

3.1.1 Scalar field evolution and initial conditions

We will consider a minimally-coupled massive scalar field φ with mass scale μ. As discussed in section 1.3.3 the equation of motion for the field is the Klein-Gordon equation

$$\left[\nabla^\nu\nabla_\nu - \mu^2\right]\varphi = 0 . \tag{3.5}$$

Throughout this chapter we will neglect the backreaction of the scalar field on the metric, which is a very good approximation for low density fields. As shown in [200], the inclusion of backreaction does not disrupt the accretion process. In particular, this is a reasonable approximation for typical DM densities. The backreaction will be order $G\rho$ where ρ is the scalar field energy density. For a typical DM density of $\rho \sim 1$ GeVcm^{-3} [115] the source term expressed in geometric units where $M = 1$ is $G\rho \sim 10^{-30}(M/10^6 M_\odot)^2$ which is $\lll 1$ even for supermassive BHs.

In the absence of the black hole's potential well a spatially homogeneous complex massive scalar simply oscillates at frequency μ as $\varphi(t) = \Phi_0 e^{-i\mu t}$. This corresponds to the case of zero angular momentum in the field, and spatially constant energy density. Adding in angular variation, in particular a spherical harmonic profile, corresponds to adding a non-zero angular momentum to the field in some direction, which may or may not be aligned with the black hole's spin. This observation motivates the choice of our initial conditions as

$$\varphi(t, \theta, \phi) = \Phi_0 \mathrm{Re}\{e^{-\mathrm{i}\mu t} Y^*_{lm}(\theta, \phi)\}, \tag{3.6}$$

where Y_{lm} are spherical harmonics. We consider different values for the dimensionless spin of the BH χ, the dimensionless ratio of the BH radius versus the scalar wavelength $\alpha_g = M\mu$, the mode numbers l, m which determine the initial the initial angular momentum of the surrounding scalar field, and the alignment angle α between the black hole and cloud spin.

The maximum size of the cloud that develops will be strongly influenced by the surrounding scalar environment. Following [198] one can define a "radius of influence" of the black hole as the radius at which the virial velocity calculated from the black hole's potential is comparable to the typical velocity dispersion of the surrounding scalar matter,

$$v^2_{\mathrm{virial}} = \frac{M}{r_i} \sim v^2_{\mathrm{disp}}. \tag{3.7}$$

The conditions at this radius will determine the characteristics of the cloud that form around the BH. Note that this is different from the superradiant case, where the scalar field is typically assumed to decay to zero at large r, with no non-zero cosmological or galactic scalar field background, and the size of the cloud is fully determined by the properties of the black hole and the scalar field mass. In that case the characteristic size is given by [138]

$$R \sim M/(M\mu)^2. \tag{3.8}$$

In this work we remain agnostic to the exact conditions, and simply characterise the cloud according to the possible physical parameters of the asymptotic scalar distribution. However, here we will briefly illustrate the physical intepretation of the quantities in the dark matter case. The energy density of the field is $\rho_E \sim \Phi_0^2\mu^2$. Thus for a typical DM density of $\sim 1\text{GeVcm}^{-3}$ and a supermassive BH of mass $10^6 M_\odot$ we would have $\Phi_0 \sim 10^{-15}(\mu M)^{-1}$ in geometric units where $M = 1$. As discussed in section 2.8 we can neglect the backreaction, and as the Klein-Gordon equation is linear the value of Φ_0 is arbitrary. We use an order 1 value which can be rescaled accordingly for different physical densities. Whilst our initial configuration is somewhat artificial, corresponding to a homogeneous radial density profile, it is nevertheless instructive in showing how different parameters of the field and BH affect the transient growth rate from a zero cloud state, and allows us to relate the change in the mass and spin of the BH to the non-trivial asymptotic conditions which characterise the scalar field far from the BH.

3.1.2 Diagnostic quantities

In this section we define a number of quantities that will allow us to quantify the growth of the scalar cloud and its effects. Further implementation details are given in appendix B.

As discussed in section 1.2.2 the Kerr metric is independent of t and ϕ and so admits two Killing vectors $\xi_1^\mu = (1,0,0,0)$ and $\xi_2^\mu = (0,0,0,1)$ in (t, R, θ, ϕ) coordinates, with associated conserved quantities. The properties of a Killing vector field and the energy-momentum tensor then imply

$$\nabla_\mu(\xi^\nu T^\mu_\nu) = \frac{1}{\sqrt{-g}}\partial_\mu(\sqrt{-g}\xi^\nu T^\mu_\nu) = 0, \tag{3.9}$$

where g is the determinant of the metric $g_{\mu\nu}$, and therefore we can define two associated conserved currents as:

$$J^\mu_t = -T^\mu_t, \tag{3.10}$$

$$J^\mu_\phi = T^\mu_\phi. \tag{3.11}$$

which obey $\nabla_\mu J^\mu = 0$ and

$$\partial_t(\sqrt{-g}J^t) = -\partial_i(\sqrt{-g}J^i). \tag{3.12}$$

Integrating both sides of (3.12) over a 3D spatial volume Σ within one spatial slice and applying the divergence theorem gives

$$\partial_t \int_\Sigma \sqrt{-g} J^t \mathrm{d}x^3 = -\int_{\partial\Sigma} \sqrt{-g} J^i \mathrm{d}S_i, \tag{3.13}$$

$$\partial_t \int_\Sigma \rho \mathrm{d}V = \int_{\partial\Sigma} \mathrm{d}F \tag{3.14}$$

where the 3D volume element is $\mathrm{d}V = \sqrt{\gamma}\ \mathrm{d}x^3$, the density is αJ^t and $\mathrm{d}S_i$ is the vector surface element and F is the flux across $\partial\Sigma$. If Σ is a sphere of constant R then $\mathrm{d}S_i = \partial_i R$. We can thus define

$$\rho_E = -\alpha T^t_t, \quad \rho_J = \alpha T^t_\phi \tag{3.15}$$

where ρ_E is the mass density and ρ_J is the density of angular momentum about the BH axis. The rate of change in the total scalar field mass or total angular momentum between the BH horizon and an outer sphere is given by the integral of the respective flux across the sphere minus that across the horizon,

$$\partial_t M_{\mathrm{cloud}} = \int_{R=R_{\mathrm{max}}} \mathrm{d}F - \int_{R=R_+} \mathrm{d}F. \tag{3.16}$$

In the limit $R_{\mathrm{max}} \to \infty$ the flux across the outer surface also corresponds to the change in the Arnowitt-Deser-Misner (ADM) mass or ADM angular momentum of the enclosed spacetime. They are therefore closely tied to physically measurable properties of the system, even at (large) finite distances, whereas the details of the distribution close to the BH are more observer dependent. Further details are given in appendix B, where this is used to validate the code evolution.

3.1.3 Numerical implementation

As described in chapter 2, we solve the second order Klein-Gordon equation by decomposing it into two coupled first order equations:

$$\partial_t \varphi = \alpha \Pi + \beta^i \partial_i \varphi\ , \tag{3.17}$$

$$\begin{aligned} \partial_t \Pi = {} & \alpha \gamma^{ij} \partial_i \partial_j \varphi + \alpha \left(K\Pi - \gamma^{ij} \Gamma^k_{ij} \partial_k \varphi - \mu^2 \varphi \right) \\ & + \partial_i \varphi \partial^i \alpha + \beta^i \partial_i \Pi\ , \end{aligned} \tag{3.18}$$

where Π is the conjugate momentum density, as defined by Eqn. (2.34) and K is the trace of the extrinsic curvature $K_{ij} = \frac{1}{2\alpha}\left(-\partial_t \gamma_{ij} + D_i \beta_j + D_j \beta_i\right)$.

We use an adapted version of the open source code GRChombo [193, 194] to solve (3.17)(3.18) on a fixed metric background in the QIK coordinates described above. The scalar field is evolved by the method of lines with 4th-order finite difference stencils, Runge Kutta time integration and a hierarchy of grids with 2:1 resolution. The value of the metric and its derivatives are calculated locally from the analytic expressions at each point. Details of code validation tests and convergence are provided in appendix B.

The size of the simulation domain is $L = 1024M$, and we use seven (2:1) refinement levels with the coarsest having 128^3 grid points, although we use the bitant symmetry[2] of the problem in Cartesian coordinates to reduce the domain to 64×128^2 points. We implement non-zero, time oscillating boundary conditions for the scalar field by extrapolating the field linearly in the radial direction from values within the numerical domain.

The form of the metric naturally imposes ingoing boundary conditions at the horizon, due to the causal structure of the black hole. At spatial infinity we extrapolate the field value within the grid radially at first order, to simulate the effects of a roughly constant energy density. This in effect allows both ingoing and outgoing modes, but can introduce unphysical effects in very long simulations – these can be easily identified by varying the domain size, but ultimately limit the time for which the growth can be studied. The time before strong boundary effects occur is of the order of the light crossing time for our simulation box of $1024M$. This is roughly 5ms for a solar mass BH and 60 days for a SMBH of mass $10^9 M_\odot$.

3.2 Analytic framework

In this section we summarise what is known for stationary solutions, and develop several approximate analytic tools and a perturbative formalism to understand the growth of the scalar hair over time in different regimes of the parameter space. These methods are then confirmed within their regime of validity by the full numerical results in Sec. 3.3.

[2] I.e. a reflection symmetry across the $z = 0$ plane.

3.2.1 Stationary solutions

There is no simple, exact analytic solution for the growth of the scalar cloud from a general initial state. However exact analytic quasi-stationary oscillatory solutions have been found which we would expect to describe the final state of the cloud which forms [18]. These solutions can generically be expressed in BL coordinates as:

$$\varphi_{lm}(t, r, \theta, \phi) = \mathrm{Re}\left\{\Phi_0 e^{-\mathrm{i}\omega t} R_{lm}(r) e^{\mathrm{i}m\phi} S_{lm}(\theta; \mathrm{i}c)\right\}, \tag{3.19}$$

where Φ_0 describes an initial amplitude. Here, $e^{im\phi}S_{lm}(\theta; \mathrm{i}c)$ are oblate spheroidal harmonics, which reduce to spherical harmonics when $c = ak = 0$, where $k = \sqrt{\omega^2 - \mu^2}$ is the (complex) momentum at infinity. When ω is real, the solutions are stationary in time, whereas if ω has an imaginary component the field grows or decays exponentially with time. The radial functions R_{lm} satisfy an equation of the form

$$\left[\partial^2_{r_*} - V(r)\right] \sqrt{r^2 + a^2} R_{lm}(r) = 0, \tag{3.20}$$

where r_* is the Kerr tortoise coordinate

$$r_* = r + \frac{2M}{r_+ - r_-}\left[r_+ \ln(r - r_+) - r_- \ln(r - r_-)\right]. \tag{3.21}$$

The general solutions are given by:

$$R_{\pm,lm}(r) = e^{\mp\frac{1}{2}\alpha z} z^{\pm\frac{1}{2}\beta}(z+1)^{\frac{1}{2}\gamma}\mathrm{HeunC}(\pm\alpha, \pm\beta, \gamma, \delta, \eta, -z), \tag{3.22}$$

where $\pm$ denotes modes which are ingoing/outgoing at the horizon. Here, HeunC is the confluent Heun function [199] with

$$\begin{aligned}
z &= \frac{r - r_+}{r_+ - r_-}, \quad \alpha = 2\mathrm{i}(r_+ - r_-)k, \quad \beta = 2\mathrm{i}\frac{(am - 2r_+M\omega)}{r_+ - r_-}, \\
\gamma &= 2\mathrm{i}\frac{(am - 2r_-M\omega)}{r_+ - r_-}, \quad \delta = -2M(r_+ - r_-)(\omega^2 + k^2), \\
\eta &= (\omega^2 + k^2)r_+^2 + \omega^2(a^2 + 2M^2) - \frac{(am - 2M\omega)^2}{2(1 - a^2/M^2)} - \lambda_{lm},
\end{aligned} \tag{3.23}$$

where λ_{lm} are the eigenvalues of the oblate spheroidal harmonics [18]. In the limit $r \to r_+$ i.e. $z \to 0$, we obtain

$$R_{\pm,lm}(r) \to \exp(\mp\mathrm{i}k_H r_*), \tag{3.24}$$

up to a constant phase factor [21], where $k_H = \omega - \frac{am}{2Mr_+}$. For the limit $r \to \infty$ there are also two independent ingoing/outgoing solutions which are independent of the spin of the black hole. In particular, for $k \neq 0$ they are

$$R^{\infty}_{\pm,lm}(r) \approx \frac{e^{\mp \mathrm{i}k(r-r_+)}}{r} z^{\mp i\kappa} e^{\pm \pi\kappa}, \tag{3.25}$$

where $\kappa = M(\omega^2 + k^2)/k$. For $\omega = \mu$ i.e. $k = 0$

$$R^{\infty}_{\pm,lm}(r) \approx r^{-3/4} e^{\mp \mathrm{i}2\mu\sqrt{2Mr}}. \tag{3.26}$$

Note that in general each ingoing/outgoing solution at the horizon tends to a linear combination of the ingoing/outgoing solutions at $r \to \infty$ [57].

For non-spinning black holes, these analytical results have been shown to match well the spatial profile of the scalar cloud after long enough times [200]. For spinning black holes, we will see that the same holds.

As mentioned in section 1.3.3, a well-known mechanism which enhances a scalar field around a spinning black hole is superradiance. In this case, the growth of hair is powered solely by the spindown of the black hole. It does not require the light boson to be dark matter, and indeed one assumes the field goes to zero far from the black hole [143]. Hence one rejects as unphysical any solutions (3.19) which have energy "entering from infinity" or "escaping the black hole horizon" (as there is no scalar field density at infinity and nothing can escape the horizon), i.e. one requires that solutions of the form (3.19) to be *ingoing* at the horizon and *outgoing* at spatial infinity, resulting in a discrete spectrum of quasi-normal modes (QNM) as discussed in section 1.2.5 with regards to gravitational oscillations. The maximum size of the boson cloud is determined by the instability condition (1.52) – as the black hole spins down Ω_H decreases until (1.52) becomes saturated [143]. Numerical simulations have shown that the maximum mass of cloud for a vector boson (Proca field) is $\sim$ 10% the mass of the black hole [205] (see also [206–209] for semi-analytic studies), and similar magnitudes are expected for the scalar case. The accretion of compact boson stars onto BHs has also been proposed as a mechanism to enhance scalar clouds [142, 210].

In contrast, in the case we study, the cloud growth is powered by the reservoir of asymptotic scalar density, i.e. the surrounding dark matter halo. The field must still be ingoing at the horizon, but we allow both ingoing and outgoing modes at infinity.

Neglecting the backreaction there is no way for non-interacting DM to radiate and lose energy, so we expect accretion to populate energy states with the same frequency ω as that of the accreting matter. In free Minkowski space, a uniform field oscillates with frequency μ and has energy μ, so we expect the scalar matter to populate marginally bound states with $\omega \approx \mu$. Scalar matter bound within some gravitational potential in a galaxy will have energy $\omega \leq \mu$, while DM with some non-zero momentum at infinity will populate $\omega > \mu$ states.

3.2.2 Effective potential

In order to examine the accretion of the scalar cloud, we seek solutions of Klein-Gordon equation in the Kerr metric which grow with time instead of just oscillating. It is convenient to recast the KG equation in the form of a simple wave equation, where one can interpret the solutions as a scattering off of a barrier of an effective potential.

For simplicity, let us first consider a Schwarzschild background metric. In this case, the KG equation can be expressed as

$$\left[\partial_t^2 - \partial_{r_*}^2 + V_{\text{eff}}(r; l, \mu)\right] \Psi_l(r, t) = 0, \tag{3.27}$$

with

$$\varphi_{lm} = \frac{1}{r} Y_{lm}(\theta, \phi) \Psi_l(r, t). \tag{3.28}$$

Equation (3.27) takes the form of a simple wave equation in one spatial dimension with effective potential

$$V_{\text{eff}}(r; l, \mu) = \left(1 - \frac{2M}{r}\right)\left(\mu^2 + \frac{2M}{r^3} + \frac{\Lambda}{r^2}\right) \tag{3.29}$$

where $\Lambda = l(l+1)$. Fig. 3.3 shows potential profiles for different values of $M\mu$ or l. We see that the potential barrier is lower for higher scalar masses, which allows the scalar matter to simply infall towards the black hole, whereas for lower masses the barrier is higher and reflects ingoing scalar waves, thus generating standing waves around the black hole. Physically, this is due to the pressure support generated by gradients of the scalar in the low mass case. These results have been studied analytically [198] and numerically [200] for $l = m = 0$. In [200] and [198] only spherically symmetric profiles were considered, however here we extend our analysis to environments where the scalar field has asymptotic angular momentum. We see that the higher the l, m, and thus the higher the asymptotic

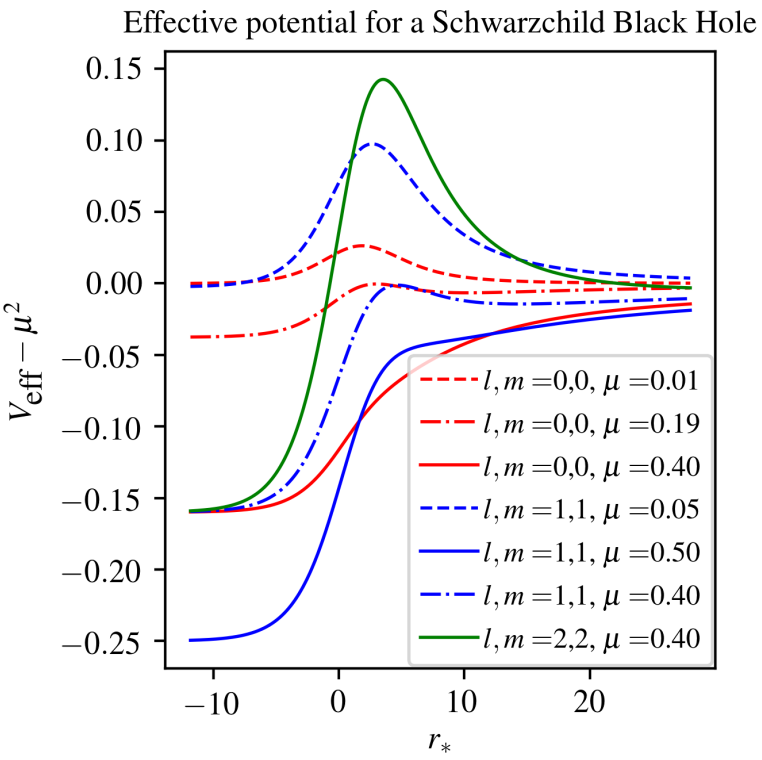

Figure 3.3: **Schwarzschild effective potential** (3.29) for $M = 1$ and different values of the scalar field mass and angular profile. As is well known, increasing the scalar angular momentum and lowering the scalar mass both tend to increase the potential barrier and thus allow stable clouds to form around the BH.

scalar angular momentum, the higher the potential barrier. Hence we expect that increasing the angular momentum of the scalar cloud will reduce the accretion rate onto the BH.

For the Kerr metric in Boyer-Linquist coordinates, the Klein-Gordon equation can be similarly written as

$$\left[\partial_t^2 - \partial_{r_*}^2 + V_{\text{eff}}(r; a, l, m, \mu) + \hat{\mathcal{L}}_1\right] \Psi_{lm}(r, \theta, t) = 0, \tag{3.30}$$

where

$$\begin{aligned}\hat{\mathcal{L}}_1 = &- \frac{\Delta}{(a^2+r^2)^2}\left[\frac{2\partial_\theta Y_{lm}}{Y_{lm}}\partial_\theta + \frac{\partial_\theta}{\sin\theta}\left(\sin\theta\partial_\theta\right)\right. \\ &\left. + a^2\sin^2\theta(\partial_t^2 + \mu^2)\right] + \frac{4imMar}{(a^2+r^2)^2}(\partial_t + \mathrm{i}\mu),\end{aligned} \tag{3.31}$$

and

$$\varphi_{lm} = \frac{Y_{lm}(\theta, \phi)\Psi_{lm}(r, \theta, t)}{\sqrt{a^2 + r^2}}. \tag{3.32}$$

For growing non-stationary solutions we cannot fully separate variables to simplify this equation. However, by writing (3.30) in this form we can see that in the limit $a \to 0$, where $\Psi_{lm}(r, \theta, t) \to \Psi_l(r, t)$, we find $\hat{\mathcal{L}}_1\Psi_{lm} \to \hat{\mathcal{L}}_1\Psi_l(r, t) = 0$ as $\partial_\theta\Psi_l(r, t) = 0$. Hence the $\hat{\mathcal{L}}_1$ operator is capturing the deviation from the simple wave equation due to the black hole's spin.

If we simply ignore the complications and mode-mixing induced by $\hat{\mathcal{L}}_1$, then V_{eff} is a quasi-effective potential given by

$$\begin{aligned}V_{\text{eff}}(r) = &\frac{\Delta}{a^2+r^2}\left[\mu^2 + \frac{a^2}{(a^2+r^2)^2} + \frac{2Mr(r^2-2a^2)}{(a^2+r^2)^3}\right. \\ &\left. + \frac{l(l+1)}{(a^2+r^2)}\right] + \frac{am(4M\mu r - am)}{(a^2+r^2)^2}.\end{aligned} \tag{3.33}$$

which is the same as that given in Arvanitaki and Dubovsky (2011) equation (21) [84]. We plot this quasi-effective potential in Fig. 3.4, where we see that it behaves in a similar way to the Schwarzschild effective potential. Again we see that decreasing the scalar mass or increasing the l, m number, and thus increasing the angular momentum, increases the potential barrier to infall. However we also see that changing the cloud and BH angular momentum from aligned ($l = m = 1$) to anti-aligned ($l = 1, m = -1$) eliminates the potential barrier, suggesting it would lead to faster accretion into the black hole. The intuition provided by these approximate "potentials" will be validated in our numerical studies.

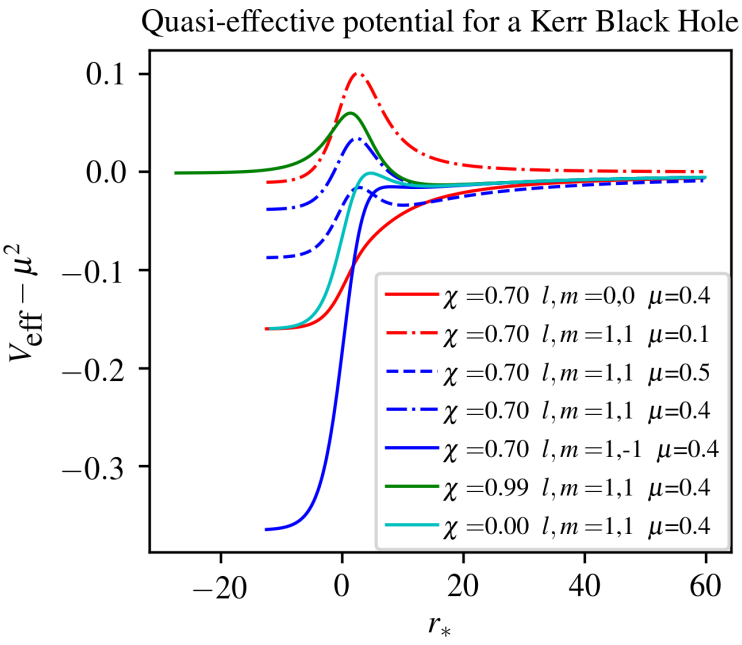

Figure 3.4: **Kerr quasi-effective potential** (3.33) for $M = 1$ and different values of the scalar mass, angular profile, and BH spin. Similarly to Fig. 3.3, we see that decreasing the scalar mass, adding a co-rotating angular momentum to the field and increasing the BH spin all tend to increase the potential barrier and therefore decrease accretion onto the BH. Note that for fixed mass and spin, the profiles are similar at larger distances, even in the co- and counter-rotating cases (green and blue solid lines).

3.2.3 Particle limit

We can also make an analytical study of the scalar field behaviour in the particle limit. A massive particle in a circular orbit around a Kerr black hole in the $z = 0$ plane has an angular momentum per unit mass given by [211]

$$h = \frac{r^2 + a^2 - 2a\sqrt{Mr}}{(r(r^2 - 3Mr + 2a\sqrt{Mr})/M)^{1/2}}. \tag{3.34}$$

Then for a complex scalar field (using the complex case to make the formula simpler) of the form $\varphi = e^{-i\mu t}Y^*_{lm}(\theta, \phi)$ we have

$$\rho_J/\rho_E = \frac{2m\left[2Ma(a\mu - m) + \mu r(a^2 + r^2)\right]}{2\mu^2\left[M(a^2 - r^2) + r(a^2 + r^2)\right] + m^2(r - 2M)}, \tag{3.35}$$

in Boyer-Lindquist coordinates in the $z = 0$ plane assuming $l + m$ is even. Strictly speaking we should only treat the scalar field with a particle rather than a wave description when $M\mu \gg 1$ so the Compton wavelength is much smaller than the size of the black hole. However this particle treatment may still provide a useful heuristic even at small $M\mu$. Fig. 3.5 shows equations (3.34) and (3.35) plotted for $m = 1$, $\chi = 0.7$ and $M\mu = 0.2, 0.4, 0.8, 1.6$. If the angular momentum exceeds the expected particle angular momentum per unit mass for a circular orbit we expect the equivalent particles will move outwards. If the angular momentum is less than expected for a circular orbit we expect they will fall towards the black hole.

3.2.4 Perturbative solutions for cloud growth

The growth of the scalar cloud can also be studied analytically with a perturbative approach for large r. We start by rewriting the Klein-Gordon equation as

$$\mathcal{L}_{KG}\varphi = 0; \quad \mathcal{L}_{KG} = \frac{-1}{\sqrt{-g}}\partial_\mu\left(g^{\mu\nu}\sqrt{-g}\partial_\nu\right) + \mu^2. \tag{3.36}$$

and choose units such that $M = 1$. For a Kerr metric in Boyer-Linquist coordinates we can multiply out the denominator and expand in powers of $1/r$

$$\mathcal{L} = \frac{\Delta\Sigma}{r^4}\mathcal{L}_{KG} = \sum_{n=0}^{6}\frac{1}{r^n}\mathcal{L}_n, \tag{3.37}$$

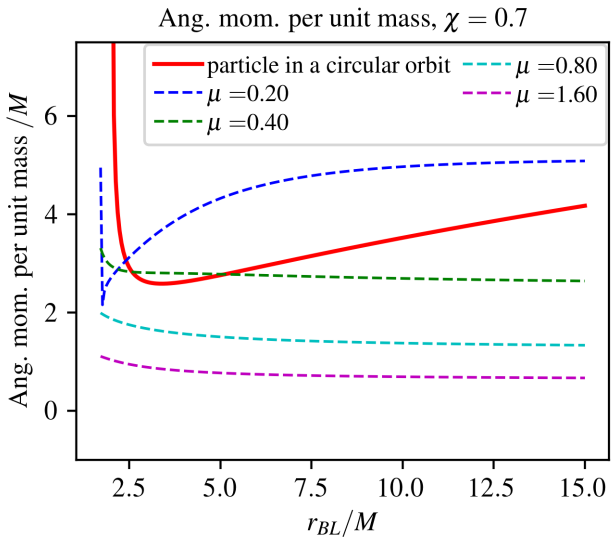

Figure 3.5: **Angular momentum per unit mass for a scalar field and an massive particle**. The solid red line shows the angular momentum per unit mass in the $z = 0$ plane for a single massive particle in a circular orbit. The dashed lines show the angular momentum per unit mass of the scalar field at $t = 0$ (given by equation (3.35)) for different initial conditions, all with $l = m = 1$ but with different μ. If the dashed line lies above the red solid line (for a circular orbit) we expect the scalar field particles to move outwards, otherwise they will fall towards the black hole. Here we see the critical case around $\mu = 0.4$ for which the cloud should concentrate close to the BH, whereas lower mass cases form clouds further out and higher mass cases accrete onto the BH.

where

$$\mathcal{L}_0 = -(\partial_t^2 + \mu^2), \tag{3.38}$$
$$\mathcal{L}_1 = 2\mu^2, \tag{3.39}$$
$$\mathcal{L}_2 = r^2\partial_r^2 + 2r\partial_r - \hat{L}^2 + a^2(1+\cos^2\theta)\mathcal{L}_0, \tag{3.40}$$
$$\mathcal{L}_3 = -2\left(2r^2\partial_r^2 + 3r\partial_r - \hat{L}^2 - a^2\mu^2 + 2a\partial_t\partial_\phi - a^2\sin^2\theta\mathcal{L}_0\right), \tag{3.41}$$
$$\mathcal{L}_4 = 2(a^2+2)(r^2\partial_r^2 + r\partial_r) + a^4\cos^2\theta\mathcal{L}_0 - a^2\partial_\phi^2 - a^2\hat{L}^2, \tag{3.42}$$
$$\mathcal{L}_5 = -2a^2(r\partial_r + 2r^2\partial_r^2), \tag{3.43}$$
$$\mathcal{L}_6 = a^4r^2\partial_r^2, \tag{3.44}$$

and $\hat{L}^2$ is the spherical harmonic operator

$$\hat{L}^2 := -\frac{\partial_\theta}{\sin\theta}(\sin\theta\partial_\theta) - \frac{\partial_\phi^2}{\sin^2\theta}. \tag{3.45}$$

Similarly, we expand the scalar field for large r as:

$$\varphi = \sum_{n=0}^{\infty}\frac{1}{r^n}\varphi_n. \tag{3.46}$$

We choose a (complex) φ_0 such that it satisfies our initial conditions and $\mathcal{L}_0\varphi_0 = 0$

$$\varphi_0 = \Phi_0 e^{-i\mu t}Y_{lm}^*(\theta,\phi), \tag{3.47}$$

where Φ_0 is a constant amplitude. Then we iteratively compute φ_n by matching powers of $1/r$:

$$\varphi_n = \mathcal{L}_0^{-1}\left(\sum_{j=0}^{n-1}\mathcal{L}_{n-j}\varphi_j\right). \tag{3.48}$$

where the operator $\mathcal{L}_0^{-1}$ acting on a general function $A(t)$ behaves as:

$$\mathcal{L}_0^{-1}A(t) = e^{-\mathrm{i}\mu t}\int_0^t e^{2\mathrm{i}\mu t_1}\int_0^{t_1} e^{-\mathrm{i}\mu t_2}A(t_2)\mathrm{d}t_2\mathrm{d}t_1. \tag{3.49}$$

Up to order r^{-2} we obtain for the complex scalar field

$$\begin{aligned}\varphi(t) \approx \varphi_0(t,\theta,\phi)\Bigg[1 + \frac{2\mathrm{i}\tau - e^{2\mathrm{i}\tau} + 1}{2\tilde{r}} \\ - \frac{2\tau^2 + 2\mathrm{i}\tau\left(\tilde{\Lambda} - 2 - e^{2\mathrm{i}\tau}\right) + (\tilde{\Lambda}-3)\left(1-e^{2\mathrm{i}\tau}\right)}{4\tilde{r}^2}\Bigg],\end{aligned} \tag{3.50}$$

where $\tilde{\Lambda} = l(l+1)/(M\mu)^2$, $\tau = \mu t$ and $\tilde{r} = r/M$, putting back in the factors of M. Finally, we obtain a solution for a real scalar field φ by taking the real part of (3.50). Note that there is no dependence on BH spin at order $\tilde{r}^{-2}$. This approximation is valid for $\tilde{r} > \tau$, and therefore it only describes the initial growth of the cloud far from the black hole, and does not describe the late stationary state of the cloud where we expect $\varphi \propto r^{-3/4}$ for $M\mu \sim 1$ [198].

Now recall from section 3.1.2 the flux element into a sphere is given by $\mathrm{d}F = -\sqrt{-g}J^R$. In QIK coordinates metric determinant $\sqrt{-g}$ goes to zero on the horizon. For the stationary solutions J^R diverges at the horizon in such a way that $\sqrt{-g}J^R$ is non-zero, however for the growing case J^R is initially zero and remains finite at finite t. This means that for finite time the flux into the horizon is zero. The energy flux into a sphere of constant R in QIK coordinates in time t is then given by

$$\begin{aligned}
\partial_t M_{\mathrm{cloud}} = \int_{R=R_{\max}} \mathrm{d}F &= \iint \Sigma \left(\frac{\partial r}{\partial R}\right) T^R_t \ \sin\theta \ \mathrm{d}\theta\mathrm{d}\phi, \\
&= \iint \Sigma \ g^{rr}\partial_t\varphi\partial_r\varphi \ \sin\theta \ \mathrm{d}\theta\mathrm{d}\phi, \\
&= \iint \Delta\partial_t\varphi\partial_r\varphi \ \sin\theta \ \mathrm{d}\theta\mathrm{d}\phi, \\
&:= 2\pi \int \mathfrak{J}_r \sin\theta \ \mathrm{d}\theta,
\end{aligned} \tag{3.51}$$

where $\mathfrak{J}^t_r := \frac{1}{2\pi}\int \Delta\partial_t\varphi\partial_r\varphi \mathrm{d}\phi$. Hence the change in the total mass of scalar field inside radius R but outside the horizon is given by

$$\delta M_{\mathrm{cloud}} = 2\pi \int \int_0^t \mathfrak{J}_r \mathrm{d}t' \sin\theta \mathrm{d}\theta. \tag{3.52}$$

Neglecting the oscillatory terms, we find the energy flux for large $\tilde{r}$ to be

described by

$$\begin{aligned}\int_0^t \mathfrak{J}_r \mathrm{d}t' = \Phi_0^2 |Y_{lm}|^2 \frac{1}{4}\Bigg\{ & \tau^2 - \frac{(1+\tilde{\Lambda})\tau^2}{\tilde{r}} + \\ & \frac{\tau^2}{2\tilde{r}^2}\Big[7\tilde{\Lambda} - \chi^2(3\cos 2\theta + 7) - 12\tilde{m}\Big] + \\ & \frac{\tau^2}{2\tilde{r}^3}\Big[(\tfrac{4}{3} - \tilde{\Lambda})\tau^2 + 2\chi^2(5\cos 2\theta - \tilde{\Lambda} + 16) + \\ & 40\tilde{m} - \tilde{\Lambda}^2 - 4\tilde{\Lambda} - 20\Big] + \frac{\tau^2}{4\tilde{r}^4}\Big[\tfrac{1}{9}\tau^4 + \\ & \tfrac{1}{6}\Big(3\chi^2(\cos 2\theta + 3) + 3\tilde{\Lambda}^2 + 35\tilde{\Lambda} - 59 + 12\tilde{m}\Big) + \\ & (6\chi^2 + 5\tilde{\Lambda} + 9)(\chi^2 \cos 2\theta + 4\tilde{m}) + 18\chi^4 + \\ & \chi^2(9\tilde{\Lambda} + 19) - 6\tilde{\Lambda}^2 + \tilde{\Lambda} - 35)\Big] + \mathcal{O}(r^{-5})\Bigg\},\end{aligned} \tag{3.53}$$

where $\tilde{m} = \chi m/(M\mu)$.

We can do the same for the angular momentum flux. For $\mathfrak{J}_r^\phi := -\frac{1}{2\pi}\int \Delta \partial_\phi \varphi \partial_r \varphi \mathrm{d}\phi$ we obtain

$$\begin{aligned}\int_0^t \mathfrak{J}_r^\phi \mathrm{d}t' = |Y_{lm}|^2 \frac{Mm}{4}\Bigg\{ & \tau^2 - \frac{\tilde{\Lambda}\tau^2}{\tilde{r}} + \\ & \frac{\tau^2}{2\tilde{r}^2}\Big[4\tilde{\Lambda} - a^2(3\cos 2\theta + 7) - 12\tilde{m}\Big] + \\ & \frac{\tau^2}{2\tilde{r}^3}\Big[(\tfrac{4}{3} - \tilde{\Lambda})\tau^2 + 2a^2(3\cos 2\theta - \tilde{\Lambda} + 11) + \\ & 24\tilde{m} + 2\tilde{\Lambda} - 20\Big] + \dots\Bigg\}.\end{aligned} \tag{3.54}$$

again neglecting the oscillating terms.

From this result we see that the primary timescale for mass growth is the oscillation period μ^{-1} and that the most important factor affecting the growth rate is the quantity $\tilde{\Lambda}$ which roughly corresponds to the angular momentum per unit mass squared. The BH spin only enters at order $1/r^2$, while the azimuthal number m appears at lowest order as $-6\tilde{m}\frac{\tau^2}{\tilde{r}^2}$. This suggests that anti-aligned BH and cloud spins with $\tilde{m} < 0$ gives faster growth than aligned spins. We can also note that the expression for the angular momentum flux is very similar to the expression for the mass flux, suggesting the angular momentum per unit mass is approximately constant in the regime of validity for this result (i.e., small t and large R).

It is also worth comparing to the expected flux for the stationary solutions in section 3.2.1. At large $r \gg M$ we find the ingoing solution to be

$$\varphi \approx \frac{\sqrt{\rho_{R_c}}}{\mu}\left(\frac{r}{R_c}\right)^{-3/4}|Y_{lm}|\cos\Big(\mu t - m\phi + 2\mu\sqrt{2Mr}\Big), \tag{3.55}$$

where ρ_{R_c} is the scalar field density at radius $R_c \gg M$. Hence

$$\mathfrak{J}_r^{\text{stationary}} = \tfrac{1}{2\pi}\int \Delta\partial_t\varphi\partial_r\varphi \mathrm{d}\phi \approx \rho_{R_c}|Y_{lm}|^2 R_c^{3/2}\sqrt{2M}, \tag{3.56}$$

which is independent of r as required for a stationary solution. If we match the asymptotic scalar field density $\rho_0 = \frac{1}{2}\Phi_0^2\mu^2$ to ρ_{R_c} then the perturbative solution (3.53) is

$$\mathfrak{J}_r^{\text{perturbative}} = \rho_{R_c}|Y_{lm}|^2\left\{t - \frac{(1+\tilde{\Lambda})t}{\tilde{r}} + \dots\right\}. \tag{3.57}$$

We can then intuit that if we start with homogenous conditions the scalar flux will grow from zero until it matches the stationary value.

3.3 Numerical results

In this section we summarise our numerical results for different values of the parameters described in Sec. 3.1. Plots display results in the time parameter τ, a dimensionless ratio of the physical time to the scalar field oscillation period, to enable clearer contact with the perturbative result. The physical time t can simply be recovered as $t = \tau/\mu$ (ie, at some τ, the physical time that has passed t is longer for smaller μ).

Where we show the profiles for the energy density as a function of radius, at each radius the density is averaged over a sphere of constant r to remove the angular dependence, and normalise against $\rho_0 = \frac{1}{2}\Phi_0^2\mu^2$, the asymptotic energy density.

3.3.1 Adding spin to the black hole, zero scalar angular momentum

We can first examine the effect of adding BH spin to the Schwarzschild case examined in [200] – that is, where there is no angular momentum in the scalar. We find that, contrary to what one might expect, adding BH spin introduces only a very mild distortion of the field profile. In Fig. 3.6 we show the radial profile of

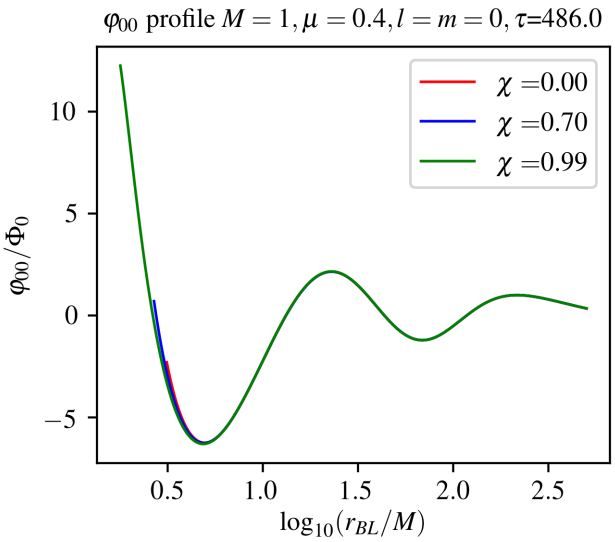

Figure 3.6: **Scalar field radial profile for different black hole spins**. The φ $l = m = 0$ component is plotted as function of radius, from the horizon outwards, for initial spherically symmetric profile $l = m = 0$ in BL coordinates. Different BH spins are shown in different colours (the start points of the lines are different as the horizon size depends on spin). We see that BH spin leads to very mild changes in the scalar cloud close to the horizon, but no significant change in the profile.

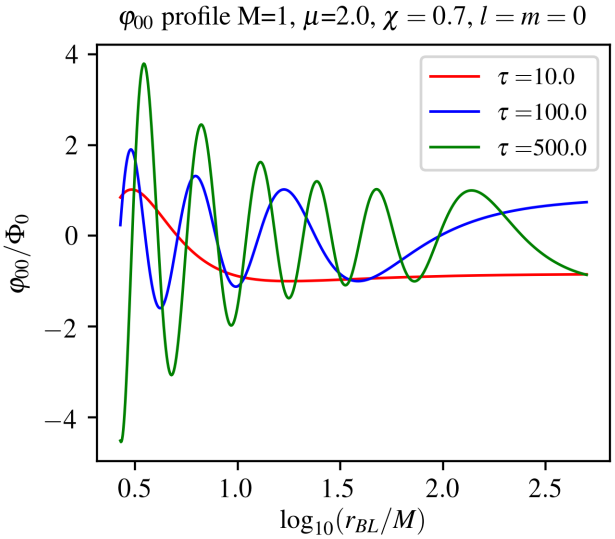

Figure 3.7: **Scalar field radial profile: evolution over time**. We plot the radial φ $l = m = 0$ mode for $M\mu = 2.0, \chi = 0.7$ for different times in BL coordinates. We see oscillations spreading out from the horizon such that the φ profile gradually converges towards the stationary solution.

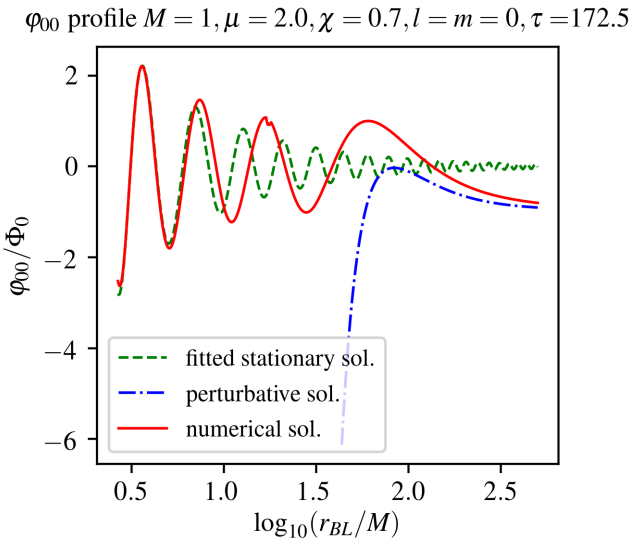

Figure 3.8: **Scalar field radial profile from simulation compared to models.** We plot the φ $l = m = 0$ mode with $M\mu = 2.0, \chi = 0.7$ and $\tau = 172.5$ in BL coordinates, and the stationary and perturbative solutions. We see that the stationary analytic solution is a good fit for the region close to the horizon, while the perturbative solution is a good fit for large r where $r \gtrsim \tau$.

the $l = m = 0$ component of a scalar field with $\mu = 0.4$, in the case when the initial field was in the $l = m = 0$ mode and thus spherically symmetric. We found similar results for the $l \neq 0$ components, with no observable excitement above the level of simulation error in the spinning cases.

In Fig. 3.7 we show the radial profile of a scalar field with $\mu = 2$ near the horizon, for a BH with dimensionless spin $\chi = 0.7$, at several different times in the evolution. As in [200] we see that from the initially flat profile, the scalar develops radial oscillations first near the BH, which then develop outwards radially over time. The field profile oscillates in time and space with frequency/wavelength set by μ.

Finally, in Fig. 3.8 we show the radial profile of a scalar field with $\mu = 2.0$, for a BH with dimensionless spin $\chi = 0.7$, and we compare the numerical with the analytical stationary and perturbative solutions discussed in section 3.2.1 and 3.2.4, respectively. We see that the stationary solution describes well the scalar field near the horizon, whereas the perturbative analytic expression describes the evolution far from the horizon, where the oscillatory behaviour has not been reached yet. The true solution interpolates between the two regimes.

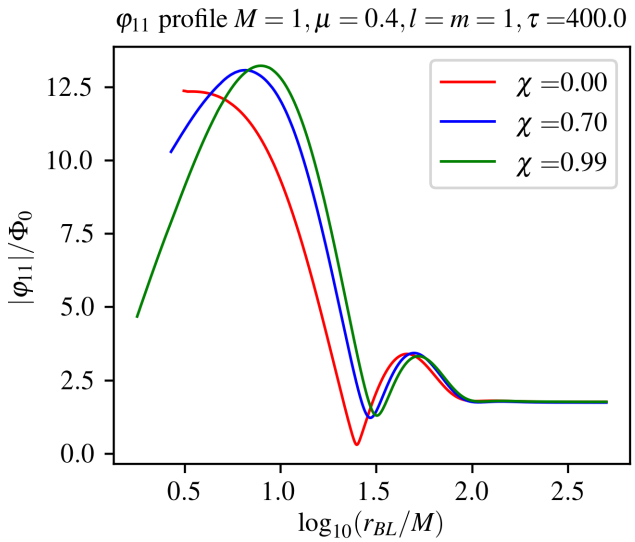

Figure 3.9: **Scalar field radial profile vs black hole spin:** $l = m = 1$. We plot the $l = m = 1$ spherical harmonic component as function of radius for an initial $l = m = 1$ angular dependence in BL coordinates. Different BH spins are shown in different colours. BH spin again leads to changes in the scalar cloud close to the horizon which are more pronounced than in the $l = m = 0$ case.

3.3.2 Adding angular momentum to the scalar, non-zero black hole spin

Next, we explore the impact of adding asymptotic angular momentum to the initial scalar field by choosing non-zero l, m spherical harmonic numbers. A typical 2D profile was shown in QIK coordinates in Fig. 3.1.

3.3.2.1 Effect of BH spin χ

In Fig. 3.9 we show the radial profile of the scalar field for simulations where the initial angular dependence was set by the $l = m = 1$ spherical harmonic. Similarly to the previous section, we only plot the component of the scalar field mode with the same l, m, as we find that the other multipoles have negligible amplitude at all times. As in Fig. 3.6, we have $M\mu = 0.4$ and different values of BH spin are shown in different colours. Changing the BH spin again modifies the profile close to the horizon, and the effect is much larger than for the $l = m = 0$ case of Fig. 3.9. We see that adding spin to the BH decreases the maximum energy density, as shown in Fig 3.10. However, further out there is little difference in the profiles, so as in the $l = m = 0$ case we see minimal impact on the flux at a large radius.

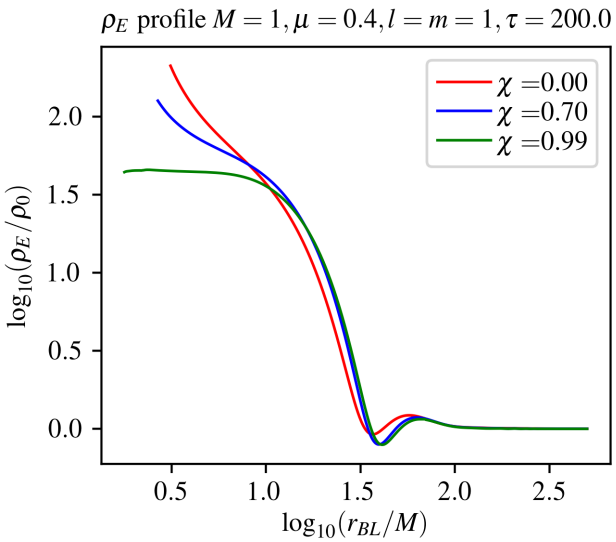

Figure 3.10: **Radial energy density profile** ρ_E averaged over a sphere for $M = 1, \mu = 0.4, l = m = 1$ and different χ. Adding spin to the BH decreases the maximum energy density (note this plot uses a lower value of τ here compared to 3.9 to illustrate the onset of the divergent behaviour).

3.3.2.2 Effect of scalar angular momentum l, m

To quantify the growth rate of the cloud we extract the cumulative conserved scalar field energy flux through a sphere at a radius $R_E \gg M$. This equals the change in total conserved scalar field energy between the BH horizon and the sphere, and at large R roughly corresponds to the change in the ADM mass of the spacetime due to the accretion (see appendix B.2). First, we show the cumulative flux for different l, m modes in Fig. 3.11, along with the analytic perturbative expression that we derived in Sec. 3.2 above, to fourth order in M/r. We show results versus $\tau = \mu t$ as discussed above. The other important timescale is the freefall timescale $t_{\rm ff} \approx R^{3/2}/\sqrt{M}$ [200], the time taken for a small particle initially at rest at $r = R$ to fall into the black hole. Radial oscillations in the profile first form near the BH, and gradually spread outwards on roughly this timescale, so we expect the stationary behaviour to be reached when these waves hit the extraction radius at approximately $t \propto R_E^{3/2}$, which is greater than the time period studied.

We see that the numerical result agrees well with the a perturbative expression for $\tau \ll r/M$ as we would expect. As τ increases the numerical result deviates from the analytic expression, with large l, m producing the largest deviation. The dominant effect is from the first order $\delta M_c \sim \tau^2(1 - (1 + \tilde{\Lambda})/\tilde{r})$ term. Larger l for

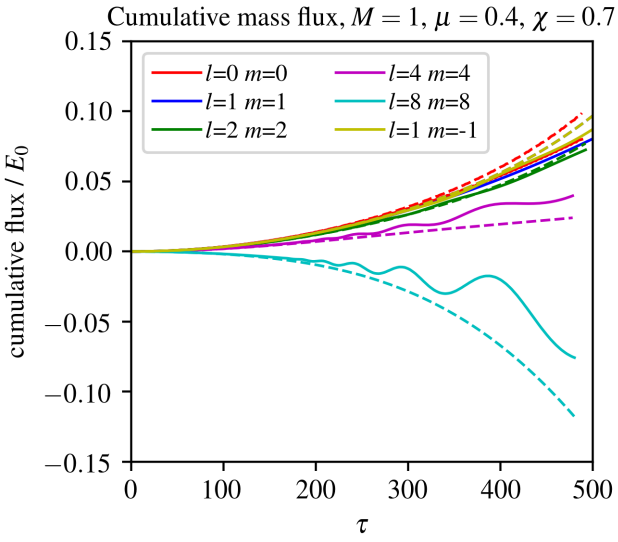

Figure 3.11: **Mass flux into the scalar field cloud vs** l, m. We plot the cumulative flux of mass into a sphere with $R_E = 300M$ around a Kerr BH for $\chi = 0.7, \mu = 0.4$ and different l, m. We normalise the flux by the quantity E_0 – the energy in a sphere of radius R_E with constant energy density $\frac{1}{2}\mu^2\varphi_0^2$. Dashed lines describe the perturbative analytic flux to order r^{-4}, and the solid lines the numerical results. We see that accretion into the sphere is reduced for higher l, m modes, with the negative flux in the highest case signalling that the cloud is forming outside R_E.

fixed μ corresponds to larger $\tilde{\Lambda}$ and thus larger cloud asymptotic angular momentum per unit mass, which increases the potential barrier to accretion, decreasing the growth rate. This is also consistent with what we saw from the effective potential and particle pictures, and physically corresponds to the fact that the cloud is forming further out from the BH – in the case of $l = m = 8$ in the figure, this is even outside the extraction sphere, hence the overall decrease in the mass. Whilst this means that the cloud is not accreted onto the BH, it generally decreases the maximum energy density in the spacetime comapred to the accreting cases, due to it being spread out over a larger volume, as shown in Fig. 3.12.

3.3.2.3 Effect of scalar mass μ

Fig. 3.13 shows the effect of changing the scalar field mass μ for fixed $\chi = 0.7$, and $l = m = 1$. We see that for $M\mu = 0.4, 2.0$ the simulation flux again deviates from the perturbative expression at roughly $\tau \sim 300$, however the small mass case $M\mu = 0.1$ shows deviation at much smaller τ. If we examine the perturbative

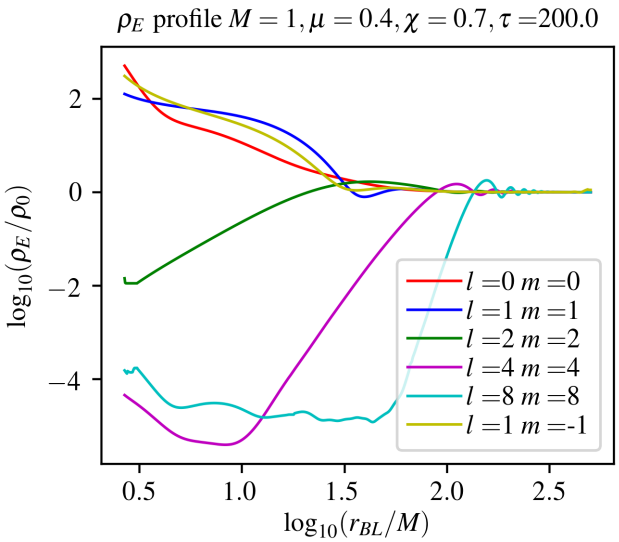

Figure 3.12: **Radial profile of the** $0, 0$ **harmonic mode of the energy density** ρ_E, i.e. the energy density is averaged over a sphere at each radius. The parameters are $M\mu = 0.4, \chi = 0.7$ and the initial scalar field is set to different l, m spherical harmonics at $t = 0$.

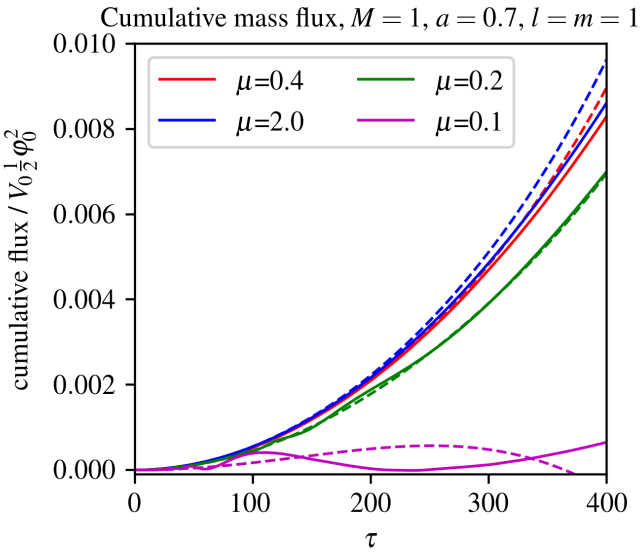

Figure 3.13: **Mass flux into the scalar field cloud vs** μ. We plot the cumulative mass flux into a sphere of $R = 300M$ for $M = 1, \chi = 0.7, \alpha = 0, l = m = 1$ and different μ, normalised by $\frac{1}{2} V_0 \varphi_0^2 = E_0/\mu^2$. This again shows good agreement with the perturbative result. We see that the very low mass cases show an oscillating behaviour in the flux as a result of the stationary wave profiles in this regime.

analytic series (3.53) expressed in terms of τ we see that μ enters chiefly as $\tilde{\Lambda} = l(l+1)/(M\mu)^2 \sim (l/\mu)^2$ (it also appears as μ^{-2} at order $\mathcal{O}(\tilde{r}^{-5})$ and above). Decreasing $M\mu$ with fixed l, m corresponds to increasing $\tilde{\Lambda}$ and thus the angular momentum per unit mass, which again leads to a decreased growth rate. In terms of the perturbative expansion a larger $\tilde{\Lambda}$ boosts the effect of higher-order terms and causes the perturbative solution to break down at smaller τ. Physically, the oscillatory behaviour of the flux is a result of the stationary wave profiles that develop in this mass regime.

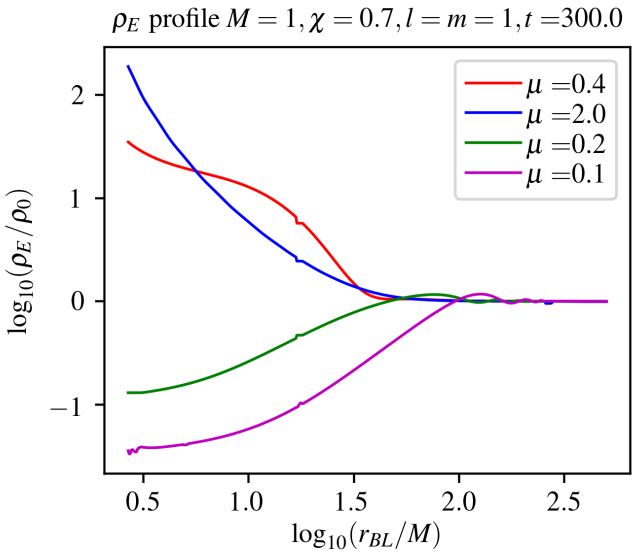

Figure 3.14: **Radial profile of the** $0, 0$ **harmonic mode of the energy density** ρ_E, i.e. the energy density is averaged over a sphere at each radius. The initial scalar field parameters are $M = 1, \chi = 0.7, l = m = 1$ and different μ. We find the maximum density occurs for the highest mass cases where we have accretion onto the BH. The results are shown at time $t = 300M$ which corresponds to $\tau = 120$ for $\mu = 0.4$.

Fig. 3.14 shows that the maximum density occurs for the highest mass cases where we have accretion onto the BH. For lower μ the cloud is concentrated further from the BH and the energy is thus more diluted. As in the superradiant case we see that the scalar mass $M\mu \sim 0.4$ is a critical value where we still support a cloud outside the horizon, rather than having an accretion flow all the way to the horizon.

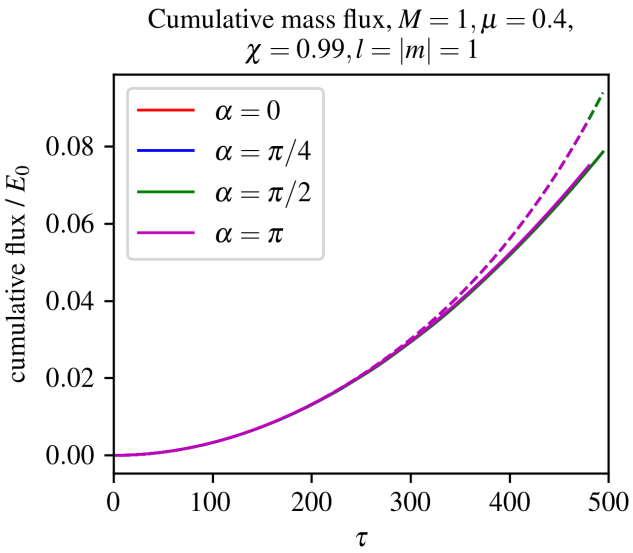

Figure 3.15: **Mass flux into the scalar field cloud vs alignment angle** α. We plot the cumulative accretion flux of mass into a sphere of $R = 300M$ around a Kerr black hole for $\mu = 0.4, \chi = 0.99, l = |m| = 1$ and different alignment angles α (the analytic result is given by equation (3.58)). At this large radius, we see little difference in the accretion rate towards the BH for different α.

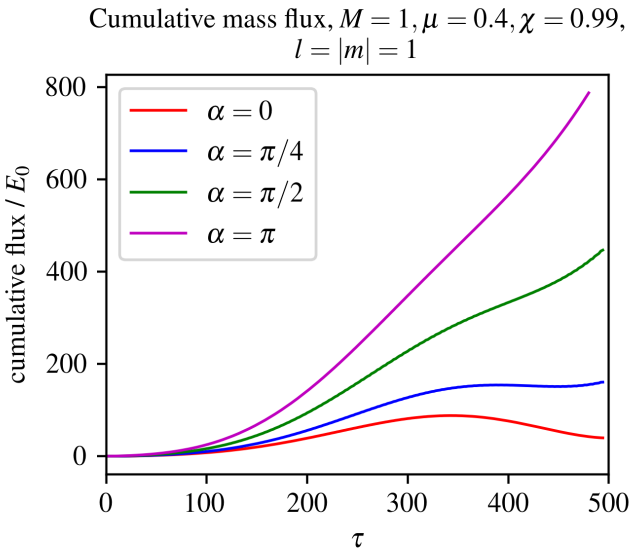

Figure 3.16: **Mass flux into the scalar field cloud vs alignment angle** α**: smaller radius**. We again plot the cumulative mass accretion flux of mass as in Fig. 3.15 but this time into a small sphere of $R = 10M$. At this radius we clearly see the effect of the misalignment in increasing the flux towards the horizon. Note we cannot apply the perturbative analytic result in equation (3.58) at this small radius.

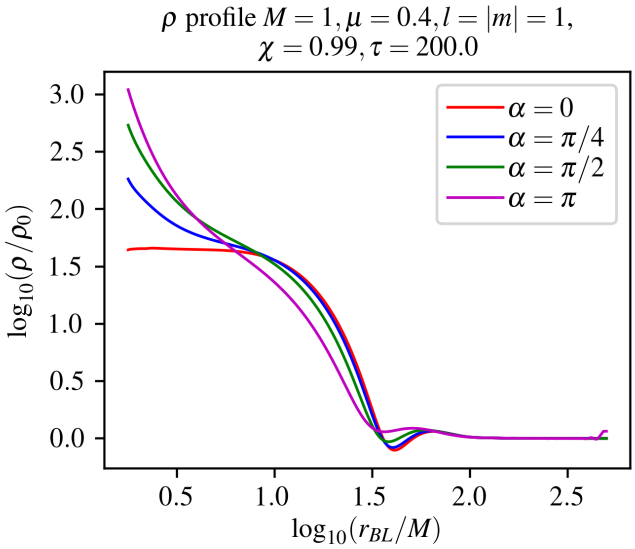

Figure 3.17: **Radial profile of the** $0, 0$ **harmonic mode of the energy density** ρ_E, i.e. energy density is extracted by averaging over a sphere at each radius. The parameters are $M\mu = 0.4, \chi = 0.7, l = |m| = 1$ and different alignment angle α. We see that the density near the BH is enhanced for misaligned spins, indicative of the higher accretion flow.

3.3.2.4 Effect of alignment angle α

Here we vary the alignment angle α[3] between the BH and cloud spin, fixing the rest of the parameters. Fig. 3.18 shows 2D profiles of the energy density in the $z = 0$ plane for different α, with fixed $\chi = 0.99$, $\mu = 0.4$, $M = 1$ and initial $l = m = 1$ angular dependence. We can see that changing α does produce significant differences in the profiles around the BH.

However Fig. 3.15 shows that changing α has only a very small effect on the total flux at a larger radius. In this figure, the solid lines describe the numerical results on the time evolution of the total flux, and the dashed lines describe the analytical estimates. As expected, the analytical solution describes the numerics well only during early times.

[3]Not to be confused with lapse α or the α parameter in the confluent Heun function.

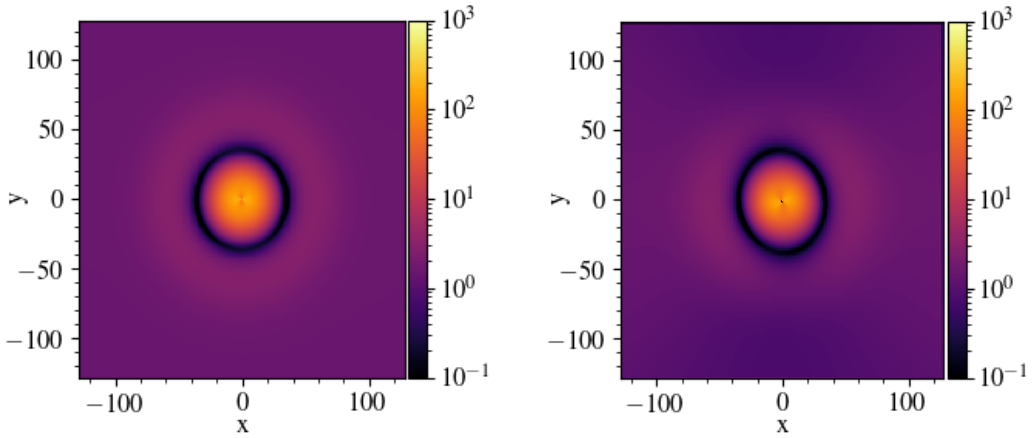

(a) $\alpha = 0$

(b) $\alpha = \pi/4$

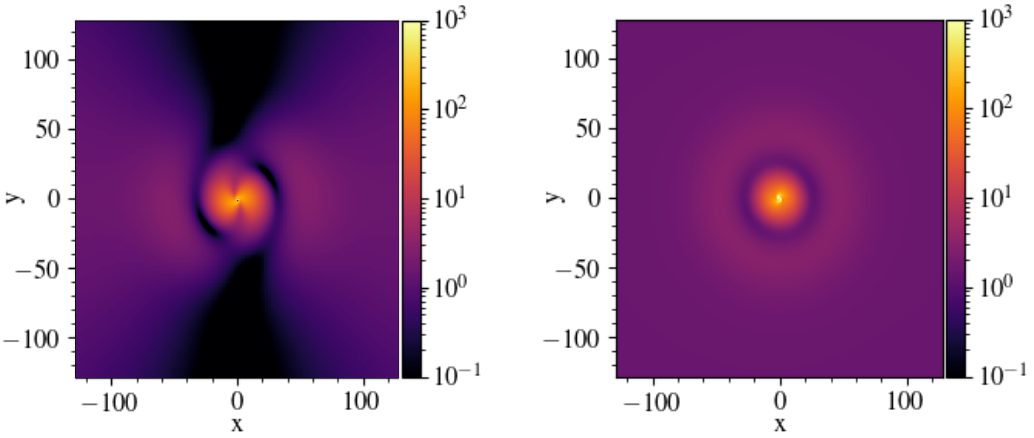

(c) $\alpha = \pi/2$

(d) $\alpha = \pi$

Figure 3.18: **Visualisation of the scalar field energy density for different** α. We show $\log_{10}(\rho_E/\rho_0)$ in the $z = 0$ plane for $\chi = 0.99, \mu = 0.4, \tau = 320$, an initial $l = m = 1$ angular profile and different alignment angle α.

In particular, for $l = |m| = 1$ the perturbative solution gives

$$\begin{aligned}\delta M_{\text{cloud}} - \delta M_{\text{cloud}}\Big|_{\alpha=0} &= 4\pi\Phi_0^2 \frac{a^2\tau^2 \sin^2(\frac{1}{2}\alpha)}{\tilde{r}^2}\Big\{3\tilde{m} \\ &\quad - \frac{3}{5}\cos^2(\tfrac{1}{2}\alpha) \\ &\quad - \frac{10\tilde{m} - 2\cos^2(\frac{1}{2}\alpha)}{\tilde{r}} + \mathcal{O}(\tilde{r}^{-2})\Big\}\end{aligned} \tag{3.58}$$

where $\tilde{m} = \chi/(M\mu)$ and again neglecting the oscillating terms. Here we see the change in δM_{cloud} due to α in (3.58) is proportional to a^2, and we can thus interpret it as the spinning black hole exerting "friction" on the scalar field and removing its angular momentum via frame dragging, making it easier for the scalar field particles to fall inwards. As the perturbative expression is proportional to $1/\tilde{r}^2$ we would expect this effect to increase at smaller r. Fig. 3.16 shows the mass flux into a sphere at a smaller radius of $R = 10M$, and the increase in growth rate on increasing α is now clearly visible.

We also saw in Fig. 3.4 how changing from $m = 1$ (aligned i.e. $\alpha = 0$) to $m = -1$ (anti-aligned i.e. $\alpha = \pi$) causes the potential barrier to vanish close the the BH, whilst further out the potentials were similar. Examination of Figs. 3.18 and 3.17 shows that for the $\alpha = \pi$ case the energy density in the $z = 0$ plane is more concentrated close to the BH vs the $\alpha = 0$ case, which is indicative of accretion onto the BH.

3.3.2.5 Comparison of angular momentum and mass growth rates

We can perform the same measurements for the conserved total angular momentum and the angular momentum flux. Fig. 3.19 shows the angular momentum flux for different l, m and the mass flux from Fig. 3.11 multiplied by m/μ. They agree closely, which confirms what we found from the perturbative solutions in section 3.2 that at $r \gg M$ the angular momentum per unit mass is approximately constant at m/μ. This is what we would expect if we model the scalar field as a collection of non-interacting classical particles which each individually conserve angular momentum.

Fig. 3.20 shows the ratio of the angular momentum density to mass density ρ_J/ρ_E (each density averaged over the sphere) vs radius divided by m/μ. Again we see that at large r this value approaches 1, indicating $\rho_J/\rho_E \approx m/\mu$, however at smaller r close to the horizon we see a distortion, which increases with increasing BH spin. We can interpret this as the BH frame dragging effect.

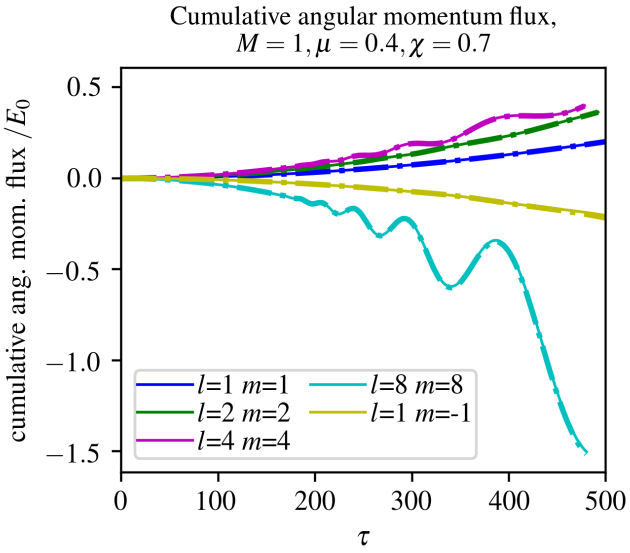

Figure 3.19: **Angular momentum flux into the scalar cloud vs scalar field initial** l, m. We plot the cumulative angular momentum flux into a sphere of $R = 300M$ (solid line) and the mass flux multiplied by m/μ (dot dashed line) for $\chi = 0.7, \mu = 0.4$ and different l, m. We see that the solid and dot dashed lines agree closely, indicating that the angular momentum per unit mass is approximately constant at m/μ.

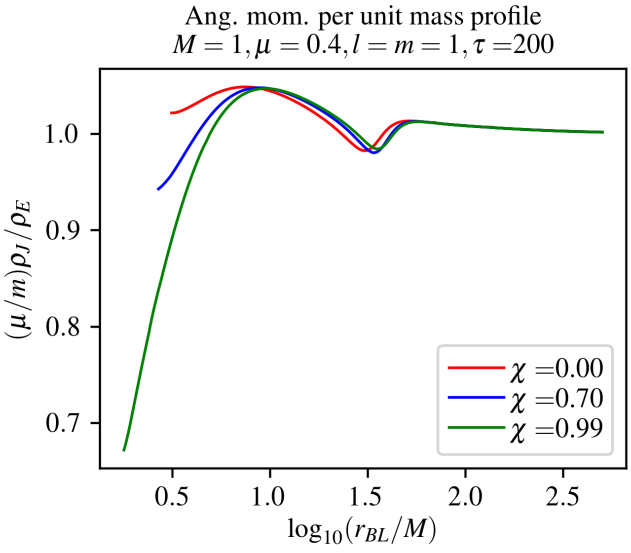

Figure 3.20: **Angular momentum per unit mass**, ρ_J/ρ_E, divided by m/μ vs the BL radius at $\tau = 200$ for different BH spin. We see that the frame dragging effect serves to increase the angular momentum close to the more highly spinning BHs.

3.4 Gravitational waves

For minimally coupled scalar hair without a direct coupling to Standard Model matter, the only way of detecting its presence is through its gravitational effects. Gravitational wave observations may then act as a probe of such scalars, for example, via the impact of a high density cloud on compact binary merger signals, or from the gravitational decay of the cloud itself.

In the latter case, it is known that a rotating non-axisymmetric mass distribution can give rise to a quasi-monochromatic gravitational wave signal at twice the oscillation frequency [143]. This signal can also be considered as arising from the annihilation of two scalar bosons to produce gravitons in the background of the black hole. Gravitational waves can also be produced from transitions between energy states of the scalar field [143]. Searches for such signals in relation to superradiant clouds have been proposed and attempted using advanced LIGO and Virgo [212–218] and explored for future detectors such as LISA [84, 219–222]. Their absence provides observational constraints on the existence of light massive real scalar fields in particular mass ranges.

Real scalar clouds formed from gravitational accretion that we study here may give rise to a similar effect due to the axisymmetric mass distribution of the clouds formed – as illustrated in Fig. 3.2(b). To the best of our knowledge, it has not previously been suggested that the simple accretion of scalar matter around BHs could give rise to such signals. In this section we therefore make a rough calculation of the size of the signal.

We will again consider marginally bound states with $\omega = \mu$. We first consider the scalar-scalar annihlation signal where the scalar field is dominated by a single $l = m$ mode. The size of the scalar cloud is determined by the dark matter environment. Following Hui et al. (2019) [198] we take the size of the cloud R_c to correspond to the radius of influence of the black hole

$$R_c \sim r_i \sim M/v^2 \sim 10^7 M \left(\frac{v_0}{v_\phi}\right)^2, \tag{3.59}$$

where v_ϕ is the typical axial velocity of the scalar field particles at R_c and $v_0 = 100\text{km s}^{-1}$ is taken to be a typical velocity scale for dark matter [198].

We make the simplifying assumption of a single mode and assume the mode number is set by the average axial velocity. The angular momentum per unit mass

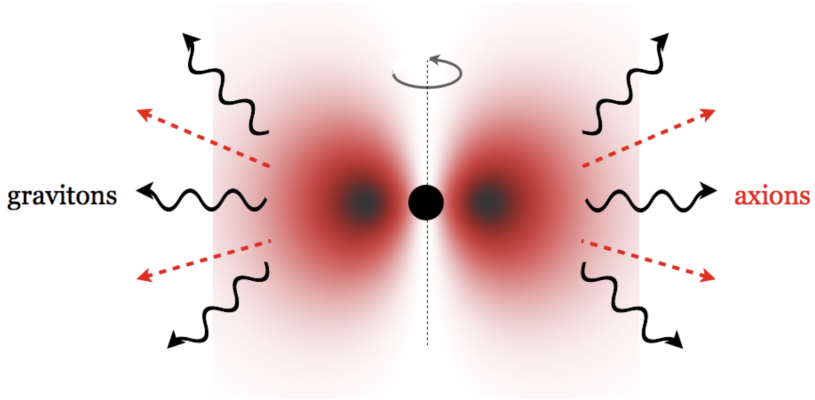

Figure 3.21: **Real scalar field cloud emitting radiation.** This figure from Arvanitaki et al. (2010) [84] shows a spinning $l = m = 1$ mode scalar cloud around a black hole. The cloud will both emit gravitational waves (shown as gravitons) due to level transitions and annihilations, and emit scalar bosons (shown as "axions") via self interactions and decay to spatial infinity. In Arvanitaki et al. the cloud is generated by superradiance, but the picture is similar for the $l = m = 1$ modes formed via accretion.

for a $l = m$ mode is approximately m/μ so

$$\begin{aligned} m/\mu &\sim v_\phi R_c, \\ m &\sim v_\phi \mu R_c. \end{aligned} \tag{3.60}$$

Let us consider a value of μ such that $m \sim 1$. Let $\alpha_g = M\mu$ be the dimensionless ratio of BH radius to scalar wavelength. Then

$$\alpha_g \sim m v_\phi \sim 10^{-3}(v_\phi/v_0), \tag{3.61}$$

so $v_\phi \sim v_0$ gives $\alpha_g \sim 10^{-3}$ and $R_c/M \sim 10^7$. The simplest way to estimate the gravitational wave emission is the quadrupole formula

$$L_{GW} \approx \frac{1}{5}\left\langle \frac{\partial^3 Q_{ij}^{TT}}{\partial t^3}\frac{\partial^3 Q_{ij}^{TT}}{\partial t^3} \right\rangle. \tag{3.62}$$

where Q_{ij}^{TT} is the quadrupole moment in the transverse traceless gauge. However this relies on the approximation that the size of the source is much smaller than the gravitational wave wavelength [223]. The ratio of cloud size to wavelength is

$$R_c/\lambda_c \sim R_c\mu \sim 10^3(v_\phi/v_0)^{-1} \gg 1, \tag{3.63}$$

so for $v_\phi \sim v_0$ the quadrupole approximation is not appropriate. The authors in [138] use the Teukolsky formalism to go beyond the quadrupole formula and derive

that for small α_g and the bound $n = 0$, $l = m = 1$ mode, the GW luminosity is approximately

$$L_{GW} \sim M_s^2 \alpha_g^{12} \mu^2 \tag{3.64}$$

where M_S is the mass of the scalar cloud. We can estimate that

$$M_S \sim \rho_{R_c} R_c^3 \tag{3.65}$$

where ρ_{R_c} is the scalar field energy density at the radius of influence R_c. Then

$$h_{GW} = \frac{2\sqrt{L_{GW}}}{d(2\mu)} \sim \frac{\rho_{R_c} R_c^3 \alpha_g^6}{d} \sim \frac{\rho_{R_c} M^3}{d}, \tag{3.66}$$

where d is the distance from the source to the detector. We can reintroduce the constants to obtain

$$h_{GW} \sim \left(\frac{G}{c^2}\right)^4 \frac{\rho_{R_c} M^3}{d}, \tag{3.67}$$

$$\sim 10^{-53} \left(\frac{\rho_{R_c}}{M_\odot \mathrm{pc}^{-3}}\right) \frac{(M/M_\odot)^3}{(d/\mathrm{pc})}. \tag{3.68}$$

As a concrete example consider the supermassive black hole at the centre of the Milky Way. Various studies have estimated the dark matter density profile of the Milky Way's halo from the galaxy rotation curve (see [224] for a review). Estimating the DM density at the centre of the galaxy is difficult as the mass is dominated by baryonic stars, and estimates are highly model dependent. Light scalar dark matter predicts a solitonic "core" of almost uniform density near the centre [117]. Nesti and Salucci (2013) [116] estimate a core density of $\rho_c \sim 0.04 M_\odot pc^{-3}$, and a core radius of $\sim$ 10kpc which appear to be typical values for cored models. Using $M = 4 \times 10^6 M_\odot$ for the mass of the supermassive black hole [116], $\rho_{R_c} = \rho_c$, and $d = 8$kpc for the distance to the centre of the Milky Way we obtain

$$h_{GW} \sim 10^{-39}. \tag{3.69}$$

The corresponding scalar mass and GW frequency are

$$\hbar\mu \sim \hbar \left(\frac{m v_0 c^2}{GM}\right) \left(\frac{v_\phi}{v_\phi}\right) (v_\phi / v_0) \tag{3.70}$$

$$\sim 10^{-20} \kappa^{-1} (v_\phi / v_0) \text{ eV}, \tag{3.71}$$

$$f \approx c\mu/\pi \sim 10^{-5} (v_\phi / v_0) \text{ Hz}, \tag{3.72}$$

and the size of the cloud is

$$R_c \sim (v_\phi/v_0)^{-2} \text{ pc}. \tag{3.73}$$

If we take $v_\phi \sim v_0$ then the frequency is outside the range of LIGO [44] and on the edge of the sensitivity range of LISA [49, 225]. The signal of $h_{GW} \sim 10^{-39}$ would also be far below the threshold of the latter even at peak sensitivity [225]. Note that this estimate would be further reduced by the fact that the DM is likely to be in a superposition of modes rather than a single coherent one. Moreover, the formula (3.64) was derived for the $n = 0$ mode, which goes to zero at $r = \infty$, while we are examining the marginally bound or $n = \infty$ mode, which is finite at $r = \infty$, so we would expect this to be suppressed due to the smaller value of $\tilde{r} = 2rM\mu^2/(1 + n + l)$ and the more spread out profile. We leave a recalculation of the [138] result for the appropriate n to future work.

Equation (3.60) suggests increasing μ would increase the typical m in which case other modes may dominate. Arvanitaki et al. (2015) [143] found that the GW emission rate from single mode scalar-scalar annihilation in bound gravitational atom states (with $\omega < \mu$) goes as

$$\Gamma_{GW} \propto \left(\frac{v_\phi}{c/2}\right)^{4l}. \tag{3.74}$$

Hence as $c \gg v_\phi \sim 100\text{km s}^{-1}$ we expect the emission to decrease for larger l (assuming the same occupation number of the respective modes). Therefore, for single mode annihilation we may consider the $l = m = 1$ case to be the most optimistic scenario.

We can also consider radiation arising from transitions between the marginally bound state at $\omega = \mu$ and lower energy states with $\omega < \mu$. These transitions will produce radiation at lower frequencies – in particular, if the average axial velocity of the scalar particles at $r = R_c$ is v_ϕ then we expect radiation at frequency $\omega \sim v_\phi/R_c \sim \mu v_\phi^2/m$. Bound states for small α_g have energies

$$\omega_{nl} \approx \mu - \frac{\mu}{2}\left(\frac{\alpha_g}{n + l + 1}\right)^2, \tag{3.75}$$

where n is a non-negative integer and related to the number of nodes in the radial direction. Consider for example a transition from a marginally bound $n = \infty, l = m = 2$ state to the ground state $n = l = m = 0$. This would produce radiation of frequency

$$\omega_{GW} \sim \frac{\mu}{2} m^2 v_\phi^2 = 2\mu v_\phi^2. \tag{3.76}$$

Due to the lower frequency of the GWs the ratio of cloud size to wavelength is now

$$R_c/\lambda \sim 10^{-3}(v_\phi/v_0) \ll 1, \tag{3.77}$$

so we can use the quadrupole formula to estimate the gravitational radiation,

$$L_{GW} \sim \omega_{GW}^6 \left(\int_{r_+}^{R_c} \rho r^4 \mathrm{d}r\right)^2, \tag{3.78}$$

$$h_{GW} \sim \frac{2\sqrt{L_{GW}}}{d\omega_{GW}} \sim \omega_{GW}^2 \int_{r_+}^{R_c} \rho r^4 \mathrm{d}r \tag{3.79}$$

$$\sim \left(\mu v_\phi^2\right)^2 \frac{\rho_{R_c} R_c^5}{d}, \tag{3.80}$$

$$\sim 10^{-40} \left(\frac{\rho_{R_c}}{M_\odot \mathrm{pc}^{-3}}\right) \frac{(M/M_\odot)^3}{(d/\mathrm{pc})(v_\phi/v_0)^4}. \tag{3.81}$$

Using the same values for the Milky Way SMBH as above this gives an amplitude of

$$h_{GW} \sim 10^{-26}(v_\phi/v_0)^{-4}. \tag{3.82}$$

with the corresponding scalar mass and GW frequency

$$\hbar\mu \sim \hbar \left(\frac{m_s c^2}{GM}\right)\left(\frac{v_\phi}{v_0}\right) \sim 10^{-20}(v_\phi/v_0)\mathrm{eV}, \tag{3.83}$$

$$f \sim 10^{-12}(v_\phi/v_0)^3 \mathrm{Hz}. \tag{3.84}$$

This frequency would be well outside the range of LIGO and LISA but may be in reach of Pulsar Timing Arrays [226]. Note again that this estimate is based on the strong assumption that the DM is all in the single mode, whereas in reality only some fraction of the total will be.

The GW emission estimates presented here are only rough guides for a single nearby source. Accurate estimates for the emission of GWs through either annihilation or level transitions would require a more detailed calculation similar to those in [138] and [227]. In addition as the mode profile is heavily determined by the scalar environment, ideally one would like to obtain more precise information about the central distribution of the DM in order to construct a more reliable estimate of the complete signal.

If dark matter is a scalar with a single mass and a relatively consistent velocity profile, both signals should be largely monochromatic. One could therefore expect a superposition of signals with a similar frequency to arise from multiple black holes in the observable volume. This could potentially lead to an enhancement

in the total GW signal. Estimates of such a stochastic quasi-monochromatic GW background have been obtained in the context of searches for superradiant clouds [143, 212, 219].

3.5 Summary and discussion

Most of the literature concerning the growth of scalar hair around black holes has focused on the superradiance mechanism. This work instead explores simple gravitational accretion driven growth of scalar fields around black holes. Specifically we have developed analytic tools to characterise the growth as a function of a range of parameters of the BH and scalar, and performed simulations of the field evolution on a fixed Kerr background to validate our results. If dark matter is composed of light bosons this should represent a common environment for astrophysical BHs.

We observed that when one includes a spin for the BH, as would be expected in a realistic astrophysical case, the accretion rates and density profiles remain almost unchanged, with only minor distortion near the horizon. Hence the behaviour of accretion onto Kerr BHs remains fundamentally very similar to that onto Schwarzschild BHs studied in [200], with the profile "spiking" around the horizon. Over time the field profiles come to resemble the analytic stationary solutions described by [198].

However, adding angular momentum to the scalar can either suppress or enhance (depending on the misalignement) its accretion onto the BH and, in the case of aligned spins, concentrates the clouds further out from the horizon. This is interesting for two reasons:

1. The specific profile which forms around the BH is important because it would directly affect potential probes of the cloud structure – e.g. dephasing in EMRIs by LISA.

2. The flux onto the BH determines how fast the BH may be spun up or how fast its mass will grow. This may have implications for the superradiant growth that would be expected to accompany the accretive growth in several regions of the parameter space studied.

Regarding the second point, it would be interesting to consider whether this competition between spin up and spin down could stall or enhance the superradiant build up in some cases, in a similar way to the studies in [228] and [145]

We have explained the cloud behaviour by reference to a quasi-effective radial potential and the orbits of equivalent particles, and developed a perturbative analytic solution for the changing field profile at large radius. This proved very effective in describing the mass and angular momentum accretion flux in the appropriate time range, and helped us understand the behaviour in the full numerical simulations.

We have not considered couplings to Standard Model matter in this work, or self interactions in the scalar field, but our work could be used to inform estimates of potential signals from such effects [229]. In the absence of such couplings, the key observational signature of the scalar field cloud would be gravitational waves. A scalar field dark matter environment may produce an imprint on the gravitational wave signal from a black hole binary merger, a scenario considered further in chapters 4 and 5. However clouds composed of a real scalar field with angular momentum, as studied here, can also should generate monochromatic gravitational wave signals directly in a similar manner as for superradiant clouds.

We estimated the magnitude of monochromatic signal that might be expected from a cloud around the supermassive black hole at the centre of the Milky Way. This indicates that a single source would not produce a signal loud enough to be detectable by any planned gravitational wave observatories, due to the limitations on the dark matter density and angular momentum. However, we note that unlike for superradiant clouds, where the cloud properties are fully determined by the properties of the black hole and the scalar mass, clouds formed from accretion have a very strong dependence on the local dark matter environment and the asymptotic conditions. Hence different assumptions about local density enhancement may produce a significantly larger signal. There is also the potential to detect a stochastic quasi-monochromatic background from a superposition of multiple sources, however again the uncertainties about the astrophysical scalar dark matter distribution on small scales makes estimating this background highly challenging.

Chapter 4

The quasi-normal modes of growing dirty black holes

The final stage of black hole formation, either from a binary merger or gravitational collapse, is a perturbed single black hole which "rings" like a bell. The gravitational waves emitted during this "ringdown" phase are dominated by a discrete set of damped oscillatory modes dubbed *quasi-normal modes* (QNM), whose frequencies are strictly determined by the underlying spacetime, and are indexed by overtone number n and angular numbers l, m (see section 1.2.5). In the case of standard General Relativity and an isolated Kerr BH, the QNM frequencies are uniquely determined by the BH mass and spin. The detection of gravitational waves from binary mergers by the Advanced LIGO/Virgo network (recently augmented by the addition of KAGRA) [44, 45, 230]) provides a means by which to directly measure these QNM frequencies [231–234] and thus probe the spacetime around black holes directly. The prospects for this field of "Black Hole Spectroscopy" will only improve as future detectors such as LISA and the Einstein Telescope come online [235–239].

Methods for calculating and studying the QNMs of Kerr BHs in standard GR, both numerical and analytic, are well established [55–58, 240–242], but only a few works have extended these techniques to cases of modified gravity or non-trivial matter environments; so called "dirty" or "hairy" black holes [148, 243–248]. A change in the black hole metric $\delta g_{\mu\nu}$, arising from modifications to GR or from the backreaction of surrounding matter, will result in a corresponding shift in QNM frequencies $\delta\omega_{nlm}$. Such effects are likely to be small [148], but have yet to be fully quantified.

One simple and physically motivated situation in which there is non-zero hair

around a black hole is where the BH accretes matter from the surrounding environment. Observational evidence of an electromagnetic counterpart to the gravitational wave event GW190521 suggested that it may be a binary black hole merger occuring within the accretion disc of an active galactic nucleus [249], meaning that "dirty" black hole mergers in matter-rich environments are not an entirely theoretical concept.

While baryonic accretion discs are perhaps the most well motivated example of matter accretion, in this work we first examine the more straightforward case of spherically symmetric accretion. We use as an illustrative example the accretion of a massive complex scalar field onto a Schwarzschild BH, for which stationary solutions are known. Such an environment could describe a black hole located inside a bosonic dark matter halo [1, 198, 200, 250, 251] or the end point of boson star mergers or collapses [142, 210, 252–258], among other scenarios. Whilst such an accreting black hole is ultimately not a truly stationary state (at some point one would expect the asymptotic source of matter feeding the accretion to be "used up"), over any short period of time the configuration is well-described by a steady state profile, with a fixed rate of flow into the horizon.

Even restricting to the case of spherical symmetry, calculating the QNM perturbations for such a growing, "dirty" BH presents several novel challenges. The first is that since the matter is continually accreting onto the BH, the BH mass increases with time, and the metric deviation acquires a time dependence, $\delta g_{\mu\nu} = \delta g_{\mu\nu}(t, r)$. Most previous works have been limited to static metric shifts $\delta g_{\mu\nu}(r)$. Numerical results have been obtained for the quasi-normal modes of scalar and electromagnetic perturbations in a time dependent Vaidya metric [259–262], however as far as we are aware perturbative analytic results for gravitational quasi-normal modes on a time dependent background have not been obtained[1].

The second challenge is that in the standard coordinate choice – Schwarzschild coordinates – the accreting matter piles up around the horizon because the time coordinate there is singular. A different choice is required to avoid the resulting divergence in the backreaction.

To overcome these challenges we combine and extend techniques from two previous works. Firstly, Cardoso et al. [263], who demonstrated a procedure of re-definitions to produce modified QNM equations (i.e. modified Zerilli and Regge-Wheeler equations) for spherically symmetric and static metric shifts on

[1]Scalar, electromagnetic and gravitational fields have different spins (spin 0, 1 and 2 respectively) so in general have different quasi-normal mode frequencies.

a Schwarzschild background, and from this a numerical code for computing the QNM shifts. Secondly, Dolan & Ottewill [264], who described a perturbative analytic technique for computing quasinormal modes of known static, spherically symmetric spacetimes. We combine these approaches to produce a novel way of computing QNMs, and show how the use of an adapted coordinate system can be used to tackle the accreting case.

This chapter is organised as follows. In Sec. 4.1 we set up the background spacetime of an accreting black hole. In Sec. 4.2 we derive the quasinormal mode equations for the perturbed metric. In Sec. 4.3 we compute an analytic perturbative expression for the QNM deviations of a growing, dirty, Schwarzschild BH and in Sec. 4.4 we give explicit results for massive complex scalar field "dirt". We summarise our results in Sec. 4.5, discuss their applications, and propose directions for future work. Appendix C provides further discussion of key steps in our work and, in particular, in sections C.2 and C.3 we verify our method by applying it to simpler, well studied examples for which we have numerical results, to demonstrate that our analytic method gives good agreement.

4.1 The perturbed metric of accreting dark matter

Consider a situation in which one has a sufficient reservoir of material far from the BH such that the system can reach an equilibrium where the loss of matter into the BH is balanced by the infall of matter from infinity, forming a long lived quasi-stationary cloud. This massive cloud will perturb the metric, and thus change the frequency of quasi-normal modes.

Full details of the perturbation theory and some further commentary are provided in appendix C.1. The general idea is that we consider two types of perturbations of the metric. First, a slowly varying perturbation $\delta g_{\mu\nu}$, order $T_{\mu\nu}$, which is the backreaction from the stationary matter, and which gives a matter-perturbed background

$$g_{\mu\nu} = g^{(0)}_{\mu\nu} + \delta g_{\mu\nu}. \tag{4.1}$$

where $g^{(0)}_{\mu\nu}$ is the Schwarzschild metric. Then we imagine adding to this modified background a much smaller perturbation, $h_{\mu\nu}$, which will oscillate at the modified quasi-normal mode frequencies and radiate to infinity as gravitational waves.

The first step in our calculation is to obtain the backreaction $\delta g_{\mu\nu}$. Let φ_m, for now, represent general "matter" fields that source Einstein's equations. The lowest perturbative order non-trivial matter field solution ${\varphi_m}^{(0)}$ satisfies the equations of motion on the Schwarzschild background

$$\nabla^{(0)}_\mu T^{\mu\nu}[{\varphi_m}^{(0)}, g^{(0)}_{ab}] = 0, \tag{4.2}$$

where we assume that $T_{\mu\nu}$ is small and $\nabla^{(0)}_\mu$ is the covariant derivative constructed with $g^{(0)}_{ab}$. The perturbation $\delta g_{\mu\nu}$, order $T_{\mu\nu}$ in smallness, then satisfies

$$\delta G_{\mu\nu}[g^{(0)}_{ab}, \delta g_{ab}] = 8\pi T_{\mu\nu}[{\varphi_m}^{(0)}, g^{(0)}_{ab}], \tag{4.3}$$

where $\delta G_{\mu\nu}$ is the first order perturbation in the Einstein Tensor.

For simplicity we will consider a spherically symmetric cloud on a spherically symmetric Schwarzschild background. Consider the ansatz of a diagonal perturbed line element of the form

$$\mathrm{d}s^2 = -(f+\delta f)\mathrm{d}t^2 + (f+\delta g)^{-1}\mathrm{d}r^2 + r^2\mathrm{d}\Omega, \tag{4.4}$$

where $f(r) = 1 - 2M/r$, $\mathrm{d}\Omega = \mathrm{d}\theta^2 + \sin^2(\theta)\mathrm{d}\phi^2$ and M is the mass of the black hole. The perturbed Einstein field equations are then

$$\delta G^t_t = \frac{1}{r^2}\partial_r(r\delta g) = 8\pi T^t_t, \tag{4.5}$$

$$\delta G^r_r = (\delta g - \delta f)/(fr^2) + \frac{1}{r^2}\partial_r(r\delta f) = 8\pi T^r_r, \tag{4.6}$$

$$\delta G^r_t = -\partial_t \delta g/r = 8\pi T^r_t. \tag{4.7}$$

Now assume that the black hole is surrounded by a cloud of accreting matter described by a density $\rho := -T^t_t$. As the background Schwarzschild metric is static, conservation of energy implies that

$$\partial_t(4\pi r^2 T^t_t) + \partial_r(4\pi r^2 T^r_t) = 0. \tag{4.8}$$

(This can also be derived from Eqs. (4.5) & (4.7)). If the density is static $\rho = \rho(r)$ then $\partial_r(4\pi r^2 T^r_t) = 0$ hence $T^r_t = \delta A/(4\pi r^2)$ for some radially constant value $\delta A(t)$ which relates to the flux into the BH at some point in time t.

If we now choose to reparametrise δg as $\delta g = -2\delta M(t,r)/r$, Eqs. (4.5) & (4.7) give

$$\partial_r \delta M = 4\pi r^2 \rho, \tag{4.9}$$

$$\partial_t \delta M = \delta A, \tag{4.10}$$

from which we can see that δM is the additional effective mass of the black hole due to the cloud, and δA is the rate of increase of mass of the BH due to accretion. Note that whilst in principle the quantities ρ and δA are independent, such that one could choose to have non-zero density of matter near the horizon, but not have any flux into the BH, in most physical situations they will be related and of the same order. This can be seen explicitly in our illustrative example for a complex scalar field below, and explains our finding that the QNM frequency shift due to the accretion is of the same order as that due to the static matter distribution.

As alluded to in the introduction, the use of Schwarzschild coordinates presents problems for realistic examples. Consider our example case of a complex scalar field φ accreting onto a BH from an asymptotically constant energy density. As discussed in [198], the stationary solution close to the horizon is

$$\varphi \to \varphi_0 e^{-\mathrm{i}\omega_s(t+r_*)} \quad r \to 2M \tag{4.11}$$

where here we denote the scalar field frequency as ω_s, and so

$$\rho \to -\frac{2|\varphi_0|^2\omega_s^2}{1-2M/r} \quad r \to 2M \tag{4.12}$$

diverges there. As a result our metric perturbation δg also diverges, which breaks our assumption that $\delta g_{\mu\nu}$ is small. This is a typical result for matter distributions with a non-zero flux into the horizon, due to the coordinate singularity of the Schwarzschild metric at the horizon.

The standard solution is to change to ingoing Eddington-Finkelstein (EF) coordinates, $v \equiv t + r_*$, where the tortoise coordinate r_* is defined as

$$\mathrm{d}r_* = \mathrm{d}r/f(r), \tag{4.13}$$

$$r_* = r + 2M\ln\left(\frac{r}{2M} - 1\right). \tag{4.14}$$

In the ingoing EF coordinates the Schwarzschild line element is

$$\mathrm{d}s^2 = -f\mathrm{d}v^2 + 2\mathrm{d}v\mathrm{d}r + r^2\mathrm{d}\Omega\ . \tag{4.15}$$

We define a perturbation in the metric $\delta\lambda(v,r)$ such that the line element is

$$\mathrm{d}s^2 = -Fe^{2\delta\lambda(v,r)}\mathrm{d}v^2 + 2e^{\delta\lambda(v,r)}\mathrm{d}v\mathrm{d}r + r^2\mathrm{d}\Omega, \tag{4.16}$$

where

$$F = f - 2\delta M(v,r)/r, \tag{4.17}$$

One can then show [265] that similarly to the Schwarzschild case

$$\partial_r \delta M = -4\pi r^2 T_v^v = 4\pi r^2 \rho_{EF}, \tag{4.18}$$

$$\partial_v \delta M = -4\pi r^2 T_v^r = \delta A, \tag{4.19}$$

where $\rho_{\rm EF} = -T_v^v$ is the energy density measured by coordinate observers in ingoing EF coordinates, and δA is the rate of increase in mass of the BH as before. In these coordinates the scalar field $\varphi(v,r) \to \varphi_0 e^{-\mathrm{i}\omega_s v}$ as $r \to 2M$, so

$$\rho_{\rm EF} = \left(f|\partial_r\varphi|^2 + \mu^2|\varphi|^2\right) \to \mu^2|\varphi_0|^2, \quad r \to 2M \tag{4.20}$$

is perfectly well behaved at the horizon. We also have

$$\begin{aligned} \partial_r \delta\lambda =& -4\pi r T_r^v = -4\pi r T_{rr} = |\partial_r\varphi|^2, \\ \to& 0, \quad r \to 2M. \end{aligned} \tag{4.21}$$

so the metric perturbation $\delta\lambda$ is also well behaved. For the scalar field we have explicitly

$$\delta A = 8\pi(2M\omega_s)^2|\varphi_0|^2, \tag{4.22}$$

In general, at any (v,r) we have

$$\delta M(v,r) = \delta A\ v + \int_{2M}^{r} 4\pi\bar{r}^2\rho_{\rm EF}\ \mathrm{d}\bar{r}, \tag{4.23}$$

$$\delta\lambda(v,r) = -\int_{2M}^{r} 4\pi\bar{r}T_{rr}\ \mathrm{d}\bar{r}. \tag{4.24}$$

For the specific case of the scalar field we find

$$\begin{aligned} \delta M(v,r) =& 8\pi(2M\omega_s)^2|\varphi_0|^2 v \\ &+ \int_{2M}^{r} 4\pi\bar{r}^2\left(f|\partial_{\bar{r}}\varphi|^2 + \mu^2|\varphi|^2\right)\mathrm{d}\bar{r}, \end{aligned} \tag{4.25}$$

$$\delta\lambda(r) = -2\int_{2M}^{r} 4\pi\bar{r}|\partial_{\bar{r}}\varphi|^2\mathrm{d}\bar{r}. \tag{4.26}$$

From this point on we will assume that, as in the case of the stationary scalar field solution, δA is a constant and $\delta\lambda$ depends only on r.

In this section we have formulated the necessary expressions for the backreaction onto a Schwarzschild black hole due to stationary accretion in ingoing EF coordinates. We can now use the resulting modified background metric to construct modified equations for the quasi-normal modes.

4.2 Quasi-normal mode equations on the perturbed background

A general spherically symmetric 4D spacetime can be written as the product of a 2D pseudo-Riemannian manifold $(\mathcal{M}, \tilde{g}_{ab})$ and the 2-sphere $(S_2, \hat{g}_{AB})$,

$$\mathrm{d}s^2 = \tilde{g}_{ab}\ \mathrm{d}x^a \mathrm{d}x^b + r^2 \hat{g}_{AB}\ \mathrm{d}x^A \mathrm{d}x^B, \tag{4.27}$$

where indices $a, b \in \{\tilde{t}, r\}$, $A, B \in \{\theta, \phi\}$, with $\tilde{t} = \tilde{t}(t, r)$. It can be shown [266, 267] that odd linear gravitational perturbations $h^{(o)}_{\mu\nu}$ about such a metric can be described by a Regge-Wheeler-like master equation,

$$\left[\tilde{\nabla}_a \tilde{\nabla}^a - V\right] \Psi = \mathfrak{S}, \tag{4.28}$$

where $\Psi(t, r)$ is a master variable encoding the perturbation and

$$V = \frac{(l+2)(l-1)}{r^2} + \frac{2}{r^2}\tilde{g}^{rr} - \frac{1}{r}\tilde{\nabla}_a \tilde{\nabla}^a r, \tag{4.29}$$

$$\tilde{\nabla}_a \tilde{\nabla}^a = \frac{1}{\sqrt{-\tilde{g}}} \partial_a \left(\sqrt{-\tilde{g}} \tilde{g}^{ab} \partial_b\right), \tag{4.30}$$

and $\mathfrak{S}$ is a matter source term derived from $T_{\mu\nu}$. To find the quasi-normal mode frequencies we solve the homogeneous equation with $\mathfrak{S} = 0$.[2] For the perturbed ingoing Eddington-Finkelstein metric $\tilde{t} = v$, $\tilde{g}^{rr} = F$, $\sqrt{-\tilde{g}} = e^{\delta\lambda}$, and so the homogeneous equation is

$$\left[2e^{-\delta\lambda}\partial_v \partial_r + e^{-\delta\lambda}\partial_r(e^{\delta\lambda} F \partial_r) - V\right] \Psi = 0, \tag{4.31}$$

$$\left[2\partial_v \partial_r + \partial_r(F_* \partial_r) - V_*\right] \Psi = 0, \tag{4.32}$$

where $F_* = e^{\delta\lambda} F$ and $v_* = e^{\delta\lambda} V$. Then

$$V_* = e^{\delta\lambda}\frac{(l+2)(l-1)}{r^2} + \frac{2}{r^2}F_* - \frac{1}{r}F_*', \tag{4.33}$$

$$\approx (1+\delta\lambda)V_- - \frac{6\delta M}{r^3} + \frac{2\delta M'}{r^2} - \delta\lambda' \frac{1}{r} f, \tag{4.34}$$

where the prime $'$ denotes ∂_r. If we take the effective BH horizon as being at $F_*(r) = 0$ then to first order the horizon radius is shifted from $2M$ to

$$\begin{aligned} r_H(v) &= 2M[1 + \delta M(v, 2M)/M], \\ &= 2M[1 + \delta A v/M]. \end{aligned} \tag{4.35}$$

[2] Unfortunately an equivalent generalisation of the even mode Zerilli equation to non-vacuum backgrounds has not been found, so we will focus on the odd modes.

We can introduce a function $Z(v,r)$ such that

$$F_*(v,r) = f_H(r)Z(v,r), \tag{4.36}$$

$$f_H := 1 - r_H/r, \tag{4.37}$$

$$Z \approx 1 + \delta Z, \tag{4.38}$$

$$\delta Z(r) \approx -\frac{2(\delta M(v,r) - \delta M(v,2M))}{r-2M} + \delta\lambda(r), \tag{4.39}$$

where our choice of definition means that δZ does not depend on v. Note that $v=0$ is defined as when the effective horizon $r_H = 2M$. Following the method of [263], we define $\Phi = \sqrt{Z}\Psi$. Then

$$\left[\partial_r(f_H\partial_r) + 2(1-\delta Z)\partial_v\partial_r - \delta Z'\partial_v - \tilde{V}\right]\Phi = 0, \tag{4.40}$$

where

$$\tilde{V} = \frac{V_*}{Z} + \frac{1}{2}Z^{-\frac{1}{2}}(Z'Z^{-\frac{1}{2}}f_H)', \tag{4.41}$$

$$\tilde{V} \approx V_* - \delta Z V_* + \tfrac{1}{2}(f\delta Z')', \tag{4.42}$$

$$\approx V_{\rm RW} + \frac{(l-2)(l+1)}{r^2}(\delta\lambda - \delta Z) + \tfrac{1}{2}(f\delta Z')' - \frac{f}{r}\delta Z', \tag{4.43}$$

to linear order in δ, where $V_{\rm RW}$ is the standard Regge-Wheeler potential (1.33).

We now wish to solve for quasi-normal mode solutions. For time independent metrics we look for solutions of the form $\Phi \sim e^{-i\omega t}u(r)$. We can write this in ingoing Eddington-Finkelstein coordinates as $\Phi \sim e^{-i\omega v}u(r)$, incorporating the factor of $e^{+i\omega r_*}$ into $u(r)$. However, as the metric now has a small linear time dependence we need to allow for the frequency and the u function to drift with v,

$$\Phi = \exp(-i\omega(v)v)u(r,v), \tag{4.44}$$

where

$$\omega(v) = \omega_0 + \delta\omega(v), \tag{4.45}$$

and ω_0 is the unperturbed Schwarzschild QNM frequency, giving

$$\Big[\partial_r(f_H\partial_r) - 2i(\partial_v(v\omega) - \delta Z\omega_0)\partial_r - (\tilde{V} - \delta Z' i\omega_0) + (2(1-\delta Z)\partial_r - \delta Z')\partial_v\Big]u(v,r) = 0. \tag{4.46}$$

This expression cannot be directly solved using our method, which requires a differential equation in a single variable. To enable this we introduce a "comoving" coordinate $\tilde{r}$ (from now on we use units where $M = 1$), which we define as

$$\tilde{r} = \frac{r}{(1 + \delta A v \sigma(r))}, \tag{4.47}$$

and where we choose function σ such that $\sigma(r) \approx 1$ for $r \ll r_0$ and $\sigma \to 0$ for $r \to \infty$. The r_0 is some constant radius much larger than the black hole but much smaller than the distance between us and the black hole (one can think of it as the size of the accreting cloud). Then we can have for $r \ll r_0$

$$\tilde{r} \approx \frac{2r}{r_H}, \quad f_H \approx 1 - \frac{2}{\tilde{r}}, \tag{4.48}$$

while for $r \gg r_0$ we recover $\tilde{r} \approx r$. We now derive the QNM equation in terms of this single variable $\tilde{r}$. We have

$$\partial_v = -\frac{\delta A r \sigma}{(1 + \delta A v \sigma)} \partial_{\tilde{r}} + \partial_v, \tag{4.49}$$

$$\partial_r = \frac{1 - \delta A \frac{v r \sigma'}{1 + \delta A v \sigma}}{(1 + \delta A v \sigma)} \partial_{\tilde{r}}. \tag{4.50}$$

where $\sigma' = \partial_r \sigma(r)$. Now let

$$\kappa_r := \left(\frac{\partial \tilde{r}}{\partial r}\right)_v = \frac{1 - \delta A \frac{v r \sigma'}{1 + \delta A v \sigma}}{(1 + \delta A v \sigma)}, \tag{4.51}$$

$$\kappa_v := \left(\frac{\partial \tilde{r}}{\partial v}\right)_r = -\frac{\delta A r \sigma}{(1 + \delta A v \sigma)}. \tag{4.52}$$

If we now define $f_A = f_H + 2\frac{\kappa_v}{\kappa_r}(1 - \delta Z)$, we have that

$$\begin{aligned} \Bigg[&\partial_{\tilde{r}}(f_A \partial_{\tilde{r}}) + \kappa_r^{-1} \left(-2i(\partial_v(v\omega) - \delta Z(r)\omega_0) + \frac{\kappa_r'}{\kappa_r} f_A + \frac{\kappa_v}{\kappa_r} \delta Z' \right) \partial_{\tilde{r}} - \\ &\kappa_r^{-2}(\tilde{V} - \delta Z'(r) \mathrm{i}\omega_0) \ + \left(2(1 - \delta Z(r))\kappa_r^{-1} \partial_{\tilde{r}} - \kappa_r^{-2} \delta Z'(r)\right) \partial_v \Bigg] u(v, \tilde{r}) = 0. \end{aligned} \tag{4.53}$$

In the regime $r \ll r_0$ Eq. (4.53) reduces to

$$\begin{aligned} \Big[&\partial_{\tilde{r}}(f_A \partial_{\tilde{r}}) - r_H \mathrm{i}(\partial_v(v\omega) - \delta Z(r)\omega_0)\partial_{\tilde{r}} - \frac{r_H^2}{4}(\tilde{V} - \delta Z'(r)\mathrm{i}\omega_0) + \\ &\left(r_H(1 - \delta Z(r))\partial_{\tilde{r}} - \frac{r_H^2}{4} \delta Z'(r) \right) \partial_v \Big] u(v, \tilde{r}) = 0, \end{aligned} \tag{4.54}$$

to order δ^2 where $f_A \approx 1 - 2/\tilde{r} - 2\delta A\tilde{r}$. We then have

$$\delta Z(r) \approx \delta Z(\tilde{r}) + (r - \tilde{r})\delta Z(r)' + \ldots, \tag{4.55}$$

$$\approx \delta Z(\tilde{r}) + \delta A v\sigma(r) r \delta Z(r)' + \ldots, \tag{4.56}$$

$$\approx \delta Z(\tilde{r}) + \mathcal{O}(\delta^2) \tag{4.57}$$

provided $\delta A v\sigma(r) r \ll 1$ for $r \ll r_0$. We can thus approximate $\delta Z(r) \approx \delta Z(\tilde{r})$, and do the same for other order δ quantities. This means we can approximate

$$\frac{r_H^2}{4}(\tilde{V} - \mathrm{i}\omega_0 \delta Z') \approx (\tilde{V}(\tilde{r}) - \mathrm{i}\omega_0 \delta Z'(\tilde{r})), \tag{4.58}$$

where primes now denote $\partial_{\tilde{r}}$. If we now look for solutions where $u = u(\tilde{r})$ we have that

$$\Omega = \frac{r_H}{2}\partial_v(v\omega) - \omega_0 \delta Z(2), \tag{4.59}$$

is independent of v. This gives us an equation in a single variable,

$$\Big[\partial_{\tilde{r}}(f_A \partial_{\tilde{r}}) - 2\mathrm{i}(\Omega - [\delta Z - \delta Z(2)]\omega_0)\partial_{\tilde{r}} - (\tilde{V}(\tilde{r}) - \mathrm{i}\omega_0 \delta Z'(\tilde{r}))\Big] u(\tilde{r}) = 0. \tag{4.60}$$

We can further simplify this by letting

$$u(\tilde{r}) = \exp\left(-\mathrm{i}\omega_0 \int^{\tilde{r}} [\delta Z(\tilde{r}) - \delta Z(2)]/f_H(\tilde{r})\, \mathrm{d}\tilde{r}\right) \tilde{u}(\tilde{r}). \tag{4.61}$$

Again neglecting $\mathcal{O}(\delta^2)$ terms this gives us

$$[\partial_{\tilde{r}}(f_A \partial_{\tilde{r}}) - 2\mathrm{i}\Omega\partial_{\tilde{r}} - (V_-(\tilde{r}) + \Delta V(\tilde{r}))]\, \tilde{u}(\tilde{r}) = 0, \tag{4.62}$$

where $\Delta V(\tilde{r})$ contains all the potential terms of order δ.

The aim of this section was to derive a differential equation in a single co-moving variable, for odd quasi-normal modes about the perturbed Schwarzschild metric associated with the growing dirty black hole we described in the previous section. The equation derived, Eq. (4.62), can now be used to compute the quasi-normal mode frequencies.

4.3 Perturbative method for computing the quasi-normal modes

While there are a host of numerical methods for calculating quasi-normal mode spectra, here we adapt the method of [264] to compute analytic, perturbative

expressions for the corrections to the spectra described by Eq. (4.62) for the fundamental $n = 0$ modes. The advantage of using this method over other numerical techniques is that we can obtain perturbative analytic expressions that make it easy to substitute in for many different matter distributions, and to analyse the eikonal high l limit.

Due to the spherical symmetry the frequencies are independent of the spherical harmonic number, m. For $\tilde{u}(\tilde{r})$, the (modified) radial part of our solution, we take an anzatz of the form

$$\tilde{u} = \exp\left(i\Omega \int^{\tilde{r}_*} Y(\tilde{r}) \mathrm{d}\tilde{r}_*\right) q(\tilde{r}), \tag{4.63}$$

The principle idea is to expand in powers of $L = l + \frac{1}{2}$ so that

$$\Omega = L\Omega_{-1} + \Omega + L^{-1}\Omega_1 + \ldots, \tag{4.64}$$

$$q(\tilde{r}) = \exp\big(S_0(\tilde{r}) + L^{-1}S_1(\tilde{r}) + \ldots\big). \tag{4.65}$$

Substituting (4.63) into (4.62), we find the modified Regge-Wheeler equation takes the form

$$\begin{aligned} &f_A q'' + [f_A' + 2i\Omega(Y-1)]q' + \\ &\left[\mathrm{i}\Omega Y' + \Omega^2 \frac{2Y - Y^2}{f_A} - \frac{L^2}{\tilde{r}^2} - V_0 - \Delta V\right] q = 0, \end{aligned} \tag{4.66}$$

where $V_0 = \frac{1}{\tilde{r}^2}(-6/\tilde{r} - 1/4)$ and

$$\begin{aligned} \Delta V =& \frac{L^2 - 9/4}{\tilde{r}^2}(\delta\lambda - \delta Z) + \tfrac{1}{2}(f_H \delta Z')' - \frac{f_H}{\tilde{r}}\delta Z' \\ &+ \frac{2\omega_0^2}{f_H}[\delta Z(r) - \delta Z(2)]. \end{aligned} \tag{4.67}$$

We can now match terms in orders of L. At order L^2 we have that

$$(2Y - Y^2)\Omega_{-1}^2 = \frac{f_A}{\tilde{r}^2}, \tag{4.68}$$

$$1 - (Y-1)^2 = \frac{f_A}{\Omega_{-1}^2 \tilde{r}^2}, \tag{4.69}$$

$$Y = 1 \pm \left(1 - \frac{f_A}{\Omega_{-1}^2 \tilde{r}^2}\right)^{1/2}. \tag{4.70}$$

Let us now focus on the quasi-normal mode boundary conditions. We want ingoing modes at the horizon and outgoing at $r \to \infty$, so

$$\tilde{u} \sim \Phi_0, \qquad r_* \to -\infty, \tag{4.71}$$

$$\tilde{u} \sim \Phi_{out} e^{2\mathrm{i}\Omega r_*}, \qquad r_* \to \infty. \tag{4.72}$$

If we take $\delta A = 0$ and $\Omega_{-1} = 1/\sqrt{27}$ as in [264] then $\tilde{r} = r$ and

$$\left(1 - \frac{f_A}{\Omega_{-1}^2 \tilde{r}^2}\right)^{1/2} = \left(1 - \frac{f27}{r^2}\right)^{1/2} = \pm\left(1 - \frac{3}{r}\right)\left(1 + \frac{6}{r}\right)^{1/2}. \tag{4.73}$$

We then can obtain the correct boundary conditions by taking

$$Y = 1 + \left(1 - \frac{3}{r}\right)\left(1 + \frac{6}{r}\right)^{1/2}. \tag{4.74}$$

This is a modified form of the ansatz used in [264] corrected for the fact that we have included a factor of r_* into the v.

We can try something similar with $\delta A \neq 0$. For small r (i.e. $r \ll r_0$) we find

$$f_A \approx f_H - 2\delta A \tilde{r} = 1 - \frac{2}{\tilde{r}} - 2\delta A \tilde{r}. \tag{4.75}$$

If $\Omega_{-1} = 1/\sqrt{27} + \delta\Omega_{-1}$, one can show that

$$Y = 1 + \left(1 - \frac{3(1+3\delta A)}{\tilde{r}}\right)\left(1 + \frac{6(1+12\delta A)}{\tilde{r}}\right)^{1/2}, \tag{4.76}$$

$$\delta\Omega_{-1} = -\sqrt{3}\delta A, \tag{4.77}$$

satisfies the order L^2 equation to order δ. The repeated root for $Y = 1$ corresponds to the null unstable circular orbit, which shifts to $r = 3\frac{r_H}{2M}(1+3\delta A)$. We also note that f_A and $Y(\tilde{r})$ have zeros at $\tilde{r} = 2 + 8\delta A + \mathcal{O}(\delta A^2)$ instead of at $\tilde{r} = 2$; however in the expression

$$\int^{\tilde{r}_*} Y(\tilde{r}) \mathrm{d}\tilde{r}_* = \int^{\tilde{r}} Y(\tilde{r})/f_A(\tilde{r})\ \mathrm{d}\tilde{r} \tag{4.78}$$

these zeros cancel so that the integral is well behaved. Hence for well behaved $q(\tilde{r})$ we obtain the correct boundary condition at $r \to r_H$.

Now let us examine the limit of large r (i.e. $r \gg r_0$). We want to confirm we obtain outgoing waves, i.e.

$$\tilde{u}(\tilde{r}) \approx \exp(2\mathrm{i}\Omega r_*) \tag{4.79}$$

as $r \to \infty$. We have $Y \approx 2 - f_A/(2\Omega_{-1}^2\tilde{r}^2) + \ldots$ so

$$\tilde{u} \to \exp\left(\mathrm{i}\Omega[2\tilde{r}_* + \frac{1}{\Omega_{-1}\tilde{r}} + \ldots]\right) q(\tilde{r}) \tag{4.80}$$

and

$$\tilde{r}_* \approx \int \left(1 - \frac{2(1+\delta A v)}{r} + \delta A(v(\sigma r)' - 2\sigma r) + \mathcal{O}(\delta A^2)\right)^{-1} \mathrm{d}r, \tag{4.81}$$

$$\approx r + 2\ln(r-2) + \delta A\left(v(2\ln(r) - (\sigma r)') - 2\sigma r\right) + \mathcal{O}(\delta A^2), \tag{4.82}$$

$$\approx r_* + \mathcal{O}(\delta). \tag{4.83}$$

Thus our anzatz does give us outgoing waves at large r, provided $q(\tilde{r})$ is suitably well behaved and σ goes to zero with large r suitably fast.

Having established our modified anzatz still satisfies the quasi-normal mode boundary conditions we can go back to solving for the Ω_n, S_n terms, using the $r \ll r_0$ limit. At order L^1 we have

$$2iS_0'(Y-1) + \mathrm{i}Y' + \frac{2\Omega_0}{\Omega_{-1}^2\tilde{r}^2} = 0. \tag{4.84}$$

If we require that S_m be continuous and differentiable at the null unstable orbit, at $\tilde{r}_c = 3(1+3\delta A)$, then setting $\tilde{r} = \tilde{r}_c$ we find

$$\Omega_0 = -\mathrm{i}\frac{\sqrt{3}}{2}\Omega_{-1}Y'(\tilde{r}_c) = -\frac{\mathrm{i}}{2\sqrt{27}} + \frac{2i}{\sqrt{3}}\delta A + \mathcal{O}(\delta^2). \tag{4.85}$$

We can also extract S_0' as

$$S_0'(\tilde{r}) = \mathrm{i}\frac{iY' + 2\Omega_0/(\Omega_{-1}\tilde{r})^2}{2(Y-1)}. \tag{4.86}$$

At order L^0 we have

$$\begin{aligned} f_A({S_0'}^2 + S_0'') + (f_A' + \mathrm{i}\omega_0\delta Z)S_0' + \frac{2\Omega_1\Omega_{-1} - \Omega_0^2}{\tilde{r}^2\Omega_{-1}^2} \\ +2iS_1'\Omega_{-1}(Y-1) - V_0 - \Delta V = 0. \end{aligned} \tag{4.87}$$

We can again set $\tilde{r} = \tilde{r}_c$ to find Ω_1, and then rearrange to obtain the function S_1'.

The above procedure can be repeated to obtain higher-order terms. For order $L^{-n}, n \geq 1$ the general expression is

$$\begin{aligned} f_A(\sum_{m=0}^{n} S_m'S_{n-m}' + S_n'') \\ + (f_A' + \mathrm{i}\omega_0\delta Z)S_n' + \frac{1}{\tilde{r}^2\Omega_{-1}^2}\sum_{m=-1}^{n+1}\Omega_m\Omega_{n-m} \\ + \mathrm{i}\Omega_n Y' + 2\mathrm{i}(Y-1)\sum_{m=-1}^{n}\Omega_m S_{n-m}' = 0. \end{aligned} \tag{4.88}$$

The next few Ω_n terms are explicitly given by:

$$\sqrt{27}\Omega_1 = -\tfrac{281}{216} + \tfrac{1135}{72}\delta A + \tfrac{9}{2}\Delta V(3), \tag{4.89}$$

$$\sqrt{27}\Omega_2 = \mathrm{i}\tfrac{1591}{7776} - \mathrm{i}\tfrac{1591}{432}\delta A + \mathrm{i}\left(\tfrac{27}{8}\Delta V''(3) + 9\Delta V'(3) + \tfrac{15}{4}\Delta V(3)\right), \tag{4.90}$$

$$\begin{aligned}\sqrt{27}\Omega_3 = &-\tfrac{710185}{1259712} + \tfrac{2922805}{419904}\delta A - \tfrac{81}{64}\Delta V^{(4)}(3) - \tfrac{21}{2}\Delta V^{(3)}(3) - \tfrac{185}{8}\Delta V''(3)\\ &- \tfrac{29}{3}\Delta V'(3) + \tfrac{1061}{144}\Delta V(3),\end{aligned} \tag{4.91}$$

$$\begin{aligned}\sqrt{27}\Omega_4 = &\mathrm{i}\tfrac{92347783}{362797056} - \mathrm{i}\tfrac{69151003}{15116544}\delta A + \mathrm{i}\Big[-\tfrac{81}{256}\Delta V^{(6)}(3) - \tfrac{171}{32}\Delta V^{(5)}(3) - \tfrac{1845}{64}\Delta V^{(4)}(3)\\ &- \tfrac{341}{6}\Delta V^{(3)}(3) - \tfrac{8087}{384}\Delta V''(3) + \tfrac{449}{16}\Delta V'(3) + \tfrac{16331}{1728}\Delta V(3)\Big],\end{aligned} \tag{4.92}$$

$$\begin{aligned}\sqrt{27}\Omega_5 = &-\tfrac{7827932509}{39182082048} - \tfrac{1376065091}{1451188224}\delta A + \tfrac{243}{4096}\Delta V^{(8)}(3) + \tfrac{27}{16}\Delta V^{(7)}(3) + \tfrac{8675}{512}\Delta V^{(6)}(3)\\ &+ \tfrac{71519}{960}\Delta V^{(5)}(3) + \tfrac{1259827}{9216}\Delta V^{(4)}(3) + \tfrac{255217}{5184}\Delta V^{(3)}(3) - \tfrac{8562439}{93312}\Delta V''(3)\\ &- \tfrac{2427761}{69984}\Delta V'(3) + \tfrac{7696651}{419904}\Delta V(3),\end{aligned} \tag{4.93}$$

$\ldots$

Note that the terms zeroth order in δ are the same as in [264], showing we obtain the correct unperturbed frequency.

If we now examine Eq. (4.59), we have that

$$\partial_v(v\omega) = (\Omega + \omega_0\delta Z(2))/(1 + \delta A v), \tag{4.94}$$

which, when integrated and Taylor expanded gives us

$$\delta\omega = \delta\Omega + \omega_0\delta Z(2) - \omega_0\tfrac{1}{2}\delta A v + \mathcal{O}(\delta^2). \tag{4.95}$$

We can rewrite this as

$$\delta\omega = \delta\varpi + \delta A(\varpi_A - \omega_0\tfrac{1}{2}v) + \mathcal{O}(\delta^2), \tag{4.96}$$

where $\delta\varpi$ is the correction with zero accretion (arising from the static matter distribution around the horizon) and $\delta A(\varpi_A - \omega_0\frac{1}{2}v)$ is the accretion term.

So far we have obtained a solution in our adapted EF coordinates of the form

$$\begin{aligned}\Psi &= \Phi/\sqrt{Z},\\ &= \exp\left(-\mathrm{i}\left[\omega_0 + \delta\varpi + \delta A(\varpi_A - \frac{\omega_0}{2}v/M)\right]v\right) Z^{-\frac{1}{2}}(r)u\left(\tilde{r}\right),\end{aligned} \tag{4.97}$$

where we have restored the factors of M. However, if we were to measure this scalar we would of course do so as asymptotic observers in t and r coordinates not v and $\tilde{r}$ coordinates. Suppose we measure the scalar fluctuation at some fixed

distance $r = R \gg 2M$ from the black hole. Then $v = r_* + t$ only changes with t. Hence we can define a local time $t' = t - R_*$, where $R_* = R + 2M \ln(R/(2M) - 1)$, such that at our position we just have $v = t'$. The origin at $t' = v = 0$ is defined by the point at which the BH mass is defined to be M, that is, when the effective black hole horizon $r_H = 2M$. Recall that we have also defined our $\tilde{r}$ coordinate such that $\tilde{r} \to r$ for $r \gg r_0$. As we expect that $R \gg r_0$ we observe

$$\Psi(t', R) \propto \exp\left(- i \left[\omega_0 + \delta\varpi + \delta A(\varpi_A - \frac{\omega_0}{2} t'/M)\right] t' \right) Z^{-\frac{1}{2}}(R) u(R). \tag{4.98}$$

This means that the effective quasi-normal mode frequency is given by

$$\omega = \omega_0 + \delta\varpi + \delta A(\varpi_A - \frac{\omega_0}{2} t'/M) + \mathcal{O}(\delta^2). \tag{4.99}$$

Note that if we are only interested in the time variation of the scalar at a fixed R we can be agnostic about the precise form of the function $\sigma(r)$, only assuming that it obeys the correct asymptotic boundary conditions.

Previous works have calculated $\delta\varpi$, assuming the accretion terms are zero. Yet as we shall see in the example of the massive complex scalar field in the next section, the contribution from the accretion terms $\delta A(\varpi_A - \frac{\omega_0}{2} t'/M)$ can in fact be larger than $\delta\varpi$. In the general case we would expect them to be at least of the same order, therefore the latter should not be neglected.

In this section we have arrived at our key result: a general formula for odd parity quasi-normal mode style solution for growing dirty black holes, which can be used to study frequencies which are perturbed by the accretion of matter and how they drift with time. It is useful to check our approach, and in particular the expansion order required for accuracy, in simpler regimes where quasi-normal mode frequencies have been calculated using other methods; we do so in App. C.3. We find that, in the static cases considered, the method is highly accurate to the 5th order expansion used, and that going to higher orders does not result in significant corrections. In the following section we apply the result to our illustrative example of scalar field accretion.

4.4 Complex massive scalar field accretion

Having set up the framework and formalism, we can now apply it to our test case: a complex massive scalar field. Once again we set $M = 1$ (see note on units).

From [198] we can approximate the φ solution for small $M\mu < 1$ and $\omega_s = \mu$ as[3]

$$\varphi \sim \varphi_0 e^{-i\mu(v-r)}, \quad 2 < r \lesssim \mu^{-2}/2, \tag{4.100}$$

$$\varphi \propto r^{-3/4} e^{-\mathrm{i}\mu(v-r_*)} \cos\Big(2\mu\sqrt{2r} - 3\pi/4\Big), \ \mu^{-2}/2 \lesssim r. \tag{4.101}$$

In the regime where $r < \mu^{-2}/2$, from Eqs. (4.23) and (4.24) we have

$$\delta A \approx 32\pi\mu^2|\varphi_0|^2 = 32\pi\rho_h, \tag{4.102}$$

$$\delta M \approx 32\pi\rho_h \left[v + \frac{1}{24}\left(2r^3 - 3r^2 - 4\right)\right], \tag{4.103}$$

$$\delta\lambda \approx 4\pi\rho_h \left[4 - r^2\right], \tag{4.104}$$

$$\delta Z \approx \frac{4}{3}\pi\rho_h \left[-7r^2 - 2r + 8\right], \tag{4.105}$$

which in turn gives

$$\begin{aligned}\Delta V(\tilde{r}) = 8\pi\rho_h \Big[&\frac{L^2}{3}\left(2 + \tilde{r}^{-1} + 2\tilde{r}^{-2}\right) - \frac{1}{6}(7\tilde{r}^2 + 16\tilde{r})\omega_0^2 \\ &- \frac{61}{12}\tilde{r}^{-1} - \frac{5}{2}\tilde{r}^{-2} - \frac{1}{3}\Big],\end{aligned} \tag{4.106}$$

where we have expressed all quantities in terms of ρ_h, the scalar field density on the horizon in ingoing EF coordinates. Substituting in these values of ΔV and δZ gives the perturbations to the quasi-normal mode frequency as

$$\begin{aligned}\delta\varpi = 32\pi\rho_h M \Big[&0.0360844L + 0.0160375\mathrm{i} \\ &- 0.0522147L^{-1} - 0.0222155\mathrm{i}L^{-2} - 0.105189L^{-3} \\ &+ 0.0307956\mathrm{i}L^{-4} - 0.245579L^{-5} + \mathcal{O}(L^{-6})\Big],\end{aligned} \tag{4.107}$$

and

$$\begin{aligned}\delta A\varpi_A = 32\pi\rho_h M \Big[&-1.73205L + 1.1547\mathrm{i} \\ &+ 3.03376L^{-1} - 0.708769\mathrm{i}L^{-2} + 1.33958L^{-3} \\ &- 0.880368\mathrm{i}L^{-4} - 0.182488L^{-5} + \mathcal{O}(L^{-6})\Big],\end{aligned} \tag{4.108}$$

where we have now restored the factors of M. We note that the accretion term, $\delta A\varpi_A$, is in fact substantially larger than the non-accretion term, $\delta\varpi$, showing

[3] Recall that in this chapter ω_s denotes the frequency of the scalar field while ω is the frequency of the gravitational QNM.

the importance of properly accounting for the accretion and the time dependence of the backreaction. Putting both contributions together we obtain

$$\begin{aligned}\delta\varpi + \delta A\varpi_A = 32\pi\rho_h M\Big[&- 1.69597L + 1.13866\mathrm{i} \\ &+ 2.98155L^{-1} - 0.730984\mathrm{i}L^{-2} + 1.23439L^{-3} \\ &- 0.849572\mathrm{i}L^{-4} - 0.428067L^{-5} + \mathcal{O}(L^{-6})\Big].\end{aligned} \tag{4.109}$$

For comparison the equivalent expression for ω_0 is

$$\begin{aligned}\omega_0 = M^{-1}\Big[&0.19245L - 0.096225\mathrm{i} - 0.250363L^{-1} \\ &+ 0.039376\mathrm{i}L^{-2} - 0.108497L^{-3} \\ &+ 0.048987\mathrm{i}L^{-4} - 0.0384483L^{-5} + \mathcal{O}(L^{-6})\Big].\end{aligned} \tag{4.110}$$

While we do not have comparable numerical results for the case of time-dependent accreting black holes, we have validated our method by comparison to numerical results for static spacetimes as discussed in appendix C.3.

Suppose we can measure the QNM ringdown signal for N oscillations before it passes below our sensitivity threshold. Then the shift in frequency with time over the course of the ringdown will be order

$$-\delta A\frac{\omega_0}{2}\frac{\Delta t'}{M} \sim -\pi N\frac{\delta A}{M} = \pi N 32\pi\rho_h M. \tag{4.111}$$

Hence if N is order 1, for a detector with a decent signal to noise ratio, then this shift with time is of a comparable size to the constant frequency change $\delta\varpi+\delta A\varpi_A$.

We can now assess how large this shift in QNM frequency actually is. For the complex scalar field the size of the deviations can be parameterised by the non-zero dimensionless accretion rate δA which is related to the density on the horizon as described above

$$\frac{\delta\omega}{\omega_0} \sim \frac{\delta\varpi + \delta A\varpi_A - \frac{1}{2}\delta A\omega_0 t'/M}{\omega_0} \sim \delta A = 32\pi\rho_h M^2. \tag{4.112}$$

Plugging in the fundamental constants we find that a fractional BH mass growth rate of $10^{-14}\mathrm{Gyr}^{-1}$ corresponds to a δA of $(M/M_\odot)^2 10^{-6}$. Assuming that the complex scalar is dark matter, we can also express δA in terms of a typical asymptotic dark matter density, as follows. For the massive scalar field with $\omega = \mu$ the density decays as $\sim r^{-3/2}$ at large r so we find

$$\rho_h \sim \rho_{R_c}\pi(\mu M)^3\left(\frac{2R_c}{M}\right)^{3/2}, \tag{4.113}$$

where ρ_{R_c} is the density at some large radius R_c which we take to be the effective radius of the cloud. If we set R_c by equating the virial velocity to a typical dispersion velocity of dark matter

$$R_c/M \sim (v_{\rm disp})^{-2} \sim \left(\frac{100\text{km s}^{-1}}{c}\right)^{-2} \sim 10^6, \tag{4.114}$$

then

$$\delta A \sim 10^{-31} \left(\frac{M}{M_\odot}\right)^2 (\mu M)^3 \left(\frac{\rho_{R_c}}{M_\odot \text{pc}^{-3}}\right). \tag{4.115}$$

Hence we see that for an asymptotic scalar field mass density of $\sim 1 M_\odot \text{pc}^{-3}$ and $M\mu < 1$ this is a very small effect. However in more extreme environments with larger matter densities or steeper density profiles the accretion may provide a more significant contribution to the frequency shift.

Whilst we have chosen a specific form as an illustrative example, one can easily choose different profiles for φ, or indeed different $T_{\mu\nu}$ profiles, compute ΔV, and substitute into the expressions for Ω to get the corresponding QNM frequency shifts.

4.5 Summary and discussion

While previous authors have attempted to estimate the QNM frequencies for "dirty" black holes, that is black holes where the metric is perturbed by a stationary or quasi-stationary cloud of matter, their analyses were limited to simple, static, spherically symmetric metric perturbations around a Schwarzschild black hole [148, 243, 244].

However, in most physical cases such a cloud results in a steady flow of matter falling into the black hole, causing the mass of the black hole and the perturbed metric to acquire a time dependence. Here we present a perturbative analytic method to estimate, for the first time, the time dependent quasi-normal mode frequencies for such a growing dirty black hole in spherical symmetry, assuming a linear time dependence. This method is based on the perturbative method of Dolan & Ottewill (2009) [264] and the techniques for dealing with perturbed Schwarzschild metrics described in Cardoso et al. (2019) [263]. While the formula we derive can be applied to any kind of matter cloud, we give an illustrative result for a massive complex scalar field, in the context of wave-like dark matter. The advantage of using the Dolan & Ottewill method is that we may obtain

perturbative analytic formulae for the frequency correction $\delta\omega$ in terms of a general $T_{\mu\nu}$. It is then easy to plug in a specific matter distribution and accretion rate.

For small L the series we obtain may not be formally convergent, however we expect that as in Dolan & Ottewill (2009) truncating the series at finite order nonetheless gives very good approximations to the frequency corrections.

For our example we find that the size of the expected frequency shifts $\delta\omega$ can be related by the matter density near the BH horizon. We find that the frequency correction due to the time dependence of the metric, which other authors have neglected, is in fact *larger* than the contribution from the static matter distribution. While these frequency shifts are tiny for typical astrophysical dark matter densities, it is possible that they could become relevant in very dense astrophysical environments.

Further details of the method are contained in appendix C. In particular, in Sec. C.2 and C.3 we have verified our method by applying it to several well studied static perturbed Schwarzschild space times, including generic potential deviations around a Schwarzschild background, a charged Reissner-Nordström black hole and a Schwarzschild de Sitter black hole, and compared to previous numerical results where available. We find excellent agreement with previous results, demonstrating the versatility and utility of this technique even in non time dependent cases, and the accuracy of the perturbative order for our method.[4]

In this work we have only treated spherically symmetric background spacetimes and hence spherically symmetric "dirt" around Schwarzschild black holes. To examine astrophysically relevant cases like baryonic accretion discs and Kerr black holes we would ideally extend this method to spacetimes and matter clouds with only axial symmetry. A major complication is that for generic axial metrics the equations of motion are in general non-separable, such that one cannot easily reduce the system to a one dimensional second order ODE. More recently other authors explored describing perturbations of an axisymmetric almost-Kerr spacetime with a set of coupled second order ODEs [268], and a similar method may allow the extension of our work to axisymmetric growing dirty black holes.

[4]We note, however, that we have restricted ourselves to odd metric perturbations, due to the difficulty in obtaining a master equation for even perturbations when matter is present.

Chapter 5

Black hole merger simulations in wave dark matter environments

The detection of gravitational waves from compact binary mergers [44–48, 98, 269] allows us to constrain their astrophysical properties, which has important implications for populations studies and gives information about their formation and evolution [52, 270–279]. In principle, GW observations can also provide a window on the environments of such binaries, since any non-zero stress-energy tensor will modify the metric in their vicinity, resulting in changes to the character of the inspiral, merger and ringdown parts of the signal. These changes could capture the effects of standard baryonic matter like plasma-filled accretion discs, or dark matter overdensities, with the spatial distribution and physical nature of the matter giving rise to distinctive signatures at each stage [148–150, 150–163].

In practice, the energy densities required to give significant effects during the inspiral and ringdown parts of the signal are in most cases high relative to the expected astrophysical values [148]. In the case of dark matter, the average galactic densities as measured from observations of galactic rotation curves are at best of the order of $M_\odot/\mathrm{pc}^3$ or $\mathrm{GeV/cm}^3$, with the local density in the Solar neighbourhood of the order $\rho_{\mathrm{DM}} \sim 0.01 M_\odot/\mathrm{pc}^3$ or $\sim 0.1 \mathrm{GeV/cm}^3$ [115–119]. As discussed in section 2.8, in the units of our NR simulations this is extremely small

$$\rho := \rho_{\mathrm{DM}} R_s^2 \sim 10^{-30} \left(\frac{\rho_{\mathrm{DM}}}{M_\odot \mathrm{pc}^{-3}}\right) \left(\frac{M}{10^6 M_\odot}\right)^2 . \tag{5.1}$$

Clearly some enhancement in the density around a black hole or other compact object relative to this value is required in order for the effect to be above numerical error in a simulation (which is a minimum requirement for it to be modelled and measurable in observational data).

Several mechanisms that create DM overdensities around isolated BHs do exist, with one well motivated one being the formation of dark matter spikes [280–285]. These arise from the accretion and adiabatic redistribution of particle dark matter in the potential well around black holes as originally suggested by Gondolo and Silk [280]. For wave-like dark matter [82, 83, 120–123, 123–125, 127–129, 131, 145, 286–294], where light bosonic particles form a condensate with astrophysical scale de Broglie wavelengths as discussed in section 1.3.2, similar accretion effects occur for which the resulting profiles have been studied in [1, 18, 139, 141, 142, 197, 198, 200, 210, 295]. The density of the cloud grown via such accretion depends strongly on the asymptotic dark matter environment, but for higher mass candidates gives a power-law enhancement close to the black hole that can be significant. At the other end of the scale, where the wavelength is significantly larger than the black hole, the gradient pressure of the field (sometimes also called the quantum pressure) resists the pile up and tends to smooth out the profile, suppressing any overdensity.

Another possible enhancement mechanism is the superradiant instability, in which a bosonic field can extract energy and angular momentum from a highly spinning black hole via repeated scattering in the ergoregion (see [21] for a review). Simulations with light massive vector fields suggest these superradiant clouds can grow to be up to $\sim 10\%$ of the mass of the black hole [205], which takes the coefficient in equation (5.1) to $\sim 10^{-5}$ in the best case, and a combination of both superradiance and accretion may lead to even higher densities [145]. The potential for such bound states to form around BH binaries has been studied in [296], as well as around neutron stars [297–300].

A key question is whether overdensities that may form around isolated objects persist during binary mergers, our main source of GW data. For example, particle DM spikes have been shown with N-body simulations to disperse for equal mass mergers, meaning that objects close to merger or with a violent merger history are likely to have lost their DM environment [274, 301, 302]. For this reason, the key targets for detecting environments are extreme mass ratio inspirals (EMRIs) with LISA [221, 303], where the cloud may still be maintained during the inspiral. Another advantage of EMRIs is that there is a higher relative impact on the curvature for a given DM density for larger black hole masses, and the dephasing in the frequency of the signal during the inspiral accumulates over many orbits that can be potentially be observed in band or across ground based and space

based detectors [304–311]. Studies of the impact of dark matter spikes [154, 156–158, 312–314] and superradiant clouds [159, 310, 315–320] on EMRIs show that they are potentially detectable with LISA observations.

Beyond the inspiral regime of EMRIs, it is also interesting to consider whether the strong gravitational non-linearities present during a roughly equal mass merger may give rise to distinctive features in the gravitational wave signal or other electromagnetic emissions.[1] These signatures provide information in a different regime to the inspiral and thus their combination could confirm a detection or provide evidence for a particular candidate. Studies of similar mass binaries necessitate the use of NR simulations, in which the Einstein equations are solved numerically for the evolution of the binary and its environment, from some initial state prior to merger until after coalescence and ringdown. Due to the computational expense, such simulations can at best cover the last few (order 10) orbits before the merger. Ultimately the goal is to generate waveform templates for binary mergers that include environmental effects, but a key question that ought to first be answered is whether, at such a late stage in the merger, such an environment will still be present at all, and if so, what spatial configuration it will have. In other words, *what is the correct initial data for the matter environment?*

In this work we study this question for the case of wave dark matter accreting onto an equal mass, non spinning BH binary, focussing on the regime where the wavelength of the scalar is of the same order as the Schwarzschild radii of the individual black holes (which is also similar to their separation at the start of an NR simulation). We begin in Sec. 5.2 by using toy simulations of fixed BH orbits to show that in this case the accretion of dark matter onto the binary is not disrupted by the orbital motion as it is for higher mass particle candidates. There is instead a quasi-stationary profile that builds up over time, providing a well-motivated initial configuration for such matter in NR simulations.

Having identified a well-motivated profile, we then study the impact of using different initial profiles on the DM evolution in Sec. 5.3. We study the profile of the matter on the background of a binary merger simulated in full General Relativity, initially neglecting the backreaction of the matter onto the binary motion. We compare cases that start with our quasi-stationary profile to more arbitrary

[1] For example, in cases where high densities are generated during the merger, certain dark matter models may have electromagnetic counterparts arising from self-annihilations, which would provide an alternative way of identifying particular candidates, such as the Peccei–Quinn QCD axion [67, 229, 321, 322].

configurations such as gaussians, and study the effect of cutting off the accretion at some finite radius.

Finally, in Sec. 5.4 we use recently developed techniques [188] to construct constraint satisfying initial data, and turn on backreaction to study the effect of superimposing the different matter profiles on a circular vacuum inspiral. Some background information on the set up is given in Sec. 5.1, and throughout this work we use geometric units where $G = c = 1$ (see note on units).

Our work builds on a number of earlier related investigations into DM environments of compact object binaries. The interaction of a black hole binary and a scalar field environment in the early-inspiral regime, where the separation is large and almost constant with time, has been explored via effective field theory [323, 324], weak field approximations [227, 250, 325–331]; perturbative schemes [219, 220, 316, 318, 332–335], and N-body and mesh numerical simulations [158, 296, 336–338]. The effect of a non-vacuum environment on the post-merger "ringdown" regime, particularly the effect on the frequencies of the characteristic quasi-normal modes has also been explored by a number of authors [2, 243, 244, 339, 340]. To model the highly relativistic and dynamical merger one must use full Numerical Relativity. An axion-like scalar field environment was considered by Yang et al. [341], simulating the effect of a thin shell of matter on the binary merger. Choudhary et al. [342] go further, starting from the last orbit before merger and using a Gaussian as an initial profile for the scalar field. They find a change in the post-merger ringdown signal caused by the increase in effective mass of the final black hole. Ikeda et. al. [296] studied the bound states that may form around binaries via superradiance, and find they can be well described with a perturbative "gravitational molecule" description. Most recently Zhang et al. [343] simulated binary mergers with a spherical scalar field shell, and examined the effect on the gravitational recoil of the binary and the scalar and gravitational radiation. They found that the scalar cloud accelerated the merger, and increased the recoil kick. Related work has also been done in modified gravity in the context of scalar-tensor theories [344–349]. We note that in works where the scalar field grows due to superradiance or a non-minimal coupling to gravity the state of an isolated BH often depends only on the properties of the BH, and not the surrounding DM environment, and the scalar field is in some sense "anchored" to the black hole. However, we emphasise that similar issues to those identified in this work regarding the ambiguity of the initial state could still arise if the

individual scalar clouds interact and form a common cloud prior to the point at which the simulation is started – in most (if not all) cases, no analytic form for a common binary cloud is known.

5.1 Modelling wave dark matter around black holes

For sub-eV dark matter the occupation number of the particles in each state is high, with the de Broglie wavelength much larger than the particle separation [120]. We can then treat it as a classical field, in particular, a scalar field for spin-0 bosonic dark matter, which results in wave-like behaviour on astrophysical scales [128] (see section 1.3.2 and [120, 122, 124] for reviews).

Specifically, the system we consider is Einstein gravity with a minimally coupled massive complex scalar field φ, described by the action

$$S = \int \mathrm{d}^4x\sqrt{-g}\left(\frac{1}{16\pi}R - \frac{1}{2}\nabla_\mu\varphi^*\nabla^\mu\varphi - V(\varphi)\right), \tag{5.2}$$

with a simple quadratic potential

$$V(\varphi) = \frac{1}{2}\mu^2\varphi^*\varphi. \tag{5.3}$$

The dynamics of the scalar field is thus governed by the Klein-Gordon equation on a curved background (1.48). In this work, as in chapter 3, we consider a regime where the scalar field wavelength is comparable in size to the black hole radius and work in terms of μ, the inverse reduced Compton wavelength which we can think of as "the scalar mass" (see note on units).

The interaction of such massive scalar fields with isolated black holes has been extensively studied, showing that long-lived scalar clouds can grow around black holes either from simple gravitational accretion from the environment [1, 123, 200, 295], or via the mechanism of superradiance for spinning black holes [21]. In the former case, as discussed in chapter 3, the solution in the asymptotically flat region far from the black holes is a spatially homogeneous oscillatory solution of the form $\varphi = \varphi_0 e^{-\mathrm{i}\mu t}$, which describes a fluid of roughly constant density and zero pressure on average – i.e. dark matter. The solution closer to the black hole is described by the Heun functions [18, 197–199], with characteristic oscillations in the spatial profile on length scales set by the scalar wavelength.

In this work we go beyond the single black hole spacetime and consider the simplest possible black hole binary with total ADM mass M: two equal mass ($M_{\rm BH} \approx 0.5M$) non-spinning black holes with an initial separation of $d \approx 12M$ on roughly circular orbits. The exact parameters are given in Table D.1, which result in an inspiral of about 10 orbits before merger with an initial orbital period $T \sim 270M$.

We study the interaction between the scalar field and the binary black hole solving the Klein-Gordon equation with different levels of approximation in the background metric:

1.- Fixed orbit simulations – the metric background is the superposition of two isotropic BH solutions, moving on circular orbits. We evolve the scalar field on this background to test whether a dark matter profile accumulates or disperses over time. See Sec. 5.2.

2.- Fully general relativistic evolution with $G = 0$ – the background is now evolved in full General Relativity, but we neglect the backreaction of the matter onto the metric to focus on the impact of the binary on the matter evolution. See Sec. 5.3.

3.- Fully general relativistic evolution with $G = 1$ – finally we turn on backreaction to study the impact of the DM environment on the binary motion. See Sec. 5.4.

In each case we take the scalar mass $\mu = 0.34M^{-1}$, corresponding to a scalar wavelength of around $\lambda_c \sim 18M$, slightly larger than the black hole separation but much smaller than the binary period. For black holes in the LVK frequency band, this corresponds to a mass of $\sim 10^{-9}$eV, while for supermassive binaries detectable with LISA it can go down to $\sim 10^{-17}$eV for a binary with ADM mass $10^9 M_\odot$. This choice was motivated by a brief study of the angular momentum flux as described in [350, 351], where it was identified as the value that gave the largest exchange of angular momentum with the binary.[2] Our simulations therefore represent a "best case" for the impact of the dark matter on the binary.

Our results are presented in the following sections, with details of the code set up and validation contained in appendix D.

[2] A more in depth study of the accretion behaviour for different masses is given in [336].

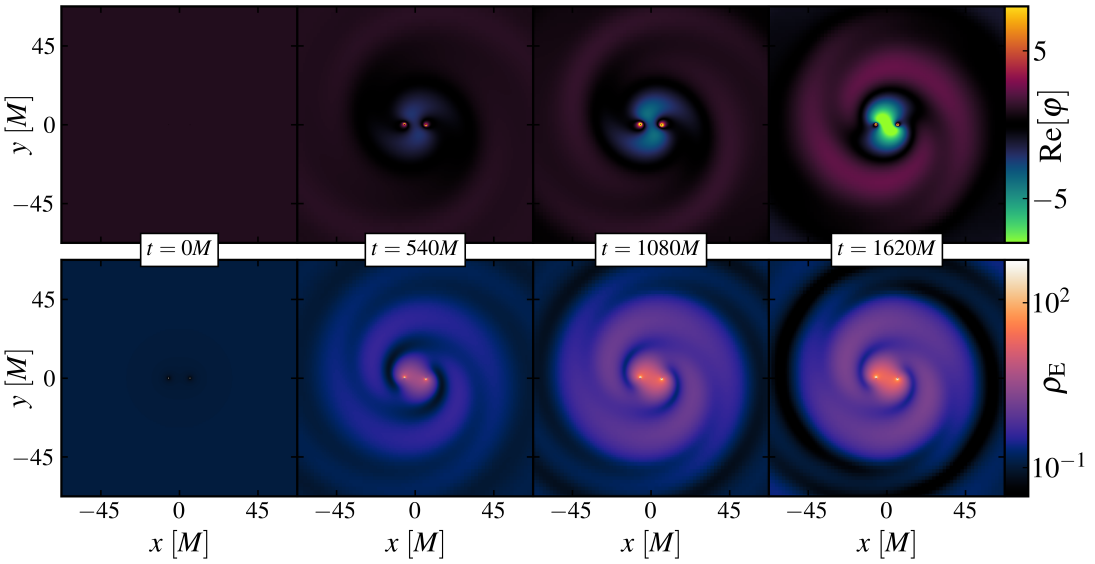

Figure 5.1: **Evolution of the real part of the scalar field (top) and energy density (bottom)** on the fixed orbit binary background after $0, 2, 4$ and 6 orbits respectively. The binary generates a scalar cloud that quickly settles into a quasi-stationary spiralling profile that grows in amplitude over time. In the centre around each black hole spikes form in the scalar field amplitude, resulting in an enhanced energy density, with an additional accumulation of matter in the potential well in the middle of the binary. Further out we see regions of both higher and lower density forming, with the patterns on a length scale related to the binary separation and scalar wavelength. Movie can be found in https://youtu.be/XevfJKLO9ec.

5.2 Fixed orbit simulations: finding the quasi-stationary profile

During the early stages of a binary merger, the black holes are widely separated and follow approximately Keplerian orbits, with emission of gravitational waves tending to circularise the orbits over time [352–355]. During this phase, the dark matter profiles of the two BHs will evolve largely independently, generating non-trivial density profiles via accretion. A common DM cloud will also tend to circularise the orbits via the effect of dynamical friction [356]. As the binary separation decreases, at some point the DM clouds will merge and interact [3], eventually forming a common cloud which is "stirred up" by the binary. It will not, therefore, have a smooth gaussian profile and will carry some angular momentum due to its

[3] See [296][310][315][316] for studies in the context of superradiance.

interaction with the spacetime curvature. To investigate the resulting configuration, we construct an approximate toy model for the late inspiral where we model the gravitational field as a superposition of two isotropic black hole metrics (i.e. Schwarzschild metrics expressed in isotropic coordinates [357])

$$\mathrm{d}s^2 = -\left(\frac{1+\Phi/2}{1-\Phi/2}\right)^2 \mathrm{d}t^2 + (1-\Phi/2)^4\,(\mathrm{d}r^2 + r^2\mathrm{d}\Omega^2), \tag{5.4}$$

where $\mathrm{d}\Omega^2 = \mathrm{d}\theta^2 + \sin^2\theta\mathrm{d}\phi^2$ and

$$\Phi(t,\boldsymbol{r}) = -\frac{Gm_1}{|\boldsymbol{r}-\boldsymbol{r}_1(t)|} - \frac{Gm_2}{|\boldsymbol{r}-\boldsymbol{r}_2(t)|} \tag{5.5}$$

is an effective gravitational potential. We impose that the black holes ($m_1 = m_2 = M_{\mathrm{BH}}$) follow circular Keplerian orbits of radius $d/2$ and frequency

$$\omega_{\mathrm{BBH}} = \sqrt{\frac{2GM_{\mathrm{BH}}}{d^3}}, \tag{5.6}$$

with their centres located at

$$\boldsymbol{r}_1(t) = \left(+\frac{d}{2}\cos(\omega_{\mathrm{BBH}}\,t),\ +\frac{d}{2}\sin(\omega_{\mathrm{BBH}}\,t),\ 0\right), \tag{5.7}$$

$$\boldsymbol{r}_2(t) = \left(-\frac{d}{2}\cos(\omega_{\mathrm{BBH}}\,t),\ -\frac{d}{2}\sin(\omega_{\mathrm{BBH}}\,t),\ 0\right). \tag{5.8}$$

Close to each of the black holes this metric tends to a Schwarzschild metric in isotropic coordinates, while far from the black holes it tends towards a weak field limit. This metric is not a solution of the Einstein equations, but is merely designed to study the way in which a common quasi-stationary profile can form in a period where the orbits are not yet rapidly decaying as at merger.

We start the simulations with the binary immersed in a homogeneous scalar field, choosing $\varphi(t=0) = \varphi_0$ and $\Pi(t=0) = -\mathrm{i}\mu\varphi_0$, and study the evolution of the scalar field over several orbits. The (real) parameter φ_0 controls the asymptotic density of the infinite reservoir, but since we neglect backreaction for this simulation, we can rescale the results to any physical asymptotic density we choose.

We find that the scalar field rapidly accretes from its asymptotic value into a cloud around the two black holes and forms a persistent spiral profile within a few orbits that co-rotates with the binary, see Fig. 5.1. The scalar field (top panel) is pushed towards large amplitudes, such that the energy density (bottom panel) around and between the black holes increases by several orders of magnitude.

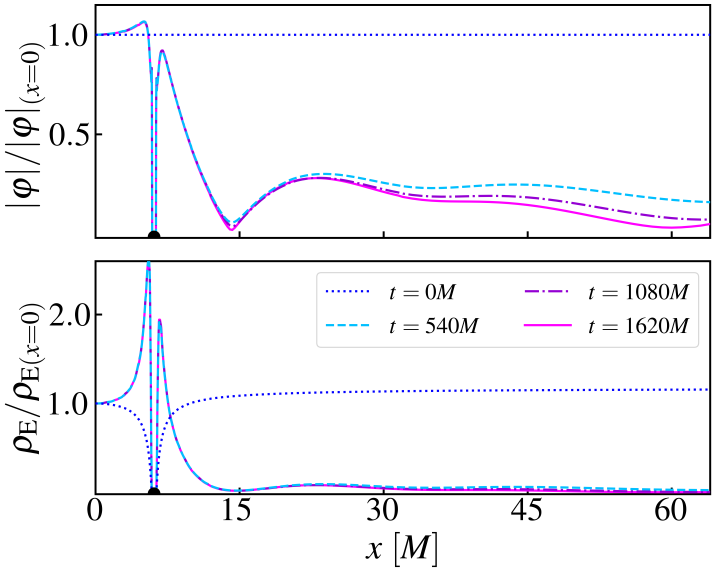

Figure 5.2: **Normalised density and scalar field profiles along half of the fixed orbit binary axis**. The black dot illustrates the location of one of the black holes. We see that after a relatively short amount of time (approximately two orbits) the field has gone from a homogeneous profile to a quasi stationary profile peaked around and between the BHs (the zero values within the horizon are due to the choice of gauge and excision conditions for the evolution). This results in a region of enhanced density in the potential well between the binary BHs.

Once the profile forms it grows over time homogeneously, fed by the asymptotic reservoir of dark matter imposed at the boundaries.

This quasi-stationary profile can be studied in more detail in Fig. 5.2, where we plot the evolution of the density and scalar field profiles along the axis of the binary, normalised relative to their central values. Even within the first two orbits, both quantities have already settled into the persistent profile that grows steadily in amplitude over time. We observe density spikes around each of the black holes, an accumulation of scalar matter in the potential well between the black holes, and smaller amplitude density peaks further away on length-scales that depend on the binary separation and scalar wavelength. The scalar cloud is significantly enhanced compared to a superposition of two of the scalar field profiles found around isolated black holes (like those studied in [1, 18, 197, 198, 200, 291]), due to the non-linear effect of the combined gravitational potential.

We note that this persistent profile contrasts with higher mass particle-like dark matter, where dark matter density spikes have been shown to disperse under the

influence of the binary motion [274, 301, 302]. The enhanced density is important both for its effect on the gravitational wave signal and also for potential direct detection for models with standard model couplings [229].

Even with this simple fixed orbit model, the finite size of the numerical domain prevents us from evolving the system for many orbits. However, the persistent and consistently growing scalar field profile shown here allows us to predict the qualitative behaviour of the cloud at late times – it seems that a common spiral shaped cloud would continue to grow until the dark matter reservoir is eventually exhausted, at which point the binary would be left with an isolated spiral shaped cloud that would gradually decay away through a combination of falling into the black hole and radiating to infinity. Assuming that the reservoir is not exhausted before merger, the cloud should continue to grow and not disperse.[4]

5.3 GR evolution with G = 0: the impact of the binary on the matter evolution

We now study the evolution of the wave dark matter on a fully general relativistic binary merger, with the Klein-Gordon equation evolved on a dynamical spacetime described by the Einstein's field equations

$$R_{\mu\nu} - \frac{1}{2} g_{\mu\nu} R = 8\pi G T_{\mu\nu}, \tag{5.9}$$

where $R_{\mu\nu}$ is the Ricci tensor, and $T_{\mu\nu}$ is the energy momentum tensor of the scalar field. To first isolate the impact of the binary on the matter evolution, we turn off the backreaction by setting Newton's constant $G = 0$ in Eqn. (5.9). This ensures that different cloud configurations evolve in the same BBH background, described by the black holes' vacuum trajectories.

The BH initial conditions are Bowen-York data [12, 167, 189–191, 202–204, 358] for the parameters in table D.1 and we solve the Hamiltonian constraint for the correction to the conformal factor arising from the non-zero boosts.

The main goal is to compare the evolution of several initial scalar field configurations. First, we observe that the profile found in our toy model with fixed orbits is close to the stationary profile for the fully GR binary solution, as we see very little transient evolution when we impose it on the binary and begin the

[4] Analytical and numerical studies have suggested that, for the typical scalar field masses used here and reasonable assumptions, clouds can survive for cosmological times [144, 145].

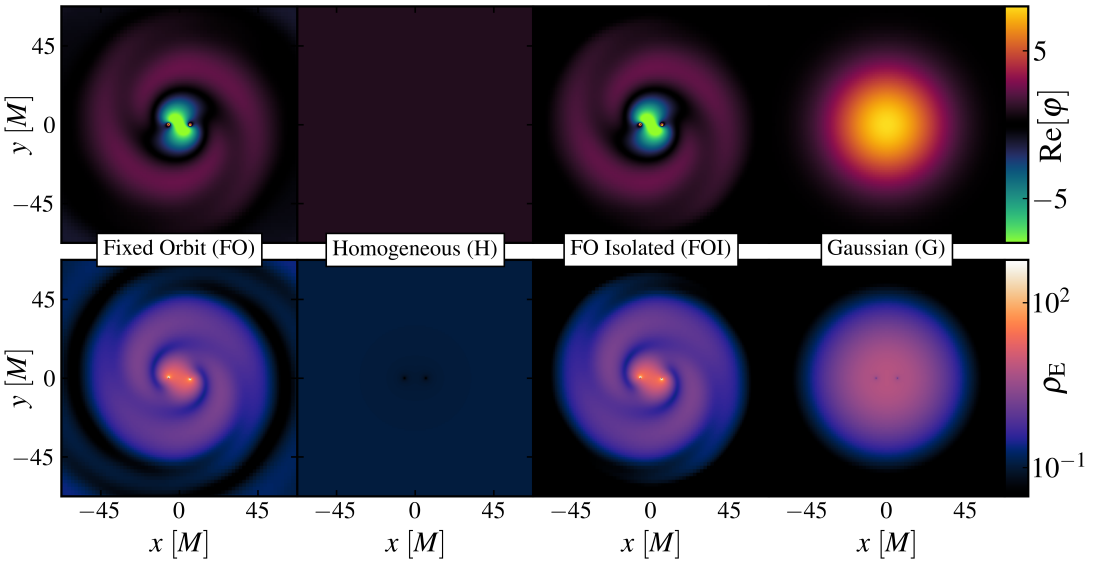

Figure 5.3: **Comparison of the initial data profiles**. From left: FO, H, FOI and G. The top row shows the real part of the scalar field, while the bottom shows the energy density on a log scale. Details on the scaling of these profiles is given in the main text and in Fig. 5.4.

evolution. This can be contrasted with other possible choices for the initial scalar field profile, such as a Gaussian, where we find significant initial transients before the preferred profile is reached.

The scalar profiles we examine can be classified into two types: extended and isolated clouds. In the former class, the energy density of the cloud reaches the boundary of our simulated domain, allowing for continued accretion from spatial infinity. (This is imposed using extrapolating boundary conditions as described in [183].) Within this class we study:

- **Fixed Orbit (FO):**
  We take as initial data the resulting quasi-stationary scalar field profile after evolving the binary in the homogeneous dark matter halo for 6 orbits $\varphi_{\rm FO}$, see Fig. 5.1. This can be considered the "most correct" initial condition for a scalar field that is still accreting up to the merger.

- **Homogeneous (H):**
  We take the same homogeneous initial profile described in the previous sec-

tion by setting $\varphi(t=0) = \varphi_0$ and $\Pi(t=0) = -\mathrm{i}\mu\varphi_0$. In this profile we still need to grow the quasi-stationary profile, so expect some transient evolution.

In the second class of initial conditions, the scalar cloud has a sufficiently large radius to cover the BBH, but the energy density goes to zero at the boundaries, reproducing an isolated cloud which has exhausted its dark matter reservoir. (For these cases we use Sommerfeld radiative boundary conditions as described in [183].) Here we study two cases:

- **Fixed Orbit Isolated (FOI):**
  We apply a $f(r) \sim \tanh[r - 60M]$ envelope to the FO scalar field profile, so that $\varphi_{\rm FOI}(t=0) = f(r)\varphi_{\rm FO}(t=0)$ and the configuration reproduces an isolated cloud which has exhausted its dark matter reservoir. Again this is a "correct" profile around the black holes, but the cut off we introduce is rather arbitrary, and therefore introduces some transient evolution in the overall shape of the cloud as it settles into a quasi-stationary, isolated profile.

- **Gaussian (G):**
  We choose a Gaussian profile for $\varphi(t=0) = \varphi_0 \exp[-r^2/\sigma^2]$ and $\Pi(t=0) = -\mathrm{i}\mu\varphi(t=0)$, where r is the distance to the centre of the binary. We use $\sigma = 1/0.03M$ and choose φ_0 so that the total mass of the initial scalar cloud is the same as the isolated fixed orbit cloud described above. We expect transient evolution in this case before we arrive at the quasi-stationary profile.

We plot 2D slices of the initial density configurations perpendicular to the binary orbital axis in Fig. 5.3.

To quantify the differences we extract the value of the scalar field profile along the line joining the BHs, see the top panel of Fig. 5.4. In the bottom panel of Fig. 5.4 we track the value of the scalar field at the centre of the binary, which provides a reasonable indication of the amount of transient evolution. We see as expected that the scalar field needs some time to settle down to the quasi-stationary configuration, with the most transient evolution in the case G and the least in FO. [5] However, even when starting from very different profiles the scalar

[5]Note that the scalar field in the FO and FOI initial data goes to zero inside the horizon. However when we evolve it in the full GR evolution in the moving puncture gauge [201, 359] it quickly relaxes to give a continuous non-zero density spike. This difference is mainly due to the

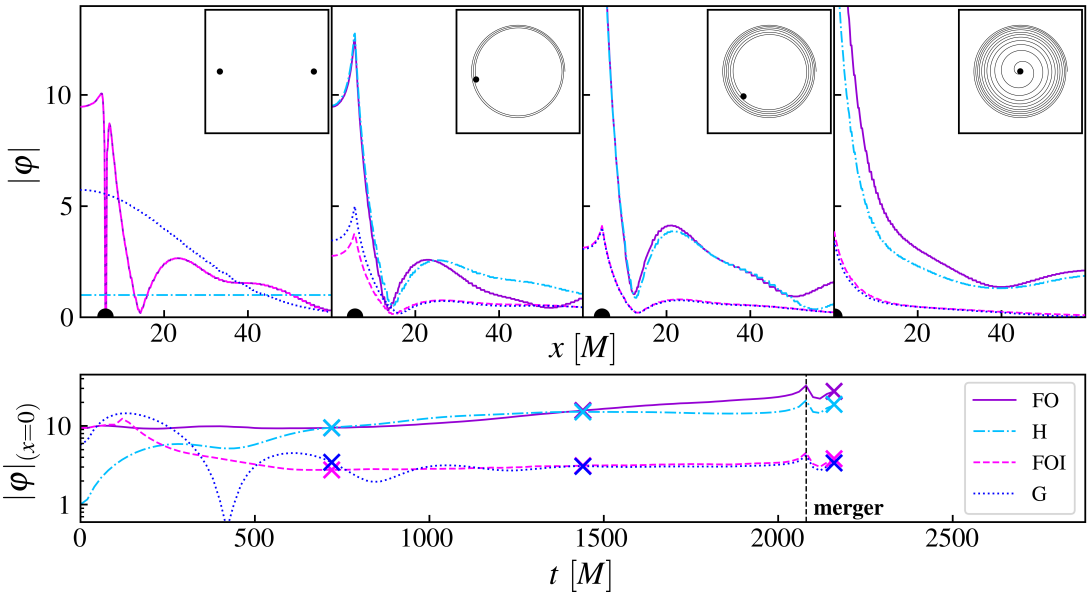

Figure 5.4: **Evolution of the scalar field $|\varphi|$ profile for different initial data.** We plot $|\varphi|$ along the axis of the binary for the different initial data profiles. The amplitudes of the fixed orbit isolated (FOI) and Gaussian profiles are normalised so that the integrated mass of the whole cloud is the same. The amplitude of the homogeneous profile is chosen to match the initial asymptotic value of the fixed orbit profile and is set to unity in these plots. The black dot illustrates the location of one of the black holes. The bottom panel plots the evolution of the scalar field amplitude at the centre of the binary with time. Markers illustrate the time of the upper panels. A movie showing the evolution of these profiles can be found in https://youtu.be/wGUUUutuiyU.

field evolves into the same kind of spiral shaped, quasi-stationary, configuration as described in section 5.2 within a few orbits. The final state post merger is a single density spike with power law tails, of the kind studied in [1, 18, 197, 198, 200, 291, 295], with solutions that can be approximated by confluent Heun functions [199].

The main difference between the extended (FO, H) and isolated (FOI, G) clouds is that the former can continue to accrete from infinity, so we see the central amplitude continuing to grow throughout the merger, increasing the density and size of the final scalar cloud. The homogeneous data accretes rapidly at the centre, and in only a few orbits reaches the fixed orbit quasi-stationary configuration. The

different choice of lapse between the fixed orbit metric and the moving punctures gauge used for the full relativistic evolution. One should thus consider the change in the sub-horizon initial scalar field profile to be an artefact of the change in gauge choice.

difference in amplitude between the final cloud from the homogeneous data and FO data is expected given that the fixed orbit data has effectively been accreting for an extra six orbital periods during our fixed-orbit simulation.

For the isolated configurations (FOI and G), the cloud does not continue to grow as there is no reservoir of DM at the boundary. In the case of FOI, because there is no asymptotic density to confine it, the cloud settles into a more distributed (but qualitatively similar) shape – this is a consequence of imposing an arbitrary cut off in the density at finite radius. The Gaussian case, on the other hand, shows strong transient behaviour with several large oscillations around the quasi-stationary profile, on a timescale roughly corresponding to the period of the binary. After $\sim$ 2-3 orbits the same configuration is reached – the fact that the final shapes and amplitudes match is a result of starting with the same cloud mass, and implies that the two cases have radiated equal amounts, and been accreted equally by the BHs, during their transient evolution.

These results demonstrate that within only a few orbits the transients in the cloud will die away and a quasi-stationary configuration will be reached, therefore for long simulations it may be sufficient to use the simpler homogeneous or Gaussian initial data. However, the initial profile can make a significant difference to the transient evolution of the scalar cloud during this time, and therefore may have an impact for shorter simulations. We have not yet considered the backreaction of matter onto the metric, but where this is included it is possible that these transient effects could impact on the black hole trajectories, as well as creating additional radiation of gravitational waves. We will discuss this further in the following section.

5.4 GR evolution with G = 1: the impact of the matter on the binary evolution

The ultimate goal of NR simulations with environments is to quantify the impact of the matter on the binary evolution, and resulting gravitational wave emission, so as to learn about the properties of the DM. To do so we must include the backreaction of the evolving matter on the metric background. We therefore restore $G = 1$ and solve the Hamiltonian and momentum constraints using the novel CTTK method [188]. In particular, we use the *hybrid* CTTK approach, where we choose a spatially varying mean curvature that depends on the energy density

distribution $K^2 = 24\pi G\rho$, where ρ is the ADM energy density, and solve the constraints obtaining corrections for both the conformal factor and traceless conformal extrinsic curvature, on top of an initial Bowen-York solution for a boosted black hole binary in vacuum. This means the matter environment introduces corrections to the effective initial momenta and bare masses of the black holes.

Now that the amplitude of our field has a physical meaning (it is related to the matter density roughly as $\rho \sim \varphi_0^2$), we quantify this by specifying the relative cloud mass to (vacuum ADM) binary mass ratio.

We superpose our profiles onto the vacuum BH parameters for the masses and momenta, and evolve the metric plus matter to merger, which we find happens faster in the presence of the DM clouds. Some dephasing[6] of the signal compared to the vacuum evolution is expected due to the effects of dynamical friction, radiation of the scalar cloud, and backreaction onto the metric, but the impact we see is unexpectedly large. Examining the black hole trajectories in Fig. 5.5 reveals that, even for light clouds where $M_{cloud}/M \approx 0.01\%$, the black holes are pushed into eccentric orbits, giving rise to large deviations from the circular trajectories that we would expect at this late stage of the inspiral and a prompt merger. We find that this effect is proportional to the energy density near the black holes, being the largest for both the extended and isolated fixed orbit profiles (FO and FOI) due to the presence of density spikes near the horizons. For the more artificial initial conditions H and G where the initial energy density near the black holes is smaller, the effect is smaller but still non-negligible. The use of the CTTK method (see section 2.7 and [188] for details) means that in general we obtain larger corrections to the effective initial black hole momenta, and smaller corrections to the effective bare masses, compared to the CTT method.[7] Nonetheless the unwanted eccentricity is an unavoidable consequence of the non-trivial matter environment, and is particularly significant where there are high energy and momentum flux densities near the black hole horizons, as in our preferred quasi-stationary solution.

Because the deviations are significant, we cannot simply extract waveforms and compare them to the vacuum case to determine how the presence of a scalar cloud impacts the gravitational wave signal, as we would not be able to conclude

[6] A difference in the rate of phase evolution resulting in a phase difference that accumulates over time.

[7] This is because unlike CTT the CTTK method uses a non-constant K to cancel terms in the Hamiltonian constraint, reducing the need to tune the bare masses to satisfy it, at the cost of adding $\partial_j K$ terms to the momentum constraint requiring larger corrections to the initial puncture momenta.

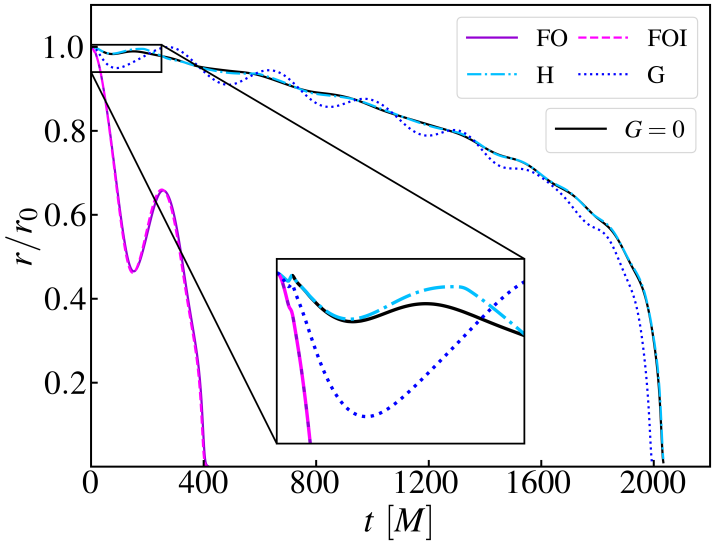

Figure 5.5: **Orbital trajectory** of one of the black holes in simulations of a vacuum binary (black line), and in binaries with total cloud mass of $M_{\rm cloud}/M = 10^{-3}$. Different colored lines depict the effect of the different scalar field profiles with the same black hole parameters.

that such signatures are caused by the presence of the scalar field rather than by the induced (physical but unwanted) eccentricity. Even if one tunes the initial momenta and masses of the black hole punctures so that their initial coordinate velocities and accelerations match the vacuum case, this is not sufficient to remove the effect. Further work is required to remove this effect. One should follow a similar method to those used to obtain low-eccentricity initial data for binary black holes in vacuum spacetimes [360–363]. In these methods, one measures the trajectory and eccentricity over 2-3 full orbits for an initial choice of input parameters, then uses a high order post-Newtonian [364] approximation or gradient descent to estimate the correction to these input parameters (typically the initial momenta and masses of the black hole punctures) needed to reduce the eccentricity. One then iterates this procedure until the desired eccentricity is achieved. Our case is more complicated because the black holes are perturbed by the backreaction from the matter distribution, which we solve for numerically. However, one could in principle obtain a similar scheme by incorporating the effect of a matter cloud into a new post-Newtonian binary model, something which is beyond the scope of this work.[8]

[8]Post-Newtonian dynamics have been explored for binaries in scalar-tensor theories [365–370] but not, as far as we are aware, for minimally coupled massive scalar field environments.

5.5 Summary and discussion

One of the key challenges in constructing reliable gravitational wave templates for BH binary mergers with environments is establishing the correct initial data for Numerical Relativity simulations, which begin only a relatively short time before the merger.

Here we conducted numerical simulations of the accretion of wave dark matter around binary black holes in fixed orbits, choosing a scalar mass that gives a large interaction with the BH binary (i.e. the regime where the wavelength of the field is similar to the Schwarzschild radii of the BHs). We found that the scalar field quickly converges to a persistent non-trivial profile, peaked around each black hole, which grows in amplitude as the accretion continues.

We then explored how different choices of initial data affected the evolution of the DM cloud during the binary merger. Our results suggest that the profile found in the fixed orbit simulations is an attractor solution, as other choices of initial data converged to the same distribution over the course of several orbits. This means that for long numerical simulations the precise choice of initial scalar profile may be unimportant, as the field will quickly converge to the quasi-stationary distribution. However for numerical simulations which only consist of a small number of orbits, the transients and the resulting loss of control over the initial data from using a non stationary profile may affect the final results. We also saw that allowing continued accretion from a scalar dark matter reservoir over the course of the merger results in a larger scalar cloud around the final black hole, confirming the importance of the local DM environment for the system's evolution.

Lastly, we obtained constraint satisfying initial data for the scalar profiles obtained from our fixed orbit simulations. To the best of our knowledge, this is the first time that environments with non-zero angular momentum have been studied in the initial conditions for DM environments around binaries. We found that naively using the parameters for a quasi-circular binary merger in vacuum will not usually produce low eccentricity orbits once matter is added, and because of this one cannot simply compare the resulting waveforms to establish the signatures of dark matter environments. For example, one may find that the merger happens sooner merely because of the increased eccentricity, and not due to effects like dynamical friction and gravitational radiation.

We conclude that a more comprehensive approach is needed to find initial data that both satisfies the Einstein constraints and produces realistic low-eccentricity

inspirals, similar to that developed for vacuum binaries [191, 358, 360–362]. This should ideally incorporate the quasi-stationary profile as part of the process of solving for the initial data, as is done in neutron star simulations [371–373], or match to a post-Newtonian model [364–369] for the matter and black holes in the late inspiral regime.

Only once the problem of initial conditions is under control can the degeneracies between the effects of a non-trivial dark matter environment and changes in other parameters of the binary be quantified, so that we can examine how to disentangle the two. We may then also extend the parameter space to include unequal mass and spinning black hole binaries, where kicks may occur [155], as well as exploring a wider range of scalar field masses, and the impact of self-interactions. The study of unequal mass ratios may also give us more insight into the effect of the scalar mass, as the two black holes would share a common environment but have different $M_{\rm BH}\mu$.

Chapter 6

Fifth forces and frame invariance

Since Einstein formulated his theory of General Relativity over a century ago [374] there has been much theoretical interest in the possibility that it is merely an approximation to a more general theory of gravity, a possibility we highlighted in part I. One of the most popular classes of theories of modified gravity are the so-called "scalar-tensor" theories [375], where the Einstein-Hilbert action

$$S = \int \mathrm{d}^4x\sqrt{-g}\left[\frac{M_{\rm Pl}^2}{2}R + L_{\rm m}\right], \tag{6.1}$$

is modified by the addition of one or more scalar fields. Here $L_{\rm m}$ is the matter part of the Lagrangian[1] and the reduced Planck mass is $M_{\rm Pl} = \sqrt{c\hbar/(8\pi G)} = \sqrt{1/(8\pi G)}$ in units where $c = \hbar = 1$. Instead of a fixed $M_{\rm Pl}$ (or alternatively a fixed Newton's constant G) we introduce a non-trivial coupling to R, giving an action of the form

$$S = \int \mathrm{d}^4x\sqrt{-g}\left[F(\boldsymbol{\varphi})R - \frac{1}{2}\partial_\mu\boldsymbol{\varphi}\cdot\partial^\mu\boldsymbol{\varphi} - W(\boldsymbol{\varphi}) + L_{\rm m}\right], \tag{6.2}$$

where the effective reduced Planck mass is now a function of the scalar field(s) $\boldsymbol{\varphi} = \{\phi_i\}$. The first and arguably simplest theory of this type is that of Brans-Dicke from 1961 [102] where $F(\phi) = -\frac{\alpha}{12}\phi^2$, $W = 0$ for a single scalar field ϕ and constant α. A modern formulation which encompasses all possible scalar-tensor theories with second-order equations of motion was first given by Horndeski [90, 375], and subsequently extended to Beyond Horndeski and then Degenerate Higher-Order Scalar-Tensor (DHOST) theories [97] which have higher-order equations of motion but maintain the same number of scalar degrees of freedom.

[1] In this chapter Lagrangian densities are denoted with curly $\mathcal{L}$, while upright L is used for the part excluding the $\sqrt{-g}$ metric factor.

As mentioned in section 1.3.1, scalar-tensor theories can be expressed in different "frames" via Weyl transformations. Equation (6.2) describes a "Jordan" frame if $F(\boldsymbol{\varphi})$ depends on $\boldsymbol{\varphi}$, however with $g_{\mu\nu} \to \Omega^2(\boldsymbol{\varphi})\tilde{g}_{\mu\nu}$ we can obtain a new action in the Einstein frame $S = \int \mathrm{d}^4x\sqrt{-\tilde{g}}\left[\frac{M_{\rm Pl}^2}{2}\tilde{R} + \cdots + L_{\rm m}(\Omega(\boldsymbol{\varphi}), \tilde{g}_{\mu\nu}, \text{matter})\right]$, where the gravity sector is now as in GR, but the matter sector picks up additional couplings to $\boldsymbol{\varphi}$.

Despite the theoretical attractions (Paul Dirac argued for a dynamical G on the basis of his large number hypothesis) generic scalar-tensor theories are severely constrained by solar system and lab observations. This is because the introduction of an additional field with a non-trivial coupling to gravity or matter can in general mediate long-range "fifth forces" [102–104]. The exchange of a new particle of mass m_s coupling to matter gives a Yukawa [105] potential

$$V_{\rm fifth}(r) = -\alpha\frac{GM_1M_2}{r}e^{-m_s r}, \tag{6.3}$$

for coupling α and masses M_1, M_2. For small enough m_s ($m_s = 0$ for Brans-Dicke) this can be probed via a range of experimental and observational tests which put extremely tight bounds on α [376–378] (see appendix E). In other words, if a theory predicts a significant long-range fifth force, like standard Brans-Dicke, it is probably ruled out.

Various screening mechanisms have been proposed to evade these constraints, whereby the fifth force is suppressed in the vicinity of matter [379]. These include chameleon mechanisms [107] where, for a suitable choice of $\Omega(\boldsymbol{\varphi})$ and Einstein frame potential, the effective mass of the scalar changes depending on the local matter density, so near large masses the fifth force becomes short range. There is also the Vainshtein mechanism and its variations [114, 380], where additional non-linear terms in the action result in a suppression of the scalar field within some radius around a matter source.

One particularly interesting type of scalar-tensor theory is one that is scale-invariant (including "Higgs-dilaton" theories where one of the scalar fields is a non-minimally coupled SM Higgs boson) [381–402], where the action, including the matter sector, has a global Weyl symmetry [403] such that there is no a-priori lengthscale. Instead the symmetry is broken dynamically as the scalar field(s) tend towards fixed equilibrium values under the influence of an expanding cosmology. This has been proposed as one element of a solution to the so-called hierarchy problem [386, 400, 404], and the phenomenological implications of such a theory

have also generated substantial interest [405–412]. There is a massless Goldstone boson associated with the spontaneously broken symmetry, termed the "dilaton", σ, and as such we might be worried about fifth-force constraints. However, it has been shown that in the Einstein frame (Garcia-Bellido et al. (2011) [388]) the dilaton only couples via terms which do not produce a long-range $1/r$ fifth force potential, avoiding the need for screening mechanisms. Ferreira, Hill & Ross (2016) [413] go further and show that, in a particular choice of Jordan frame, the dilaton completely decouples from the matter sector, and therefore contributes no fifth force at all.

This leads to the question: how can we relate these results in different choices of frame? Are there frames in which we can recover a long-range fifth force? Indeed, to what extent are generic scalar-tensor theories of this type really physically equivalent in different frames? While on a classical level one should not expect a redefinition of variables to change the physics or physical results, once you include quantum corrections this becomes no longer obvious (this is sometimes called the "cosmological frame problem" [414]). Copeland et al. [415] and Burrage et al. [416] explicitly calculated the fifth forces for a three-scalar-field toy model, which becomes a Higgs-dilaton theory for a certain choice of parameters, in first the Einstein frame [415] and a Jordan frame [416], and showed that at lowest perturbative order the results are the same. There has also been extensive work examining the general question of frame (in)equivalence from numerous points of view, mostly focused on cosmological applications [417–439].

In particular, Falls & Herrero-Valea [439–441] and Finn et al. [442, 443] developed a formalism to characterise exactly how the quantum effective action must transform non-trivially between frames. Finn et al. [442, 443] adopts the covariant approach [444–446], pioneered by Vilkovisky and DeWitt [447–449], whereby frame transformations are described in terms of a coordinate changes on a field-space manifold, and constructs a fully covariant quantum effective action, extending the Vilkovisky-DeWitt unique effective action to theories with fermion fields.

Here we show how this formalism, and the covariant geometric approach, can be applied to the problem of computing fifth forces, and to scale-invariant scalar-tensor theories in particular. We extend the geometric approach to show how choices of frame can be characterised in a geometric manner: as choices of submanifold in a higher dimensional general field space. Frame invariance becomes

manifest, and we see how the choice of frame is better thought of not as a dichotomy between "Jordan" and "Einstein", but as a continuum one can smoothly traverse. We also see how scale-invariant scalar-tensor gravity evades fifth force constraints in all possible frames.

The structure of this chapter is as follows: section 6.1 lays out the background theory; section 6.2 describes the new geometric approach to frame fixing, and in section 6.3 we apply it to calculations of fifth forces. We focus on the scale-invariant theory in section 6.4, and briefly discuss one-loop corrections from the choice of *physical* spacetime in section 6.5. Finally we conclude with a discussion of our results and future directions.

6.1 Background

6.1.1 The dilaton and scale-invariant gravity

Under the Weyl transformation $g_{\mu\nu} = \Omega^2 \tilde{g}_{\mu\nu}$ the Jordan frame action (6.2) for some integer number of scalar fields $\boldsymbol{\varphi} = \{\phi_i\}$ becomes

$$\begin{aligned} S = \int \mathrm{d}^4x\sqrt{-\tilde{g}}\Big[& F(\boldsymbol{\varphi})\Omega^2\left(\tilde{R} - 6(\tilde{\nabla}\ln\Omega)^2 - 6\tilde{\Box}\ln\Omega\right) \\ & - \Omega^2\frac{1}{2}\sum_i \partial_\mu\phi_i\partial^\mu\phi_i - \Omega^4 W(\boldsymbol{\varphi}) + \Omega^4 L_\mathrm{m}\Big], \end{aligned} \tag{6.4}$$

where $(\tilde{\nabla}v)^2 := (\tilde{\nabla}_\mu v)(\tilde{\nabla}^\mu v)$. Let

$$\begin{aligned} \Omega &= \exp(\sigma), & \tilde{F}(\sigma,\tilde{\boldsymbol{\varphi}}) &= \Omega^2 F(\boldsymbol{\varphi}), & \tilde{\phi}_i &= \Omega\phi_i, \\ \tilde{K} &= \frac{1}{2}\sum_i \tilde{\phi}^2 + 6\tilde{F}, & \tilde{W}(\sigma,\tilde{\boldsymbol{\varphi}}) &= \Omega^4 W(\boldsymbol{\varphi}), & \tilde{L}_\mathrm{m} &= \Omega^4 L_\mathrm{m}, \end{aligned} \tag{6.5}$$

Then we obtain

$$\begin{aligned} S = \int \mathrm{d}^4x\sqrt{-\tilde{g}}\Big[& \tilde{F}(\sigma,\tilde{\boldsymbol{\varphi}})\left(\tilde{R} - 6(\tilde{\nabla}\sigma)^2 - 6\tilde{\Box}\sigma\right) \\ & - \frac{1}{2}\sum_i \tilde{\phi}_i^2(\tilde{\nabla}\sigma)^2 + (\tilde{\nabla}_\mu\sigma)\sum_i \tilde{\phi}_i\tilde{\nabla}^\mu\tilde{\phi}_i \\ & - \frac{1}{2}\sum_i \partial_\mu\tilde{\phi}_i\partial^\mu\tilde{\phi}_i - \tilde{W}(\sigma,\tilde{\boldsymbol{\varphi}}) + \tilde{L}_\mathrm{m}\Big]. \end{aligned} \tag{6.6}$$

Integrating by parts gives

$$\begin{aligned} S = \int \mathrm{d}^4x\sqrt{-\tilde{g}}\Big[& \tilde{F}(\sigma,\tilde{\boldsymbol{\varphi}})\tilde{R} - \tilde{K}(\sigma,\tilde{\boldsymbol{\varphi}})(\tilde{\nabla}\sigma)^2 \\ & + \tilde{\nabla}_\mu\sigma\tilde{\nabla}^\mu\tilde{K}(\sigma,\tilde{\boldsymbol{\varphi}}) - \frac{1}{2}\sum_i \partial_\mu\tilde{\phi}_i\partial^\mu\tilde{\phi}_i - \tilde{W}(\sigma,\tilde{\boldsymbol{\varphi}}) + \tilde{L}_\mathrm{m}\Big]. \end{aligned} \tag{6.7}$$

The Euler-Lagrange equation for the dilaton σ gives

$$\begin{aligned}\tilde{\Box}\tilde{K} - 2(\tilde{K} - \partial_\sigma \tilde{K})\tilde{\Box}\sigma - 2\tilde{\nabla}_\mu(\tilde{K} - \partial_\sigma \tilde{K})\tilde{\nabla}^\mu\sigma = \\ = -\partial_\sigma \tilde{W} - \tilde{R}\partial_\sigma \tilde{F},\end{aligned} \tag{6.8}$$

where $\partial_\sigma := \frac{\partial}{\partial\sigma}$. We can see from the transformation rules (6.5) that if we choose $F(\boldsymbol{\varphi})$ to be quadratic in ϕ_i, the potential $W(\boldsymbol{\varphi})$ to be quartic in ϕ_i, and the L_m to also rescale appropriately[2], then the action becomes *scale-invariant* and $\partial_\sigma \tilde{F} = \partial_\sigma \tilde{W} = 0$. The dilaton is then massless, and appears in the action only via its derivatives.

$$\begin{aligned}S = \int \mathrm{d}^4x\sqrt{-\tilde{g}}\Big[\tilde{F}(\tilde{\boldsymbol{\varphi}})\tilde{R} - \tilde{K}(\tilde{\boldsymbol{\varphi}})(\tilde{\nabla}\sigma)^2 \\ + \tilde{\nabla}_\mu\sigma\tilde{\nabla}^\mu\tilde{K}(\tilde{\boldsymbol{\varphi}}) - \frac{1}{2}\sum_i \partial_\mu\tilde{\phi}_i\partial^\mu\tilde{\phi}_i - \tilde{W}(\tilde{\boldsymbol{\varphi}}) + \tilde{L}_\mathrm{m}\Big].\end{aligned} \tag{6.9}$$

If we then choose Ω such that $\tilde{K} = const.$ we obtain the particular Jordan frame described in [413] and we see that the dilaton completely decouples from the other scalar fields and the other matter terms in $\tilde{L}_\mathrm{m}$. The equation of motion for the dilaton reduces to a simple wave equation $\tilde{\Box}\sigma = 0$ satisfied by a homogeneous solution $\sigma = 0$. As a result there are no fifth forces from the dilaton.[3] Although scale invariance requires that there cannot be a cosmological constant in the action, it can be shown that under the influence of an expanding universe the background values of the ϕ_i tend to constants [383, 413], producing an effective reduced Planck mass $\sqrt{\left\langle 2\tilde{F}\right\rangle}$, and an effective cosmological constant $\left\langle \tilde{W}/(2\tilde{F})\right\rangle$, where $\langle\dots\rangle$ denotes setting the fields to their background value.

6.1.2 The covariant formalism

To convert our *classical* scalar-tensor theory to the language of Quantum Field Theory (QFT) and the path integral formulism we start by defining the partition functional

$$Z[J] = \int [\mathcal{D}^N\Phi] e^{-S[\boldsymbol{\varphi}] - J_a\Phi^a}, \tag{6.10}$$

where $[\mathcal{D}^N\Phi]$ is an appropriate measure over the function space for fields $\boldsymbol{\Phi} = \{\Phi^i\}$, and J_a is a source term. We use $i, j\dots$ indices to denote field species and $a, b\dots$

[2]Here we consider $\tilde{L}_\mathrm{m}$ that are fully independent of σ; the most general scale-invariant theory may include derivative couplings to $\partial_\mu\sigma$ from higher dimension operators [413].

[3]There is still a coupling between gravity and the dilaton via its contribution to the stress energy tensor $T_{\mu\nu}$, and thus sourcing curvature according to standard General Relativity, however this contribution also vanishes for $\sigma = 0$.

to denote DeWitt indices spanning both field species and position or momentum [440].

A frame transformation is a field reparameterisation $\Phi^i \to \tilde{\Phi}^i(\mathbf{\Phi})$. In the covariant formalism we describe this as a transformation of coordinates on a "configuration space" or "field space" manifold [443]. This has an associated line element $\mathrm{d}s^2 = C_{ab}\mathrm{d}\Phi^a\mathrm{d}\Phi^b$ where a, b. We would like our path integral, action and measure to be frame/reparameterisation invariant, which leads us to define

$$[\mathcal{D}^N\Phi] = V_{\text{gauge}}^{-1}\sqrt{\det(C_{ab})}\Pi_a\frac{\mathrm{d}\Phi^a}{\sqrt{2\pi}}, \tag{6.11}$$

where $V_{\text{gauge}} = \int \Pi_a \frac{\mathrm{d}\xi^a}{\sqrt{2\pi}}\sqrt{\det(\sigma_{ab}(\mathbf{\Phi}))}$ accounts for the volume of the gauge group (see [440]), where $\mathrm{d}\xi^a$ are the generators of the Lie algebra and σ_{ab} is another metric. For the moment we assume all the fields are bosonic, however this formalism has also been extended to include fermionic fields [443] as we discuss later. To ensure diffeomorphism invariance of the free action, the preferred field space metric for four dimensions is [442, 443]

$$C_{ab} = \frac{\bar{g}_{\mu\nu}}{4}\frac{\delta^2 S}{\delta(\partial_\mu\Phi^a)\delta(\partial_\mu\Phi^b)} = C_{ij}\bar{\delta}^{(4)}(x_a - x_b), \tag{6.12}$$

where the delta function enforces locality. We assume $\sigma_{ab} = \sigma_{\mu\nu}\bar{\delta}^{(4)}(x_a - x_b)$ is also ultra-local [440]. The $\bar{g}_{\mu\nu}$ is the physical, or preferred, spacetime metric which satisfies dimensionless line element $\mathrm{d}\bar{s}^2 = \bar{g}_{\mu\nu}\mathrm{d}x^\mu\mathrm{d}x^\nu$. Defining $\bar{g}_{\mu\nu}$ is important to overcome the ambiguity between the physical space time metric and the gravity quantum field $g_{\mu\nu}$ [440, 442, 443]. The two are related by

$$\bar{g}_{\mu\nu} = l^{-2}(\mathbf{\Phi})g_{\mu\nu}, \tag{6.13}$$

$$= e^{-2\sigma_{\text{phys}}}g_{\mu\nu}, \tag{6.14}$$

$$= e^{2(\sigma-\sigma_{\text{phys}})}\tilde{g}_{\mu\nu}, \tag{6.15}$$

where $l(\mathbf{\Phi})$ is an effective Planck length [443], and the functional derivatives are defined using the barred metric, and $\bar{\delta}^{(4)}(x)$ is defined such that $\int \mathrm{d}^4x\sqrt{\bar{g}}\bar{\delta}^{(4)}(x) = 1$. For an action with kinetic term

$$S = \int \mathrm{d}^4x \left[-N_{ij}\tilde{g}^{\mu\nu}\partial_\mu\Phi^i\partial_\nu\Phi^j + \dots\right], \tag{6.16}$$

(summation implied) the associated field space metric is

$$C_{ij} = e^{2(\sigma-\sigma_{\text{phys}})}N_{ij}. \tag{6.17}$$

In theories without gravity we can take $\sigma_{\rm phys} = \sigma$ and canonically normalise the kinetic term so that $N_{ij} = const.$, allowing us to neglect the field space metric entirely as it only contributes a overall constant to the path integral. However, in theories with gravity the choice of $\sigma_{\rm phys}$ is important, and C_{ij} can have non-trivial dependence on the fields Φ^i. In order to obtain perturbative scattering amplitudes we expand about a flat Minkowski background $g_{\mu\nu} \approx \eta_{\mu\nu} + h_{\mu\nu}$. With a trivial field space metric we can use the background field approach to obtain Feynman rules with vertex coefficients and propagators given by

$$\lambda_{ab\ldots c} = \mathrm{i} \left\langle \partial_{(a}\partial_b \ldots \partial_{c)} S \right\rangle , \tag{6.18}$$

$$\Delta^{ab} = \mathrm{i} \left\langle \partial_a \partial_b S \right\rangle^{-1} , \tag{6.19}$$

where $a, b\ldots$ are once again DeWitt indices in either position or momentum space, the factors of i come from the Wick rotation and $\langle \ldots \rangle$ denotes $(\ldots)|_{\mathbf{\Phi}=\mathbf{\Phi}_0}$ setting the fields to their background or equilibrium values $\mathbf{\Phi}_0$. The $(a, b\ldots c)$ denotes symmeterisation over the indices. To incorporate the field space determinant we can take either of two approaches. The first is to work out the contribution of the field space metric to the effective Lagrangian via

$$\sqrt{\det(C_{ab})} = \exp\left\{ \frac{1}{2} \mathrm{Tr}\left(\ln\left(C_{ab} \right) \right) \right\} , \tag{6.20}$$

$$= \exp\left\{ \frac{1}{2} \bar{\delta}^{(4)}(0) \int \mathrm{d}^4 x \sqrt{\bar{g}}\ \mathrm{Tr}\left(\ln\left(C_{ij}(x) \right) \right) \right\} , \tag{6.21}$$

then expand in powers of the coupling constants [441], with suitable regularisation for the delta function divergence [450]. Alternatively one can modify the Feynman rules by promoting partial derivatives to covarient field space derivatives [442, 443]

$$\lambda_{ab\ldots c} \to \mathrm{i} \left\langle \nabla_{(a}\nabla_b \ldots \nabla_{c)} S \right\rangle , \tag{6.22}$$

$$\Delta^{ab} \to \mathrm{i} \left\langle \nabla_a \nabla_b S \right\rangle^{-1} . \tag{6.23}$$

As S is a field space scalar, the n-vertex $\lambda_{ab\ldots c}$ is a $\binom{0}{n}$ rank field space tensor, and the propagator Δ^{ab} is $\binom{2}{0}$ tensor. For Feynman diagrams with external legs we also need to define the external factor

$$X^a = \left\langle \frac{\partial \Phi^a}{\partial \chi} \right\rangle , \tag{6.24}$$

where χ is the physical external field connected to that leg, a field space scalar. This makes X^a a field space vector. The contribution to a matrix element for

a particular diagram shape will involve putting combinations of these together, and summing over the field indices. As these are all tensors the resulting object will be a field space scalar, and hence frame invariant. In subsequent sections we will demonstrate how this works for computations of fifth forces, and extend the no-fifth-force result for the scale-invariant theory to all frames.

6.2 Selecting a frame: a geometric approach

We can make an observation from section 6.1.1: choosing a frame for a theory with N fields $\{\phi_i, g_{\mu\nu}\}$ is equivalent to taking the $N+1$ field action then imposing a constraint $q(\tilde{\boldsymbol{\varphi}}) = q(\sigma, \tilde{\phi}_i) = 0$ on the dilaton and rescaled fields. In terms of the covariant formalism, this means we can consider the field space of the theory in a particular frame as a N dimensional *submanifold* of the appropriate generic $N+1$ dimensional manifold, the field space of a more general theory.[4]

Adapting the technique usually applied for gauge fixing, in terms of the path integral we can impose this constraint using delta functions

$$\begin{aligned} Z[0] &= \int \mathcal{D}^N\Phi \sqrt{\det(C_{ab})} e^{-S[\boldsymbol{\varphi}]}, \\ &= \int \mathcal{D}^{N+1}\tilde{\Phi} \sqrt{\det(G_{ab})} \prod_x \left[|\partial_i q(\tilde{\boldsymbol{\varphi}})|_x \delta(q(\tilde{\boldsymbol{\varphi}}(x)))\right] e^{-S[\tilde{\boldsymbol{\varphi}}]}, \end{aligned} \tag{6.25}$$

where $G_{ab} = G_{ij}\bar{\delta}^{(4)}(x_i - x_j)$ is the metric on the $N+1$ field space, $|\partial_i q(\tilde{\boldsymbol{\varphi}})|_x$ denotes the magnitude of the field space gradient of q at spacetime location x, we count the dilaton σ as an additional $\tilde{\Phi}$ field and we omit the V_{gauge} factor for clarity. We may express

$$G_{ij}\mathrm{d}\tilde{\Phi}^i\mathrm{d}\tilde{\Phi}^j = \alpha^2\mathrm{d}q^2 + 2\beta_i\mathrm{d}q\mathrm{d}\Phi^i + C_{ij}\mathrm{d}\Phi^i\mathrm{d}\Phi^j. \tag{6.26}$$

where $\alpha = |\partial_i q|^{-1}$. For $\beta_i = 0$ (we are free to choose this), we have

$$G_{ij}\mathrm{d}\tilde{\Phi}^i\mathrm{d}\tilde{\Phi}^j = \left[\alpha^2\partial_{\tilde{\Phi}^i}q\partial_{\tilde{\Phi}^j}q + \tilde{C}_{ij}\right]\mathrm{d}\tilde{\Phi}^i\mathrm{d}\tilde{\Phi}^j. \tag{6.27}$$

where $\tilde{C}_{ij} = C_{kl}\frac{\partial\Phi^k}{\partial\tilde{\Phi}^i}\frac{\partial\Phi^l}{\partial\tilde{\Phi}^j}$. Then $\det(G_{ab}) = \det(\tilde{C}_{ab})\prod_x[\alpha(x)^2]$, so

$$Z[0] = \int \mathcal{D}^{N+1}\tilde{\Phi}\sqrt{\det(\tilde{C}_{ab})}\prod_x\left[\delta(q(\tilde{\boldsymbol{\varphi}}(x)))\right]e^{-S[\tilde{\boldsymbol{\varphi}}]}. \tag{6.28}$$

[4]Strictly speaking the field space manifolds are infinite dimensional, as they have N or $N+1$ degrees of freedom at each spatial point. However, for clarity we shall just refer to them as "N" or "$N+1$ dimensional", counting the number of field species.

We may note that $\tilde{C}_{ab}$ is then the metric one would derive from simply considering the Lagrangian expressed in terms of the $N+1$ $\tilde{\Phi}^i$ fields. We can express the delta functions via the limit

$$Z[0] = \lim_{\xi\to 0}\int \mathcal{D}^{N+1}\tilde{\Phi}\sqrt{\det(\tilde{C}_{ab})}\prod_x\left[\frac{1}{\sqrt{2\pi\xi}}e^{-\frac{1}{2\xi}q(\tilde{\boldsymbol{\varphi}}(x))^2}\right]e^{-S[\tilde{\boldsymbol{\varphi}}]}, \tag{6.29}$$

$$= \lim_{\xi\to 0}\left[\left(\frac{1}{\sqrt{2\pi\xi}}\right)^{\mathcal{V}}\int \mathcal{D}^{N+1}\tilde{\Phi}\sqrt{\det(\tilde{C}_{ab})}\exp\left\{-\int \mathrm{d}^4x\sqrt{-\tilde{g}}\left(\tilde{L}-\frac{1}{2\xi}q^2\right)\right\}\right], \tag{6.30}$$

where $\mathcal{V}$ is an (infinite) measure of the spacetime volume. We then have propagator

$$\begin{aligned}\Delta^{ab} &= \mathrm{i}\left\langle\nabla_a\nabla_b S\right\rangle^{-1},\\ &= \mathrm{i}\lim_{\xi\to 0}\left[\left\langle\tilde{\nabla}_a\tilde{\nabla}_b\int \mathrm{d}^4x\sqrt{-\tilde{g}}\left(\tilde{L}-\frac{1}{2\xi}q^2\right)\right\rangle\right]^{-1}.\end{aligned} \tag{6.31}$$

The DeWitt indices are somewhat unwieldy, as they span an infinite number of dimensions. As our theory is local, if DeWitt index a corresponds to position x and field species i, then the derivative of the action with respect to a corresponds to a derivative of the Lagrangian at x with respect to field i, $\tilde{\nabla}_a S = \tilde{\nabla}_i\mathcal{L}|_x$ where $\tilde{\nabla}_i$ is the covariant field derivative for metric $\tilde{C}_{ij}$, allowing us to convert between the two. Assuming a flat background spacetime this gives the finite dimensional propagator

$$\Delta^{ij} = \lim_{\xi\to 0}\left[\tilde{\Delta}^{-1}_{ij}-\frac{1}{\mathrm{i}\xi}q_iq_j\right]^{-1}, \tag{6.32}$$

where $\tilde{\Delta}^{ij}$ is the unconstrained propagator in the $N+1$ field space and $q_i := \langle\partial_i q\rangle$ the normal covector to the submanifold at $\tilde{\boldsymbol{\Phi}} = \tilde{\boldsymbol{\Phi}}_0$. Now consider rotating rotating coordinates in field space such that the direction q_i lies along one axis, call it axis n. Then

$$\Delta^{-1}_{ij} = \tilde{\Delta}^{-1}_{ij} - |q|^2\frac{\dot{\mathrm{i}}}{\xi}\delta_{in}\delta_{jn}, \tag{6.33}$$

$$= \begin{bmatrix}\tilde{\Delta}^{-1}_{pq} & \tilde{\Delta}^{-1}_{pn}\\ \tilde{\Delta}^{-1}_{np} & \tilde{\Delta}^{-1}_{nn}+|q|^2\mathrm{i}\xi^{-1},\end{bmatrix}. \tag{6.34}$$

where p, q range across all indices other than n and $|q|$ is the magnitude of q_i. Let $\zeta^{-1} = \tilde{\Delta}^{-1}_{nn} + |q|^2\mathrm{i}\xi^{-1}$ (with no summation implied by repeated n). Then

$$\Delta^{ij} = \begin{bmatrix}(\tilde{\Delta}^{-1}_{pq}-\zeta\tilde{\Delta}^{-1}_{nq}\tilde{\Delta}^{-1}_{pn})^{-1} & -\zeta(\tilde{\Delta}^{-1}_{pq}-\zeta\tilde{\Delta}^{-1}_{nq}\tilde{\Delta}^{-1}_{pn})^{-1}\tilde{\Delta}^{-1}_{pn}\\ -\zeta\tilde{\Delta}^{-1}_{nq}(\tilde{\Delta}^{-1}_{pq}-\zeta\tilde{\Delta}^{-1}_{nq}\tilde{\Delta}^{-1}_{pn})^{-1} & \zeta+\zeta^2\tilde{\Delta}^{-1}_{nq}(\tilde{\Delta}^{-1}_{pq}-\zeta\tilde{\Delta}^{-1}_{nq}\tilde{\Delta}^{-1}_{pn})^{-1}\tilde{\Delta}^{-1}_{pn}\end{bmatrix}^{ij}. \tag{6.35}$$

To lowest order in ζ this is

$$\Delta^{ij} = \begin{bmatrix} (\tilde{\Delta}^{-1}_{pq})^{-1} & -\zeta(\tilde{\Delta}^{-1}_{pq})^{-1}\tilde{\Delta}^{-1}_{pn} \\ -\zeta\tilde{\Delta}^{-1}_{nq}(\tilde{\Delta}^{-1}_{pq})^{-1} & \zeta \end{bmatrix}^{ij}. \tag{6.36}$$

where summation is implied over repeated indices p, q. We can then see that taking $\xi \to 0$ and therefore $\zeta \to 0$ gives

$$\Delta^{ij} = \begin{bmatrix} (\tilde{\Delta}^{-1}_{pq})^{-1} & 0 \\ 0 & 0 \end{bmatrix}^{ij}. \tag{6.37}$$

This means that taking the limit $\xi \to 0$ effectively zeros out the contribution from variations in the fields in the direction of q_i, which makes sense as we can interpret this as taking the mass of field $q_i\tilde{\phi}_i$ to infinity. We can write this as

$$\Delta^{-1}_{ij} = \left(\delta^k_i - n^k n_i\right)\left(\delta^l_j - n^l n_j\right)\tilde{\Delta}^{-1}_{kl} = P^k_i P^l_j \tilde{\Delta}^{-1}_{kl}, \tag{6.38}$$

where P^k_i is the projection operator onto the submanifold. This means that we have

$$\Delta^{-1}_{ab} = -\mathrm{i}P^c_a P^d_b \langle \tilde{\nabla}_c \tilde{\nabla}_d S\rangle = -\mathrm{i}\langle \nabla_a \nabla_b S\rangle, \tag{6.39}$$

where $P^b_a = P^j_i \bar{\delta}^{(4)}(x_a - x_b)$ is the DeWitt-indexed projection operator, $\tilde{\nabla}_a$ is the covarient derivative on the $N+1$ field manifold, and ∇_a the covarient derivative on the N field manifold, confirming that this new geometric approach is consistent with the covariant formalism.

6.3 Computing fifth forces with the geometric approach

Let us now see how this geometric approach affects the computation of fifth forces. Our generic Lagrangian is of the form

$$\mathcal{L} = \sqrt{-g}\left[F(\boldsymbol{\varphi})R - \frac{1}{2}\partial_\mu\phi_i\partial^\mu\phi_i - W(\boldsymbol{\varphi}) + L_{\mathrm{m}} + L_{\mathrm{gauge}}\right]. \tag{6.40}$$

with some integer number of scalar fields. We include a gauge fixing term of the form $\sqrt{-g}L_{\mathrm{gauge}} = \frac{1}{2}\sigma_{\mu\nu}\Xi^\mu\Xi^\nu$, which we choose to be the scalar-tensor gauge term used by Copeland et al. [415]

$$L_{\mathrm{gauge}} = \frac{1}{2}F(\boldsymbol{\varphi})g_{\mu\nu}\left[\Gamma^\mu - \nabla^\mu \ln F\right]\left[\Gamma^\nu - \nabla^\nu \ln F\right], \tag{6.41}$$

where $\Gamma^\mu = g^{\nu\rho}\Gamma^\mu_{\nu\rho}$ is the contraction of the spactime connection, $\sigma_{\mu\nu} = F(\boldsymbol{\varphi})g_{\mu\nu}$ and $\Xi^\mu = \Gamma^\mu - \nabla^\mu \ln F$. In place of V^{-1}_{gauge} we have the appropriate Fadeev-Popov determinant $V_{FP} = \det\left(\delta\Xi^\mu/\delta\xi^\nu\right) := \det\left(Q^\mu_\nu\right)$ where ξ^μ are the degrees of gauge freedom [440, 443]. This will in turn contribute a ghost term $\mathcal{L}_{gh} = -\bar{c}_\mu Q^\mu_\nu c^\nu$ [440], but as this only contributes at loop order we shall neglect it here. For the matter terms we include a single fermion field ψ, standing in for (eg.) the standard model electron,

$$L_{\text{m}} = -\bar{\psi}\left[\text{i}\overleftrightarrow{\not{\nabla}} + y(\boldsymbol{\varphi})\right]\psi, \tag{6.42}$$

where the Higgs-like term $\bar{\psi}y(\boldsymbol{\varphi})\psi$ gives the fermion a mass with $y(\boldsymbol{\varphi}) = y_i\phi_i$ (with implied summation). The operator $\overleftrightarrow{\not{\nabla}}$ is defined as $\overleftrightarrow{\not{\nabla}} = \frac{1}{2}\left(\overrightarrow{\not{\nabla}} - \overleftarrow{\not{\nabla}}\right)$ where $\not{\nabla} = E^{a\mu}\gamma_a\partial_\mu$ is the covariant Dirac operator with $E^{a\mu}$ the vierbein such that $g^{\mu\nu} = E^{\mu a}E^{\nu b}\eta_{ab}$ [413]. As we now have fermions in our theory, to account for the fermion anticommuntation we need to promote the field space to a *super*manifold [448, 451], the field space metric to a *super*matrix, and replace the $\det(C_{ab})$ in the path integral with $\text{sdet}(C_{ab})$, a *super*determinant. We also redefine $\lambda_{ab\ldots c} = i\left\langle\nabla_{\{a}\nabla_b\ldots\nabla_{c\}}S\right\rangle$, where $\{a, b, \ldots c\}$ denotes *super*symmeterisation, where we add a factor of -1 every time we swap fermion indices. Apart from the need to keep track of minus signs from fermion permutations this does not change the results from the previous sections (more details of the supermanifold construction can be found in [443]).

Let the total number of field species, including the scalar fields, fermions and graviton, be N. Linearising around a background Minkowski metric gives

$$\begin{aligned}\mathcal{L} = &-\frac{F}{2}\frac{1}{2}P^{\alpha\beta,\tau\rho}\partial_\mu h_{\alpha\beta}\partial^\nu h_{\tau\rho} + \frac{1}{2}(\partial_i F)\eta^{\alpha\beta}\partial_\mu\phi_i\partial^\mu h_{\alpha\beta}\\ &-\frac{1}{2}\left(\delta_{ij} - \frac{\partial_i F\partial_j F}{F}\right)\partial_\mu\phi_i\partial^\mu\phi_j\\ &- W(\boldsymbol{\varphi}) - \bar{\psi}\left[\text{i}\overleftrightarrow{\not{\partial}} + y(\boldsymbol{\varphi})\right]\psi\\ &+\frac{1}{2}h_{\alpha\beta}P^{\alpha\beta,\tau\rho}i\bar{\psi}\gamma_\tau\overleftrightarrow{\partial}_\rho\psi + \frac{1}{2}h\bar{\psi}y(\phi)\psi + \ldots\end{aligned} \tag{6.43}$$

where $P^{\alpha\beta,\tau\rho} := \frac{1}{2}\left[\eta^{\alpha\tau}\eta^{\beta\rho} + \eta^{\alpha\rho}\eta^{\beta\tau} - \eta^{\alpha\beta}\eta^{\tau\rho}\right]$, $h := h^\mu_\mu$, here i, j index scalar field species and ∂_i derivatives with respect to the scalar fields, and $\mu, \nu, \alpha, \beta, \tau, \rho$ are

all spacetime indices. Introducing the general Weyl transformation we obtain[5]

$$\begin{aligned}\tilde{\mathcal{L}} =& -\frac{\tilde{F}}{2}\frac{1}{2}P^{\alpha\beta,\tau\rho}\partial_\mu\tilde{h}_{\alpha\beta}\partial^\mu\tilde{h}_{\tau\rho} + \frac{1}{2}(\partial_i\tilde{F})\eta^{\alpha\beta}\partial_\mu\tilde{\phi}_i\partial^\mu\tilde{h}_{\alpha\beta} \\ &+ \frac{1}{2}(\partial_\sigma\tilde{F})\eta^{\alpha\beta}\partial_\mu\sigma\partial^\mu\tilde{h}_{\alpha\beta} - \frac{1}{2}\left(\delta_{ij} - \frac{\partial_i\tilde{F}\partial_j\tilde{F}}{\tilde{F}}\right)\partial_\mu\tilde{\phi}_i\partial^\mu\tilde{\phi}_j \\ &- \tilde{W}(\tilde{\boldsymbol{\varphi}},\sigma) + \partial_\mu\sigma\left(\partial_i\tilde{K} - \frac{\partial_\sigma\tilde{F}\partial_i\tilde{F}}{2\tilde{F}}\right)\partial^\mu\tilde{\phi}_i \\ &- \left(\tilde{K} - \partial_\sigma\tilde{K} + \frac{(\partial_\sigma\tilde{F})^2}{2\tilde{F}}\right)\partial_\mu\sigma\partial^\mu\sigma \\ &- \bar{\psi}'\left[\mathrm{i}\overleftrightarrow{\not{\partial}} - y_i\tilde{\phi}_i\right]\psi' + \frac{1}{2}\tilde{h}_{\alpha\beta}P^{\alpha\beta,\tau\rho}i\bar{\psi}'\gamma_\tau\overleftrightarrow{\partial}_\rho\psi' \\ &+ \frac{1}{2}\tilde{h}\bar{\psi}'y(\tilde{\phi})\psi' + \dots\end{aligned} \tag{6.44}$$

with an additional field and degree of freedom, and where the fermion field is rescaled as $\psi' = e^{3\sigma/2}\psi$. By adding σ we now have $N+1$ field species in the Lagrangian. The equilibrium or background field values define a point in the field space. Expanding around these expected field values, and this point, we have

$$\begin{aligned}\tilde{\mathcal{L}} =& -\frac{M_{\rm Pl}^2}{4}\frac{1}{2}P^{\alpha\beta,\tau\rho}\partial_\mu\tilde{h}_{\alpha\beta}\partial^\mu\tilde{h}_{\tau\rho} + \frac{1}{2}(\partial_i\tilde{F})\partial_\mu\tilde{\Phi}^i\partial^\mu\tilde{h}_{\alpha\beta} \\ &- \frac{1}{2}N_{ij}\partial^\mu\tilde{\Phi}^i\partial_\mu\tilde{\Phi}^j - \frac{1}{2}M_{ij}\tilde{\Phi}^i\tilde{\Phi}^j \\ &- \bar{\psi}'\left[\mathrm{i}\overleftrightarrow{\not{\partial}} - m_\Psi - y_i\tilde{\Phi}^i\right]\psi' + \frac{1}{2}\tilde{h}_{\alpha\beta}P^{\alpha\beta,\tau\rho}i\bar{\psi}'\gamma_\tau\overleftrightarrow{\partial}_\rho\psi' \\ &+ \frac{1}{2}\tilde{h}\bar{\psi}'m_\psi\psi' + \dots,\end{aligned} \tag{6.45}$$

where we use $\tilde{\Phi}^i$ to denote deviations from the background values in all the scalar fields, including the dilaton σ and $\tilde{\phi}_i$. The mass term $M_{ij} = \partial_i\partial_j\tilde{W}$. We may further simplify this by including the graviton field(s) in $\{\tilde{\Phi}^i\}$ as well, giving

$$\begin{aligned}\tilde{\mathcal{L}} =& -\frac{1}{2}N_{ij}\partial^\mu\tilde{\Phi}^i\partial_\mu\tilde{\Phi}^j - \frac{1}{2}M_{ij}\tilde{\Phi}^i\tilde{\Phi}^j \\ &- \bar{\psi}'\left[\mathrm{i}\overleftrightarrow{\not{\partial}} - m_\Psi - \tilde{\phi}_i y_i\right]\psi' + \dots,\end{aligned} \tag{6.46}$$

where

$$y_{h_{\alpha\beta}} = \frac{1}{2}\left[\mathrm{i}P^{\alpha\beta,\tau\rho}\gamma_\tau\overleftrightarrow{\partial}_\rho + \eta^{\alpha\beta}m_\psi\right]. \tag{6.47}$$

[5]The ghost terms also rescale such that $\sigma_{\mu\nu} \to \tilde{\sigma}_{\mu\nu} = \tilde{F}(\tilde{\boldsymbol{\varphi}})\tilde{g}_{\mu\nu}$ and $\Xi^\mu \to \tilde{\Xi}^\mu = \tilde{\Gamma}^\mu - \tilde{\nabla}^\mu \ln\tilde{F}$ where $\tilde{\Gamma}^\mu$ and $\tilde{\nabla}^\mu$ are constructed using $\tilde{g}_{\mu\nu}$.

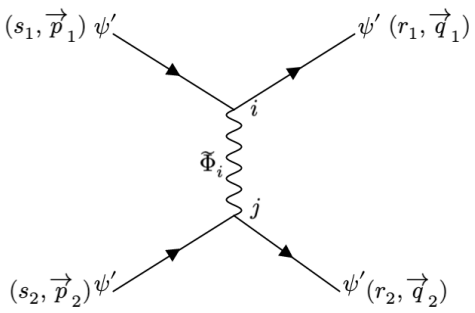

Figure 6.1: ***t*-channel tree diagram for fermion-fermion scattering.**

and we take the $\overleftrightarrow{\partial}_\rho$ operator as only acting on the fermion fields. The lowest order contribution to fermion-fermion scattering is from tree diagrams of the form of Fig. 6.1. This contributes a matrix element of the form

$$\begin{aligned} \mathrm{i}\mathcal{M} =& X^c(\bar{\psi}, \vec{p}_1, s_1)\lambda_{cda}X^d(\psi, \vec{q}_1, r_1)\Delta^{ab}\dots \\ &\dots X^e(\bar{\psi}, \vec{p}_2, s_2)\lambda_{efb}X^f(\psi, \vec{q}_2, r_2), \end{aligned} \tag{6.48}$$

where here a, b, c, d, e, f are all DeWitt indices. If $\langle\sigma\rangle = 0$, then

$$X^a(\bar{\psi}, \vec{p}_1, s_1) = \delta^a_{\bar{\psi}'(\vec{p}_1, s_1)}\bar{u}(\vec{p}_1, s_1), \tag{6.49}$$

and

$$\begin{aligned} &X^c(\bar{\psi}, \vec{p}_1, s_1)\lambda_{cda}X^d(\psi, \vec{q}_1, r_1) = \dots \\ &\dots \mathrm{i}\bar{u}(\vec{p}_1, s_1)\left\langle\partial_{\{\bar{\psi}(\vec{p}_1, s_1)}\partial_{\psi(\vec{q}_1, r_1)\}}\nabla_a S\right\rangle u(\vec{q}_1, r_1), \\ &= \mathrm{i}\bar{u}(\vec{p}_1, s_1)\left\langle\partial_{\{\bar{\psi}(\vec{p}_1, s_1)}\partial_{\psi(\vec{q}_1, r_1)\}}\partial_a S\right\rangle u(\vec{q}_1, r_1) := \lambda_a. \end{aligned} \tag{6.50}$$

Note that this is a field space co-vector. The matrix element is then

$$\mathrm{i}\mathcal{M} = \lambda_a\Delta^{ab}\lambda_b \tag{6.51}$$

The contribution to the effective potential from this matrix element is given by

$$V_{\text{eff}}(r) = -\frac{1}{4\pi r}\frac{1}{2m_\psi^2}\sum_j \mathrm{res}_{k=k_j}\left(ke^{\mathrm{i}kr}\mathcal{M}(\boldsymbol{k})\right), \tag{6.52}$$

where $\vec{k} = \vec{p}_1 - \vec{q}_1$ is the exchange momentum between the fermions, and k_j are the poles of the enclosed expression in the upper complex half plane. V_{eff} includes both the standard gravitational potential (from graviton exchange) and any fifth force terms.

To evaluate this in a particular frame we need to impose a constraint to go from the $N+1$ fields to the physical N fields. The standard approach is to do this at Lagrangian level. In the Einstein frame $\tilde{F} = const.$, so if we impose this the explicit coupling between the graviton and the scalar fields dissapears, however there can be a kinetic coupling between the scalar $\tilde{\phi}_i$ fields and the dilaton due to the $(\partial_i \tilde{K})\partial_\mu \tilde{\phi}_i \partial^\mu \sigma$ term. Conversely, if we choose the special Jordan frame where $\tilde{K} = const.$ then we have a non-trivial kinetic coupling between the graviton and the scalar fields due to $\frac{1}{2}(\partial_i \tilde{F})\eta^{\alpha\beta}\partial_\mu \tilde{\phi}_i \partial^\mu \tilde{h}_{\alpha\beta} + \frac{1}{2}(\partial_\sigma \tilde{F})\eta^{\alpha\beta}\partial_\mu \sigma \partial^\mu \tilde{h}_{\alpha\beta}$, but remove the kinetic dilaton-$\tilde{\phi}_i$ couplings. Hence we can think of the frame transformation as a simple exchange between different bosonic degrees of freedom.

The disadvantage of this approach is that it requires you to redo the entire calculation for each choice of frame, even at tree level, as you need to work out the correct dynamical fields, potential, couplings, and propagator. In the geometric approach from section 6.2 we start by calculating everything in the general $N+1$ space. Let $\tilde{\lambda}_i$ denote the couplings to the external fermion legs in this space for field species i, then explicitly we have

$$\tilde{\lambda}_{\tilde{\phi}_i} = \mathrm{i} y_i \bar{u}(\vec{p}, s) u(\vec{q}, r), \tag{6.53}$$

$$\tilde{\lambda}_\sigma = 0, \tag{6.54}$$

$$\tilde{\lambda}_{\tilde{h}_{\alpha\beta}} = \frac{\mathrm{i}}{4} \bar{u}(\vec{p}, s) \left[-P^{\alpha\beta,\tau\rho} \gamma_\tau (p+q)_\rho + 2 m_\psi \eta^{\alpha\beta} \right] u(\vec{q}, r). \tag{6.55}$$

The boson propagator with DeWitt indices is given by

$$\begin{aligned} \tilde{\Delta}^{ab} &= \mathrm{i} \left\langle \tilde{\nabla}_a \tilde{\nabla}_b S \right\rangle^{-1} = \mathrm{i} \left[\langle \partial_a \partial_b S \rangle + \langle \Gamma^c_{ab} \rangle \langle \partial_c S \rangle \right]^{-1}, \\ &= \mathrm{i} \langle \partial_a \partial_b S \rangle^{-1}, \end{aligned} \tag{6.56}$$

as the equilibrium field values satisfy $\partial_a S = 0$, which gives field index propagator

$$\tilde{\Delta}^{ij} = \mathrm{i} \left[-N_{ij}(p-q)^2 - M_{ij} \right]^{-1} = \mathrm{i} \left[N_{ij} t - M_{ij} \right]^{-1}. \tag{6.57}$$

The Mandelstam variable $t = -(q_1 - p_1)^2$. Then to obtain the matrix element in the frame defined by constraint $q(\tilde{\mathbf{\Phi}}) = 0$ we project the tensors onto the submanifold, giving

$$\begin{aligned} \mathrm{i}\mathcal{M} &= (\tilde{\lambda}_j P^j_i) \lim_{\xi \to 0} \left[\tilde{\Delta}^{-1}_{ij} + \frac{i}{\xi} q_i q_j \right]^{-1} (P^k_j \tilde{\lambda}_k), \\ &= (\tilde{\lambda}_j P^j_i) \left[P^l_i \tilde{\Delta}^{-1}_{lm} P^m_j \right]^{-1} (P^k_j \tilde{\lambda}_k), \\ &= (\tilde{\lambda}_j P^j_i) \left[P^l_i (N_{lm} t - M_{lm}) P^m_j \right]^{-1} (P^k_j \tilde{\lambda}_k). \end{aligned} \tag{6.58}$$

All that is needed to evaluate this in different frames is to change the choice of normal vector q_i. It may not seem immediately apparent that taking projections of $N+1$ space tensors on different submanifolds should necessarily produce the desired invariant result. However, the important point is that only the N field space is really "physical". The $N+1$ field space is constructed in such a way as to ensure that each submanifold is really just a representation of the N dimensional field space in a different frame, i.e. different field "coordinates". Hence provided that the underlying objects are tensors, which they are, frame invariance is guaranteed. Also note that at tree level there are no effects from a non-trivial field space metric $\tilde{C}_{ab}$. These effects can only manifest at 1-loop order or higher.[6]

6.4 Scale-invariant theory

We can see how this works in the particular case of a scale-invariant theory. To make it scale-invariant we make $F(\boldsymbol{\varphi})$ quadratic in ϕ_i and $W(\boldsymbol{\varphi})$ quartic in ϕ_i, such that

$$\tilde{F}(\boldsymbol{\varphi}) := -\frac{1}{12}\sum_i \alpha_i \tilde{\phi}_i^2, \tag{6.59}$$

$$\tilde{K}(\boldsymbol{\varphi}) = \frac{1}{2}\sum_i (1-\alpha_i)\tilde{\phi}_i^2, \tag{6.60}$$

$$\tilde{W}(\boldsymbol{\varphi}) := \sum_{ij} W_{ij}\tilde{\phi}_i^2\tilde{\phi}_j^2. \tag{6.61}$$

For non-trivial values of α_i the Einstein frame, $\tilde{F} = const.$, and the particularly interesting Jordan frame, $\tilde{K} = const.$, describe surfaces, typically ellipsoids, in the $N+1$ dimensional field space. The associated constraints are $q = \tilde{F} - M_{\rm Pl}^2/2$ and $q = \tilde{K} - K_0$ for the Einstein and special Jordan frame respectively. We can also recover the starting action with the constraint $q = \sigma$, which fixes the dilaton to be zero. For an especially simple example consider a theory with two scalar fields, ϕ_1, ϕ_2 and $\alpha_1 = -1, \alpha_2 = 0, y_1 = 0, y_2 = 1/\sqrt{6}$. In the generalised theory we have three scalar fields plus the graviton $\tilde{\phi}_i = \{\sigma, \tilde{\phi}_1, \tilde{\phi}_2, \tilde{h}_{\mu\nu}\}$ and

$$\langle \partial_i \tilde{F} \rangle \propto (0,\ 1,\ 0,\ 0), \tag{6.62}$$

$$\langle \partial_i \tilde{K} \rangle \propto (0,\ 2\langle\tilde{\phi}_1\rangle,\ \langle\tilde{\phi}_2\rangle,\ 0), \tag{6.63}$$

$$\langle \partial_i \sigma \rangle = (1,\ 0,\ 0,\ 0), \tag{6.64}$$

[6] Something that should be expected as we know the classical theory must be frame invariant.

as normal vectors to the submanifold for each of the three cases. The fermion mass is $m_\psi = \langle\tilde{\phi}_2\rangle/\sqrt{6}$ and effective reduced Planck mass $M_{\rm Pl} = \langle\tilde{\phi}_1\rangle/\sqrt{6}$, which can be used to fix the equilibrium field values $\langle\tilde{\phi}_i\rangle$ in terms of the masses. The requirement that $\langle\partial_i\tilde{W}\rangle = 0$ in turn fixes W_{ij} and the mass matrix M_{ij} up to an overall constant.[7] Thinking about this theory in terms of the geometric picture outlined in section 6.2, we can immediately see that there is no simple dichotomy between the Einstein frame and the Jordan frame. Instead there is a continuum of frames, characterised by different choices of constraint q and normal vectors q_i. Indeed, if we choose a normal vector $q_i = (\sin\theta,\ \cos\theta,\ 0,\ 0)$ as we rotate in generalised field space from $\theta = 0$ to $\theta = 1$ we can smoothly transform from a completely-Einstein frame to a completely-Jordan frame, encompassing everything in between. Provided one adopts the fully covariant formalism described above, one can be confident of obtaining the same physical results, including the lack of fifth forces, for all frames.

6.5 The field space metric and higher-order corrections

At one-loop order and higher we need to consider the effect of the non-trivial field space metric. One can use the quantum effective action formalism to include quantum corrections non-perturbatively, and much work has gone into developing a frame and/or gauge invariant effective action following the model of DeWitt and Vilkovisky [447, 449, 452–459]. Here however we will examine how corrections from the non-trivial metric arise perturbatively purely from the level of the Feynman rules and the geometric approach. As described above, because our theory now includes fermions we need to extend the formalism in section 6.1.2 following the method in Finn et al. [443], promoting the metric to a supermatrix on a supermanifold. To obtain this metric for our theory we first express the Lagrangian (6.44) as

$$\mathcal{L} = -\tfrac{1}{2}N_{AB}(\tilde{\Phi})\eta^{\mu\nu}\partial_\mu\tilde{\Phi}^A\partial_\nu\tilde{\Phi}^B - \tilde{H}(\tilde{\Phi})^{\mu\nu}i\bar{\psi}'\gamma_\mu\overleftrightarrow{\partial}_\nu\psi' + \dots, \tag{6.65}$$

where $\tilde{\Phi}^A$ includes all the bosonic fields, this time we have not expanded N_{AB} around the background field values, and $\tilde{H}^{\mu\nu} = (\eta^{\mu\nu} - \frac{1}{2}\tilde{h}_{\alpha\beta}P^{\alpha\beta,\mu\nu} + \dots)$ to first

[7] $M_{ij} = g\begin{bmatrix} m_\psi^2 & m_\psi M_{\rm Pl} \\ m_\psi M_{\rm Pl} & M_{\rm Pl}^2 \end{bmatrix}$ for i,j covering $\{\tilde{\phi}_1, \tilde{\phi}_2\}$, for some dimensionless constant g.

order in fields. Let $\tilde{H} := \frac{1}{4}\tilde{H}^{\mu}_{\mu} = \left(1 + \frac{1}{8}\tilde{h} + \dots\right)$ then we find

$$\tilde{C}_{ij} = -\begin{bmatrix} N_{AB} - \frac{\partial_A \tilde{H}\partial_B \tilde{H}}{2\tilde{H}}\bar{\psi}'\psi' & -\frac{1}{2}\partial_B \tilde{H}\bar{\psi}' & \frac{1}{2}\partial_B \tilde{H}\psi' \\ \frac{1}{2}\partial_A \tilde{H}\bar{\psi}' & 0 & \tilde{H} \\ -\frac{1}{2}\partial_A \tilde{H}\psi' & -\tilde{H} & 0 \end{bmatrix}, \tag{6.66}$$

for fields $\{\tilde{\Phi}^A, \psi', \bar{\psi}'\}$ and where we have suppressed the fermion spinor indices throughout. The inverse metric is given by

$$\tilde{C}^{ij} = -\begin{bmatrix} (N^{-1})^{AB} & -\frac{1}{2\tilde{H}}(N^{-1})^{AC}\partial_C \tilde{H}\psi' & -\frac{1}{2\tilde{H}}(N^{-1})^{AC}\partial_C \tilde{H}\bar{\psi}' \\ \frac{1}{2\tilde{H}}\partial_C \tilde{H}(N^{-1})^{CB}\psi' & 0 & -\tilde{H}^{-1} \\ \frac{1}{2\tilde{H}}\partial_C \tilde{H}(N^{-1})^{CB}\bar{\psi} & \tilde{H}^{-1} & 0 \end{bmatrix}. \tag{6.67}$$

The non-zero Christoffel symbols are then

$$\Gamma^{A}_{BC} = \frac{1}{2}(N^{-1})^{AD}\left(\partial_B N_{DC} + \partial_C N_{DB} - \partial_D N_{BC}\right), \tag{6.68}$$

$$\Gamma^{\psi'}_{BC} = \left[\frac{\partial_B \tilde{H}\partial_C \tilde{H}}{4\tilde{H}^2} + \frac{\partial_B\partial_C \tilde{H} - \frac{1}{2}\partial_D \tilde{H}(N^{-1})^{DE}(\partial_B N_{EC} + \partial_C N_{EB} - \partial_E N_{BC})}{2\tilde{H}}\right]\psi', \tag{6.69}$$

$$\Gamma^{\psi'}_{B\psi'} = \frac{1}{2\tilde{H}}\partial_B \tilde{H}, \tag{6.70}$$

plus the appropriate conjugates. However, we need to include the correction from the choice of physical spacetime metric as discussed in section 6.1.2 giving

$$\tilde{C}_{ij}[\text{correct}] = e^{2(\sigma - \sigma_{\text{phys}})}\tilde{C}_{ij}[\text{from } \tilde{g} \text{ frame}]. \tag{6.71}$$

Let $\Delta\sigma := \sigma - \sigma_{\text{phys}}$. If our physical or preferred frame (where $\tilde{g}_{\mu\nu} = \bar{g}_{\mu\nu}$) is the Einstein frame, then $\Delta\sigma = \ln\left(2\tilde{F}/M_{\text{Pl}}^2\right)$, if it is the $\tilde{K} = K_0 = const$ Jordan frame we need $\Delta\sigma = \ln\left(\tilde{K}/K_0\right)$, and if it is the original $\sigma = 0$ Jordan frame we have $\Delta\sigma = \sigma$. Note that in all cases $\partial_i\Delta\sigma \propto q_i$. A non-zero $\Delta\sigma$ gives corrections to the field space Christoffel symbols of

$$\delta\Gamma^{a}_{bc} = \frac{1}{2}\left(\delta^a_c\partial_b\Delta\sigma + \delta^a_b\partial_c\Delta\sigma - \tilde{C}_{bc}\tilde{C}^{ad}\partial_d\Delta\sigma\right), \tag{6.72}$$

and thus corrections to the vertex factors $\tilde{\lambda}_{ab\dots c}$.[8] Can changing $\Delta\sigma$, and thus the physical spacetime metric, recover a fifth force for the scale-invariant theory? At

[8] If DeWitt index a corresponds to field species i and position x then $\partial_a\Delta\sigma = \partial_i\Delta\sigma|_x$.

one-loop order we consider three-point and four-point vertices. For a three-point vertex connected to three bosonic internal fields we have

$$\begin{aligned}\tilde{\lambda}_{abc} =& \mathrm{i}\left\langle \nabla_{\{a}\nabla_b\nabla_{c\}}S\right\rangle = \mathrm{i}\left\langle \nabla_{\{a}\nabla_b\partial_{c\}}S\right\rangle \\ =& \mathrm{i}\left\langle \partial_{\{a}\partial_b\partial_{c\}}S - \left(\Gamma^d_{bc}\partial_a\partial_d S + \Gamma^d_{ab}\partial_c\partial_d S + \Gamma^d_{ac}\partial_b\partial_d S\right)\right\rangle,\end{aligned} \tag{6.73}$$

so the contribution from $\Delta\sigma$ is

$$\begin{aligned}&\delta\tilde{\lambda}_{abc}(\Delta\sigma) = \\ &-\mathrm{i}\frac{1}{2}\left\langle \delta^d_c\partial_b\Delta\sigma + \delta^d_b\partial_c\Delta\sigma - \tilde{C}_{bc}\tilde{C}^{ed}\partial_e\Delta\sigma\right\rangle\langle\partial_a\partial_d S\rangle \\ &+ \text{permutations.}\end{aligned} \tag{6.74}$$

Let us choose to do the calculation in the preferred frame (remember we are free to choose the frame as the covariant formalism guarantees us frame invariance). Recall that when we apply the frame fixing the propagator will remove any contributions in the direction of q_i, so as the terms $\partial_b\Delta\sigma$ and $\partial_c\Delta\sigma$ only couple to that field direction those terms don't contribute, leaving

$$\begin{aligned}\delta\tilde{\lambda}_{abc} =& \mathrm{i}\frac{1}{2}\left\langle \tilde{C}_{bc}\tilde{C}^{de}\partial_e\Delta\sigma\right\rangle\langle\partial_a\partial_d S\rangle \\ &+ \text{permutations},\end{aligned} \tag{6.75}$$

which simplifies to

$$\delta\tilde{\lambda}_{abc} = -\mathrm{i}\frac{1}{2}\left\langle N_{bc}M_{ad}(N^{-1})^{de}\partial_e\Delta\sigma\right\rangle + \text{perms.} \tag{6.76}$$

To get a long-range fifth force potential at loop order we need a a, b, c to correspond to massless fields (the dilaton and the graviton). However, if a, b, c are massless, then $M_{ad} = 0$ so $\delta\tilde{\lambda}_{abc} = 0$ regardless of $\Delta\sigma$.

The other three-point vertex we need to consider is one connected to one external fermion leg, one internal fermion field, and one internal massless boson, given by

$$\begin{aligned}\tilde{\lambda}_{a\psi'} &= \mathrm{i}\left\langle \nabla_{\{a}\nabla_{\psi'\}}(X^b\partial_b S)\right\rangle \\ &= \mathrm{i}\left\langle \partial_{\{a}\partial_{\psi'\}}(X^b\partial_b S)\right\rangle - \mathrm{i}\left\langle \Gamma^c_{\{a\psi'\}}X^b(\partial_c\partial_b S)\right\rangle,\end{aligned} \tag{6.77}$$

where X^a is again the field space vector defining the external, physical, field (note that this means the vertex factor is only a rank-2 field space tensor). Then from the same argument as before we get the contribution from $\Delta\sigma$ as

$$\delta\tilde{\lambda}_{a\psi'} = -\mathrm{i}\frac{1}{2}\left\langle \tilde{C}_{\{a\psi'\}}\tilde{C}^{cd}\partial_d\Delta\sigma\right\rangle\left\langle X^b(\partial_c\partial_b S)\right\rangle. \tag{6.78}$$

For an additional fifth force we need the internal a field to be the dilaton, but $\tilde{H}$ is independent of σ so $\tilde{C}_{\{\sigma\psi'\}} = \delta\tilde{\lambda}_{a\psi'} = 0$ regardless of $\Delta\sigma$. While we do not consider the four-point vertex diagrams here, one can in principle calculate corrections from $\Delta\sigma$ for those in a similar manner. The ghost fields do contribute at one-loop order, however by construction the ghost part of the field space metric is trivial, and thus the ghost vertices do not pick up corrections from $\Delta\sigma$ (reflecting the fact they are artificial fields).

These results suggest that even changing $\Delta\sigma$, which corresponds to changing the *physical spacetime* $\bar{g}_{\mu\nu}$ (or if you prefer Planck length $l(\mathbf{\Phi})$), not merely the choice of frame, still does not break the suppression of dilaton fifth forces for scale-invariant gravity, at least to one-loop order.

6.6 Summary and discussion

In this work we have shown how one can apply the covariant, geometric formalism to show how scale-invariant scalar-tensor theories evade fifth force constraints in *all* frames, even including quantum corrections. By considering the choice of frame in a fully geometric manner – as a selection of a submanifold, or normal direction, in the field space of a generalised theory – we can see that not only is the usual dichotomy of "Jordan frame" versus "Einstein frame" really a continuum of frame slices, but that the results of fifth force calculations for any scalar-tensor theory can be made manifestly frame invariant, up to all perturbative orders. Indeed to a large extent we should consider fixing the frame to be directly analogous to fixing the gauge: the frame choice is merely a redundancy of our mathematics.[9]

We have neglected vector gauge fields from the matter Lagrangian, however these can be straightforwardly included. A covector field A_μ is Weyl invariant and transforms simply as $A_\mu \to \tilde{A}_\mu$, and the canonical gauge kinetic term $\mathcal{L} \supset -\sqrt{-g}\frac{1}{4}g^{\mu\rho}g^{\nu\sigma}F_{\mu\nu}F_{\rho\sigma}$ is likewise Weyl invariant. Hence adding vector bosons to the scale-invariant theory does not break the scale-invariance, and we conclude that they too decouple from the dilaton [413]. The addition of vector bosons also does not change our conclusions about general frame invariance: they can simply

[9] One could counter by pointing out that, unlike for the gauge, there is always a "preferred" or "metric" frame, the one where quantum field $g_{\mu\nu} = \bar{g}_{\mu\nu}$ the metric of physical spacetime. However, absent a full theory of quantum gravity, the extent to which the two should be equal is an open question.

be included as additional degrees of freedom in our field space, much like the graviton or scalar fields (with appropriate gauge fixing terms).

While here we have assumed a flat background spacetime, this approach can be extended to include background spacetimes which are only conformally flat, such as flat FRW. Instead of working on the curved spacetime background, we can change to a frame with a flat background via conformal factor $\Omega = a(\eta)$. The background curvature in one frame can instead be interpreted as a non-zero background value of the dilaton, $\langle\sigma\rangle = \ln(a(\eta))$ in another. Scalar-tensor theories of this form are of cosmological interest as models of inflation [381, 382, 390, 398, 460, 461, 461], hence it would be worth investigating to see how a similar maximally geometric approach might aid calculations in inflationary background and give confidence when transforming between frames.

Although we considered the full quantum field theory we have neglected discussion of regularisation and renormalisation, focusing on the results at tree level and lowest perturbative order most relevant for fifth force constraints. Any dimensionful renormalisation scale μ must transform appropriately between frames [440]. For the scale-invariant theory one can avoid introducing introducing external length scales by making μ a function of the scalar fields, $\mu(\boldsymbol{\varphi})$, such that it acquires a stable value in the same manner as the effective Planck mass[10], and $\mu(\boldsymbol{\varphi})$ then transforms between frames analogous to $F(\boldsymbol{\varphi})$ [413, 462–467]. This "internal" or scale-invariant renormalisation also avoids the scale or trace anomalies that can arise from renormalisation with an external mass scale [413, 439].

Usually one would need to specify a frame before renormalising, however it would be interesting to investigate if instead one could first implement a perturbative renormalisation to arbitrary order in the general $N + 1$ field theory, as described above, then merely project onto your desired sub-manifold to extract results for a particular frame, and whether one would then naturally obtain the necessary frame dependence for the renormalisation mass scale and other parameters. It would also be interesting to examine how this framework might be extended to frame-independent quantum formulations of scalar-tensor theories with higher-order derivative terms, such as Horndeski or DHOST theory [95–97].

[10] As the background scalar fields $\boldsymbol{\varphi}$ tend to constants under the influence of an expanding cosmology, so does $\mu(\boldsymbol{\varphi})$.

Chapter 7

Conclusions

Novel fundamental scalar fields are well motivated as possible solutions to a range of unsolved problems in modern physics. In this thesis we have conducted theoretical analytic and numerical studies of novel fundamental fields in the context of black holes and General Relativity, across a range of regimes.

In the first part we described the background material. Chapter 1 reviewed the basics of General Relativity, scalar fields and black holes, and why we should care about them. Then in chapter 2 we described the essential concepts of Numerical Relativity, and the GRChombo code used for this thesis.

In part II we described the original research that makes up the bulk of thesis. In chapters 3, 4 and 5 we focused on minimally coupled light scalar field dark matter and its interaction with black holes and black hole binaries. In 6 we considered a quite different topic: non-minimally coupled scalar fields in the context of scalar-tensor modified gravity. The key findings are summarised below.

7.1 Black holes and scalar clouds: accretion

We have very strong evidence that dark matter exists and makes up a large percentage of the universe, it has to consist of something, and light "axion-like" scalar fields are one of the best motivated candidates. One notable feature of this light "wave-like" dark matter is that it can form long-lived clouds around black holes and black hole binaries. This raises the possibility of testing its existence with gravitational wave observations.

In chapter 3 we examined the accretion of scalar field dark matter around black holes, what may be a more ubiquitous process than the more commonly studied superradiance mechanism. Comparing our numerical simulations with the

zero-spin Schwarzschild case in [200], we saw that adding realistic spin values does not significantly change the accretion rates or the density profile, as the effect of the black hole spin is concentrated near the black hole horizon. We observed a smooth transition from the homogeneous background to known analytic stationary solutions [198], with the region of influence of the black hole moving outwards over time. Adding asymptotic angular momentum to the scalar can either suppress or enhance (depending on the misalignement) its accretion rate, and in the case of aligned spins concentrates the clouds further out from the horizon. The cloud behaviour was explained by reference to a quasi-effective radial potential and the orbits of equivalent particles, and we developed a perturbative analytic solution to describe the changing field profile at large radius and small times.

Finally we estimated the monochromatic gravitational wave signal that might be be produced by accreting cloud around the supermassive black hole at the centre of the galaxy. Our results suggest such a signal would not be detectable by any planned gravitational wave observatories. However, unlike with clouds derived from superradiance, the size of the accretion driven cloud is heavily dependent on ones assumptions about the local dark matter environment close to the black hole, and thus different assumptions, or a superposition of sources, could lead to an observable signal.

7.2 Black holes and scalar clouds: quasi-normal modes

We also explored the interaction of accreting scalar field dark matter clouds with black hole binaries. In chapter 4 we examined the final "ringdown" of the daughter black hole, and for the first time derived a general perturbative formula for how an *accreting* matter cloud would perturb the characteristic quasi normal mode (QNM) frequencies due to the backreaction onto the metric. We obtained an expression for the perturbed frequency of the frequency shift of the form

$$\boxed{\omega = \omega_0 + \delta\varpi + \delta A(\varpi_A - \frac{\omega_0}{2}t'/M) + \mathcal{O}(\delta^2),} \tag{7.1}$$

where ω_0 is the QNM frequency in vacuum, δA is the accretion rate and $\delta\varpi, \delta A\varpi_A$ are small corrections. Our results can be applied to an arbitrary spherically symmetric matter cloud, but when applied to the particular case of accreting scalar field dark matter we found that the accretion dependent term $\delta A\varpi_A$, previously

neglected, is actually around ~ 50 times larger than the non-accretion term $\delta\varpi$. We also verified our method on several well studied vacuum spacetimes, finding excellent agreement with alternative numerical approaches.

Extending our method to more realistic cases with axisymmetric accretion disks is challenging, as the equations become non-separable. Nonetheless this remains an area of ongoing research, and of great interest to the field of precision black hole spectroscopy.

7.3 Black holes and scalar clouds: binary mergers

Having examined the impact of scalar field dark matter clouds on the "ringdown" regime of the gravitational wave signal, in chapter 5 we sought to investigate the first two regimes of a black hole binary merger: the early inspiral and highly relativistic merger regimes.

To determine the realistic initial data for the scalar field, we first sought to investigate the early inspiral regime. We conducted numerical simulations of the accretion of wave dark matter from a homogeneous environment around binary black holes in fixed Keplerian orbits, choosing a scalar mass that gives the largest interaction with the BH binary. We found that the scalar field quickly converges to a persistent non-trivial profile, which grows in amplitude as the accretion continues.

We then explored how different choices of initial data affected the evolution of the dark matter cloud during the highly relativistic merger regime. Our results suggest that the profile found in the fixed orbit simulations is an attractor solution, as other choices of initial data converged to the same distribution over the course of several orbits. This means that for long numerical simulations the precise choice of initial scalar field data may be unimportant, as the field will quickly converge to the quasi-stationary distribution. However for numerical simulations which only consist of a small number of orbits, the transients and the resulting loss of control over the initial data may strongly affect the final results.

Lastly, we obtained and tested constraint-satisfying initial data for the scalar profiles obtained from our fixed orbit simulations. To the best of our knowledge, this is the first time that realistic environments with non zero angular momentum have been applied to black hole binary mergers. We found that naively

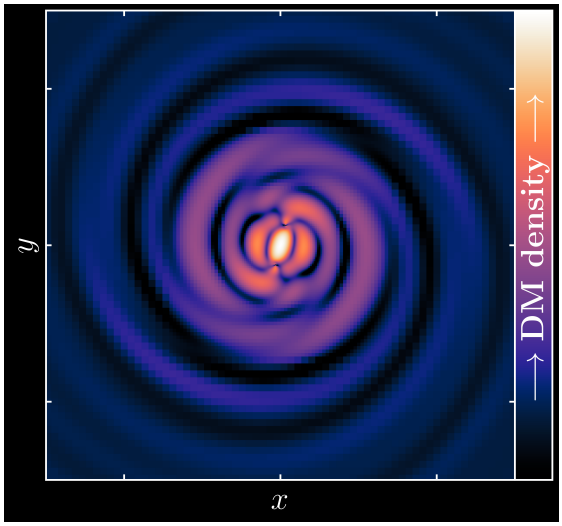

Figure 7.1: **Scalar dark matter cloud around a black hole binary**. Illustrative plot of the energy density of a scalar dark matter cloud accreting around a black hole binary. This simulation used a slightly larger scalar mass than used in chapter 5, with $M\mu \sim 2.0$, which results in a spiral profile with more tightly spaced (and therefore more dramatic) oscillations.

using the parameters for a quasi-circular binary merger in vacuum will not usually produce low eccentricity orbits once matter is added, and hence one *cannot* simply compare the resulting gravitational waveforms. Instead a more comprehensive approach is needed to find initial data that both satisfies the Einstein constraints and produces realistic low-eccentricity inspirals, similar to that developed for vacuum binaries [191, 358, 360–362], but incorporating the dynamics of the scalar field quasi-stationary profile in a quasi-equilibrium or post-Newtonian model [364–369, 371–373]. Further study of the precise effects of the backreaction from the matter on the black hole bare masses and momenta may also provide a guide to help tune the parameters to achieve the desired quasi-circular orbits.

7.4 Beyond GR: fifth forces and frame invariance

Novel fundamental scalar fields are also of interest in the context of modified gravity, proposed to address a range of unsolved problems in cosmology and fundamental theoretical physics. A major limitation on such scalar-tensor theories are the observational constraints on fifth forces. It has been shown that, in particular frames, for scale-invariant scalar-tensor theories fifth forces constraints are evaded

or dramatically suppressed [388, 413]. However it has also been shown that when considered as a full quantum theory, scalar-tensor gravity in different frames may not be equivalent, even producing different observable results [414, 439–441].

In chapter 6 the covariant formulism of Vilkovisky, DeWitt [447–449] and others [440, 442–446] was used to obtain a new geometric approach to frame choice for scalar-tensor theories, which in turn was used to show how scale-invariant scalar-tensor theories evade fifth force constraints in *all* frames, even including quantum corrections. By considering the choice of frame in a fully geometric manner – as a selection of a submanifold, or normal direction, in the field space of a generalised theory – we can see that not only is the usual dichotomy of "Jordan frame" versus "Einstein frame" really a continuum of frame slices, but that the results of fifth force calculations for any scalar-tensor theory can be made manifestly frame invariant, up to all perturbative orders. Indeed to a large extent we should consider fixing the frame to be directly analogous to fixing the gauge: the frame choice is merely a redundancy of our mathematics.

There remains much work to be done, as here we neglect a detailed discussion of regularisation and renormalisation, the UV-limit for quantum gravity, vector boson fields and the full particle standard model, a dynamic cosmological background spacetime, and higher-order scalar-tensor theories of modified gravity. Nonetheless, this remains a significant step towards understanding and applying frame-choice in scalar modified gravity theories in a rigorous or semi-rigorous manner, with application to cosmology and astrophysics.

In a future paper we will also examine the possibility of detecting scalar radiation from binary black hole mergers in scalar-tensor gravity. We will examine how such signals might be generated from binary mergers, either inside a scalar field dark matter environment or generated from couplings to higher-order curvature terms, how they propagate through space to us, and how we might detect them observationally, and attempt to predict how tightly we could constrain the parameters of the scalar-tensor theory given current and planned observatories.

To conclude, the original research presented in this thesis represents a significant advancement in the theoretical study of novel scalar fields, black holes, and strong gravity.

Part III

Extra Material

Appendix A

Numerical Relativity

A.1 The Lie derivative

The Lie derivative $\mathcal{L}_{\vec{v}}$ of a tensor is a measure of how much it changes as you move in the direction parallel to v^μ. Consider moving from x^μ to $x'^\mu = x^\mu + \epsilon v^\mu$, where ϵ is infinitesimal. In flat Euclidean space we can define the rate of change for tensor $T^{a\cdots}_{b\ldots}$ as

$$\partial_{\vec{v}} T^{a\cdots}_{b\ldots} = \lim_{\epsilon\to 0} \frac{T^{a\cdots}_{b\ldots}(x'^\mu) - T^{a\cdots}_{b\ldots}(x^\mu)}{\epsilon}. \tag{A.1}$$

In a curved manifold we also need to take account of the fact that tensors change under coordinate transformations, and express $T^{a\cdots}_{b\ldots}(x^\mu)$ in terms of the primed coordinates, so we are comparing like with like. The transformation rule is given in (1.2). Then the Lie derivative is

$$\mathcal{L}_{\vec{v}} T^{a\cdots}_{b\ldots} = \lim_{\epsilon\to 0} \frac{T^{a\cdots}_{b\ldots}(x'^\mu) - T'^{a\cdots}_{b\ldots}(x^\mu)}{\epsilon}, \tag{A.2}$$

where the primed $T'^{a\cdots}_{b\ldots}(x^\mu)$ denotes the tensor at point x^μ, but expressed in the primed x'^μ coordinates via a passive coordinate transformation. From the definition in (A.2) one can derive the formula for the Lie derivative of a general type (n, m) tensor $T^{a_1\ldots a_n}_{b_1\ldots b_m}$ in index notation as

$$\begin{aligned}\mathcal{L}_{\vec{v}} T^{a_1\ldots a_n}_{b_1\ldots b_m} &= v^\lambda \nabla_\lambda T^{a_1\ldots a_n}_{b_1\ldots b_m} \\ &+ T^{\lambda\ldots a_n}_{b_1\ldots b_m} \nabla_\lambda v^{a_1} + \ldots + T^{a_1\ldots\lambda}_{b_1\ldots b_m} \nabla_\lambda v^{a_n} \\ &- T^{a_1\ldots a_n}_{\lambda\ldots b_m} \nabla_{b_1} v^\lambda - \ldots - T^{a_1\ldots a_n}_{b_1\ldots\lambda} \nabla_{b_m} v^\lambda,\end{aligned} \tag{A.3}$$

where we can use the covariant derivative ∇_μ in place of the partial derivative ∂_μ as long as we are using the Levi-Civita connection defined in (1.4). The Lie derivative is linear, so that $\mathcal{L}_{\vec{X}+\vec{Y}} T^{a\cdots}_{b\ldots} = \mathcal{L}_{\vec{X}} T^{a\cdots}_{b\ldots} + \mathcal{L}_{\vec{Y}} T^{a\cdots}_{b\ldots}$.

A.2 The CCZ4 evolution equations

In the CCZ4 formalism used in the full NR simulations with GRChombo in chapter 5 the spatial metric is decomposed as

$$\gamma_{ij} = \frac{1}{\chi}\tilde{\gamma}_{ij}, \quad \det(\tilde{\gamma}_{ij}) = 1, \quad \chi = \det(\gamma_{ij})^{-1/3}. \tag{A.4}$$

The extrinsic curvature is decomposed into its trace $K = \gamma^{ij}K_{ij}$ and conformal traceless part $\tilde{A}_{ij}$ with $\tilde{\gamma}^{ij}\tilde{A}_{ij} = 0$,

$$K_{ij} = \frac{1}{\chi}\left(\tilde{A}_{ij} + \frac{1}{3}K\tilde{\gamma}_{ij}\right), \tag{A.5}$$

and we define the *conformal connection functions* $\tilde{\Gamma}^i = \tilde{\gamma}^{jk}\tilde{\Gamma}^i_{jk}$ where $\tilde{\Gamma}^i_{jk}$ are the connection coefficients associated with the conformal spatial metric $\tilde{\gamma}_{ij}$. We decompose the Z^μ vector into $\Theta = -n^\mu Z_\mu$ and define

$$\hat{\Gamma}^i = \tilde{\Gamma}^i + 2\tilde{\gamma}^{i\mu}Z_\mu. \tag{A.6}$$

The complete evolution variables, including the gauge functions and the matter, are $\{\varphi, \Pi, \alpha, \beta^i, B^i, \chi, \tilde{\gamma}_{ij}, K, \tilde{A}_{ij}, \Theta, \hat{\Gamma}^i\}$. Using the moving punctures gauge the complete evolution equations are [178, 183]

$$\partial_t\varphi = \alpha\Pi + \beta^i\partial_i\varphi, \tag{A.7}$$

$$\partial_t\Pi = \alpha\gamma^{ij}\partial_i\partial_j\varphi + \alpha\left(K\Pi - \Gamma^k\partial_k\varphi - \frac{\mathrm{d}V(\varphi)}{\mathrm{d}\varphi}\right) + \partial_i\varphi\partial^i\alpha + \beta^i\partial_i\Pi, \tag{A.8}$$

$$\partial_t\alpha = -2\alpha(K - 2\Theta) + \beta^i\partial_i\alpha, \tag{A.9}$$

$$\partial_t\beta^i = \tfrac{3}{4}B^i, \tag{A.10}$$

$$\partial_t B^i = \tfrac{3}{4}\alpha\partial_t\tilde{\Gamma}^i - B^i, \tag{A.11}$$

$$\partial_t\chi = \beta^k\partial_k\chi + \tfrac{2}{3}\chi(\alpha K - \partial_k\beta^k), \tag{A.12}$$

$$\partial_t\tilde{\gamma}_{ij} = \beta^k\partial_k\tilde{\gamma}_{ij} + 2\tilde{\gamma}_{k(i}\partial_{j)}\beta^k - 2\alpha\tilde{A}_{ij} - \tfrac{2}{3}\tilde{\gamma}_{ij}\partial_k\beta^k, \tag{A.13}$$

$$\begin{aligned}\partial_t K = &-D^iD_i\alpha + \beta^k\partial_k K + \alpha\left({}^{(3)}R + 2D_iZ^i + \tfrac{2}{3}K^2 - 2\Theta K\right)\\ &- 3\kappa_1(1+\kappa_2)\Theta + 4\pi\alpha(S - 3\rho),\end{aligned} \tag{A.14}$$

$$\begin{aligned}\partial_t\tilde{A}_{ij} = &\beta^k\partial_k\tilde{A}_{ij} + \chi\left[-D_iD_j\alpha + \alpha({}^{(3)}R_{ij} + 2D_{(i}Z_{j)} - 8\pi S_{ij}\right]^{\mathrm{TF}}\\ &+ \alpha\tilde{A}_{ij}(K - 2\Theta) - 2\alpha\tilde{A}_{il}\tilde{A}^l_j + 2\tilde{A}_{k(i}\partial_{j)}\beta^k\\ &- \tfrac{2}{3}\tilde{A}_{ij}\partial_k\beta^k + \beta^k\partial_k\tilde{A}_{ij},\end{aligned} \tag{A.15}$$

$$\partial_t \Theta = \tfrac{1}{2}\alpha \left({}^{(3)}R + 2D_i Z^i - \tilde{A}_{ij}\tilde{A}^{ij} + \tfrac{2}{3}K^2 - 2\Theta K \right) - Z^i \partial_i \alpha + \beta^k \partial_k \Theta - \kappa_1(2+\kappa_2)\Theta - 8\pi\alpha\rho, \tag{A.16}$$

$$\begin{aligned}\partial_t \hat{\Gamma}^i = {} & 2\alpha \left(\tilde{\Gamma}^i_{jk}\tilde{A}^{jk} - \tfrac{3}{2}\tilde{A}^{ij}\partial_j \ln\chi - \tfrac{2}{3}\tilde{\gamma}^{ij}\partial_j K \right) - 2\tilde{A}^{ij}\partial_j \alpha + \tilde{\gamma}^{kl}\partial_k\partial_l\beta^i \\ & + 2\tilde{\gamma}^{ki}\left(\alpha\partial_k\Theta - \Theta\partial_k\alpha - \tfrac{2}{3}\alpha K Z_k\right) + \tfrac{1}{3}\tilde{\gamma}^{ik}\partial_k\partial_l\beta^l + \tfrac{2}{3}\tilde{\Gamma}^i\partial_k\beta^k \\ & - \tilde{\Gamma}^k\partial_k\beta^i + 2\kappa_3\left(\tfrac{2}{3}\tilde{\gamma}^{ij}Z_j\partial_k\beta^k - \tilde{\gamma}^{jk}Z_j\partial_k\beta^i\right) + \beta^k\partial_k\hat{\Gamma}^i \\ & - 2\kappa_1\tilde{\gamma}^{ij}Z_j - 16\pi\alpha\tilde{\gamma}^{ij}S_j,\end{aligned} \tag{A.17}$$

where D_i is the covariant derivative for the spatial metric γ_{ij} and $[\cdot]^{\mathrm{TF}}$ denotes the trace-free part of the enclosed expression. Note the additional damping parameter, κ_3, in (A.17) which by default we set to 1. As discussed in section 2.4 we set the other damping terms to $\kappa_1 = 0.1$ and $\kappa_2 = 0$. The decomposed parts of the energy-momentum tensor are

$$\rho = n^\mu n^\nu T_{\mu\nu}, \quad S_i = -P^\mu_i n^\nu T_{\mu\nu}, \quad S_{ij} = P^\mu_i P^\nu_j T_{\mu\nu}, \quad S = \gamma^{ij}S_{ij}. \tag{A.18}$$

As discussed in chapter 3, when dealing with the fixed background simulations we can neglect equations (A.9) to (A.17) and only evolve (A.7) & (A.8), which correspond to two equations for a real scalar field and four equations for a complex scalar field.

Appendix B

The growth of accretion driven scalar hair around Kerr black holes

B.1 Code validation and coordinate choice

As discussed in the main text, we evolve the field on a fixed background Kerr metric in Quasi-Isotropic Kerr (QIK) coordinates.

The metric is validated by checking that the numerically calculated Hamiltonian and Momentum constraints converge to zero with increasing resolution, as do the time derivatives of the metric components, i.e. $\partial_t \gamma_{ij} = \partial_t K_{ij} = 0$ (calculated using the ADM expressions). This ensures that the metric which is implemented is indeed stationary in the chosen gauge, consistent with it being fixed over the field evolution. The outer horizon at $R = r_+$ is spherical and therefore it retains a finite limit even in the limit $\chi \to 1$. However, as noted above, the use of QIK coordinates necessitates the use of an analytic continuation of the lapse in which its value becomes negative within the horizon. To see why this is useful in comparison to the positive continuation, note that the solution within the horizon describes a mirror universe, rather than a BH interior, so this choice corresponds to running time "backwards" in this region. As a consequence any matter will fall towards the grid centre, i.e. towards asymptotic spatial infinity in the mirror universe. One does not then in principle need to excise within the horizon, but in practise we do stil excise some part of the interior to prevent any spikes developing.

The advantage of these coordinates is their simple relation to the BL coordinates in which we perform our perturbative analysis. The downside is that since they correspond to the asymptotic observers, the lapse goes to zero and time

freezes around the horizon. Thus ingoing waves tend to "bunch up" there. Given sufficient resolution outside the outer horizon, the ingoing nature of the metric prevents the errors this introduces from propagating into the region far from the BH, and unresolved waves are effectively damped away by grid precision close to the horizon. Provided we are not interested in extracting quantities very close to the horizon, these coordinates work in practise.

An alternative set of coordinates are Kerr-Schild coordinates [468]. This form has the advantage of being horizon penetrating, in other words without a coordinate singularity at the horizon. The metric can be split into

$$g_{\mu\nu} = \eta_{\mu\nu} + 2H(x^\mu) l_\mu l_\nu, \tag{B.1}$$

where $\eta_{\mu\nu}$ is the Minkowski metric, $H = Mr/\Sigma$, and l^μ is an ingoing null vector given by

$$l^\mu = \left(-1, 1, 0, -\frac{2a}{a^2 + r^2}\right), \tag{B.2}$$

written out in coordinates $\{t, r, \theta, \phi\}$. These relate to the Boyer-Lindquist coordinates via

$$t_{KS} = t_{BL} + \frac{2M}{r_+ - r_-}\left(r_+ \ln\left|\frac{r}{r_+} - 1\right| - r_- \ln\left|\frac{r}{r_-} - 1\right|\right), \tag{B.3}$$

$$\phi_{KS} = \phi_{BL} + \frac{a}{r_+ - r_-} \ln\left|\frac{r - r_+}{r - r_-}\right| + 2\tan^{-1}\left(\frac{a}{r}\right). \tag{B.4}$$

Taking $a = 0$ one can show these coordinates reduce to ingoing Eddington-Finkelstein (EF) coordinates rather than Schwarzchild, with ingoing EF null coordinate $v = r + t_{KS}$. This makes it more difficult to interpret results expressed in Kerr-Schild coordinates from the perspective of a distant observer as t_{KS} is no longer their measured time at finite r. Taking $a = 0$ and setting $u = t + r$ one can show that the radial coordinate r corresponds to that of ingoing Eddington-Finkelstein rather than Schwarzschild coordinates. This makes it more difficult to interpret results expressed in Kerr-Schild coordinates from the perspective of a distant observer as t_{KS} is no longer their measured time at finite r. For simplicity of presentation we have presented results in QIK coordinates only, but we have checked that we obtain physically consistent results in both gauges, and that our diagnostics can be reconciled in both cases, see for example Fig. B.1.

B.2 Conserved fluxes

In Numerical Relativity it is conventional to decompose the energy-momentum tensor into purely spatial quantities as

$$T_{\mu\nu} = \rho n_\mu n_\nu + S_\mu n_\nu + n_\mu S_\nu + S_{\mu\nu}, \tag{B.5}$$

(see chapter 2). The ρ and S^i are the energy and momentum densities respectively measured by the Eulerian observers, that is, observers moving normal to the spatial hypersurfaces in the 3+1 ADM decomposition. These are not the same as the time-like observers for which the conserved quantities are defined. We can obtain the expressions for the conserved quantities in terms of the standard ADM quantities as follows:

$$\rho_E = -\alpha T^t_t = \alpha\rho - \beta_i S^i, \tag{B.6}$$

$$\rho_J = S_\phi, \tag{B.7}$$

$$J^i_t = \alpha\,\gamma^{ij}\left(\alpha S_j - \beta^k S_{jk}\right) - \beta^i \rho_E, \tag{B.8}$$

$$J^i_\phi = \alpha\gamma^{ij} S_{j\phi} - \beta^i \rho_J. \tag{B.9}$$

Another common quantity of interest is the ADM mass of the spacetime [12] defined as

$$M_{\rm ADM} = \frac{1}{16\pi}\lim_{r\to\infty}\int_{\partial\Sigma}(\partial_i h^{ij} - \partial^i h^j_j)\mathrm{d}S_i, \tag{B.10}$$

where we assume that the boundary surface is in the weak field limit

$$g_{\mu\nu} = \eta_{\mu\nu} + h_{\mu\nu}, \tag{B.11}$$

where $h_{\mu\nu}$ is small. In our case if we include the backreaction we find

$$h_{\mu\nu} = h^{BH}_{\mu\nu} + h^{\varphi}_{\mu\nu}, \tag{B.12}$$

where $h^{BH}_{\mu\nu}$ is from the BH background metric and $h^{\varphi}_{\mu\nu}$ from the scalar field back-reaction. As (B.10) is linear in $h_{\mu\nu}$ these give seperable contributions to $M_{\rm ADM}$. Perturbing the Einstein equations to first order gives

$$\begin{aligned} 8\pi T^i_t &= \tfrac{1}{2}(\partial_t[\partial_j h^{ij} - \partial^i h^j_j] + \partial^2_t h^{it} + \partial^i\partial_\mu h^\mu_t - \partial_\mu\partial^\mu h^i_t) + \mathcal{O}(h^2), \\ &= \tfrac{1}{2}\partial_t[\partial_j h^{ij} - \partial^i h^j_j] + \mathcal{O}(h^2), \end{aligned} \tag{B.13}$$

using the synchronous gauge $h_{\mu t} = 0$. Given that the BH background is fixed in time, we then recover

$$\partial_t M_{\rm ADM} = \lim_{r\to\infty}\int_{\partial\Sigma}\sqrt{-g}T^i_t\mathrm{d}S_i + \mathcal{O}(h^2), \tag{B.14}$$

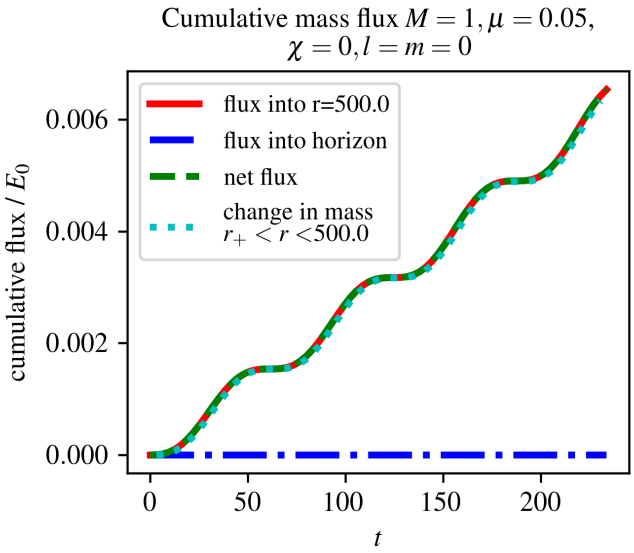

Figure B.1: **Code check: mass flux conservation**. The cumulative mass flux into a sphere radius $R = 500M$, into the horizon of the BH, the net flux and the change in cloud mass measured from integrating the density ρ_E, for $M\mu = 0.05, \chi = l = m = 0$ in Kerr-Schild coordinates. We see good agreement between the change in cloud mass and the net mass flux.

where we can reintroduce $\sqrt{-g}$ as in the weak field limit $\sqrt{-g} = 1 + \mathcal{O}(h)$. Hence if we choose a large enough radius sphere the flux across the surface, and thus the change in the mass within the sphere (3.16), approximates to the change in the ADM mass which would be measured.

We have verified that the integral of the scalar field mass flux over a sphere does correspond to the change in scalar field mass inside the sphere in both QIK coordinates (Fig. B.2) and the alternative Kerr-Schild coordinates (Fig. B.1).

B.3 Convergence tests

In this section we illustrate our tests of the numerical convergence of our code. As we use fourth order finite difference stencils to evolve the field, we expect our errors to decrease with N, the number of grid cells, as N^{-4}. The first quantity we test is the scalar field mass flux into a sphere of $R = 300M$, a quantity we explored in Sec. 3.3. We compute the flux for the most challenging case studied of high scalar mass $\alpha_g = M\mu = 2.0$, high spin $\chi = 0.99$ and large scalar angular momentum $l = m = 8$. The results for $N = 32, 64, 128, 256$ are shown in Fig. B.4. By eye we see good agreement for $N \geq 128$ which corresponds to the resolution used ($N = 128$). To test the convergence we also plot the difference between the

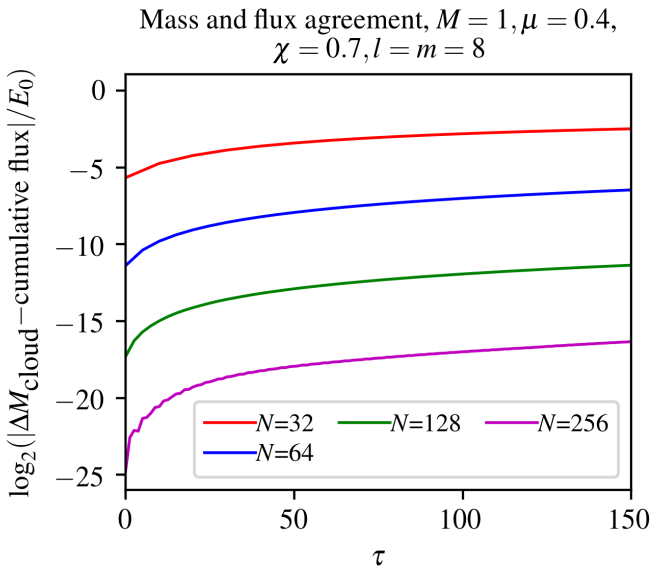

Figure B.2: **Convergence test: mass flux conservation**. We plot the difference between the change in mass inside a sphere radius $R = 300M$ measured from integrating the density ρ_E, and the cumulative mass flux into the sphere. This difference should be zero for an infinite resolution simulation. We show values for $M\mu = 2.0, \chi = 0.99, l = m = 8$ and different N again plotted on a log scale. We see that again doubling N decreases the error by a factor of $\sim 2^{-4}$ each time, indicating 4th order convergence.

flux f on doubling the resolution from N to $2N$ (Fig. B.3). We would expect this difference to decrease by $\sim 2^{-4}$ on doubling N, and indeed this is approximately what we observe.

Finally, we examine the difference between the change in total mass inside a sphere radius $R = 300$ and the cumulative flux into the sphere. As we established in Sec. 3.1.2 this difference should be zero. Fig. B.2 shows the difference in QIK coordinates for increasing N. We can see that the difference is both small for our typical choice of $N = 128$ and it decreases by approximately 2^{-4} on doubling N as we expected.

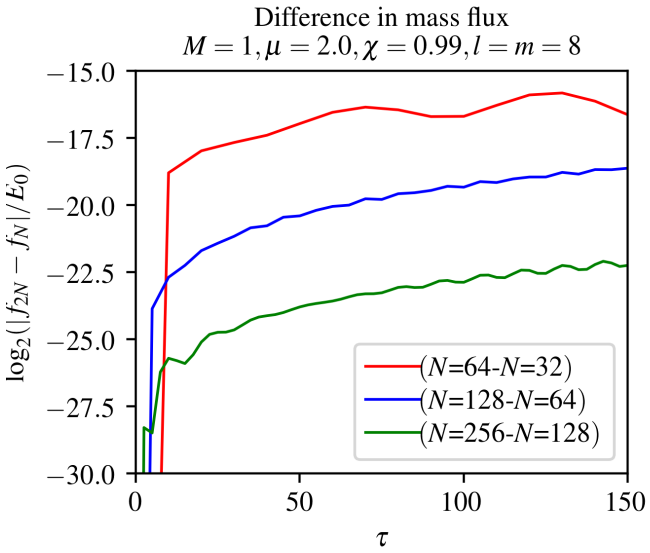

Figure B.3: **Convergence test: relative error in mass flux**. We now plot the change in the mass flux through $R = 300M$ on doubling N for $M\mu = 2.0, \chi = 0.99, l = m = 8$ plotted on a log scale. We see the difference in flux decreases by a factor of $\sim 2^{-4}$ each time, indicating we do indeed have 4th order convergence.

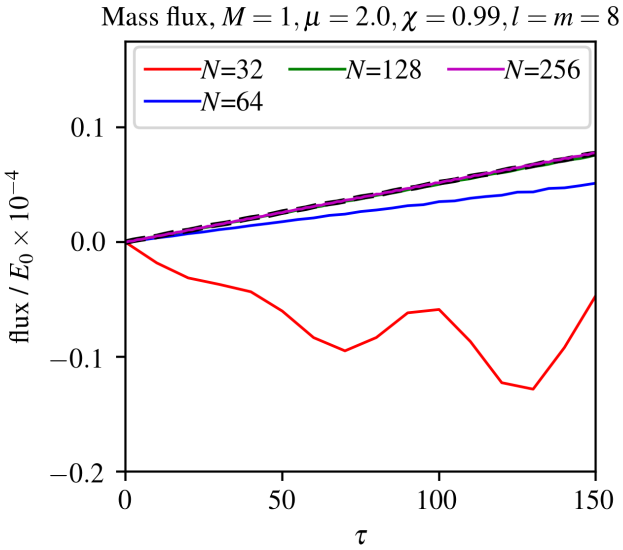

Figure B.4: **Mass flux: improvement with resolution**. We plot the mass flux through $R = 300M$ for different N and in the most challenging case studied $M\mu = 2.0, \chi = 0.99, l = m = 8$. We see good agreement by eye for $N \geq 128$ which corresponds to the values used. The black dashed line is the perturbative analytic solution which we expect to diverge from the true numerical solution at later times, but provides a guide to the expected result at early times.

Appendix C

The quasi-normal modes of growing dirty black holes

C.1 Perturbation theory

To find QNM for perturbed BH spacetimes we need two metric perturbations

$$g_{\mu\nu} = g^{(0)}_{\mu\nu} + \epsilon g^{(1)}_{\mu\nu} + \zeta g^{(2)}_{\mu\nu}, \tag{C.1}$$

where ϵ and ζ are both small, but $\zeta \ll \epsilon$. The larger perturbation $\epsilon g^{(1)}_{\mu\nu}$ is static or slowly varying and captures the change to the metric from additional fields, modifications to GR, or the backreaction from clouds of matter. This perturbation is denoted $\delta g_{\mu\nu}$ earlier in previous sections. The smaller perturbation $\zeta g^{(2)}_{\mu\nu}$ is the one which will oscillate at the quasi-normal mode frequencies. The $g^{(0)}_{\mu\nu}$ is a vaccuum background BH metric.

We have two sets of equations for the metric g_{ab} and the matter fields φ_m: the Einstein field equations

$$G_{\mu\nu}[g_{ab}] = 8\pi T_{\mu\nu}[\varphi_m, g_{ab}], \tag{C.2}$$

and the equation of motion

$$\nabla_\mu[g_{ab}] T^{\mu\nu}[\varphi_m, g_{ab}] = 0. \tag{C.3}$$

Here we will assume GR and assume $g^{(1)}_{\mu\nu}$ comes from the matter backreaction, and assume $T_{\mu\nu}$ to be order ϵ with $T_{\mu\nu} = \epsilon \tilde{T}_{\mu\nu}$. We will also expand φ_m as

$$\varphi_m = {\varphi_m}^{(0)} + \epsilon {\varphi_m}^{(1)} + \zeta {\varphi_m}^{(2)} + \dots \tag{C.4}$$

First let us expand in powers of ζ. At order ζ^0 we have

$$G_{\mu\nu}[g_{ab}^{(0)} + \epsilon g_{ab}^{(1)}] = \epsilon 8\pi \tilde{T}_{\mu\nu}[{\varphi_m}^{(0)} + \epsilon {\varphi_m}^{(1)}, g_{ab}^{(0)} + \epsilon g_{ab}^{(1)}], \tag{C.5}$$

and

$$\epsilon \nabla_\mu [g_{ab}^{(0)} + \epsilon g_{ab}^{(1)}] T^{\mu\nu}[{\varphi_m}^{(0)} + \epsilon {\varphi_m}^{(1)}, g_{ab}^{(0)} + \epsilon g_{ab}^{(1)}] = 0. \tag{C.6}$$

We can then expand in powers of ϵ. At order ϵ^0 we have $G_{\mu\nu}[g_{ab}^{(0)}] = 0$ as $g_{ab}^{(0)}$ is a vacuum solution. At order ϵ we have

$$\frac{\delta G_{\mu\nu}}{\delta g_{ab}}[g_{pq}^{(0)}] g_{ab}^{(1)} = 8\pi \tilde{T}_{\mu\nu}[{\varphi_m}^{(0)}, g_{ab}^{(0)}], \tag{C.7}$$

and

$$\nabla_\mu^{(0)} T^{\mu\nu}[{\varphi_m}^{(0)}, g_{ab}^{(0)}] = 0, \tag{C.8}$$

which can be solved for the zeroth order field solution ${\varphi_m}^{(0)}$ and the backreaction $g_{\mu\nu}^{(1)}$. At order ζ^1 we obtain

$$\begin{aligned}
&\frac{\delta G_{\mu\nu}}{\delta g_{ab}}[g_{pq}^{(0)} + \epsilon g_{pq}^{(1)}] g_{ab}^{(2)} = \\
&\quad \epsilon 8\pi \frac{\delta \tilde{T}_{\mu\nu}}{\delta \varphi_m}[{\varphi_m}^{(0)} + \epsilon {\varphi_m}^{(1)}, g_{pq}^{(0)} + \epsilon g_{pq}^{(1)}] {\varphi_m}^{(2)} \\
&\quad + \epsilon 8\pi \frac{\delta \tilde{T}_{\mu\nu}}{\delta g_{ab}}[{\varphi_m}^{(0)} + \epsilon {\varphi_m}^{(1)}, g_{pq}^{(0)} + \epsilon g_{pq}^{(1)}] g_{ab}^{(2)} + \dots, \\
&= \epsilon 8\pi \left(\frac{\delta \tilde{T}_{\mu\nu}}{\delta \varphi_m}[{\varphi_m}^{(0)}, g_{pq}^{(0)}] {\varphi_m}^{(2)} + \frac{\delta \tilde{T}_{\mu\nu}}{\delta g_{ab}}[{\varphi_m}^{(0)}, g_{pq}^{(0)}] g_{ab}^{(2)} \right) \\
&\quad + \mathcal{O}(\epsilon^2).
\end{aligned} \tag{C.9}$$

Then let ${\varphi_m}^{(2)} = \tilde{\varphi}_m^{(2)} + \chi^{(2)}$ such that

$$\frac{\delta \tilde{T}_{\mu\nu}}{\delta \varphi_m}[{\varphi_m}^{(0)}, g_{pq}^{(0)}] \chi^{(2)} + \frac{\delta \tilde{T}_{\mu\nu}}{\delta g_{ab}}[{\varphi_m}^{(0)}, g_{pq}^{(0)}] g_{ab}^{(2)} = 0. \tag{C.10}$$

Then

$$\frac{\delta G_{\mu\nu}}{\delta g_{ab}}[g_{pq}^{(0)} + \epsilon g_{pq}^{(1)}] g_{ab}^{(2)} = \frac{\delta \tilde{T}_{\mu\nu}}{\delta \varphi_m}[{\varphi_m}^{(0)}, g_{pq}^{(0)}] \tilde{\varphi}_m^{(2)}, \tag{C.11}$$

$$\epsilon \nabla_\mu [g_{pq}^{(0)}] \left(\frac{\delta T^{\mu\nu}}{\delta \varphi_m}[{\varphi_m}^{(0)}, g_{ab}^{(0)}] \tilde{\varphi}_m^{(2)} \right) = 0, \tag{C.12}$$

to order ϵ. We see that (C.11) and (C.12) can be written as

$$\mathcal{L}_{\mu\nu}^{ab} g_{ab}^{(2)} = S_{\mu\nu} \tilde{\varphi}_m^{(2)}, \tag{C.13}$$

$$\mathcal{E} \tilde{\varphi}_m^{(2)} = 0, \tag{C.14}$$

where $\mathcal{E}, \mathcal{L}^{ab}_{\mu\nu}, S_{\mu\nu}$ are differential operators. Eq. (C.14) provides an equation of motion for $\tilde{\varphi}^{(2)}_m$, which then provides a source term $S_{\mu\nu}\tilde{\varphi}^{(2)}_m$ to the equation of motion for the metric perturbation $g^{(2)}_{\mu\nu}$. The perturbed quasi-normal modes are solutions of the homogeneous, unsourced equation

$$\mathcal{L}^{ab}_{\mu\nu} g^{(2)}_{ab} = 0. \tag{C.15}$$

When decomposed into odd tensor harmonics, Eq. (C.13) gives Eq. (4.28) where the source term $\mathfrak{S}$ is explicitly (see for example [61])

$$\mathfrak{S}^{lm} = -r^2 \frac{l(l+1)}{(l-1)(l+2)} \epsilon^{ab} \tilde{\nabla}_a \int \Delta T_{Ab} \, (X^A_{lm})^* \mathrm{d}\Omega, \tag{C.16}$$

$$X^A_{lm} = -\epsilon^{AB} \hat{\nabla}_B Y^{lm}(\theta, \phi), \tag{C.17}$$

$$\Delta T_{\mu\nu} = \frac{\delta T_{\mu\nu}}{\delta \varphi_m} \tilde{\varphi}^{(2)}_m, \tag{C.18}$$

where ϵ^{ab} is the Levi-Civita symbol, $\hat{\nabla}_A$ is the covariant derivative on the 2-sphere, " * " denotes complex conjugation and $Y^{lm}(\theta, \phi)$ are the complex spherical harmonics.

C.2 Method in Schwarzschild coordinates

If the metric perturbation is time independent and sufficiently well behaved near the horizon we do not need to introduce ingoing EF coordinates and can instead repeat the derivation in the more familiar Schwarzschild coordinates, which we shall do now.

Let us again consider a perturbed Schwarzschild background metric of the form

$$ds^2 = -(f + \delta f)\mathrm{d}t^2 + (f + \delta g)^{-1}\mathrm{d}r^2 + r^2 \mathrm{d}\Omega, \tag{C.19}$$

where we require $\delta f(r), \delta g(r) \ll 1$ in Schwarzschild coordinates. For odd modes in general, and for even modes in vacuum, this gives a modified QNM master equation of the form

$$\Big[F_* \partial_r (F_* \partial_r) + (\omega^2 - F\, V_*)\Big]\Psi = 0, \tag{C.20}$$

$$F := f + \delta f, \tag{C.21}$$

$$F_*(r) := \sqrt{(f + \delta f)(f + \delta g)} \approx 1 - \frac{2M}{r} + \frac{\delta f(r) + \delta g(r)}{2}, \tag{C.22}$$

$$V_*(r) = V_\pm(r) + \delta V(r), \tag{C.23}$$

where here we use $V_\pm$ to denote the Zerilli/Regge-Wheeler potentials for even/odd modes and we have let $\Psi(t,r) = e^{-i\omega t}\Psi(r)$. In Eq. (C.20) we allow the δV to be an arbitrary function of r, containing both the terms arising from metric perturbations $\delta f, \delta g$, as we saw in the previous section, as well as from (for example) modified gravity effects. The only requirement we will impose is that δV is small compared to the zeroth order potential $V_\pm$. If $\delta g \neq 0$ the location of the BH horizon will be shifted to

$$r_H = 2M\left[1 - \delta g(2M)\right]. \tag{C.24}$$

We can then rewrite $F_*(r)$ as

$$\begin{aligned} F_*(r) =& f_H(r)Z(r), && \text{(C.25)}\\ f_H(r) :=& \left(1 - \frac{r_H}{r}\right), && \text{(C.26)}\\ Z(r) =& 1 + \delta Z(r), && \text{(C.27)}\\ \delta Z(r) =& \frac{r\frac{\delta f(r)+\delta g(r)}{2} - 2M\delta g(2M)}{r - 2M}, && \text{(C.28)} \end{aligned}$$

again working to first order in all perturbed quantities. Note that for δZ to be well behaved at $r = 2M$ we need $\delta f(2M) = \delta g(2M)$. In the case with no modified gravity and with $g(2M) = f(2M) = 0$ we can directly compare to the expressions from section 4.2 and find

$$\delta\lambda = (\delta f - \delta g)/(2f), \tag{C.29}$$

and

$$\delta V = \frac{f}{r}\left(\frac{2\delta Z}{r} - \delta Z'\right) - \frac{2\delta\lambda}{r^2}\left(1 - \frac{3M}{r}\right). \tag{C.30}$$

If we again define $\Phi := \sqrt{Z}\Psi$ Eq. (C.20) can be rewritten as

$$f_H\frac{\partial}{\partial r}\left[f_H\frac{\partial\Phi}{\partial r}\right] + \left[\frac{\omega^2}{Z^2} - f_H V\right]\Phi = 0, \tag{C.31}$$

where to first order in δ

$$V = V_\pm + \delta V + (\delta f - 2\delta Z)V_\pm + \tfrac{1}{2}(f_H\delta Z')', \tag{C.32}$$

and we seperate the ω term as

$$\begin{aligned} \omega/Z^2 &= \omega^2[1 - 2\delta Z(r_H)] - 2\omega_0^2[\delta Z(r) - \delta Z(r_H)],\\ &= \Omega^2 - 2\omega_0^2[\delta Z(r) - \delta Z(2M)], \end{aligned} \tag{C.33}$$

to first order in small quantities. We can also rewrite the potentials $V_\pm$ in terms of r_H:

$$V_+ = \tilde{V}_+ + \delta\tilde{V}_+ \tag{C.34a}$$

$$V_- = \tilde{V}_- + \delta\tilde{V}_- \tag{C.34b}$$

where

$$\tilde{V}_+ = \frac{(\ell+2)(\ell-1)}{3r^2} + \frac{r_H}{r^3} + \frac{2(\ell+2)^2(\ell-1)^2(\ell^2+\ell+1)}{3(3r_H+(\ell+2)(\ell-1)r)^2} \tag{C.35a}$$

$$\delta\tilde{V}_+ = \delta g(2M)\left(\frac{2M}{r^3} - \frac{8M(\ell+2)^2(\ell-1)^2(\ell^2+\ell+1)}{3(6M+(\ell+2)(\ell-1)r)^3}\right) \tag{C.35b}$$

$$\tilde{V}_- = \frac{\ell(\ell+1)}{r^2} + \frac{r_H}{r^3}(1-s^2) \tag{C.35c}$$

$$\delta\tilde{V}_- = \delta g(2M)\frac{2M}{r^3}(1-s^2). \tag{C.35d}$$

Finally we obtain

$$f_H\frac{\partial}{\partial r}\left[f_H\frac{\partial\Phi}{\partial r}\right] + \left[\Omega^2 - f_H\left(\tilde{V}_\pm + \Delta V\right)\right]\Phi = 0 \tag{C.36}$$

where ΔV again collects all the order δ terms, both from the original potential perturbation δV as well as from modified geometry terms. Explicitly,

$$\begin{aligned}\Delta V = \delta V + \delta\tilde{V}_\pm + \tilde{V}_\pm\left(\delta f/f_H - 2\delta Z\right)\\ + \tfrac{1}{2}(f_H\delta Z')' + \frac{2\omega_0^2}{f_H}\left[\delta Z(r) - \delta Z(2M)\right].\end{aligned} \tag{C.37}$$

Unlike in the time dependent case ω and Ω are related by a simple constant rescaling

$$\Omega = \omega\left(1 - \delta Z(2M)\right). \tag{C.38}$$

We can relate $\delta Z(2M)$ to $\delta f, \delta g$ through use of l'Hôpital's rule:

$$\delta Z(2M) = \delta g(2M) + M\left[\delta f'(2M) + \delta g'(2M)\right]. \tag{C.39}$$

If we then again apply the method of [264] we find solutions of the form

$$\omega = \omega_0 + \omega_0\delta Z(2M) + \delta\Omega(\Delta v), \tag{C.40}$$

from which we one can verify that the perturbative expressions for $\delta\Omega(\Delta V)$ match those we derived in the main text with δA set to zero. The full expressions for general spin s are given in appendix D of [2].

Table C.1: Comparison between the analytic results presented here and the numeric results of Cardoso et al for the $\ell = 2$ odd parity gravitational QNM deviation $\Delta\omega$ to order L^{-8}.

p	$2M\Delta\omega$ (analytic)	$2M\Delta\omega$ (numeric)	% error $\Delta\omega_R$	% error $\Delta\omega_I$
0	0.243747+0.0913876i	0.247252+0.0926431i	-1.41747	-1.3552
1	0.158967+0.0180090i	0.159855+0.0182085i	-0.555267	-1.09556
2	0.0966513-0.00277561i	0.0966322-0.0024155i	0.019719	14.9086
3	0.0585225-0.00410688i	0.0584908-0.00371786i	0.0542632	10.4635
4	0.0366465-0.000745599i	0.0366794-0.000438698i	-0.0896896	69.9573
5	0.0240123+0.00249465i	0.0240379+0.00273079i	-0.106785	-8.64721

Table C.2: Comparison between the analytic results presented here and the numeric results of Cardoso et al for the $\ell = 2$ even parity gravitational QNM deviation $\Delta\omega$ to order L^{-8}.

p	$2M\Delta\omega$ (analytic)	$2M\Delta\omega$ (numeric)	% error $\Delta\omega_R$	% error $\Delta\omega_I$
0	0.224732+0.0916972 i	0.22325+0.09312 i	0.663953	-1.52787
1	0.153719+0.0195864 i	0.154195+0.019927ii	-0.308834	-1.70931
2	0.0974921-0.00328011 i	0.0978817-0.0034275 i	-0.398015	-4.30028
3	0.0614226-0.00618217 i	0.0616142-0.0064403 i	-0.310969	-4.00799
4	0.0399055-0.00334236 i	0.0400156-0.0036191 i	-0.275227	-7.64665
5	0.0271051+0.0000307656 i	0.0271849-0.0002403 i	-0.293483	-112.803

C.3 Testing the method

We do not have numerical results for the QNM perturbations of a growing dirty black hole to compare to the analytic results derived in the previous section. However we can apply the same techniques to several other examples in Schwarzschild coordinates for which results have been previously obtained - specifically, power law potentials, exponential potentials, Reissner-Nordstrom and de Sitter. In particular, we confirm that the 5th order perturbative expansion of the frequency shift should be sufficiently accurate, and that higher corrections will not significantly change the result.

C.3.1 Power law potentials

First we will try potential deviations δV about a pure Schwarzschild background, such that $\delta f = \delta g = 0$. To compare with the numerical results of Cardoso et al. (2019) [263], we will first assume the following form for the potential deviations

Table C.3: Comparison between the analytic results presented here and the numeric results of Cardoso et al. (2019) [263] for an exponential potential deviation for the even parity gravitational modes to order L^{-8}.

ℓ	$2M\Delta\omega$ (analytic)	$2M\Delta\omega$ (numeric)	% error $\Delta\omega_R$	% error $\Delta\omega_I$
2	0.439353+0.108479 i	0.438579+0.110111 i	0.176484	-1.48256
3	0.274923+0.0447816 i	0.274902+0.0448262 i	0.00780032	-0.0996234
4	0.202828+0.0250234 i	0.202826+0.0250268 i	0.000874023	-0.013268
5	0.161632+0.0161213 i	0.161632+0.0161217 i	0.000123541	-0.002308

(for both Regge-Wheeler and Zerilli type equations):

$$\delta V = \frac{\alpha}{(2M)^2}\left(\frac{2M}{r}\right)^p, \; p \geq 0. \tag{C.41}$$

and α is a dimensionless constant. In Cardoso et al., p is assumed to be an integer and numeric results for QNM deviations are provided for values of p from 0 to 50. In this section we will first compare the analytic results at integer values to the Cardoso et al. values before allowing p to vary continuously.

Tables C.1 and C.2 show a comparison for the first few values of p for the odd and even parity $\ell = 2$ gravitational QNMs respectively to order L^{-8}. We see that very good agreement between the two methods is found in the real part of the frequency deviation $\Delta\omega_R$, with slightly worse agreement in the imaginary part $\Delta\omega_I$. Note that some of the percentage errors can be misleading when the values of the deviations are extremely close to 0, for example in the case of the $p = 5$ deviation for the $\ell = 2$ even parity QNM.

We've seen that for potential deviations of the form given in Eq. (C.41) the analytic QNM deviations presented here compare well with those calculated numerically as long as the index p doesn't exceed around 15, though this 'guide' is dependent on the angular harmonic index ℓ (good agreement is found for larger p with high ℓ) and on whether the perturbations are of scalar, vector, or gravitational type.

Fig. C.1 shows a plot of the numeric results of Cardoso et al. with the analytic QNM deviations presented here, for both the $\ell = 2$ odd and even parity gravitational QNMs. In this case we are allowing p to be continuous for the analytic results. Good agreement is shown between the two methods up to around $p = 10$, at which point the imaginary component of the analytic $\Delta\omega$ starts to visibly deviate from the numeric results. We find that above around $p = 15$ large

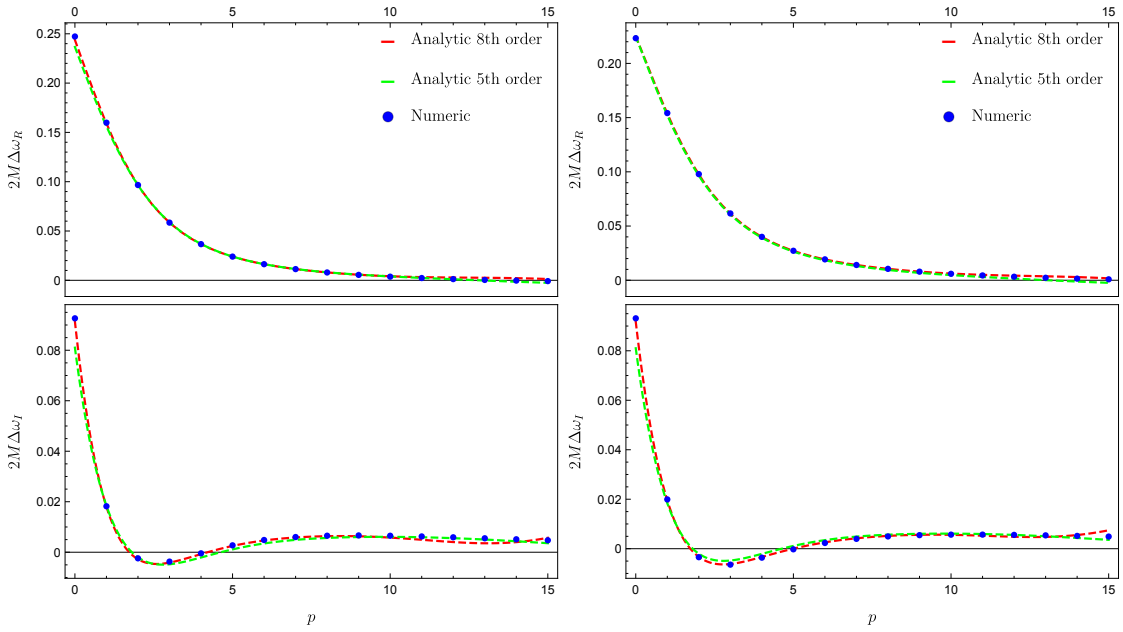

Figure C.1: **Power law potential quasi-normal modes**. We compare the analytic results presented here and the numeric results of Cardoso et al. (2019) [263] for the $\ell = 2$ odd (left panel) and even (right panel) parity $\Delta\omega$ to order L^{-8} (red) and order L^{-5} (green).

deviations from the numeric results are seen in both the $\Delta\omega_R$ and $\Delta\omega_I$, with the analytic curve showing oscillatory behaviour. We do not have an explanation for this shortcoming at the moment, so clearly the analytic results are best restricted for use up to $p \approx 15$. Similar behaviour is seen for vector and scalar perturbations, with better agreement between the analytic and numeric results found for larger values of ℓ.

C.3.2 Exponential potential

We will now study more unconventional potential deviations and again compare the analytic QNM deviation results with those calculated numerically. First, we consider the addition of an exponential function to the potential:

$$\delta V = \frac{1}{(2M)^2} \exp\left(\frac{2M}{r}\right). \tag{C.42}$$

If we use the Taylor series representation of the exponential function we can write Eq. (C.42) as a sum of integer powers of $2M/r$, thus allowing us to use the results of Cardoso et al. as a comparison for the analytic results. Table C.3 gives the

deviations calculated with both methods for the $\ell = 2-5$ even parity gravitational modes, with extremely good agreement found between the two methods.

C.3.3 Reissner-Nordström background

Following Dolan & Ottewill (2009) [264] we can write the unperturbed master equation for the charged Reissner-Nordström black hole as

$$f_q \frac{\partial}{\partial r}\left[f_q \frac{\partial \Psi}{\partial r}\right] + \left[\omega^2 - f_q V_\pm\right]\Psi = 0, \tag{C.43}$$

where $q = Q/M$ the charge-to-mass ratio, $f_q(r) = 1 - 2M/r + q^2M^2/r^2$, and the odd mode potential is

$$V_- = \frac{L^2 - 1/4}{r^2} - \frac{M\kappa_s}{r^3} + \frac{q^2M^2\eta_s}{r^4}, \tag{C.44}$$

where

$$\eta_s, \kappa_s = \begin{cases} 2,\ -2 & s = 0 \\ 4,\ 3 - \sqrt{9 + 4q^2(L^2 - 9/4)} & s = 1 \\ 4,\ 3 + \sqrt{9 + 4q^2(L^2 - 9/4)} & s = 2. \end{cases} \tag{C.45}$$

The Reissner-Nordström metric is

$$\mathrm{d}s^2 = -f_q \mathrm{d}t^2 + f_q^{-1}\mathrm{d}r^2 + r^2\mathrm{d}\Omega. \tag{C.46}$$

Consider the weakly charged case where $q \ll 1$. In that limit we can assign

$$\delta f(r) = \delta g(r) = q^2M^2/r^2, \tag{C.47}$$

$$\delta V(r) = q^2\left[\frac{M(\frac{3}{2} - \frac{2}{3}L^2)}{r^3} + \frac{4M^2}{r^4}\right]. \tag{C.48}$$

This gives for the $n = 0$, $l = 2$ odd mode (again to order L^{-8})

$$\omega_{QNM} = \omega_0 + \frac{(0.0252499 - 0.00267011\mathrm{i})q^2}{M} + \mathcal{O}(q^3), \tag{C.49}$$

which compares favourably to the numerical result from Cardoso et al. of

$$\omega_{QNM} = \omega_0 + \frac{(0.0258177 - 0.002824\mathrm{i})q^2}{M} + \mathcal{O}(q^3), \tag{C.50}$$

with a relative difference of $2.2\%, 5.4\%$ between the two for the real and imaginary parts respectively.

C.3.4 De Sitter background

In Schwarzschild de Sitter (SdS) spacetime the line element takes the form

$$\mathrm{d}s^2 = -f_{\delta\Lambda}\mathrm{d}t^2 + f_{\delta\Lambda}^{-1}\mathrm{d}r^2 + r^2\mathrm{d}\Omega \tag{C.51}$$

where $f_{\delta\Lambda}(r) = 1 - 2M/r - \delta\Lambda r^2/3$. The master equation is

$$f_{\delta\Lambda}\frac{\partial}{\partial r}\left[f_{\delta\Lambda}\frac{\partial\Psi}{\partial r}\right] + \left[\omega^2 - f_{\delta\Lambda}V_{\pm}\right]\Psi = 0, \tag{C.52}$$

where $V_{\pm}$ again denote the standard Zerilli/Regge-Wheeler potentials. Let $\delta\tilde{\Lambda} = \delta\Lambda M^2$. If we take $\delta\tilde{\Lambda} \ll 1$ we can proceed as before

$$\delta f(r) = \delta g(r) = -\delta\Lambda r^2/3, \quad \delta V(r) = 0. \tag{C.53}$$

For the $n = 0$, $l = 2$ odd mode to order L^{-8} we find

$$\omega_{QNM} = \omega_0 + (-1.67328 + 0.332735\mathrm{i})\delta\tilde{\Lambda}/M + \mathcal{O}(\delta\tilde{\Lambda}^2). \tag{C.54}$$

The equivalent calculation for non-linear $\delta\Lambda$ dependence to order L^{-6} (see Tattersall (2018) [469])) gives

$$\begin{aligned}\omega_{QNM} =& \omega_0 + (-1.67328 + 0.332735\mathrm{i})\delta\tilde{\Lambda}/M + \\ & (-3.90506 + 1.15466\mathrm{i})\delta\tilde{\Lambda}^2/M + \\ & (-16.9027 + 5.13741\mathrm{i})\delta\tilde{\Lambda}^3/M + \mathcal{O}(\delta\tilde{\Lambda}^4),\end{aligned} \tag{C.55}$$

so for small $\delta\tilde{\Lambda}$ we have excellent agreement with the non-linear calculation with a fraction of the effort. Note that this is mathematically equivalent to the case of non-accreting uniform density dark matter as described in [148] equation (67) with $\delta\Lambda = 8\pi\rho_{DM}$.

Appendix D

Black hole merger simulations in wave dark matter environments

D.1 Numerical implementation and convergence tests

For the simple fixed orbit model described in section 5.2 we only solve equations (2.34) and (2.35) in such a background. We excise (set the evolution variables to zero) within a small region around each black hole centre, inside the horizon, to avoid numerical errors, and evaluate the values of the metric components and their derivatives analytically at each point on the grid. For the highly relativistic merger, in addition to solving Eqns. (2.34) and (2.35), we solve the full Einstein equations numerically. For this we use the CCZ4 formalism [178], as described in chapter 2 and appendix A.2, with the moving puncture gauge [184, 185, 359, 470, 471]. The parameters for the initial state of the black hole binary are given in table D.1.

d/M	12.21358
$M_{\rm BH}/M$	0.48847892320123
$\lvert p_x\rvert/M$	5.10846×10^{-4}
$\lvert p_y\rvert/M$	8.41746×10^{-2}
$\lvert p_z\rvert/M$	0
T/M	271.34

Table D.1: **Black hole binary initial parameters.**[2] The black holes are initially aligned along the x axis in the $z = 0$ plane, with initial momenta $\vec{p}_1 = (-|p_x|, +|p_y|, 0)$ for the BH with initial position $\vec{r}_1 = (d/2, 0, 0)$ and $\vec{p}_2 = (+|p_x|, -|p_y|, 0)$ for the one at $\vec{r}_2 = (-d/2, 0, 0)$.

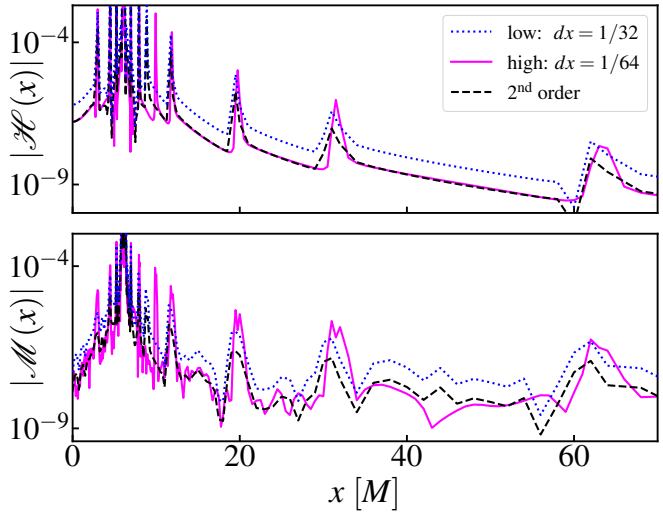

Figure D.1: **Convergence test: constraint satisfying initial data**. We show convergence in the absolute value of the error in the Hamiltonian and momentum constraints for the the fixed orbit initial data (the most sharply peaked, and therefore most difficult, choice of initial scalar field data) at time $t = 0$. The error is consistent with the 2nd order finite difference stencils used in the CTTK solver [188].

In both cases we use the open-source Numerical Relativity code GRChombo [193, 194] with adaptive mesh refinement [183], described in section 2.9.

We use a simulation box length $L = 512M$ and 8 levels of mesh refinement (See Figs. D.1 and D.2 for convergence tests). Taking advantage of the symmetry in the xy plane we impose reflecting boundary conditions at $z = 0$, while for the other boundaries we impose either first order extrapolating boundary conditions (matching the first derivative on the exterior ghost cells to that inside the simulation grid) or Sommerfeld boundary conditions.

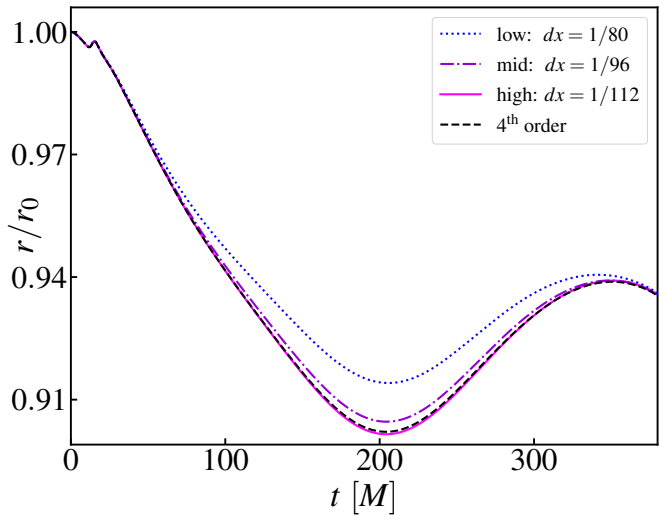

Figure D.2: **Convergence test: black hole puncture trajectory.** Here we show the radial position of one of the black hole punctures for a BBH with $G = 1$ and a scalar cloud of $M_{\text{cloud}}/M = 10^{-5}$ for different resolutions. The black dashed line represents the expected values for $dx = 1/112$ if the simulation had 4th order convergence, which match the measured pink solid line and hence infer that the decrease in the error is consistent with 4^{th} order stencils used in the evolution code.

Appendix E

Fifth force constraints

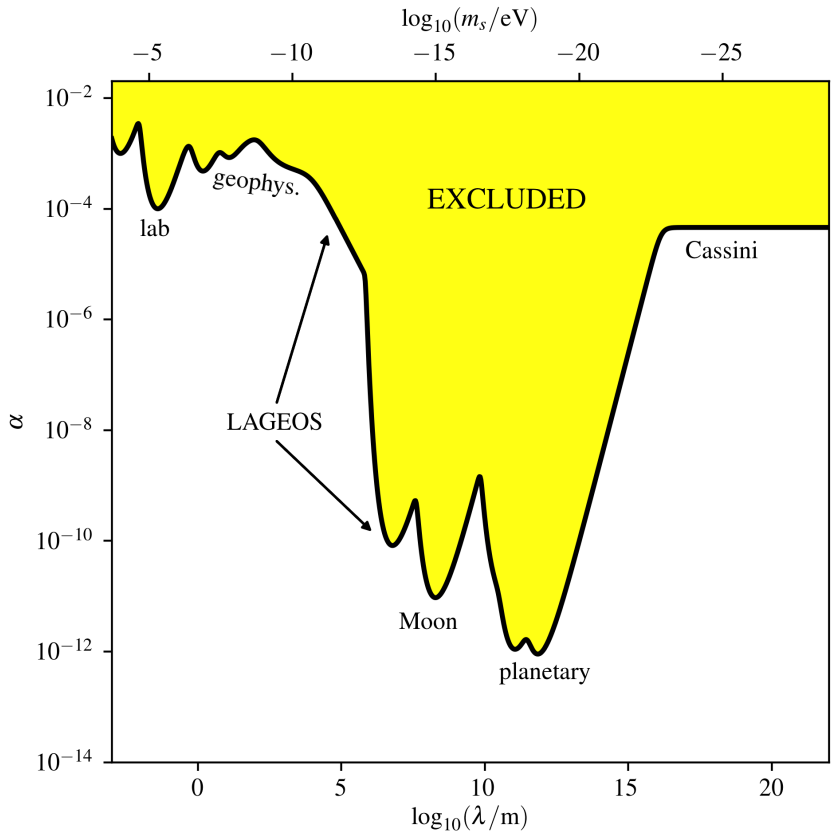

Figure E.1: **Fifth force constraints**. Summary of the 2σ constraints from current experimental and observational data on Yukawa-like fifth forces across a range of length scales and the corresponding mass scales. Different experiments test different scales: here we include lab experiments [472–475], geophysical tests [476, 477], results using the LAGEOS I & II satellites [476, 478], Lunar Laser Ranging (LLR) with the Moon [479, 480], planetary constraints [481–484], and Shapiro time delay with the Cassini mission [377, 485]. The latter constraint extends to massless fields $m_s = 0$.

Bibliography

[1] J. Bamber, K. Clough, P. G. Ferreira, L. Hui, and M. Lagos, "Growth of accretion driven scalar hair around Kerr black holes," *Phys. Rev. D* **103** no. 4, (2021) 044059, arXiv:2011.07870 [gr-qc].

[2] J. Bamber, O. J. Tattersall, K. Clough, and P. G. Ferreira, "Quasinormal modes of growing dirty black holes," *Phys. Rev. D* **103** no. 12, (2021) 124013, arXiv:2103.00026 [gr-qc].

[3] J. Bamber, J. C. Aurrekoetxea, K. Clough, and P. G. Ferreira, "Black hole merger simulations in wave dark matter environments," *Phys. Rev. D* **107** no. 2, (2023) 024035, arXiv:2210.09254 [gr-qc].

[4] J. Bamber, "Fifth forces and frame invariance," *Phys. Rev. D* **107** no. 2, (2023) 024013, arXiv:2210.06396 [gr-qc].

[5] D. Stanzione, J. West, R. T. Evans, T. Minyard, O. Ghattas, and D. K. Panda, "Frontera: The evolution of leadership computing at the national science foundation," in *Practice and Experience in Advanced Research Computing*, PEARC '20, p. 106–111. Association for Computing Machinery, New York, NY, USA, 2020. https://doi.org/10.1145/3311790.3396656.

[6] T. Kobayashi, "Experimental verification of the standard model of particle physics," *Proceedings of the Japan Academy, Series B* **97** no. 5, (2021) 211–235.

[7] J. Erler and M. Schott, "Electroweak Precision Tests of the Standard Model after the Discovery of the Higgs Boson," *Prog. Part. Nucl. Phys.* **106** (2019) 68–119, arXiv:1902.05142 [hep-ph].

[8] **Event Horizon Telescope** Collaboration, K. Akiyama *et al.*, "First M87 Event Horizon Telescope Results. VI. The Shadow and Mass of the Central Black Hole," *Astrophys. J. Lett.* **875** no. 1, (2019) L6, arXiv:1906.11243 [astro-ph.GA].

[9] **Event Horizon Telescope** Collaboration, K. Akiyama *et al.*, "First Sagittarius A* Event Horizon Telescope Results. VI. Testing the Black Hole Metric," *Astrophys. J. Lett.* **930** no. 2, (2022) L17.

[10] A. Einstein, "On the electrodynamics of moving bodies," *Annalen Phys.* **17** (1905) 891–921.

[11] R. M. Wald, "Teaching general relativity," arXiv:gr-qc/0511073.

[12] M. Alcubierre, *Introduction to 3+1 Numerical Relativity*, vol. 140 of *International Series of Monographs on Physics*. Oxford University Press, Oxford, 2008.

[13] J. A. Wheeler and K. W. Ford, *Geons, black holes and quantum foam : a life in physics*. W.W. Norton & Company, New York, 1998.

[14] S. M. Carroll, *Spacetime and geometry : an introduction to general relativity*, ch. 6. Addison Wesley, San Francisco ; Harlow, 2003.

[15] K. Schwarzschild, "On the gravitational field of a mass point according to Einstein's theory," *Sitzungsber. Preuss. Akad. Wiss. Berlin (Math. Phys.)* **1916** (1916) 189–196, arXiv:physics/9905030.

[16] D. Tong, "Lectures on general relativity." 2019. http://www.damtp.cam.ac.uk/user/tong/gr.html.

[17] R. P. Kerr, "Gravitational field of a spinning mass as an example of algebraically special metrics," *Phys. Rev. Lett.* **11** (1963) 237–238.

[18] H. S. Vieira, V. B. Bezerra, and C. R. Muniz, "Exact solutions of the Klein-Gordon equation in the Kerr-Newman background and Hawking radiation," *Annals Phys.* **350** (2014) 14–28, arXiv:1401.5397 [gr-qc].

[19] R. Penrose, "Gravitational collapse: The role of general relativity," *Riv. Nuovo Cim.* **1** (1969) 252–276.

[20] Z. Stuchlík, M. Kološ, and A. Tursunov, "Penrose Process: Its Variants and Astrophysical Applications," *Universe* **7** no. 11, (2021) 416.

[21] R. Brito, V. Cardoso, and P. Pani, "Superradiance: New Frontiers in Black Hole Physics," *Lect. Notes Phys.* **906** (2015) pp.1–237, arXiv:1501.06570 [gr-qc].

[22] B. Carter, "Axisymmetric Black Hole Has Only Two Degrees of Freedom," *Phys. Rev. Lett.* **26** (1971) 331–333.

[23] W. Israel, "Event horizons in static electrovac space-times," *Commun. Math. Phys.* **8** (1968) 245–260.

[24] M. Heusler, "No hair theorems and black holes with hair," *Helv. Phys. Acta* **69** no. 4, (1996) 501–528, arXiv:gr-qc/9610019.

[25] C. A. R. Herdeiro and E. Radu, "Asymptotically flat black holes with scalar hair: a review," *Int. J. Mod. Phys. D* **24** no. 09, (2015) 1542014, arXiv:1504.08209 [gr-qc].

[26] C. Bambi, A. D. Dolgov, and A. A. Petrov, "Black holes as antimatter factories," *JCAP* **09** (2009) 013, arXiv:0806.3440 [astro-ph].

[27] C. Bambi, "Astrophysical Black Holes: A Review," *PoS* **MULTIF2019** (2020) 028, arXiv:1906.03871 [astro-ph.HE].

[28] L. Hui and A. Nicolis, "No-Hair Theorem for the Galileon," *Phys. Rev. Lett.* **110** (2013) 241104, arXiv:1202.1296 [hep-th].

[29] A. A. H. Graham and R. Jha, "Nonexistence of black holes with noncanonical scalar fields," *Phys. Rev. D* **89** no. 8, (2014) 084056, arXiv:1401.8203 [gr-qc]. [Erratum: Phys.Rev.D 92, 069901 (2015)].

[30] T. P. Sotiriou, "Black Holes and Scalar Fields," *Class. Quant. Grav.* **32** no. 21, (2015) 214002, arXiv:1505.00248 [gr-qc].

[31] T. Jacobson, "Primordial black hole evolution in tensor scalar cosmology," *Phys. Rev. Lett.* **83** (1999) 2699–2702, arXiv:astro-ph/9905303.

[32] S. E. Woosley and A. Heger, "The Pair-Instability Mass Gap for Black Holes," *Astrophys. J. Lett.* **912** no. 2, (2021) L31, arXiv:2103.07933 [astro-ph.SR].

[33] D. Croon, S. D. McDermott, and J. Sakstein, "New physics and the black hole mass gap," *Phys. Rev. D* **102** no. 11, (2020) 115024, arXiv:2007.07889 [gr-qc].

[34] C. Bambi, "Astrophysical Black Holes: A Compact Pedagogical Review," *Annalen Phys.* **530** (2018) 1700430, arXiv:1711.10256 [gr-qc].

[35] J. E. Greene, J. Strader, and L. C. Ho, "Intermediate-mass black holes," *Annual Review of Astronomy and Astrophysics* **58** no. 1, (2020) 257–312. https://doi.org/10.1146/annurev-astro-032620-021835.

[36] A. Escrivà, F. Kuhnel, and Y. Tada, "Primordial Black Holes," arXiv:2211.05767 [astro-ph.CO].

[37] B. J. Carr and S. W. Hawking, "Black holes in the early Universe," *Mon. Not. Roy. Astron. Soc.* **168** (1974) 399–415.

[38] I. Vidaña, "A short walk through the physics of neutron stars," *Eur. Phys. J. Plus* **133** no. 10, (2018) 445, arXiv:1805.00837 [nucl-th].

[39] P. D. Lasky, "Gravitational Waves from Neutron Stars: A Review," *Publ. Astron. Soc. Austral.* **32** (2015) e034, arXiv:1508.06643 [astro-ph.HE].

[40] Y. Lim and J. W. Holt, "Neutron Star Radii, Deformabilities, and Moments of Inertia from Experimental and Ab Initio Theory Constraints of the ^{208}Pb Neutron Skin Thickness," *Galaxies* **10** no. 5, (2022) 99, arXiv:2204.09000 [nucl-th].

[41] F. Özel and P. Freire, "Masses, Radii, and the Equation of State of Neutron Stars," *Ann. Rev. Astron. Astrophys.* **54** (2016) 401–440, arXiv:1603.02698 [astro-ph.HE].

[42] J. M. Lattimer and M. Prakash, "The physics of neutron stars," *Science* **304** (2004) 536–542, arXiv:astro-ph/0405262.

[43] C.-M. Chen, J. M. Nester, and W.-T. Ni, "A brief history of gravitational wave research," *Chin. J. Phys.* **55** (2017) 142–169, arXiv:1610.08803 [gr-qc].

[44] **LIGO Scientific** Collaboration, J. Aasi *et al.*, "Advanced LIGO," *Class. Quant. Grav.* **32** (2015) 074001, arXiv:1411.4547 [gr-qc].

[45] **VIRGO** Collaboration, F. Acernese *et al.*, "Advanced Virgo: a second-generation interferometric gravitational wave detector," *Class. Quant. Grav.* **32** no. 2, (2015) 024001, arXiv:1408.3978 [gr-qc].

[46] **LIGO Scientific, Virgo** Collaboration, B. P. Abbott *et al.*, "Observation of Gravitational Waves from a Binary Black Hole Merger," *Phys. Rev. Lett.* **116** no. 6, (2016) 061102, arXiv:1602.03837 [gr-qc].

[47] **LIGO Scientific, VIRGO, KAGRA** Collaboration, R. Abbott *et al.*, "GWTC-3: Compact Binary Coalescences Observed by LIGO and Virgo During the Second Part of the Third Observing Run," (11, 2021) , arXiv:2111.03606 [gr-qc].

[48] **KAGRA** Collaboration, T. Akutsu *et al.*, "Overview of KAGRA: Detector design and construction history," *PTEP* **2021** no. 5, (2021) 05A101, arXiv:2005.05574 [physics.ins-det].

[49] **LISA** Collaboration, P. McNamara, S. Vitale, and K. Danzmann, "LISA Pathfinder," *Class. Quant. Grav.* **25** (2008) 114034.

[50] M. Maggiore *et al.*, "Science Case for the Einstein Telescope," *JCAP* **03** (2020) 050, arXiv:1912.02622 [astro-ph.CO].

[51] D. Reitze *et al.*, "Cosmic Explorer: The U.S. Contribution to Gravitational-Wave Astronomy beyond LIGO," *Bull. Am. Astron. Soc.* **51** no. 7, (2019) 035, arXiv:1907.04833 [astro-ph.IM].

[52] P. Schmidt, "Gravitational Waves From Binary Black Hole Mergers: Modeling and Observations," *Front. Astron. Space Sci.* **7** (2020) 28.

[53] L. Blanchet, "Gravitational Radiation from Post-Newtonian Sources and Inspiralling Compact Binaries," *Living Rev. Rel.* **17** (2014) 2, arXiv:1310.1528 [gr-qc].

[54] A. L. Piro, B. Giacomazzo, and R. Perna, "The Fate of Neutron Star Binary Mergers," *Astrophys. J. Lett.* **844** no. 2, (2017) L19, arXiv:1704.08697 [astro-ph.HE].

[55] K. D. Kokkotas and B. G. Schmidt, "Quasinormal modes of stars and black holes," *Living Rev. Rel.* **2** (1999) 2, arXiv:gr-qc/9909058.

[56] H.-P. Nollert, "TOPICAL REVIEW: Quasinormal modes: the characteristic 'sound' of black holes and neutron stars," *Class. Quant. Grav.* **16** (1999) R159–R216.

[57] E. Berti, V. Cardoso, and A. O. Starinets, "Quasinormal modes of black holes and black branes," *Class. Quant. Grav.* **26** (2009) 163001, arXiv:0905.2975 [gr-qc].

[58] R. A. Konoplya and A. Zhidenko, "Quasinormal modes of black holes: From astrophysics to string theory," *Rev. Mod. Phys.* **83** (2011) 793–836, arXiv:1102.4014 [gr-qc].

[59] O. J. Tattersall and P. G. Ferreira, "Quasinormal modes of black holes in Horndeski gravity," *Phys. Rev. D* **97** no. 10, (2018) 104047, arXiv:1804.08950 [gr-qc].

[60] A. Nagar and L. Rezzolla, "Gauge-invariant non-spherical metric perturbations of Schwarzschild black-hole spacetimes," *Class. Quant. Grav.* **22** (2005) R167, arXiv:gr-qc/0502064. [Erratum: Class.Quant.Grav. 23, 4297 (2006)].

[61] K. Martel and E. Poisson, "Gravitational perturbations of the Schwarzschild spacetime: A Practical covariant and gauge-invariant formalism," *Phys. Rev. D* **71** (2005) 104003, arXiv:gr-qc/0502028.

[62] S. A. Teukolsky, "Perturbations of a rotating black hole. 1. Fundamental equations for gravitational electromagnetic and neutrino field perturbations," *Astrophys. J.* **185** (1973) 635–647.

[63] S. Chandrasekhar, *The mathematical theory of black holes*. Oxford University Press, 1985.

[64] S. Carlip, "Quantum gravity: A Progress report," *Rept. Prog. Phys.* **64** (2001) 885, arXiv:gr-qc/0108040.

[65] C. Kiefer, "Quantum gravity – an unfinished revolution," 2, 2023. arXiv:2302.13047 [gr-qc].

[66] G. Dvali, "A Lecture on the Hierarchy Problem and Gravity,". https://cds.cern.ch/record/2120792.

[67] **Particle Data Group** Collaboration, R. L. Workman, "Review of Particle Physics," *PTEP* **2022** (2022) 083C01.

[68] R. H. Brandenberger, "Back reaction of cosmological perturbations and the cosmological constant problem," in *18th IAP Colloquium on the Nature of Dark Energy: Observational and Theoretical Results on the Accelerating Universe*. 10, 2002. arXiv:hep-th/0210165.

[69] L. Amendola and S. Tsujikawa, *Dark Energy: Theory and Observations*. Cambridge University Press, 1, 2015.

[70] D. Scott, "The standard model of cosmology: A skeptic's guide," *Proc. Int. Sch. Phys. Fermi* **200** (2020) 133–153, arXiv:1804.01318 [astro-ph.CO].

[71] A. Padilla, "Lectures on the Cosmological Constant Problem," arXiv:1502.05296 [hep-th].

[72] S. Weinberg, "The Cosmological Constant Problem," *Rev. Mod. Phys.* **61** (1989) 1–23.

[73] V. A. Rubakov, "Cosmology and dark matter," *CERN Yellow Rep. School Proc.* **5** (2022) 129, arXiv:1912.04727 [hep-ph].

[74] A. H. Guth, "The Inflationary Universe: A Possible Solution to the Horizon and Flatness Problems," *Phys. Rev. D* **23** (1981) 347–356.

[75] J. Martin, C. Ringeval, and V. Vennin, "Encyclopædia Inflationaris," *Phys. Dark Univ.* **5-6** (2014) 75–235, arXiv:1303.3787 [astro-ph.CO].

[76] **ATLAS** Collaboration, G. Aad *et al.*, "Observation of a new particle in the search for the Standard Model Higgs boson with the ATLAS detector at the LHC," *Phys. Lett. B* **716** (2012) 1–29, arXiv:1207.7214 [hep-ex].

[77] **CMS** Collaboration, S. Chatrchyan *et al.*, "Observation of a New Boson at a Mass of 125 GeV with the CMS Experiment at the LHC," *Phys. Lett. B* **716** (2012) 30–61, arXiv:1207.7235 [hep-ex].

[78] L. Di Luzio, M. Giannotti, E. Nardi, and L. Visinelli, "The landscape of QCD axion models," *Phys. Rept.* **870** (2020) 1–117, arXiv:2003.01100 [hep-ph].

[79] D. I. Kazakov, "Prospects of elementary particle physics," *Usp. Fiz. Nauk* **189** no. 4, (2019) 387–401.

[80] R. D. Peccei and H. R. Quinn, "CP Conservation in the Presence of Instantons," *Phys. Rev. Lett.* **38** (1977) 1440–1443.

[81] R. D. Peccei, "The Strong CP problem and axions," *Lect. Notes Phys.* **741** (2008) 3–17, arXiv:hep-ph/0607268.

[82] D. J. E. Marsh, "Axion Cosmology," *Phys. Rept.* **643** (2016) 1–79, arXiv:1510.07633 [astro-ph.CO].

[83] A. Arvanitaki, S. Dimopoulos, S. Dubovsky, N. Kaloper, and J. March-Russell, "String Axiverse," *Phys. Rev. D* **81** (2010) 123530, arXiv:0905.4720 [hep-th].

[84] A. Arvanitaki and S. Dubovsky, "Exploring the String Axiverse with Precision Black Hole Physics," *Phys. Rev. D* **83** (2011) 044026, arXiv:1004.3558 [hep-th].

[85] D. J. E. Marsh, E. R. M. Tarrant, E. J. Copeland, and P. G. Ferreira, "Cosmology of Axions and Moduli: A Dynamical Systems Approach," *Phys. Rev. D* **86** (2012) 023508, arXiv:1204.3632 [hep-th].

[86] T. Clifton, P. G. Ferreira, A. Padilla, and C. Skordis, "Modified Gravity and Cosmology," *Phys. Rept.* **513** (2012) 1–189, arXiv:1106.2476 [astro-ph.CO].

[87] T. P. Sotiriou, "Gravity and Scalar Fields," *Lect. Notes Phys.* **892** (2015) 3–24, arXiv:1404.2955 [gr-qc].

[88] S. Tsujikawa, "Modified gravity models of dark energy," *Lect. Notes Phys.* **800** (2010) 99–145, arXiv:1101.0191 [gr-qc].

[89] G. Wolschin, ed., *Lectures on cosmology: accelerated expansion of the Universe*. Springer, Berlin, 2010.

[90] G. W. Horndeski, "Second-order scalar-tensor field equations in a four-dimensional space," *Int. J. Theor. Phys.* **10** (1974) 363–384.

[91] O. J. Tattersall and P. G. Ferreira, "Forecasts for Low Spin Black Hole Spectroscopy in Horndeski Gravity," *Phys. Rev. D* **99** no. 10, (2019) 104082, arXiv:1904.05112 [gr-qc].

[92] S. Hou, Y. Gong, and Y. Liu, "Polarizations of Gravitational Waves in Horndeski Theory," *Eur. Phys. J. C* **78** no. 5, (2018) 378, arXiv:1704.01899 [gr-qc].

[93] R. Kase and S. Tsujikawa, "Dark energy in Horndeski theories after GW170817: A review," *Int. J. Mod. Phys. D* **28** no. 05, (2019) 1942005, arXiv:1809.08735 [gr-qc].

[94] T. P. Sotiriou and V. Faraoni, "f(R) Theories Of Gravity," *Rev. Mod. Phys.* **82** (2010) 451–497, arXiv:0805.1726 [gr-qc].

[95] J. Gleyzes, D. Langlois, F. Piazza, and F. Vernizzi, "Healthy theories beyond Horndeski," *Phys. Rev. Lett.* **114** no. 21, (2015) 211101, arXiv:1404.6495 [hep-th].

[96] J. Gleyzes, D. Langlois, F. Piazza, and F. Vernizzi, "Exploring gravitational theories beyond Horndeski," *JCAP* **02** (2015) 018, arXiv:1408.1952 [astro-ph.CO].

[97] D. Langlois, "Dark energy and modified gravity in degenerate higher-order scalar–tensor (DHOST) theories: A review," *Int. J. Mod. Phys. D* **28** no. 05, (2019) 1942006, arXiv:1811.06271 [gr-qc].

[98] **LIGO Scientific, Virgo** Collaboration, B. P. Abbott *et al.*, "GW170817: Observation of Gravitational Waves from a Binary Neutron Star Inspiral," *Phys. Rev. Lett.* **119** no. 16, (2017) 161101, arXiv:1710.05832 [gr-qc].

[99] **LIGO Scientific, Virgo, Fermi-GBM, INTEGRAL** Collaboration, B. P. Abbott *et al.*, "Gravitational Waves and Gamma-rays from a Binary Neutron Star Merger: GW170817 and GRB 170817A," *Astrophys. J. Lett.* **848** no. 2, (2017) L13, arXiv:1710.05834 [astro-ph.HE].

[100] J. Sakstein and B. Jain, "Implications of the Neutron Star Merger GW170817 for Cosmological Scalar-Tensor Theories," *Phys. Rev. Lett.* **119** no. 25, (2017) 251303, arXiv:1710.05893 [astro-ph.CO].

[101] A. Emir Gümrükçüoğlu, M. Saravani, and T. P. Sotiriou, "Hořava gravity after GW170817," *Phys. Rev. D* **97** no. 2, (2018) 024032, arXiv:1711.08845 [gr-qc].

[102] C. Brans and R. H. Dicke, "Mach's principle and a relativistic theory of gravitation," *Phys. Rev.* **124** (1961) 925–935.

[103] T. Damour and G. Esposito-Farese, "Tensor multiscalar theories of gravitation," *Class. Quant. Grav.* **9** (1992) 2093–2176.

[104] E. Poisson and C. M. Will, *Gravity: Newtonian, Post-Newtonian, Relativistic*. Cambridge University Press, 2014.

[105] H. Yukawa, "On the Interaction of Elementary Particles I," *Proc. Phys. Math. Soc. Jap.* **17** (1935) 48–57.

[106] J. Khoury and A. Weltman, "Chameleon cosmology," *Phys. Rev. D* **69** (2004) 044026, arXiv:astro-ph/0309411.

[107] C. Burrage and J. Sakstein, "Tests of Chameleon Gravity," *Living Rev. Rel.* **21** no. 1, (2018) 1, arXiv:1709.09071 [astro-ph.CO].

[108] K. Hinterbichler and J. Khoury, "Symmetron Fields: Screening Long-Range Forces Through Local Symmetry Restoration," *Phys. Rev. Lett.* **104** (2010) 231301, arXiv:1001.4525 [hep-th].

[109] K. Hinterbichler, J. Khoury, A. Levy, and A. Matas, "Symmetron Cosmology," *Phys. Rev. D* **84** (2011) 103521, arXiv:1107.2112 [astro-ph.CO].

[110] J. Sakstein, *Astrophysical Tests of Modified Gravity*. PhD thesis, Cambridge U., DAMTP, 2014. arXiv:1502.04503 [astro-ph.CO].

[111] P. Brax, C. van de Bruck, A.-C. Davis, and D. Shaw, "The Dilaton and Modified Gravity," *Phys. Rev. D* **82** (2010) 063519, arXiv:1005.3735 [astro-ph.CO].

[112] T. Damour and A. M. Polyakov, "The String dilaton and a least coupling principle," *Nucl. Phys. B* **423** (1994) 532–558, arXiv:hep-th/9401069.

[113] A. I. Vainshtein, "To the problem of nonvanishing gravitation mass," *Phys. Lett. B* **39** (1972) 393–394.

[114] E. Babichev and C. Deffayet, "An introduction to the Vainshtein mechanism," *Class. Quant. Grav.* **30** (2013) 184001, arXiv:1304.7240 [gr-qc].

[115] M. Pato, F. Iocco, and G. Bertone, "Dynamical constraints on the dark matter distribution in the Milky Way," *JCAP* **12** (2015) 001, arXiv:1504.06324 [astro-ph.GA].

[116] F. Nesti and P. Salucci, "The Dark Matter halo of the Milky Way, AD 2013," *JCAP* **07** (2013) 016, arXiv:1304.5127 [astro-ph.GA].

[117] Z. Li, J. Shen, and H.-Y. Schive, "Testing the Prediction of Fuzzy Dark Matter Theory in the Milky Way Center," (1, 2020) , arXiv:2001.00318 [astro-ph.GA].

[118] I. De Martino, T. Broadhurst, S. H. H. Tye, T. Chiueh, and H.-Y. Schive, "Dynamical Evidence of a Solitonic Core of $10^9 M_\odot$ in the Milky Way," *Phys. Dark Univ.* **28** (2020) 100503, arXiv:1807.08153 [astro-ph.GA].

[119] I. Ablimit, G. Zhao, C. Flynn, and S. A. Bird, "The Rotation Curve, Mass Distribution and Dark Matter Content of the Milky Way from Classical Cepheids," *Astrophys. J.* **895** no. 1, (2020) L12, arXiv:2004.13768 [astro-ph.GA].

[120] L. Hui, "Wave Dark Matter," *Ann. Rev. Astron. Astrophys.* **59** (2021) 247–289, arXiv:2101.11735 [astro-ph.CO].

[121] E. G. M. Ferreira, "Ultra-light dark matter," *Astron. Astrophys. Rev.* **29** no. 1, (2021) 7, arXiv:2005.03254 [astro-ph.CO].

[122] L. A. Ureña López, "Brief Review on Scalar Field Dark Matter Models," *Front. Astron. Space Sci.* **6** (2019) 47.

[123] L. Hui, J. P. Ostriker, S. Tremaine, and E. Witten, "Ultralight scalars as cosmological dark matter," *Phys. Rev. D* **95** no. 4, (2017) 043541, arXiv:1610.08297 [astro-ph.CO].

[124] J. C. Niemeyer, "Small-scale structure of fuzzy and axion-like dark matter," *Prog. Part. Nucl. Phys.* **113** (2020) 103787, arXiv:1912.07064 [astro-ph.CO].

[125] W. Hu, R. Barkana, and A. Gruzinov, "Cold and fuzzy dark matter," *Phys. Rev. Lett.* **85** (2000) 1158–1161, arXiv:astro-ph/0003365.

[126] W. J. G. de Blok, "The Core-Cusp Problem," *Adv. Astron.* **2010** (2010) 789293, arXiv:0910.3538 [astro-ph.CO].

[127] P. Sikivie, "The emerging case for axion dark matter," *Phys. Lett. B* **695** (2011) 22–25, arXiv:1003.2426 [astro-ph.GA].

[128] H.-Y. Schive, T. Chiueh, and T. Broadhurst, "Cosmic Structure as the Quantum Interference of a Coherent Dark Wave," *Nature Phys.* **10** (2014) 496–499, arXiv:1406.6586 [astro-ph.GA].

[129] L. Hui, A. Joyce, M. J. Landry, and X. Li, "Vortices and waves in light dark matter," *JCAP* **01** (2021) 011, arXiv:2004.01188 [astro-ph.CO].

[130] A. Burkert, "Fuzzy Dark Matter and Dark Matter Halo Cores," *Astrophys. J.* **904** no. 2, (2020) 161, arXiv:2006.11111 [astro-ph.GA].

[131] H. Deng, M. P. Hertzberg, M. H. Namjoo, and A. Masoumi, "Can Light Dark Matter Solve the Core-Cusp Problem?," *Phys. Rev. D* **98** no. 2, (2018) 023513, arXiv:1804.05921 [astro-ph.CO].

[132] N. Bar, D. Blas, K. Blum, and S. Sibiryakov, "Galactic rotation curves versus ultralight dark matter: Implications of the soliton-host halo relation," *Phys. Rev. D* **98** no. 8, (2018) 083027, arXiv:1805.00122 [astro-ph.CO].

[133] A. Bañares Hernández, A. Castillo, J. Martin Camalich, and G. Iorio, "Fuzzy dark matter confronts rotation curves of nearby dwarf irregular galaxies," arXiv:2304.05793 [astro-ph.GA].

[134] M. Safarzadeh and D. N. Spergel, "Ultra-light Dark Matter is Incompatible with the Milky Way's Dwarf Satellites," arXiv:1906.11848 [astro-ph.CO].

[135] D. J. E. Marsh and J. C. Niemeyer, "Strong Constraints on Fuzzy Dark Matter from Ultrafaint Dwarf Galaxy Eridanus II," *Phys. Rev. Lett.* **123** no. 5, (2019) 051103, arXiv:1810.08543 [astro-ph.CO].

[136] K. K. Rogers and H. V. Peiris, "Strong Bound on Canonical Ultralight Axion Dark Matter from the Lyman-Alpha Forest," *Phys. Rev. Lett.* **126** no. 7, (2021) 071302, arXiv:2007.12705 [astro-ph.CO].

[137] B. T. Chiang, J. P. Ostriker, and H.-Y. Schive, "Can ultralight dark matter explain the age-velocity dispersion relation of the Milky Way disc: A revised and improved treatment," arXiv:2211.07452 [astro-ph.GA].

[138] R. Brito, V. Cardoso, and P. Pani, "Black holes as particle detectors: evolution of superradiant instabilities," *Class. Quant. Grav.* **32** no. 13, (2015) 134001, arXiv:1411.0686 [gr-qc].

[139] S. L. Detweiler, "KLEIN-GORDON EQUATION AND ROTATING BLACK HOLES," *Phys. Rev. D* **22** (1980) 2323–2326.

[140] C. Flammer, *Spheroidal wave functions*. Stanford Research Institute monograph. Stanford University Press, Stanford, Calif., 1957.

[141] D. Baumann, H. S. Chia, J. Stout, and L. ter Haar, "The Spectra of Gravitational Atoms," *JCAP* **12** (2019) 006, arXiv:1908.10370 [gr-qc].

[142] N. Sanchis-Gual, M. Zilhão, C. Herdeiro, F. Di Giovanni, J. A. Font, and E. Radu, "Synchronized gravitational atoms from mergers of bosonic stars," *Phys. Rev. D* **102** no. 10, (2020) 101504(R), arXiv:2007.11584 [gr-qc].

[143] A. Arvanitaki, M. Baryakhtar, and X. Huang, "Discovering the QCD Axion with Black Holes and Gravitational Waves," *Phys. Rev. D* **91** no. 8, (2015) 084011, arXiv:1411.2263 [hep-ph].

[144] V. Cardoso, T. Ikeda, R. Vicente, and M. Zilhão, "Parasitic black holes: The swallowing of a fuzzy dark matter soliton," *Phys. Rev. D* **106** no. 12, (2022) L121302, arXiv:2207.09469 [gr-qc].

[145] L. Hui, Y. T. A. Law, L. Santoni, G. Sun, G. M. Tomaselli, and E. Trincherini, "Black hole superradiance with (dark) matter accretion," (8, 2022) , arXiv:2208.06408 [gr-qc].

[146] J. Barranco, A. Bernal, J. C. Degollado, A. Diez-Tejedor, M. Megevand, M. Alcubierre, D. Nunez, and O. Sarbach, "Schwarzschild black holes can wear scalar wigs," *Phys. Rev. Lett.* **109** (2012) 081102, arXiv:1207.2153 [gr-qc].

[147] D. D. Doneva, F. M. Ramazanoğlu, H. O. Silva, T. P. Sotiriou, and S. S. Yazadjiev, "Scalarization," arXiv:2211.01766 [gr-qc].

[148] E. Barausse, V. Cardoso, and P. Pani, "Can environmental effects spoil precision gravitational-wave astrophysics?," *Phys. Rev. D* **89** no. 10, (2014) 104059, arXiv:1404.7149 [gr-qc].

[149] V. Cardoso and A. Maselli, "Constraints on the astrophysical environment of binaries with gravitational-wave observations," *Astron. Astrophys.* **644** (2020) A147, arXiv:1909.05870 [astro-ph.HE].

[150] N. Yunes, B. Kocsis, A. Loeb, and Z. Haiman, "Imprint of Accretion Disk-Induced Migration on Gravitational Waves from Extreme Mass Ratio Inspirals," *Phys. Rev. Lett.* **107** (2011) 171103, arXiv:1103.4609 [astro-ph.CO].

[151] B. Kocsis, N. Yunes, and A. Loeb, "Observable Signatures of EMRI Black Hole Binaries Embedded in Thin Accretion Disks," *Phys. Rev. D* **84** (2011) 024032, arXiv:1104.2322 [astro-ph.GA].

[152] K. Eda, Y. Itoh, S. Kuroyanagi, and J. Silk, "New Probe of Dark-Matter Properties: Gravitational Waves from an Intermediate-Mass Black Hole Embedded in a Dark-Matter Minispike," *Phys. Rev. Lett.* **110** no. 22, (2013) 221101, arXiv:1301.5971 [gr-qc].

[153] C. F. B. Macedo, P. Pani, V. Cardoso, and L. C. B. Crispino, "Into the lair: gravitational-wave signatures of dark matter," *Astrophys. J.* **774** (2013) 48, arXiv:1302.2646 [gr-qc].

[154] A. Coogan, G. Bertone, D. Gaggero, B. J. Kavanagh, and D. A. Nichols, "Measuring the dark matter environments of black hole binaries with gravitational waves," *Phys. Rev. D* **105** no. 4, (2022) 043009, arXiv:2108.04154 [gr-qc].

[155] V. Cardoso and C. F. B. Macedo, "Drifting through the medium: kicks and self-propulsion of binaries within accretion discs and other environments," *Mon. Not. Roy. Astron. Soc.* **498** no. 2, (2020) 1963–1972, arXiv:2008.01091 [astro-ph.HE].

[156] G. Bertone and T. Tait, M. P., "A new era in the search for dark matter," *Nature* **562** no. 7725, (2018) 51–56, arXiv:1810.01668 [astro-ph.CO].

[157] P. S. Cole, A. Coogan, B. J. Kavanagh, and G. Bertone, "Measuring dark matter spikes around primordial black holes with Einstein Telescope and Cosmic Explorer," *Phys. Rev. D* **107** no. 8, (2023) 083006, arXiv:2207.07576 [astro-ph.CO].

[158] B. J. Kavanagh, D. A. Nichols, G. Bertone, and D. Gaggero, "Detecting dark matter around black holes with gravitational waves: Effects of dark-matter dynamics on the gravitational waveform," *Phys. Rev. D* **102** no. 8, (2020) 083006, arXiv:2002.12811 [gr-qc].

[159] O. A. Hannuksela, K. W. K. Wong, R. Brito, E. Berti, and T. G. F. Li, "Probing the existence of ultralight bosons with a single gravitational-wave measurement," *Nature Astron.* **3** no. 5, (2019) 447–451, arXiv:1804.09659 [astro-ph.HE].

[160] M. Baryakhtar *et al.*, "Dark Matter In Extreme Astrophysical Environments," in *2022 Snowmass Summer Study*. 3, 2022. arXiv:2203.07984 [hep-ph].

[161] R. Alves Batista *et al.*, "EuCAPT White Paper: Opportunities and Challenges for Theoretical Astroparticle Physics in the Next Decade," (10, 2021) , arXiv:2110.10074 [astro-ph.HE].

[162] L. Zwick, A. Derdzinski, M. Garg, P. R. Capelo, and L. Mayer, "Dirty waveforms: multiband harmonic content of gas-embedded gravitational wave sources," *Mon. Not. Roy. Astron. Soc.* **511** no. 4, (2022) 6143–6159, arXiv:2110.09097 [astro-ph.HE].

[163] V. Cardoso and F. Duque, "Environmental effects in gravitational-wave physics: Tidal deformability of black holes immersed in matter," *Phys. Rev. D* **101** no. 6, (2020) 064028, arXiv:1912.07616 [gr-qc].

[164] T. W. Baumgarte and S. L. Shapiro, *Numerical Relativity: Solving Einstein's Equations on the Computer*. Cambridge University Press, 2010.

[165] J. Winicour, "Characteristic Evolution and Matching," *Living Rev. Rel.* **15** no. 1, (2012) 2.

[166] R. L. Arnowitt, S. Deser, and C. W. Misner, "The Dynamics of general relativity," *Gen. Rel. Grav.* **40** (2008) 1997–2027, arXiv:gr-qc/0405109.

[167] J. W. York, Jr., "Kinematics and Dynamics of General Relativity," in *Workshop on Sources of Gravitational Radiation*, pp. 83–126. 1978.

[168] L. C. Evans, *Partial differential equations*. Graduate studies in mathematics ; 19. American Mathematical Society, Providence, R.I., 2nd ed. ed., 2010.

[169] D. Hilditch, "An Introduction to Well-posedness and Free-evolution," *Int. J. Mod. Phys. A* **28** (2013) 1340015, arXiv:1309.2012 [gr-qc].

[170] M. Alcubierre, B. Bruegmann, P. Diener, M. Koppitz, D. Pollney, E. Seidel, and R. Takahashi, "Gauge conditions for long term numerical black hole evolutions without excision," *Phys. Rev. D* **67** (2003) 084023, arXiv:gr-qc/0206072.

[171] F. S. Bemfica, M. M. Disconzi, and J. Noronha, "Causality and existence of solutions of relativistic viscous fluid dynamics with gravity," *Phys. Rev. D* **98** no. 10, (2018) 104064, arXiv:1708.06255 [gr-qc].

[172] T. Nakamura, K. Oohara, and Y. Kojima, "General Relativistic Collapse to Black Holes and Gravitational Waves from Black Holes," *Prog. Theor. Phys. Suppl.* **90** (1987) 1–218.

[173] M. Shibata and T. Nakamura, "Evolution of three-dimensional gravitational waves: Harmonic slicing case," *Phys. Rev. D* **52** (1995) 5428–5444.

[174] T. W. Baumgarte and S. L. Shapiro, "On the numerical integration of Einstein's field equations," *Phys. Rev. D* **59** (1998) 024007, arXiv:gr-qc/9810065.

[175] F. Pretorius, "Numerical relativity using a generalized harmonic decomposition," *Class. Quant. Grav.* **22** (2005) 425–452, arXiv:gr-qc/0407110.

[176] F. Pretorius, "Evolution of binary black hole spacetimes," *Phys. Rev. Lett.* **95** (2005) 121101, arXiv:gr-qc/0507014.

[177] J. Centrella, J. G. Baker, B. J. Kelly, and J. R. van Meter, "Black-hole binaries, gravitational waves, and numerical relativity," *Rev. Mod. Phys.* **82** (2010) 3069, arXiv:1010.5260 [gr-qc].

[178] D. Alic, C. Bona-Casas, C. Bona, L. Rezzolla, and C. Palenzuela, "Conformal and covariant formulation of the Z4 system with constraint-violation damping," *Phys. Rev. D* **85** (2012) 064040, arXiv:1106.2254 [gr-qc].

[179] C. Bona, T. Ledvinka, C. Palenzuela, and M. Zacek, "General covariant evolution formalism for numerical relativity," *Phys. Rev. D* **67** (2003) 104005, arXiv:gr-qc/0302083.

[180] C. Gundlach, J. M. Martin-Garcia, G. Calabrese, and I. Hinder, "Constraint damping in the Z4 formulation and harmonic gauge," *Class. Quant. Grav.* **22** (2005) 3767–3774, arXiv:gr-qc/0504114.

[181] S. Bernuzzi and D. Hilditch, "Constraint violation in free evolution schemes: Comparing BSSNOK with a conformal decomposition of Z4," *Phys. Rev. D* **81** (2010) 084003, arXiv:0912.2920 [gr-qc].

[182] D. Alic, W. Kastaun, and L. Rezzolla, "Constraint damping of the conformal and covariant formulation of the Z4 system in simulations of binary neutron stars," *Phys. Rev. D* **88** no. 6, (2013) 064049, arXiv:1307.7391 [gr-qc].

[183] M. Radia, U. Sperhake, A. Drew, K. Clough, P. Figueras, E. A. Lim, J. L. Ripley, J. C. Aurrekoetxea, T. França, and T. Helfer, "Lessons for adaptive mesh refinement in numerical relativity," *Class. Quant. Grav.* **39** no. 13, (2022) 135006, arXiv:2112.10567 [gr-qc].

[184] J. G. Baker, J. Centrella, D.-I. Choi, M. Koppitz, and J. van Meter, "Gravitational wave extraction from an inspiraling configuration of merging black holes," *Phys. Rev. Lett.* **96** (2006) 111102, arXiv:gr-qc/0511103.

[185] M. Campanelli, C. O. Lousto, P. Marronetti, and Y. Zlochower, "Accurate evolutions of orbiting black-hole binaries without excision," *Phys. Rev. Lett.* **96** (2006) 111101, arXiv:gr-qc/0511048.

[186] M. Hannam, S. Husa, F. Ohme, B. Bruegmann, and N. O'Murchadha, "Wormholes and trumpets: The Schwarzschild spacetime for the moving-puncture generation," *Phys. Rev. D* **78** (2008) 064020, arXiv:0804.0628 [gr-qc].

[187] W. Tichy, "The initial value problem as it relates to numerical relativity," *Rept. Prog. Phys.* **80** no. 2, (2017) 026901, arXiv:1610.03805 [gr-qc].

[188] J. C. Aurrekoetxea, K. Clough, and E. A. Lim, "CTTK: a new method to solve the initial data constraints in numerical relativity," *Class. Quant. Grav.* **40** no. 7, (2023) 075003, arXiv:2207.03125 [gr-qc].

[189] J. M. Bowen, "General form for the longitudinal momentum of a spherically symmetric source," *General Relativity and Gravitation* **11** (1979) 227–231.

[190] J. M. Bowen and J. W. York, Jr., "Time asymmetric initial data for black holes and black hole collisions," *Phys. Rev. D* **21** (1980) 2047–2056.

[191] K. A. Dennison, T. W. Baumgarte, and H. P. Pfeiffer, "Approximate initial data for binary black holes," *Phys. Rev. D* **74** (2006) 064016, arXiv:gr-qc/0606037.

[192] F. Foucart, P. Laguna, G. Lovelace, D. Radice, and H. Witek, "Snowmass2021 Cosmic Frontier White Paper: Numerical relativity for next-generation gravitational-wave probes of fundamental physics," arXiv:2203.08139 [gr-qc].

[193] T. Andrade *et al.*, "GRChombo: An adaptable numerical relativity code for fundamental physics," *J. Open Source Softw.* **6** no. 68, (2021) 3703, arXiv:2201.03458 [gr-qc].

[194] K. Clough, P. Figueras, H. Finkel, M. Kunesch, E. A. Lim, and S. Tunyasuvunakool, "GRChombo : Numerical Relativity with Adaptive Mesh Refinement," *Class. Quant. Grav.* **32** no. 24, (2015) 245011, arXiv:1503.03436 [gr-qc].

[195] M. Adams *et al.*, "Chombo software package for AMR applications - design document," tech. rep., Lawrence Berkeley National Laboratory, 12, 2015.

[196] M. J. Berger and J. Oliger, "Adaptive Mesh Refinement for Hyperbolic Partial Differential Equations," *J. Comput. Phys.* **53** (1984) 484.

[197] N. M. Santos and C. A. R. Herdeiro, "Stationary scalar and vector clouds around Kerr–Newman black holes," *Int. J. Mod. Phys. D* **29** no. 11, (2020) 2041013, arXiv:2005.07201 [gr-qc].

[198] L. Hui, D. Kabat, X. Li, L. Santoni, and S. S. C. Wong, "Black Hole Hair from Scalar Dark Matter," *JCAP* **06** (2019) 038, arXiv:1904.12803 [gr-qc].

[199] M. Hortacsu, "Heun Functions and Some of Their Applications in Physics," *Adv. High Energy Phys* (2012) 23–39, arXiv:1101.0471 [math-ph].

[200] K. Clough, P. G. Ferreira, and M. Lagos, "Growth of massive scalar hair around a Schwarzschild black hole," *Phys. Rev. D* **100** no. 6, (2019) 063014, arXiv:1904.12783 [gr-qc].

[201] Y. T. Liu, Z. B. Etienne, and S. L. Shapiro, "Evolution of near-extremal-spin black holes using the moving puncture technique," *Phys. Rev. D* **80** (2009) 121503(R), arXiv:1001.4077 [gr-qc].

[202] S. R. Brandt and E. Seidel, "The Evolution of distorted rotating black holes. 1: Methods and tests," *Phys. Rev. D* **52** (1995) 856–869, arXiv:gr-qc/9412072.

[203] S. R. Brandt and E. Seidel, "The Evolution of distorted rotating black holes. 3: Initial data," *Phys. Rev. D* **54** (1996) 1403–1416, arXiv:gr-qc/9601010.

[204] H. Okawa, H. Witek, and V. Cardoso, "Black holes and fundamental fields in Numerical Relativity: initial data construction and evolution of bound states," *Phys. Rev. D* **89** no. 10, (2014) 104032, arXiv:1401.1548 [gr-qc].

[205] W. E. East and F. Pretorius, "Superradiant Instability and Backreaction of Massive Vector Fields around Kerr Black Holes," *Phys. Rev. Lett.* **119** no. 4, (2017) 041101, arXiv:1704.04791 [gr-qc].

[206] C. A. R. Herdeiro and E. Radu, "Dynamical Formation of Kerr Black Holes with Synchronized Hair: An Analytic Model," *Phys. Rev. Lett.* **119** no. 26, (2017) 261101, arXiv:1706.06597 [gr-qc].

[207] P. Pani, V. Cardoso, L. Gualtieri, E. Berti, and A. Ishibashi, "Perturbations of slowly rotating black holes: massive vector fields in the Kerr metric," *Phys. Rev. D* **86** (2012) 104017, arXiv:1209.0773 [gr-qc].

[208] S. R. Dolan, "Instability of the Proca field on Kerr spacetime," *Phys. Rev. D* **98** no. 10, (2018) 104006, arXiv:1806.01604 [gr-qc].

[209] J. Percival and S. R. Dolan, "Quasinormal modes of massive vector fields on the Kerr spacetime," *Phys. Rev. D* **102** no. 10, (2020) 104055, arXiv:2008.10621 [gr-qc].

[210] K. Clough, T. Dietrich, and J. C. Niemeyer, "Axion star collisions with black holes and neutron stars in full 3D numerical relativity," *Phys. Rev. D* **98** no. 8, (2018) 083020, arXiv:1808.04668 [gr-qc].

[211] Z. K. Kurmakaev, "Circular orbits in the Kerr metric," *Soviet Astronomy* **18** (Aug., 1974) 110.

[212] C. Palomba *et al.*, "Direct constraints on ultra-light boson mass from searches for continuous gravitational waves," *Phys. Rev. Lett.* **123** (2019) 171101, arXiv:1909.08854 [astro-ph.HE].

[213] L. Sun, R. Brito, and M. Isi, "Search for ultralight bosons in Cygnus X-1 with Advanced LIGO," *Phys. Rev. D* **101** no. 6, (2020) 063020, arXiv:1909.11267 [gr-qc]. [Erratum: Phys.Rev.D 102, 089902 (2020)].

[214] M. Isi, L. Sun, R. Brito, and A. Melatos, "Directed searches for gravitational waves from ultralight bosons," *Phys. Rev. D* **99** no. 8, (2019) 084042, arXiv:1810.03812 [gr-qc]. [Erratum: Phys.Rev.D 102, 049901 (2020)].

[215] H. Yoshino and H. Kodama, "Gravitational radiation from an axion cloud around a black hole: Superradiant phase," *PTEP* **2014** (2014) 043E02, arXiv:1312.2326 [gr-qc].

[216] K. K. Y. Ng, O. A. Hannuksela, S. Vitale, and T. G. F. Li, "Searching for ultralight bosons within spin measurements of a population of binary black hole mergers," *Phys. Rev. D* **103** no. 6, (2021) 063010, arXiv:1908.02312 [gr-qc].

[217] K. K. Y. Ng, S. Vitale, O. A. Hannuksela, and T. G. F. Li, "Constraints on Ultralight Scalar Bosons within Black Hole Spin Measurements from the LIGO-Virgo GWTC-2," *Phys. Rev. Lett.* **126** no. 15, (2021) 151102, arXiv:2011.06010 [gr-qc].

[218] K. K. Y. Ng, M. Isi, C.-J. Haster, and S. Vitale, "Multiband gravitational-wave searches for ultralight bosons," *Phys. Rev. D* **102** no. 8, (2020) 083020, arXiv:2007.12793 [gr-qc].

[219] R. Brito, S. Ghosh, E. Barausse, E. Berti, V. Cardoso, I. Dvorkin, A. Klein, and P. Pani, "Gravitational wave searches for ultralight bosons with LIGO and LISA," *Phys. Rev. D* **96** no. 6, (2017) 064050, arXiv:1706.06311 [gr-qc].

[220] E. Berti, R. Brito, C. F. B. Macedo, G. Raposo, and J. L. Rosa, "Ultralight boson cloud depletion in binary systems," *Phys. Rev. D* **99** no. 10, (2019) 104039, arXiv:1904.03131 [gr-qc].

[221] E. Barausse *et al.*, "Prospects for Fundamental Physics with LISA," *Gen. Rel. Grav.* **52** no. 8, (2020) 81, arXiv:2001.09793 [gr-qc].

[222] V. Baibhav *et al.*, "Probing the nature of black holes: Deep in the mHz gravitational-wave sky," *Exper. Astron.* **51** no. 3, (2021) 1385–1416, arXiv:1908.11390 [astro-ph.HE].

[223] K. D. Kokkotas, "Gravitational Wave Astronomy," *Rev. Mod. Astron.* **20** (2008) 140, arXiv:0809.1602 [astro-ph].

[224] Y. Sofue, "Rotation Curve of the Milky Way and the Dark Matter Density," *Galaxies* **8** no. 2, (2020) 37, arXiv:2004.11688 [astro-ph.GA].

[225] T. Robson, N. J. Cornish, and C. Liu, "The construction and use of LISA sensitivity curves," *Class. Quant. Grav.* **36** no. 10, (2019) 105011, arXiv:1803.01944 [astro-ph.HE].

[226] P. K. Dahal, "Review of Pulsar Timing Array for Gravitational Wave Research," *J. Astrophys. Astron.* **41** no. 1, (2020) 8, arXiv:2002.01954 [astro-ph.IM].

[227] A. Khmelnitsky and V. Rubakov, "Pulsar timing signal from ultralight scalar dark matter," *JCAP* **02** (2014) 019, arXiv:1309.5888 [astro-ph.CO].

[228] G. Ficarra, P. Pani, and H. Witek, "Impact of multiple modes on the black-hole superradiant instability," *Phys. Rev. D* **99** no. 10, (2019) 104019, arXiv:1812.02758 [gr-qc].

[229] G.-W. Yuan, Z. Xia, C. Tang, Y. Zhao, Y.-F. Cai, Y. Chen, J. Shu, and Q. Yuan, "Testing the ALP-photon coupling with polarization measurements of Sagittarius A*," *Journal of Cosmology and Astroparticle Physics* **2021** no. 03, (Mar, 2021) 018, arXiv:2008.13662 [astro-ph.HE].

[230] **KAGRA** Collaboration, K. Somiya, "Detector configuration of KAGRA: The Japanese cryogenic gravitational-wave detector," *Class. Quant. Grav.* **29** (2012) 124007, arXiv:1111.7185 [gr-qc].

[231] **KAGRA, LIGO Scientific, VIRGO** Collaboration, B. P. Abbott *et al.*, "Prospects for Observing and Localizing Gravitational-Wave Transients with Advanced LIGO, Advanced Virgo and KAGRA," *Living Rev. Rel.* **21** no. 1, (2018) 3, arXiv:1304.0670 [gr-qc].

[232] G. Carullo, W. Del Pozzo, and J. Veitch, "Observational Black Hole Spectroscopy: A time-domain multimode analysis of GW150914," *Phys. Rev. D* **99** no. 12, (2019) 123029, arXiv:1902.07527 [gr-qc]. [Erratum: Phys.Rev.D 100, 089903 (2019)].

[233] M. Giesler, M. Isi, M. A. Scheel, and S. Teukolsky, "Black Hole Ringdown: The Importance of Overtones," *Phys. Rev. X* **9** no. 4, (2019) 041060, arXiv:1903.08284 [gr-qc].

[234] M. Isi, M. Giesler, W. M. Farr, M. A. Scheel, and S. A. Teukolsky, "Testing the no-hair theorem with GW150914," *Phys. Rev. Lett.* **123** no. 11, (2019) 111102, arXiv:1905.00869 [gr-qc].

[235] E. Berti, V. Cardoso, and C. M. Will, "Black hole spectroscopy with LISA," *AIP Conf. Proc.* **873** no. 1, (2006) 82–88.

[236] M. Punturo *et al.*, "The Einstein Telescope: A third-generation gravitational wave observatory," *Class. Quant. Grav.* **27** (2010) 194002.

[237] M. Cabero, J. Westerweck, C. D. Capano, S. Kumar, A. B. Nielsen, and B. Krishnan, "Black hole spectroscopy in the next decade," *Phys. Rev. D* **101** no. 6, (2020) 064044, arXiv:1911.01361 [gr-qc].

[238] O. Dreyer, B. J. Kelly, B. Krishnan, L. S. Finn, D. Garrison, and R. Lopez-Aleman, "Black hole spectroscopy: Testing general relativity through gravitational wave observations," *Class. Quant. Grav.* **21** (2004) 787–804, arXiv:gr-qc/0309007.

[239] E. Berti *et al.*, "Testing General Relativity with Present and Future Astrophysical Observations," *Class. Quant. Grav.* **32** (2015) 243001, arXiv:1501.07274 [gr-qc].

[240] H. T. Cho, A. S. Cornell, J. Doukas, T. R. Huang, and W. Naylor, "A New Approach to Black Hole Quasinormal Modes: A Review of the Asymptotic Iteration Method," *Adv. Math. Phys.* **2012** (2012) 281705, arXiv:1111.5024 [gr-qc].

[241] V. Ferrari and L. Gualtieri, "Quasi-Normal Modes and Gravitational Wave Astronomy," *Gen. Rel. Grav.* **40** (2008) 945–970, arXiv:0709.0657 [gr-qc].

[242] T. R. Govindarajan and V. Suneeta, "Quasinormal modes of AdS black holes: A Superpotential approach," *Class. Quant. Grav.* **18** (2001) 265–276, arXiv:gr-qc/0007084.

[243] P. T. Leung, Y. T. Liu, W. M. Suen, C. Y. Tam, and K. Young, "Quasinormal modes of dirty black holes," *Phys. Rev. Lett.* **78** (1997) 2894–2897, arXiv:gr-qc/9903031.

[244] A. J. M. Medved, D. Martin, and M. Visser, "Dirty black holes: Quasinormal modes for 'squeezed' horizons," *Class. Quant. Grav.* **21** (2004) 2393–2405, arXiv:gr-qc/0310097.

[245] A. Nagar, O. Zanotti, J. A. Font, and L. Rezzolla, "On the accretion-induced QNM excitation of a Schwarzschild black hole," *Phys. Rev. D* **75** (2007) 044016, arXiv:gr-qc/0610131.

[246] A. B. Nielsen and O. Birnholz, "Gravitational wave bounds on dirty black holes," *Astron. Nachr.* **340** no. 1-3, (2019) 116–120.

[247] J. Matyjasek, "Quasinormal modes of dirty black holes in the two-loop renormalizable effective gravity," *Phys. Rev. D* **102** (2020) 124046, arXiv:2009.10793 [gr-qc].

[248] R. A. Konoplya, Z. Stuchlík, and A. Zhidenko, "Echoes of compact objects: new physics near the surface and matter at a distance," *Phys. Rev. D* **99** no. 2, (2019) 024007, arXiv:1810.01295 [gr-qc].

[249] M. J. Graham *et al.*, "Candidate Electromagnetic Counterpart to the Binary Black Hole Merger Gravitational Wave Event S190521g," *Phys. Rev. Lett.* **124** no. 25, (2020) 251102, arXiv:2006.14122 [astro-ph.HE].

[250] L. Annulli, V. Cardoso, and R. Vicente, "Response of ultralight dark matter to supermassive black holes and binaries," *Phys. Rev. D* **102** no. 6, (2020) 063022, arXiv:2009.00012 [gr-qc].

[251] L. Annulli, V. Cardoso, and R. Vicente, "Stirred and shaken: Dynamical behavior of boson stars and dark matter cores," *Phys. Lett. B* **811** (2020) 135944, arXiv:2007.03700 [astro-ph.HE].

[252] C. Palenzuela, I. Olabarrieta, L. Lehner, and S. L. Liebling, "Head-on collisions of boson stars," *Phys. Rev. D* **75** (2007) 064005, arXiv:gr-qc/0612067.

[253] C. Palenzuela, L. Lehner, and S. L. Liebling, "Orbital Dynamics of Binary Boson Star Systems," *Phys. Rev. D* **77** (2008) 044036, arXiv:0706.2435 [gr-qc].

[254] M. Bezares, C. Palenzuela, and C. Bona, "Final fate of compact boson star mergers," *Phys. Rev. D* **95** no. 12, (2017) 124005, arXiv:1705.01071 [gr-qc].

[255] T. Helfer, D. J. E. Marsh, K. Clough, M. Fairbairn, E. A. Lim, and R. Becerril, "Black hole formation from axion stars," *JCAP* **03** (2017) 055, arXiv:1609.04724 [astro-ph.CO].

[256] T. Helfer, E. A. Lim, M. A. Garcia, and M. A. Amin, "Gravitational Wave Emission from Collisions of Compact Scalar Solitons," *Phys. Rev. D* **99** no. 4, (2019) 044046, arXiv:1802.06733 [gr-qc].

[257] J. Y. Widdicombe, T. Helfer, and E. A. Lim, "Black hole formation in relativistic Oscillaton collisions," *JCAP* **01** (2020) 027, arXiv:1910.01950 [astro-ph.CO].

[258] J. Y. Widdicombe, T. Helfer, D. J. Marsh, and E. A. Lim, "Formation of Relativistic Axion Stars," *JCAP* **10** (2018) 005, arXiv:1806.09367 [astro-ph.CO].

[259] E. Abdalla, C. B. M. H. Chirenti, and A. Saa, "Quasinormal modes for the Vaidya metric," *Phys. Rev. D* **74** (2006) 084029, arXiv:gr-qc/0609036.

[260] C.-G. Shao, B. Wang, E. Abdalla, and R.-K. Su, "Quasinormal modes in time-dependent black hole background," *Phys. Rev. D* **71** (2005) 044003, arXiv:gr-qc/0410025.

[261] X. He, B. Wang, S.-F. Wu, and C.-Y. Lin, "Quasinormal modes of black holes absorbing dark energy," *Phys. Lett. B* **673** (2009) 156–160, arXiv:0901.0034 [gr-qc].

[262] K. Lin, Y. Liu, W.-L. Qian, B. Wang, and E. Abdalla, "Quasinormal modes for the Vaidya metric in asymptotically anti–de Sitter spacetime," *Phys. Rev. D* **100** no. 6, (2019) 065018, arXiv:1909.04347 [gr-qc].

[263] V. Cardoso, M. Kimura, A. Maselli, E. Berti, C. F. B. Macedo, and R. McManus, "Parametrized black hole quasinormal ringdown: Decoupled equations for nonrotating black holes," *Phys. Rev. D* **99** no. 10, (2019) 104077, arXiv:1901.01265 [gr-qc].

[264] S. R. Dolan and A. C. Ottewill, "On an Expansion Method for Black Hole Quasinormal Modes and Regge Poles," *Class. Quant. Grav.* **26** (2009) 225003, arXiv:0908.0329 [gr-qc].

[265] E. Babichev, V. Dokuchaev, and Y. Eroshenko, "Backreaction of accreting matter onto a black hole in the Eddington-Finkelstein coordinates," *Class. Quant. Grav.* **29** (2012) 115002, arXiv:1202.2836 [gr-qc].

[266] D. Brizuela and J. M. Martin-Garcia, "Hamiltonian theory for the axial perturbations of a dynamical spherical background," *Class. Quant. Grav.* **26** (2009) 015003, arXiv:0810.4786 [gr-qc].

[267] O. Brodbeck, M. Heusler, and O. Sarbach, "The Generalization of the Regge-Wheeler equation for selfgravitating matter fields," *Phys. Rev. Lett.* **84** (2000) 3033, arXiv:gr-qc/9906090.

[268] R. Ghosh, N. Franchini, S. H. Völkel, and E. Barausse, "Quasi-normal modes of non-separable perturbation equations: the scalar non-Kerr case," arXiv:2303.00088 [gr-qc].

[269] M. Bailes *et al.*, "Gravitational-wave physics and astronomy in the 2020s and 2030s," *Nature Rev. Phys.* **3** no. 5, (2021) 344–366.

[270] L. Barack *et al.*, "Black holes, gravitational waves and fundamental physics: a roadmap," *Class. Quant. Grav.* **36** no. 14, (2019) 143001, arXiv:1806.05195 [gr-qc].

[271] **LIGO Scientific, Virgo** Collaboration, B. P. Abbott *et al.*, "Binary Black Hole Population Properties Inferred from the First and Second Observing Runs of Advanced LIGO and Advanced Virgo," *Astrophys. J. Lett.* **882** no. 2, (2019) L24, arXiv:1811.12940 [astro-ph.HE].

[272] A. Nishizawa, E. Berti, A. Klein, and A. Sesana, "eLISA eccentricity measurements as tracers of binary black hole formation," *Phys. Rev. D* **94** no. 6, (2016) 064020, arXiv:1605.01341 [gr-qc].

[273] E. Barausse, J. Bellovary, E. Berti, K. Holley-Bockelmann, B. Farris, B. Sathyaprakash, and A. Sesana, "Massive Black Hole Science with eLISA," *J. Phys. Conf. Ser.* **610** no. 1, (2015) 012001, arXiv:1410.2907 [astro-ph.HE].

[274] B. J. Kavanagh, D. Gaggero, and G. Bertone, "Merger rate of a subdominant population of primordial black holes," *Phys. Rev. D* **98** no. 2, (2018) 023536, arXiv:1805.09034 [astro-ph.CO].

[275] C. Talbot and E. Thrane, "Determining the population properties of spinning black holes," *Phys. Rev. D* **96** no. 2, (2017) 023012, arXiv:1704.08370 [astro-ph.HE].

[276] M. Mapelli, "Binary Black Hole Mergers: Formation and Populations," *Front. Astron. Space Sci.* **7** (2020) 38.

[277] K. Breivik, C. L. Rodriguez, S. L. Larson, V. Kalogera, and F. A. Rasio, "Distinguishing Between Formation Channels for Binary Black Holes with LISA," *Astrophys. J. Lett.* **830** no. 1, (2016) L18, arXiv:1606.09558 [astro-ph.GA].

[278] G. Fragione and B. Kocsis, "Black hole mergers from an evolving population of globular clusters," *Phys. Rev. Lett.* **121** no. 16, (2018) 161103, arXiv:1806.02351 [astro-ph.GA].

[279] V. Cardoso and P. Pani, "Testing the nature of dark compact objects: a status report," *Living Rev. Rel.* **22** no. 1, (2019) 4, arXiv:1904.05363 [gr-qc].

[280] P. Gondolo and J. Silk, "Dark matter annihilation at the galactic center," *Phys. Rev. Lett.* **83** (1999) 1719–1722, arXiv:astro-ph/9906391.

[281] F. Ferrer, A. M. da Rosa, and C. M. Will, "Dark matter spikes in the vicinity of Kerr black holes," *Phys. Rev. D* **96** no. 8, (2017) 083014, arXiv:1707.06302 [astro-ph.CO].

[282] G. Bertone, "Dark matter spikes and mini-spikes," *Frascati Phys. Ser.* **45** (2007) 313–320.

[283] N. Speeney, A. Antonelli, V. Baibhav, and E. Berti, "Impact of relativistic corrections on the detectability of dark-matter spikes with gravitational waves," *Phys. Rev. D* **106** no. 4, (2022) 044027, arXiv:2204.12508 [gr-qc].

[284] T. Lacroix, "Dynamical constraints on a dark matter spike at the Galactic Centre from stellar orbits," *Astron. Astrophys.* **619** (2018) A46, arXiv:1801.01308 [astro-ph.GA].

[285] E. de Jong, J. C. Aurrekoetxea, and E. A. Lim, "Primordial black hole formation with full numerical relativity," *JCAP* **03** no. 03, (2022) 029, arXiv:2109.04896 [astro-ph.CO].

[286] D. Grin, M. A. Amin, V. Gluscevic, R. Hlŏzek, D. J. E. Marsh, V. Poulin, C. Prescod-Weinstein, and T. L. Smith, "Gravitational probes of ultra-light axions," (4, 2019) , arXiv:1904.09003 [astro-ph.CO].

[287] M. J. Stott, "Ultralight Bosonic Field Mass Bounds from Astrophysical Black Hole Spin," (9, 2020) , arXiv:2009.07206 [hep-ph].

[288] A. El-Zant, Z. Roupas, and J. Silk, "Ejection of supermassive black holes and implications for merger rates in fuzzy dark matter haloes," *Mon. Not. Roy. Astron. Soc.* **499** no. 2, (2020) 2575–2586, arXiv:2009.10167 [astro-ph.GA].

[289] R. Brito, S. Chakrabarti, S. Clesse, C. Dvorkin, J. Garcia-Bellido, J. Meyers, K. K. Y. Ng, A. L. Miller, S. Shandera, and L. Sun, "Snowmass2021 Cosmic Frontier White Paper: Probing dark matter with small-scale astrophysical observations," (3, 2022) , arXiv:2203.15954 [hep-ph].

[290] D. Traykova, K. Clough, T. Helfer, E. Berti, P. G. Ferreira, and L. Hui, "Dynamical friction from scalar dark matter in the relativistic regime," *Phys. Rev. D* **104** no. 10, (2021) 103014, arXiv:2106.08280 [gr-qc].

[291] P. Brax, J. A. Cembranos, and P. Valageas, "Fate of scalar dark matter solitons around supermassive galactic black holes," *Phys. Rev. D* **101** no. 2, (2020) 023521, arXiv:1909.02614 [astro-ph.CO].

[292] R. Brito, V. Cardoso, and H. Okawa, "Accretion of dark matter by stars," *Phys. Rev. Lett.* **115** no. 11, (2015) 111301, arXiv:1508.04773 [gr-qc].

[293] D. J. E. Marsh and A.-R. Pop, "Axion dark matter, solitons and the cusp–core problem," *Mon. Not. Roy. Astron. Soc.* **451** no. 3, (2015) 2479–2492, arXiv:1502.03456 [astro-ph.CO].

[294] M. Khlopov, B. A. Malomed, and I. B. Zeldovich, "Gravitational instability of scalar fields and formation of primordial black holes," *Mon. Not. Roy. Astron. Soc.* **215** (1985) 575–589.

[295] N. Sanchis-Gual, J. C. Degollado, P. Izquierdo, J. A. Font, and P. J. Montero, "Quasistationary solutions of scalar fields around accreting black holes," *Phys. Rev. D* **94** no. 4, (2016) 043004, arXiv:1606.05146 [gr-qc].

[296] T. Ikeda, L. Bernard, V. Cardoso, and M. Zilhão, "Black hole binaries and light fields: Gravitational molecules," *Phys. Rev. D* **103** no. 2, (2021) 024020, arXiv:2010.00008 [gr-qc].

[297] F. V. Day and J. I. McDonald, "Axion superradiance in rotating neutron stars," *JCAP* **10** (2019) 051, arXiv:1904.08341 [hep-ph].

[298] V. Cardoso, R. Brito, and J. L. Rosa, "Superradiance in stars," *Phys. Rev. D* **91** no. 12, (2015) 124026, arXiv:1505.05509 [gr-qc].

[299] M. Richartz and A. Saa, "Superradiance without event horizons in General Relativity," *Phys. Rev. D* **88** (2013) 044008, arXiv:1306.3137 [gr-qc].

[300] V. Cardoso, P. Pani, and T.-T. Yu, "Superradiance in rotating stars and pulsar-timing constraints on dark photons," *Phys. Rev. D* **95** no. 12, (2017) 124056, arXiv:1704.06151 [gr-qc].

[301] D. Merritt and M. Milosavljevic, "Dynamics of dark matter cusps," in *4th International Heidelberg Conference on Dark Matter in Astro and Particle Physics*, pp. 79–89. 5, 2002. arXiv:astro-ph/0205140.

[302] G. Bertone and D. Merritt, "Time-dependent models for dark matter at the Galactic Center," *Phys. Rev. D* **72** (2005) 103502, arXiv:astro-ph/0501555.

[303] S. Barsanti, A. Maselli, T. P. Sotiriou, and L. Gualtieri, "Detecting massive scalar fields with Extreme Mass-Ratio Inspirals," arXiv:2212.03888 [gr-qc].

[304] A. Maselli, N. Franchini, L. Gualtieri, T. P. Sotiriou, S. Barsanti, and P. Pani, "Detecting fundamental fields with LISA observations of gravitational waves from extreme mass-ratio inspirals," *Nature Astron.* **6** no. 4, (2022) 464–470, arXiv:2106.11325 [gr-qc].

[305] N. Xie and F. P. Huang, "Imprints of ultralight axions on the gravitational wave signals of neutron star-black hole binary," (7, 2022) , arXiv:2207.11145 [hep-ph].

[306] O. A. Hannuksela, K. C. Y. Ng, and T. G. F. Li, "Extreme dark matter tests with extreme mass ratio inspirals," *Phys. Rev. D* **102** no. 10, (2020) 103022, arXiv:1906.11845 [astro-ph.CO].

[307] P. Amaro-Seoane, "Relativistic dynamics and extreme mass ratio inspirals," *Living Rev. Rel.* **21** no. 1, (2018) 4, arXiv:1205.5240 [astro-ph.CO].

[308] L. Polcar, G. Lukes-Gerakopoulos, and V. Witzany, "Extreme mass ratio inspirals into black holes surrounded by matter," *Phys. Rev. D* **106** no. 4, (2022) 044069, arXiv:2205.08516 [gr-qc].

[309] P. Amaro-Seoane, J. R. Gair, M. Freitag, M. Coleman Miller, I. Mandel, C. J. Cutler, and S. Babak, "Astrophysics, detection and science applications of intermediate- and extreme mass-ratio inspirals," *Class. Quant. Grav.* **24** (2007) R113–R169, arXiv:astro-ph/0703495.

[310] D. Baumann, G. Bertone, J. Stout, and G. M. Tomaselli, "Sharp Signals of Boson Clouds in Black Hole Binary Inspirals," *Phys. Rev. Lett.* **128** no. 22, (2022) 221102, arXiv:2206.01212 [gr-qc].

[311] V. Cardoso, K. Destounis, F. Duque, R. Panosso Macedo, and A. Maselli, "Gravitational Waves from Extreme-Mass-Ratio Systems in Astrophysical Environments," *Phys. Rev. Lett.* **129** no. 24, (2022) 241103, arXiv:2210.01133 [gr-qc].

[312] G.-L. Li, Y. Tang, and Y.-L. Wu, "Probing dark matter spikes via gravitational waves of extreme-mass-ratio inspirals," *Sci. China Phys. Mech. Astron.* **65** no. 10, (2022) 100412, arXiv:2112.14041 [astro-ph.CO].

[313] X.-J. Yue and Z. Cao, "Dark matter minispike: A significant enhancement of eccentricity for intermediate-mass-ratio inspirals," *Phys. Rev. D* **100** no. 4, (2019) 043013, arXiv:1908.10241 [astro-ph.HE].

[314] X.-J. Yue and W.-B. Han, "Gravitational waves with dark matter minispikes: the combined effect," *Phys. Rev. D* **97** no. 6, (2018) 064003, arXiv:1711.09706 [gr-qc].

[315] D. Baumann, G. Bertone, J. Stout, and G. M. Tomaselli, "Ionization of gravitational atoms," *Phys. Rev. D* **105** no. 11, (2022) 115036, arXiv:2112.14777 [gr-qc].

[316] D. Baumann, H. S. Chia, and R. A. Porto, "Probing Ultralight Bosons with Binary Black Holes," *Phys. Rev. D* **99** no. 4, (2019) 044001, arXiv:1804.03208 [gr-qc].

[317] T. K. Poddar, S. Mohanty, and S. Jana, "Constraints on ultralight axions from compact binary systems," *Phys. Rev. D* **101** no. 8, (2020) 083007, arXiv:1906.00666 [hep-ph].

[318] J. Zhang and H. Yang, "Dynamic Signatures of Black Hole Binaries with Superradiant Clouds," *Phys. Rev. D* **101** no. 4, (2020) 043020, arXiv:1907.13582 [gr-qc].

[319] S. Barsanti, N. Franchini, L. Gualtieri, A. Maselli, and T. P. Sotiriou, "Extreme mass-ratio inspirals as probes of scalar fields: Eccentric equatorial orbits around Kerr black holes," *Phys. Rev. D* **106** no. 4, (2022) 044029, arXiv:2203.05003 [gr-qc].

[320] M. C. Ferreira, C. F. B. Macedo, and V. Cardoso, "Orbital fingerprints of ultralight scalar fields around black holes," *Phys. Rev. D* **96** no. 8, (2017) 083017, arXiv:1710.00830 [gr-qc].

[321] T. D. P. Edwards, M. Chianese, B. J. Kavanagh, S. M. Nissanke, and C. Weniger, "Unique Multimessenger Signal of QCD Axion Dark Matter," *Phys. Rev. Lett.* **124** no. 16, (2020) 161101, arXiv:1905.04686 [hep-ph].

[322] C. Kouvaris, T. Liu, and K.-F. Lyu, "Radio Signals from Axion Star-Neutron Star Binaries," (2, 2022) , arXiv:2202.11096 [astro-ph.HE].

[323] L. K. Wong, "Superradiant scattering by a black hole binary," *Phys. Rev. D* **100** no. 4, (2019) 044051, arXiv:1905.08543 [hep-th].

[324] L. K. Wong, "Evolution of diffuse scalar clouds around binary black holes," *Phys. Rev. D* **101** no. 12, (2020) 124049, arXiv:2004.03570 [hep-th].

[325] D. Blas, D. L. Nacir, and S. Sibiryakov, "Ultralight Dark Matter Resonates with Binary Pulsars," *Phys. Rev. Lett.* **118** no. 26, (2017) 261102, arXiv:1612.06789 [hep-ph].

[326] D. Blas, D. López Nacir, and S. Sibiryakov, "Secular effects of ultralight dark matter on binary pulsars," *Phys. Rev. D* **101** no. 6, (2020) 063016, arXiv:1910.08544 [gr-qc].

[327] D. C. Ribeiro, M. Zilhão, and V. Cardoso, "Binary superradiance: A numerical study," *Phys. Rev. D* **105** no. 8, (2022) 084004, arXiv:2201.13407 [gr-qc].

[328] T. Liu and K.-F. Lyu, "The BH-PSR Gravitational Molecule," (7, 2021) , arXiv:2107.09971 [astro-ph.HE].

[329] M. Kavic, S. L. Liebling, M. Lippert, and J. H. Simonetti, "Accessing the axion via compact object binaries," *JCAP* **08** (2020) 005, arXiv:1910.06977 [astro-ph.HE].

[330] M. Bošković, F. Duque, M. C. Ferreira, F. S. Miguel, and V. Cardoso, "Motion in time-periodic backgrounds with applications to ultralight dark matter haloes at galactic centers," *Phys. Rev. D* **98** (2018) 024037, arXiv:1806.07331 [gr-qc].

[331] S. S. Dave and S. Digal, "Field excitation in fuzzy dark matter near a strong gravitational wave source," *Phys. Rev. D* **105** no. 2, (2022) 024039, arXiv:2106.05812 [gr-qc].

[332] M. W. Horbatsch and C. P. Burgess, "Cosmic Black-Hole Hair Growth and Quasar OJ287," *JCAP* **05** (2012) 010, arXiv:1111.4009 [gr-qc].

[333] T. Takahashi and T. Tanaka, "Axion clouds may survive the perturbative tidal interaction over the early inspiral phase of black hole binaries," *JCAP* **10** (2021) 031, arXiv:2106.08836 [gr-qc].

[334] T. Takahashi, H. Omiya, and T. Tanaka, "Axion cloud evaporation during inspiral of black hole binaries: The effects of backreaction and radiation," *PTEP* **2022** no. 4, (2022) 043E01, arXiv:2112.05774 [gr-qc].

[335] B. Su, Z.-Z. Xianyu, and X. Zhang, "Probing Ultralight Bosons with Compact Eccentric Binaries," *Astrophys. J.* **923** no. 1, (2021) 114, arXiv:2107.13527 [gr-qc].

[336] G. Ficarra, "Scalar field dynamics around black holes: superradiant instabilities and binary evolution," in *55th Rencontres de Moriond on Gravitation*. 5, 2021. arXiv:2105.05918 [gr-qc].

[337] M. Rozner, E. Grishin, Y. B. Ginat, A. P. Igoshev, and V. Desjacques, "Axion resonances in binary pulsar systems," *JCAP* **03** (2020) 061, arXiv:1904.01958 [astro-ph.CO].

[338] V. Cardoso, F. Duque, and T. Ikeda, "Tidal effects and disruption in superradiant clouds: a numerical investigation," *Phys. Rev. D* **101** no. 6, (2020) 064054, arXiv:2001.01729 [gr-qc].

[339] C. Zhang, T. Zhu, X. Fang, and A. Wang, "Imprints of dark matter on gravitational ringing of supermassive black holes," *Phys. Dark Univ.* **37** (2022) 101078, arXiv:2201.11352 [gr-qc].

[340] C. Zhang, T. Zhu, and A. Wang, "Gravitational axial perturbations of Schwarzschild-like black holes in dark matter halos," *Phys. Rev. D* **104** no. 12, (2021) 124082, arXiv:2111.04966 [gr-qc].

[341] Q. Yang, L.-W. Ji, B. Hu, Z.-J. Cao, and R.-G. Cai, "An axion-like scalar field environment effect on binary black hole merger," *Res. Astron. Astrophys.* **18** no. 6, (2018) 065, arXiv:1706.00678 [gr-qc].

[342] S. Choudhary, N. Sanchis-Gual, A. Gupta, J. C. Degollado, S. Bose, and J. A. Font, "Gravitational waves from binary black hole mergers surrounded by scalar field clouds: Numerical simulations and observational implications," *Phys. Rev. D* **103** no. 4, (2021) 044032, arXiv:2010.00935 [gr-qc].

[343] Y.-P. Zhang, M. Gracia-Linares, P. Laguna, D. Shoemaker, and Y.-X. Liu, "Gravitational recoil from binary black hole mergers in scalar field clouds," *Phys. Rev. D* **107** no. 4, (2023) 044039, arXiv:2209.11814 [gr-qc].

[344] J. Healy, T. Bode, R. Haas, E. Pazos, P. Laguna, D. Shoemaker, and N. Yunes, "Late Inspiral and Merger of Binary Black Holes in Scalar-Tensor Theories of Gravity," *Class. Quant. Grav.* **29** (2012) 232002, arXiv:1112.3928 [gr-qc].

[345] E. Berti, V. Cardoso, L. Gualtieri, M. Horbatsch, and U. Sperhake, "Numerical simulations of single and binary black holes in scalar-tensor theories: circumventing the no-hair theorem," *Phys. Rev. D* **87** no. 12, (2013) 124020, arXiv:1304.2836 [gr-qc].

[346] Z. Cao, P. Galaviz, and L.-F. Li, "Binary black hole mergers in $f(R)$ theory," *Phys. Rev. D* **87** no. 10, (2013) 104029, arXiv:1608.07816 [gr-qc].

[347] H. Witek, L. Gualtieri, P. Pani, and T. P. Sotiriou, "Black holes and binary mergers in scalar Gauss-Bonnet gravity: scalar field dynamics," *Phys. Rev. D* **99** no. 6, (2019) 064035, arXiv:1810.05177 [gr-qc].

[348] M. Okounkova, "Numerical relativity simulation of GW150914 in Einstein dilaton Gauss-Bonnet gravity," *Phys. Rev. D* **102** no. 8, (2020) 084046, arXiv:2001.03571 [gr-qc].

[349] M. Okounkova, M. Isi, K. Chatziioannou, and W. M. Farr, "Gravitational wave inference on a numerical-relativity simulation of a black hole merger beyond general relativity," *Phys. Rev. D* **107** no. 2, (2023) 024046, arXiv:2208.02805 [gr-qc].

[350] K. Clough, "Continuity equations for general matter: applications in numerical relativity," *Class. Quant. Grav.* **38** no. 16, (2021) 167001, arXiv:2104.13420 [gr-qc].

[351] R. Croft, "Local Continuity of Angular Momentum and Noether Charge for Matter in General Relativity," (3, 2022) , arXiv:2203.13845 [gr-qc].

[352] P. C. Peters, "Gravitational Radiation and the Motion of Two Point Masses," *Phys. Rev.* **136** (1964) B1224–B1232.

[353] A. Krolak and B. F. Schutz, "Coalescing binaries — Probe of the universe," *Gen. Rel. Grav.* **19** (1987) 1163–1171.

[354] V. Cardoso, C. F. B. Macedo, and R. Vicente, "Eccentricity evolution of compact binaries and applications to gravitational-wave physics," *Phys. Rev. D* **103** no. 2, (2021) 023015, arXiv:2010.15151 [gr-qc].

[355] C. M. Will, "Compact binary inspiral: Nature is perfectly happy with a circle," *Class. Quant. Grav.* **36** no. 19, (2019) 195013, arXiv:1906.08064 [gr-qc].

[356] N. Becker, L. Sagunski, L. Prinz, and S. Rastgoo, "Circularization versus eccentrification in intermediate mass ratio inspirals inside dark matter spikes," *Phys. Rev. D* **105** no. 6, (2022) 063029, arXiv:2112.09586 [gr-qc].

[357] H. A. Buchdahl, "Isotropic Coordinates and Schwarzschild Metric," *International Journal of Theoretical Physics* **24** no. 7, (July, 1985) 731–739.

[358] G. B. Cook, "Initial data for numerical relativity," *Living Rev. Rel.* **3** (2000) 5, arXiv:gr-qc/0007085.

[359] M. Hannam, S. Husa, B. Bruegmann, J. A. Gonzalez, U. Sperhake, and N. O. Murchadha, "Where do moving punctures go?," *J. Phys. Conf. Ser.* **66** (2007) 012047, arXiv:gr-qc/0612097.

[360] H. P. Pfeiffer, D. A. Brown, L. E. Kidder, L. Lindblom, G. Lovelace, and M. A. Scheel, "Reducing orbital eccentricity in binary black hole simulations," *Class. Quant. Grav.* **24** (2007) S59–S82, arXiv:gr-qc/0702106.

[361] S. Habib, A. Ramos-Buades, E. A. Huerta, S. Husa, R. Haas, and Z. Etienne, "Initial Data and Eccentricity Reduction Toolkit for Binary Black Hole Numerical Relativity Waveforms," *Class. Quant. Grav.* **38** no. 12, (2021) 125007, arXiv:2011.08878 [gr-qc].

[362] A. Buonanno, L. E. Kidder, A. H. Mroue, H. P. Pfeiffer, and A. Taracchini, "Reducing orbital eccentricity of precessing black-hole binaries," *Phys. Rev. D* **83** (2011) 104034, arXiv:1012.1549 [gr-qc].

[363] A. Ramos-Buades, S. Husa, and G. Pratten, "Simple procedures to reduce eccentricity of binary black hole simulations," *Phys. Rev. D* **99** no. 2, (2019) 023003, arXiv:1810.00036 [gr-qc].

[364] L. Blanchet, "Gravitational radiation from post-Newtonian sources and inspiralling compact binaries," *Living Rev. Rel.* **9** (2006) 4.

[365] L. Bernard, "Dynamics of compact binary systems in scalar-tensor theories: Equations of motion to the third post-Newtonian order," *Phys. Rev. D* **98** no. 4, (2018) 044004, arXiv:1802.10201 [gr-qc].

[366] F.-L. Julié and E. Berti, "Post-Newtonian dynamics and black hole thermodynamics in Einstein-scalar-Gauss-Bonnet gravity," *Phys. Rev. D* **100** no. 10, (2019) 104061, arXiv:1909.05258 [gr-qc].

[367] K. Yagi, L. C. Stein, N. Yunes, and T. Tanaka, "Post-Newtonian, Quasi-Circular Binary Inspirals in Quadratic Modified Gravity," *Phys. Rev. D* **85** (2012) 064022, arXiv:1110.5950 [gr-qc]. [Erratum: Phys.Rev.D 93, 029902 (2016)].

[368] B. Shiralilou, T. Hinderer, S. M. Nissanke, N. Ortiz, and H. Witek, "Nonlinear curvature effects in gravitational waves from inspiralling black hole binaries," *Phys. Rev. D* **103** no. 12, (2021) L121503, arXiv:2012.09162 [gr-qc].

[369] B. Shiralilou, T. Hinderer, S. M. Nissanke, N. Ortiz, and H. Witek, "Post-Newtonian gravitational and scalar waves in scalar-Gauss–Bonnet gravity," *Class. Quant. Grav.* **39** no. 3, (2022) 035002, arXiv:2105.13972 [gr-qc].

[370] P. Brax, A.-C. Davis, S. Melville, and L. K. Wong, "Spin-orbit effects for compact binaries in scalar-tensor gravity," *JCAP* **10** (2021) 075, arXiv:2107.10841 [gr-qc].

[371] W. Tichy, "Constructing quasi-equilibrium initial data for binary neutron stars with arbitrary spins," *Phys. Rev. D* **86** (2012) 064024, arXiv:1209.5336 [gr-qc].

[372] K. Kyutoku, M. Shibata, and K. Taniguchi, "Reducing orbital eccentricity in initial data of binary neutron stars," *Phys. Rev. D* **90** no. 6, (2014) 064006, arXiv:1405.6207 [gr-qc].

[373] A. Tsokaros, K. Uryū, and L. Rezzolla, "New code for quasiequilibrium initial data of binary neutron stars: Corotating, irrotational, and slowly spinning systems," *Phys. Rev. D* **91** no. 10, (2015) 104030, arXiv:1502.05674 [gr-qc].

[374] A. Einstein, *The collected papers of Albert Einstein.* Princeton University Press, Princeton, N.J., 1987.

[375] T. Kobayashi, "Horndeski theory and beyond: a review," *Rept. Prog. Phys.* **82** no. 8, (2019) 086901, arXiv:1901.07183 [gr-qc].

[376] P. A. González, M. Olivares, E. Papantonopoulos, and Y. Vásquez, "Constraints on scalar–tensor theory of gravity by solar system tests," *Eur. Phys. J. C* **80** no. 10, (2020) 981, arXiv:2002.03394 [gr-qc].

[377] B. Bertotti, L. Iess, and P. Tortora, "A test of general relativity using radio links with the Cassini spacecraft," *Nature* **425** (2003) 374–376.

[378] P. C. C. Freire, N. Wex, G. Esposito-Farese, J. P. W. Verbiest, M. Bailes, B. A. Jacoby, M. Kramer, I. H. Stairs, J. Antoniadis, and G. H. Janssen, "The relativistic pulsar-white dwarf binary PSR J1738+0333 II. The most stringent test of scalar-tensor gravity," *Mon. Not. Roy. Astron. Soc.* **423** (2012) 3328, arXiv:1205.1450 [astro-ph.GA].

[379] P. Brax, "Screening mechanisms in modified gravity," *Class. Quant. Grav.* **30** (2013) 214005.

[380] A. Dima and F. Vernizzi, "Vainshtein Screening in Scalar-Tensor Theories before and after GW170817: Constraints on Theories beyond Horndeski," *Phys. Rev. D* **97** no. 10, (2018) 101302, arXiv:1712.04731 [gr-qc].

[381] P. G. Ferreira, C. T. Hill, and G. G. Ross, "Scale-Independent Inflation and Hierarchy Generation," *Phys. Lett. B* **763** (2016) 174–178, arXiv:1603.05983 [hep-th].

[382] S. Casas, M. Pauly, and J. Rubio, "Higgs-dilaton cosmology: An inflation–dark-energy connection and forecasts for future galaxy surveys," *Phys. Rev. D* **97** no. 4, (2018) 043520, arXiv:1712.04956 [astro-ph.CO].

[383] P. G. Ferreira, C. T. Hill, J. Noller, and G. G. Ross, "Inflation in a scale invariant universe," *Phys. Rev. D* **97** no. 12, (2018) 123516, arXiv:1802.06069 [astro-ph.CO].

[384] M. Shaposhnikov and D. Zenhausern, "Scale invariance, unimodular gravity and dark energy," *Phys. Lett. B* **671** (2009) 187–192, arXiv:0809.3395 [hep-th].

[385] W. Buchmuller and N. Dragon, "Dilatons in Flat and Curved Space-time," *Nucl. Phys. B* **321** (1989) 207–231.

[386] M. Shaposhnikov and D. Zenhausern, "Quantum scale invariance, cosmological constant and hierarchy problem," *Phys. Lett. B* **671** (2009) 162–166, arXiv:0809.3406 [hep-th].

[387] D. Blas, M. Shaposhnikov, and D. Zenhausern, "Scale-invariant alternatives to general relativity," *Phys. Rev. D* **84** (2011) 044001, arXiv:1104.1392 [hep-th].

[388] J. Garcia-Bellido, J. Rubio, M. Shaposhnikov, and D. Zenhausern, "Higgs-Dilaton Cosmology: From the Early to the Late Universe," *Phys. Rev. D* **84** (2011) 123504, arXiv:1107.2163 [hep-ph].

[389] J. Garcia-Bellido, J. Rubio, and M. Shaposhnikov, "Higgs-Dilaton cosmology: Are there extra relativistic species?," *Phys. Lett. B* **718** (2012) 507–511, arXiv:1209.2119 [hep-ph].

[390] F. Bezrukov, G. K. Karananas, J. Rubio, and M. Shaposhnikov, "Higgs-Dilaton Cosmology: an effective field theory approach," *Phys. Rev. D* **87** no. 9, (2013) 096001, arXiv:1212.4148 [hep-ph].

[391] T. Henz, J. M. Pawlowski, A. Rodigast, and C. Wetterich, "Dilaton Quantum Gravity," *Phys. Lett. B* **727** (2013) 298–302, arXiv:1304.7743 [hep-th].

[392] J. Rubio and M. Shaposhnikov, "Higgs-Dilaton cosmology: Universality versus criticality," *Phys. Rev. D* **90** (2014) 027307, arXiv:1406.5182 [hep-ph].

[393] G. K. Karananas and M. Shaposhnikov, "Scale invariant alternatives to general relativity. II. Dilaton properties," *Phys. Rev. D* **93** no. 8, (2016) 084052, arXiv:1603.01274 [hep-th].

[394] I. Bars, P. Steinhardt, and N. Turok, "Local Conformal Symmetry in Physics and Cosmology," *Phys. Rev. D* **89** no. 4, (2014) 043515, arXiv:1307.1848 [hep-th].

[395] F. Bezrukov, J. Rubio, and M. Shaposhnikov, "Living beyond the edge: Higgs inflation and vacuum metastability," *Phys. Rev. D* **92** no. 8, (2015) 083512, arXiv:1412.3811 [hep-ph].

[396] Y. Fujii, "Scalar-tensor theory of gravitation and spontaneous breakdown of scale invariance," *Phys. Rev. D* **9** (1974) 874–876.

[397] M. Shaposhnikov and A. Tokareva, "Anomaly-free scale symmetry and gravity," arXiv:2201.09232 [hep-th].

[398] G. K. Karananas, M. Shaposhnikov, and S. Zell, "Field redefinitions, perturbative unitarity and Higgs inflation," *JHEP* **06** (2022) 132, arXiv:2203.09534 [hep-ph].

[399] G. K. Karananas, M. Shaposhnikov, A. Shkerin, and S. Zell, "Scale and Weyl invariance in Einstein-Cartan gravity," *Phys. Rev. D* **104** no. 12, (2021) 124014, arXiv:2108.05897 [hep-th].

[400] M. Shaposhnikov and A. Shkerin, "Gravity, Scale Invariance and the Hierarchy Problem," *JHEP* **10** (2018) 024, arXiv:1804.06376 [hep-th].

[401] D. M. Ghilencea, "Non-metric geometry as the origin of mass in gauge theories of scale invariance," *Eur. Phys. J. C* **83** no. 2, (2023) 176, arXiv:2203.05381 [hep-th].

[402] J. Rubio, "Scale symmetry, the Higgs and the Cosmos," *PoS* **CORFU2019** (2020) 074, arXiv:2004.00039 [gr-qc].

[403] H. Weyl, *Raum, Zeit, Materie : Vorlesungen über allgemeine Relativitätstheorie.* J. Springer, Berlin, 2., unveründ. aufl. ed., 1919.

[404] R. Foot, A. Kobakhidze, K. L. McDonald, and R. R. Volkas, "A Solution to the hierarchy problem from an almost decoupled hidden sector within a classically scale invariant theory," *Phys. Rev. D* **77** (2008) 035006, arXiv:0709.2750 [hep-ph].

[405] K. Kamada, T. Kobayashi, T. Takahashi, M. Yamaguchi, and J. Yokoyama, "Generalized Higgs inflation," *Phys. Rev. D* **86** (2012) 023504, arXiv:1203.4059 [hep-ph].

[406] R. N. Greenwood, D. I. Kaiser, and E. I. Sfakianakis, "Multifield Dynamics of Higgs Inflation," *Phys. Rev. D* **87** (2013) 064021, arXiv:1210.8190 [hep-ph].

[407] M. Rinaldi and L. Vanzo, "Inflation and reheating in theories with spontaneous scale invariance symmetry breaking," *Phys. Rev. D* **94** no. 2, (2016) 024009, arXiv:1512.07186 [gr-qc].

[408] N. D. Barrie, A. Kobakhidze, and S. Liang, "Natural Inflation with Hidden Scale Invariance," *Phys. Lett. B* **756** (2016) 390–393, arXiv:1602.04901 [gr-qc].

[409] D. M. Ghilencea and T. Harko, "Cosmological evolution in Weyl conformal geometry," (10, 2021) , arXiv:2110.07056 [gr-qc].

[410] D. M. Ghilencea, "Standard Model in Weyl conformal geometry," *Eur. Phys. J. C* **82** no. 1, (2022) 23, arXiv:2104.15118 [hep-ph].

[411] M. Aoki, J. Kubo, and J. Yang, "Inflation and dark matter after spontaneous Planck scale generation by hidden chiral symmetry breaking," *JCAP* **01** no. 01, (2022) 005, arXiv:2109.04814 [hep-ph].

[412] P. G. Ferreira and O. J. Tattersall, "Scale Invariant Gravity and Black Hole Ringdown," *Phys. Rev. D* **101** no. 2, (2020) 024011, arXiv:1910.04480 [gr-qc].

[413] P. G. Ferreira, C. T. Hill, and G. G. Ross, "No fifth force in a scale invariant universe," *Phys. Rev. D* **95** no. 6, (2017) 064038, arXiv:1612.03157 [gr-qc].

[414] S. Karamitsos and A. Pilaftsis, "On the Cosmological Frame Problem," *PoS* **CORFU2017** (2018) 036, arXiv:1801.07151 [hep-th].

[415] E. J. Copeland, P. Millington, and S. S. Muñoz, "Fifth forces and broken scale symmetries in the Jordan frame," *JCAP* **02** no. 02, (2022) 016, arXiv:2111.06357 [hep-th].

[416] C. Burrage, E. J. Copeland, P. Millington, and M. Spannowsky, "Fifth forces, Higgs portals and broken scale invariance," *JCAP* **11** (2018) 036, arXiv:1804.07180 [hep-th].

[417] S. Capozziello, R. de Ritis, and A. A. Marino, "Some aspects of the cosmological conformal equivalence between 'Jordan frame' and 'Einstein frame'," *Class. Quant. Grav.* **14** (1997) 3243–3258, arXiv:gr-qc/9612053.

[418] S. Capozziello, P. Martin-Moruno, and C. Rubano, "Physical non-equivalence of the Jordan and Einstein frames," *Phys. Lett. B* **689** (2010) 117–121, arXiv:1003.5394 [gr-qc].

[419] S. Nojiri and S. D. Odintsov, "Quantum dilatonic gravity in (D = 2)-dimensions, (D = 4)-dimensions and (D = 5)-dimensions," *Int. J. Mod. Phys. A* **16** (2001) 1015–1108, arXiv:hep-th/0009202.

[420] A. Y. Kamenshchik and C. F. Steinwachs, "Question of quantum equivalence between Jordan frame and Einstein frame," *Phys. Rev. D* **91** no. 8, (2015) 084033, arXiv:1408.5769 [gr-qc].

[421] M. Postma and M. Volponi, "Equivalence of the Einstein and Jordan frames," *Phys. Rev. D* **90** no. 10, (2014) 103516, arXiv:1407.6874 [astro-ph.CO].

[422] N. Banerjee and B. Majumder, "A question mark on the equivalence of Einstein and Jordan frames," *Phys. Lett. B* **754** (2016) 129–134, arXiv:1601.06152 [gr-qc].

[423] S. Pandey and N. Banerjee, "Equivalence of Jordan and Einstein frames at the quantum level," *Eur. Phys. J. Plus* **132** no. 3, (2017) 107, arXiv:1610.00584 [gr-qc].

[424] E. Alvarez and J. Conde, "Are the string and Einstein frames equivalent?," *Mod. Phys. Lett. A* **17** (2002) 413–420, arXiv:gr-qc/0111031.

[425] A. Karam, T. Pappas, and K. Tamvakis, "Frame-dependence of higher-order inflationary observables in scalar-tensor theories," *Phys. Rev. D* **96** no. 6, (2017) 064036, arXiv:1707.00984 [gr-qc].

[426] S. Pandey, S. Pal, and N. Banerjee, "Equivalence of Einstein and Jordan frames in quantized anisotropic cosmological models," *Annals Phys.* **393** (2018) 93–106, arXiv:1611.07043 [gr-qc].

[427] M. Bounakis and I. G. Moss, "Gravitational corrections to Higgs potentials," *JHEP* **04** (2018) 071, arXiv:1710.02987 [hep-th].

[428] A. Karam, A. Lykkas, and K. Tamvakis, "Frame-invariant approach to higher-dimensional scalar-tensor gravity," *Phys. Rev. D* **97** no. 12, (2018) 124036, arXiv:1803.04960 [gr-qc].

[429] V. Faraoni and E. Gunzig, "Einstein frame or Jordan frame?," *Int. J. Theor. Phys.* **38** (1999) 217–225, arXiv:astro-ph/9910176.

[430] F. Briscese, E. Elizalde, S. Nojiri, and S. D. Odintsov, "Phantom scalar dark energy as modified gravity: Understanding the origin of the Big Rip singularity," *Phys. Lett. B* **646** (2007) 105–111, arXiv:hep-th/0612220.

[431] S. Capozziello, S. Nojiri, S. D. Odintsov, and A. Troisi, "Cosmological viability of f(R)-gravity as an ideal fluid and its compatibility with a matter dominated phase," *Phys. Lett. B* **639** (2006) 135–143, arXiv:astro-ph/0604431.

[432] S. Bahamonde, S. D. Odintsov, V. K. Oikonomou, and M. Wright, "Correspondence of $F(R)$ Gravity Singularities in Jordan and Einstein Frames," *Annals Phys.* **373** (2016) 96–114, arXiv:1603.05113 [gr-qc].

[433] S. Bahamonde, S. D. Odintsov, V. K. Oikonomou, and P. V. Tretyakov, "Deceleration versus acceleration universe in different frames of $F(R)$ gravity," *Phys. Lett. B* **766** (2017) 225–230, arXiv:1701.02381 [gr-qc].

[434] E. Frion and C. R. Almeida, "Affine quantization of the Brans-Dicke theory: Smooth bouncing and the equivalence between the Einstein and Jordan frames," *Phys. Rev. D* **99** no. 2, (2019) 023524, arXiv:1810.00707 [gr-qc].

[435] T. Chiba and M. Yamaguchi, "Conformal-Frame (In)dependence of Cosmological Observations in Scalar-Tensor Theory," *JCAP* **10** (2013) 040, arXiv:1308.1142 [gr-qc].

[436] G. Domènech and M. Sasaki, "Conformal Frame Dependence of Inflation," *JCAP* **04** (2015) 022, arXiv:1501.07699 [gr-qc].

[437] C. F. Steinwachs and A. Y. Kamenshchik, "Non-minimal Higgs Inflation and Frame Dependence in Cosmology," *AIP Conf. Proc.* **1514** no. 1, (2013) 161–164, arXiv:1301.5543 [gr-qc].

[438] L. Järv, K. Kannike, L. Marzola, A. Racioppi, M. Raidal, M. Rünkla, M. Saal, and H. Veermäe, "Frame-Independent Classification of Single-Field Inflationary Models," *Phys. Rev. Lett.* **118** no. 15, (2017) 151302, arXiv:1612.06863 [hep-ph].

[439] M. Herrero-Valea, "Anomalies, equivalence and renormalization of cosmological frames," *Phys. Rev. D* **93** no. 10, (2016) 105038, arXiv:1602.06962 [hep-th].

[440] K. Falls and M. Herrero-Valea, "Frame (In)equivalence in Quantum Field Theory and Cosmology," *Eur. Phys. J. C* **79** no. 7, (2019) 595, arXiv:1812.08187 [hep-th].

[441] M. Herrero-Valea, "A Path (Integral) to Scale Invariance," (7, 2020) , arXiv:2007.04335 [hep-th].

[442] K. Finn, *Geometric Approaches to Quantum Field Theory*. PhD thesis, Department of Physics and Astronomy, University of Manchester, Manchester, UK, GRID:grid.5379.8, Manchester U., 2021.

[443] K. Finn, V. Gattus, S. Karamitsos, and A. Pilaftsis, "Geometrising the Micro-Cosmos on a Supermanifold," *PoS* **CORFU2021** (2022) 080, arXiv:2204.00123 [hep-th].

[444] D. Burns, S. Karamitsos, and A. Pilaftsis, "Frame-Covariant Formulation of Inflation in Scalar-Curvature Theories," *Nucl. Phys. B* **907** (2016) 785–819, arXiv:1603.03730 [hep-ph].

[445] I. G. Moss, "Covariant one-loop quantum gravity and Higgs inflation," (9, 2014) , arXiv:1409.2108 [hep-th].

[446] T. Cohen, N. Craig, X. Lu, and D. Sutherland, "On-Shell Covariance of Quantum Field Theory Amplitudes," *Phys. Rev. Lett.* **130** no. 4, (2023) 041603, arXiv:2202.06965 [hep-th].

[447] B. S. DeWitt, "The effective action," in *Les Houches School of Theoretical Physics: Architecture of Fundamental Interactions at Short Distances*, P. Ramond and R. Stora, eds., pp. 1023–1058. North-Holland, Amsterdam, 1987.

[448] B. S. DeWitt, *Supermanifolds*. Cambridge monographs on mathematical physics. Cambridge University Press, Cambridge, second edition. ed., 1991.

[449] G. A. Vilkovisky, "The Unique Effective Action in Quantum Field Theory," *Nucl. Phys. B* **234** (1984) 125–137.

[450] E. Brezin, J. Zinn-Justin, and J. C. Le Guillou, "Renormalization of the Nonlinear Sigma Model in (Two + Epsilon) Dimension," *Phys. Rev. D* **14** (1976) 2615.

[451] A. Rogers, *Supermanifolds : theory and applications*. Ebook central. World Scientific, Singapore ; Hackensack, NJ, 2007.

[452] G. A. Vilkovisky, "The Gospel According to DeWitt," in *Quantum Theory of Gravity: Essays in honor of the 60th birthday of Bryce S. DeWitt*, S. M. Christensen, ed., pp. 169–209. Adam Hilger Ltd, 1984.

[453] P. Ellicott and D. J. Toms, "On the New Effective Action in Quantum Field Theory," *Nucl. Phys. B* **312** (1989) 700–714.

[454] S. Aashish, S. Panda, A. A. Tinwala, and A. Vidyarthi, "Covariant effective action for scalar-tensor theories of gravity," *JCAP* **10** (2021) 006, arXiv:2104.12713 [hep-th].

[455] B. L. Giacchini, T. de Paula Netto, and I. L. Shapiro, "On the Vilkovisky-DeWitt approach and renormalization group in effective quantum gravity," *JHEP* **10** (2020) 011, arXiv:2009.04122 [hep-th].

[456] R. Casadio, A. Kamenshchik, and I. Kuntz, "Background independence and field redefinitions in quantum gravity," *Annals Phys.* **449** (2023) 169203, arXiv:2210.04368 [hep-th].

[457] I. Kuntz, R. Casadio, and A. Kamenshchik, "Covariant singularities: A brief review," *Mod. Phys. Lett. A* **37** no. 10, (2022) 2230007, arXiv:2203.11259 [hep-th].

[458] R. Casadio, A. Kamenshchik, and I. Kuntz, "Absence of covariant singularities in pure gravity," *Int. J. Mod. Phys. D* **31** no. 01, (2022) 2150130, arXiv:2008.09387 [gr-qc].

[459] R. Casadio, A. Kamenshchik, and I. Kuntz, "Covariant singularities in quantum field theory and quantum gravity," *Nucl. Phys. B* **971** (2021) 115496, arXiv:2102.10688 [hep-th].

[460] F. L. Bezrukov and M. Shaposhnikov, "The Standard Model Higgs boson as the inflaton," *Phys. Lett. B* **659** (2008) 703–706, arXiv:0710.3755 [hep-th].

[461] M. P. Hertzberg, "On Inflation with Non-minimal Coupling," *JHEP* **11** (2010) 023, arXiv:1002.2995 [hep-ph].

[462] F. Bezrukov, A. Magnin, M. Shaposhnikov, and S. Sibiryakov, "Higgs inflation: consistency and generalisations," *JHEP* **01** (2011) 016, arXiv:1008.5157 [hep-ph].

[463] S. Mooij, M. Shaposhnikov, and T. Voumard, "Hidden and explicit quantum scale invariance," *Phys. Rev. D* **99** no. 8, (2019) 085013, arXiv:1812.07946 [hep-th].

[464] M. Shaposhnikov and K. Shimada, "Asymptotic Scale Invariance and its Consequences," *Phys. Rev. D* **99** no. 10, (2019) 103528, arXiv:1812.08706 [hep-ph].

[465] P. G. Ferreira, C. T. Hill, and G. G. Ross, "Weyl Current, Scale-Invariant Inflation and Planck Scale Generation," *Phys. Rev. D* **95** no. 4, (2017) 043507, arXiv:1610.09243 [hep-th].

[466] D. M. Ghilencea, Z. Lalak, and P. Olszewski, "Two-loop scale-invariant scalar potential and quantum effective operators," *Eur. Phys. J. C* **76** no. 12, (2016) 656, arXiv:1608.05336 [hep-th].

[467] D. M. Ghilencea, "Manifestly scale-invariant regularization and quantum effective operators," *Phys. Rev. D* **93** no. 10, (2016) 105006, arXiv:1508.00595 [hep-ph].

[468] R. A. Matzner, M. F. Huq, and D. Shoemaker, "Initial data and coordinates for multiple black hole systems," *Phys. Rev. D* **59** (1999) 024015, arXiv:gr-qc/9805023.

[469] O. J. Tattersall, "Kerr–(anti–)de Sitter black holes: Perturbations and quasinormal modes in the slow rotation limit," *Phys. Rev. D* **98** no. 10, (2018) 104013, arXiv:1808.10758 [gr-qc].

[470] C. Bona, J. Masso, E. Seidel, and J. Stela, "A New formalism for numerical relativity," *Phys. Rev. Lett.* **75** (1995) 600–603, arXiv:gr-qc/9412071.

[471] J. R. van Meter, J. G. Baker, M. Koppitz, and D.-I. Choi, "How to move a black hole without excision: Gauge conditions for the numerical evolution of a moving puncture," *Phys. Rev. D* **73** (2006) 124011, arXiv:gr-qc/0605030.

[472] J. Ke, J. Luo, C.-G. Shao, Y.-J. Tan, W.-H. Tan, and S.-Q. Yang, "Combined Test of the Gravitational Inverse-Square Law at the Centimeter Range," *Phys. Rev. Lett.* **126** no. 21, (2021) 211101.

[473] S.-Q. Yang, B.-F. Zhan, Q.-L. Wang, C.-G. Shao, L.-C. Tu, W.-H. Tan, and J. Luo, "Test of the Gravitational Inverse Square Law at Millimeter Ranges," *Phys. Rev. Lett.* **108** (2012) 081101.

[474] M. V. Moody and H. J. Paik, "Gauss's law test of gravity at short range," in *28th Rencontres de Moriond: Perspectives in Neutrinos, Atomic Physics and Gravitation*, pp. 403–408. 1993.

[475] R. D. Newman, E. C. Berg, and P. E. Boynton, "Tests of the gravitational inverse square law at short ranges," *Space Sci. Rev.* **148** (2009) 175–190.

[476] E. Fischbach and C. L. Talmadge, *The Search for Non-Newtonian Gravity*. Springer Science, New York, 1999.

[477] P. Baldi, E. G. Campari, G. Casula, S. Focardi, and F. Palmonari, "Testing newton's inverse square law at intermediate scales," *Phys. Rev. D* **64** (2001) 082001.

[478] D. M. Lucchesi and R. Peron, "LAGEOS II pericenter general relativistic precession (1993–2005): Error budget and constraints in gravitational physics," *Phys. Rev. D* **89** no. 8, (2014) 082002.

[479] E. G. Adelberger, B. R. Heckel, and A. E. Nelson, "Tests of the gravitational inverse square law," *Ann. Rev. Nucl. Part. Sci.* **53** (2003) 77–121, arXiv:hep-ph/0307284.

[480] A. Bassi, L. Cacciapuoti, *et al.*, "A way forward for fundamental physics in space," *npj Microgravity* **8** (11, 2022) 49.

[481] E. V. Pitjeva and N. P. Pitjev, "Relativistic effects and dark matter in the Solar system from observations of planets and spacecraft," *Mon. Not. Roy. Astron. Soc.* **432** (2013) 3431, arXiv:1306.3043 [astro-ph.EP].

[482] E. V. Pitjeva and N. P. Pitjev, "Masses of the Main Asteroid Belt and the Kuiper Belt from the Motions of Planets and Spacecraft," *Astronomy Letters* **44** no. 8-9, (Aug., 2018) 554–566, arXiv:1811.05191 [astro-ph.EP].

[483] L. Iorio, "Calculation of the Uncertainties in the Planetary Precessions with the Recent EPM2017 Ephemerides and their Use in Fundamental Physics and Beyond," *Astron. J.* **157** no. 6, (2019) 220, arXiv:1810.13415 [gr-qc]. [Erratum: Astron.J. 165, 76 (2023)].

[484] F. De Marchi and G. Cascioli, "Testing General Relativity in the Solar System: present and future perspectives," *Class. Quant. Grav.* **37** no. 9, (2020) 095007, arXiv:1911.05561 [gr-qc].

[485] S. Hou and Y. Gong, "Constraints on Horndeski Theory Using the Observations of Nordtvedt Effect, Shapiro Time Delay and Binary Pulsars," *Eur. Phys. J. C* **78** no. 3, (2018) 247, arXiv:1711.05034 [gr-qc].